

Université de Liège
Faculté des Sciences Appliquées

Finite Element Modelling
in Structural and Petroleum Geology

par
Jean-Dominique BARNICHON

Thèse défendue, avec succès, le 7 janvier 1998,
pour l'obtention du grade scientifique de Docteur en Sciences Appliquées

devant un jury composé de :

D. Jongmans, Chargé de Cours à l'Université de Liège, Président,
R. Charlier, Chargé de Cours à l'Université de Liège, Promoteur
F. Bonnechère, Professeur à l'Université de Liège,
S. Cescotto, Professeur à l'Université de Liège,
J. Cosgrove, Senior Lecturer à l'Imperial College de Londres,
F. Darve, Professeur à l'INP de Grenoble,
D. Fourmaintraux, Professeur à l'Université de Paris VI,
W. Sassi, Dr., Chercheur à l'Institut Français du Pétrole,
J-P. Vilotte, Dr., Chercheur à l'Institut de Physique du Globe de Paris.

Collection des Publications de la Faculté des Sciences Appliquées n°186
Année académique 1997-1998

Summary

This thesis is dedicated to the study of structural and petroleum geology problems. To this purpose, a frictional elastoplastic law based on the Van Eekelen criterion is formulated, which avoids the classical drawbacks of the Drücker Prager criterion. Also, a 2D automatic adaptive re-meshing algorithm is developed for complex multidomains configurations, in order to overcome the limitation of the Lagrangian mesh. Details of the hydromechanical formulation implemented in the LAGAMINE FE code in a large strain context are presented.

Application cases (reproduction of sandbox simulation, study of a hydrocarbon trap) concentrate on the study of the strain localisation and potential fracturation using different criteria. In the first case, re-meshing technique allowed to reproduce successfully analogue experiment of thrusting propagation. In the second case, a detailed study based on different initial conditions has brought new insight to the reactivated origin of some faults and has allowed to obtain information on the potential fracturing of the hydrocarbon reservoir unit. As an academic case, the study of anorthosite diapirism is carried out, which confirms the validity of the petrological model of diapirism. Eventually, the hydromechanical coupling effects between a layered porous medium and a fault are illustrated on a simple case.

Table of Contents

Summary	i
Notation, symbols	vii
Abbreviations, some definitions	xi
Chapter 1 - Introduction	1
1.1 Structural geology and geomechanics	3
1.2 Some methods used for the modelling in structural geology	4
1.3 Objectives of this research	5
1.4 Outline of the thesis	6
1.5 Original contributions	7
Chapter 2 - Mechanical modelling of geomaterials : finite elements and constitutive laws	9
2.1 Introduction	11
2.2 Large strain finite element formulation for mechanical analysis	12
2.2.1 Referential, strain and stress	12
2.2.2 Constitutive relations	13
2.2.3 Equilibrium condition	13
2.2.4 Finite element discretisation	14
2.2.4.1 Solid finite elements	14
2.2.4.2 Contact finite elements	17
2.2.4.2.1 Contact between a deformable solid (Ω^U) and a rigid solid (Ω^D)	19
2.2.4.2.2 Contact between two deformable solids (Ω^U) and (Ω^D)	20
2.2.5 General algorithm of the <i>LAGAMINE</i> code for mechanical analysis	20
2.3 Frictional elastoplastic constitutive laws for geomaterials	23
2.3.1 Incremental general elastoplastic formulation	23
2.3.2 Yield surfaces for frictional behaviour of geomaterials	26
2.3.2.1 Stress invariants and stress space	27
2.3.2.2 Mohr Coulomb criterion (MC)	28
2.3.2.3 Drucker-Prager criterion (DP)	29
2.3.2.4 Van Eekelen criterion (VE)	32
2.3.2.5 Convexity condition for the Van Eekelen surface	36
2.3.2.5.1 Exponent n	36
2.3.2.5.2 Friction angle values	37
2.3.2.5.3 The ratio between ϕ_C and ϕ_E	37
2.3.2.5.4 Conclusion on the convexity condition	37
2.3.2.6 Comparison between MC, DP and VE yield criteria	38
2.3.2.7 Frictionless behaviour	39
2.3.2.8 Traction behaviour (apex regime)	40

2.3.3 Integration of the elastoplastic constitutive relation	41
2.3.3.1 Elastic predictor	41
2.3.3.2 Plastic corrector	42
2.3.3.3 Test of the integration algorithm	46
2.3.3.4 Sub step integration	47
2.3.3.5 Implementation in the <i>LAGAMINE</i> code	47
2.4 Some other constitutive laws for geomaterials	48
2.4.1 An elastoviscoplastic law	48
2.4.2 Contact laws	48
2.4.2.1 Coulomb frictional model	48
2.4.2.2 Other laws	49
2.5 Initiation of the stress state	51
2.6 Predictive models for strain localisation and failure	53
2.6.1 Scalar indicators of strain localisation estimated from plasticity theory	53
2.6.2 Directions of failure estimated from plasticity theory	54
2.6.3 Rice bifurcation criterion	54
2.6.4 Wallace-Bott shape ratio of the stress tensor	56
2.7 Conclusion	58
Chapter 3 - Coupled hydromechanical behaviour of porous geomaterials : finite elements and constitutive laws	59
3.1 Introduction	61
3.2 Classical poromechanics	62
3.2.1 Definition of the granular porous medium, hypotheses	62
3.2.2 Problem formulation	63
3.2.2.1 Kinematics of the porous medium	63
3.2.2.1.1 Eulerian description of the fluid kinematics	63
3.2.2.1.2 Lagrangian description of the fluid kinematics	63
3.2.2.2 Variation in fluid mass content, fluid mass conservation	63
3.2.3 Constitutive laws	64
3.2.3.1 Linearised fluid state equation	64
3.2.3.2 Flow behaviour	65
3.2.3.3 Linear poroelastic behaviour in infinitesimal transformation	65
3.2.3.4 Poroplastic behaviour in infinitesimal transformation	68
3.3 Poromechanical formulation in the <i>LAGAMINE</i> code in finite strain	70
3.3.1 Formulation for the solid phase	70
3.3.1.1 Mechanical law	70
3.3.1.2 Apparent specific mass up-date	70
3.3.1.3 Porosity up-date	71
3.3.1.4 Equilibrium	71
3.3.2 Formulation for the fluid phase	71
3.3.2.1 Flow law	72
3.3.2.2 Storage law	72

3.3.2.3 Permeability up-date	72
3.3.2.4 Equilibrium	73
3.3.3 Coupling stiffness matrixes	73
3.3.4 Summary	73
3.4 Consolidation of a soil layer in infinitesimal transformation	75
3.4.1 Analytical solution	75
3.4.2 Finite element representation	76
3.4.3 Comparison between analytical and finite element solution	76
3.5 Conclusion	78
Chapter 4 - Localisation and adaptive re-meshing	79
4.1 Introduction	81
4.2 Re-meshing decision	82
4.2.1 Error estimation	82
4.2.2 Distortion criterion	83
4.3 Re-meshing strategy	84
4.3.1 Overview	84
4.3.2 Analysis of the current configuration (program <i>CRECOU</i>)	84
4.3.3 Generation of the new mesh for the solid domain (program <i>GMAILL</i>)	86
4.3.4 Reconstruction of boundary conditions and global data (program <i>CREDAT</i>)	87
4.3.5 Transfer of the solution and state variable fields (program <i>INTERP</i>)	87
4.3.5.1 Original transfer method	88
4.3.5.2 Developed transfer method	90
4.3.5.2.1 Nodal extrapolation of integration point values (in the old mesh)	90
4.3.5.2.2 Interpolation of nodal fields of M^F to points (nodes or integration points) of M^S	90
4.3.5.3 Transfer of contact data	93
4.3.6 Plastic admissibility	93
4.3.7 Equilibrium of the initial state	94
4.4 Additional improvements	96
4.4.1 Update of the initial configuration	96
4.4.2 Introduction of passive markers of the finite displacement	96
4.5 Conclusion	97
Chapter 5 - Influence of the limit surface shape on the stress state in geomechanical simulations	99
5.1 Introduction	101
5.2 Particularities of geological stress fields, implications for geomechanical simulations ..	102
5.3 Application case 1 : simulation of the stress state in an anticline structure	107
5.3.1 Initial model	107
5.3.2 Results	108

5.3.2.1 Coulomb's mobilised friction angle profiles	108
5.3.2.2 Stress profiles	109
5.3.2.3 Dilatancy influence	111
5.3.2.4 Stress overestimation	112
5.4 Application case 2 : modelling with frictional interfaces	113
5.5 Conclusion	115
Chapter 6 - Simulation of forward thrust propagation in sandbox experiments	117
6.1 Introduction	119
6.2 Simulation of thrusting in sandbox experiments	120
6.3 Finite element simulation of thrusting propagation	121
6.3.1 Initial geometry, boundary conditions and rheological parameters	121
6.3.2 Model 1	123
6.3.3 Model 2	131
6.3.4 Interpretation and comparison of the results	138
6.4 Conclusion	139
Chapter 7 - Diapiric emplacement of the Egersund-Ogna anorthosite massif	141
7.1 Introduction	143
7.2 The diapirism : a brief review	144
7.2.1 Mechanism of diapirism	144
7.2.2 Modelling, state of the art	145
7.3 The Egersund-Ogna anorthosite massif, South Norway	146
7.3.1 Regional geology	146
7.3.2 Depth and timing of emplacement, gravity data	146
7.3.3 Lithological profile	148
7.3.4 Constitutive flow laws for the continental crust	149
7.3.5 Computation of rheological profiles	150
7.4 Diapir model 1	154
7.4.1 Initial geometry, boundary conditions	154
7.4.2 Constitutive laws	155
7.4.3 Results	156
7.5 Anorthosite thickness and viscosity influence : diapir models 2, 3 and 4	162
7.6 Comparison with field observations	164
7.7 Conclusion	165
Chapter 8 - The Garret El Gueffoul anticline structure : faulting and fracturing	167
8.1 Introduction	169
8.2 Geological settings of the Ahnet basin	170
8.2.1 Regional geology and stratigraphy	170
8.2.2 Palaeo-structural evolution of the Ahnet basin	173

8.3 The Garret El Gueffoul anticline structure	174
8.3.1 Presentation	174
8.3.2 Problems raised and aim of the modelling	174
8.3.3 Initial geometry, boundary conditions and rheological parameters	177
8.4 Two dimensional models from the present day geometry	181
8.4.1 Model 0 with no detachment fault	181
8.4.2 Model 1 with full detachment fault	182
8.4.3 Model 2 with full detachment fault	183
8.4.4 Model 3 with partial detachment fault	184
8.4.5 Interpretation	193
8.4.5.1 Origin of the forward reverse fault 1	193
8.4.5.2 Origin of the backward faults 2 in the western limb	193
8.4.5.3 Loading direction, plane strain assumption	196
8.4.6 Implication for the reservoir fracturing	196
8.4.7 Conclusion	197
8.5 Two dimensional models from the pre-Hercynian geometry	198
8.5.1 Model 4 with full detachment fault	198
8.5.2 Model 5 with partial detachment fault	199
8.5.3 Interpretation	209
8.5.4 Implication for the reservoir fracturing	209
8.6 Three dimensional models from the present day geometry	211
8.6.1 Initial geometry and boundary conditions	211
8.6.2 Results	214
8.7 Conclusion	220
Chapter 9 - Hydromechanical modelling of compaction	223
9.1 Introduction	225
9.2 A simple compaction model with fault	226
9.2.1 Models with low sedimentation rate	229
9.2.2 Models with very high sedimentation rate	229
9.3 Conclusion	235
Chapter 10 - General conclusion and perspectives	237
10.1 General conclusion	239
10.2 Perspectives	240
Appendix	241
References	245

Notation

$(\dot{}), \frac{d()}{dt}$	time derivative
$()'$	effective (or drained) component in case of HM coupling
a	scalar
\mathbf{a}, a_i	vector
\mathbf{a}, a_{ij}	second order tensor
\mathbf{a}, a_{ijkl}	fourth order tensor
$a(\mathbf{x})$	scalar field
$\mathbf{a}(\mathbf{x})$	tensorial field
δ_{ij} or \mathbf{I}	unit tensor
$\text{Det}(\mathbf{a}), \mathbf{a} $	determinant of \mathbf{A}
\mathbf{a}^{-1}	inverse of a tensor
\mathbf{a}^T	transpose of a tensor
$\nabla \mathbf{a}, \frac{\partial a}{\partial x_i}$	gradient of a scalar field

Operators on vectors :

$\mathbf{c}=\mathbf{a}\cdot\mathbf{b}, c=a_i b_i$	scalar product
$\mathbf{c}=\mathbf{a}\otimes\mathbf{b}, c_{ij}=a_i b_j$	tensorial product
$\nabla \mathbf{a}, \frac{\partial a_i}{\partial x_j}$	gradient of a vector field
$\text{div } \mathbf{a}, \frac{\partial a_i}{\partial x_i}$	divergence of a vector field

Operators on tensors :

$\mathbf{c}=\mathbf{a}:\mathbf{b}, c=a_{ij} b_{ij}$ or $c_{ij}=a_{ijkl} b_{kl}$	scalar product
$\text{div } \mathbf{a}, \frac{\partial a_{ij}}{\partial x_i}$	divergence of a second order tensor field

Latin symbols

\mathbf{B}	Biot tensor
B_p, B_c	hardening coefficients of the <i>PLASOL</i> law
B_S	Skempton coefficient
b	Biot coefficient (if isotropy $\mathbf{B}=\mathbf{b}\mathbf{I}$)
\mathbf{C}^e	Elastic compliance matrix
\mathbf{C}^{ep}	Elastoplastic compliance matrix
c	cohesion
ck_0	parameter in the Kozeny-Carman porosity-permeability relation
$dsig$	specific weight used to initiate a stress state

E	Young modulus
E_f	fluid Young modulus
E'	effective Young modulus (relates to the skeleton)
e	void ratio
\mathbf{F}	strain gradient
\mathbf{F}	nodal forces
\mathbf{F}_g	body forces
f	yield criterion
G	elastic shear modulus
\mathbf{G}	natural strain tensor
\mathbf{g}	vector describing the shear band mode (in chapter 2)
\mathbf{g}	vector of gravity acceleration
g	flow potential
H	yield limit of the <i>IRSID</i> elastoviscoplastic law
\mathbf{I}	unit tensor
I_σ	first stress invariant
$II_{\hat{\sigma}}$	second deviatoric stress invariant
$III_{\hat{\sigma}}$	third deviatoric stress invariant
\mathbf{J}	Jacobian matrix
J	volume variation between initial and current configuration
K	elastic bulk modulus (undrained if HM coupling)
K'	drained elastic bulk modulus if HM coupling
K_f	fluid elastic bulk modulus
K_P	contact penalty coefficient on contact pressure
K'	skeleton elastic bulk modulus
K_τ	contact penalty coefficient on contact tangential stress
K_0	ratio between the horizontal and the vertical stress component
\mathbf{K}	global stiffness matrix
\mathbf{k}	element stiffness matrix
K	permeability coefficient
\mathbf{K}	permeability tensor
k	intrinsic permeability
\mathbf{L}	velocity gradient
M	Biot modulus
m	change in fluid mass content, or storage
n	exponent in the Van Eekelen yield criterion formulation
n	exponent in the power law (chapter 8)
n	porosity
n^p	plastic porosity
N_{intv}	number of sub-intervals for the integration of the stress-strain relation

p	pressure (mean stress)
p_f	fluid pressure
Q	volume flux
q	surface flux
R	Wallace-Bott stress shape ratio
S	mode of Rice bifurcation
Sh	shortening applied
T	Fault transmissivity
\mathbf{t}, t_i	surface forces vector
\mathbf{u}, u_i	displacement vector
V	volume
\mathbf{v}, v_i	velocity vector
\mathbf{v}^d	Darcy's fluid velocity
\mathbf{v}^r	effective fluid velocity
\mathbf{w}	fluid mass vector

Greek letters

$\Delta()$	increment
Γ	reference configuration
Φ	isoparametric interpolation function
Ω	domain
$d\Omega$	elementary domain
$\partial\Omega$	domain boundary
$\partial\omega$	boundary segment
α	kinematic scalar indicator of localisation
β	Lode angle
δ	virtual quantity
δ_{ij}	Kronecker delta
$\boldsymbol{\varepsilon}, \varepsilon_{ij}$	strain tensor
ε_{eq}	equivalent strain
ε_{eq}^p	equivalent plastic strain
$\varepsilon_{eq(l)}$	local equivalent strain, i.e. for which the reference configuration is not the initial one, but any arbitrary configuration between the initial and the current configuration.
ε_m	mean or volumetric strain
ϕ	friction angle
ϕ_C	friction angle for triaxial compression stress paths
ϕ_E	friction angle for triaxial extension stress paths
ϕ_m	Coulomb's mobilised friction angle
γ	specific weight

η	local co-ordinate
η	viscosity
η^*	linearised viscosity
κ	internal variables
λ	plastic multiplier
λ_C	distance between contact interfaces
μ	fault friction coefficient
μ_f	fluid dynamic viscosity
ν	Poisson coefficient
ν'	effective Poisson coefficient (relates to the skeleton)
ρ	specific mass]
ρ_a	apparent specific mass
ρ_f	fluid specific mass
ρ_s	grain specific mass
σ, σ_{ij}	stress tensor
σ', σ'_{ij}	effective stress tensor
$\hat{\sigma}, \hat{\sigma}_{ij}$	deviatoric stress tensor
$\tilde{\sigma}, \tilde{\sigma}_{ij}$	Jaumann derivative of the stress tensor
$\sigma_1^*, \sigma_2^*, \sigma_3^*$	projection of the principal stress on the deviatoric plane
σ_C	contact stress vector
σ_{eq}	equivalent stress
σ_h	horizontal component of stress
σ_m	mean pressure
σ_N	contact pressure
σ_v	vertical component of stress
τ	contact shear stress
ω	spin rate tensor
ξ	local co-ordinate
ξ	vector of local co-ordinates
ψ	dilatancy angle
ψ_C	dilatancy angle for triaxial compression stress paths
ψ_E	dilatancy angle for triaxial extension stress paths
ζ	local co-ordinate
ζ^{glo}	global error
ζ^{loc}	local error

Abbreviations

CPU	Computing Per Unit time
DP	Drücker Prager
FE	Finite element
HAOM	High Alumina Orthopyroxene Megacrysts
HM	HydroMechanical
i.p.	Integration points
Ma	10^6 years
MC	Mohr Coulomb
VE	Van Eekelen

Some definitions

offset of a fault :	relative displacement between the two blocks which are separated by a fault. As plane strain 2D models are considered, it correspond to the dip-slip component heave
reverse or thrust fault :	fault resulting from compression in which the hanging wall (upper block) has an upward movement relative to the footwall (lower block).
forward reverse fault :	fault which relative movement has the same orientation than the general displacement induced by tectonic loading.
backward reverse fault :	fault which relative movement has the opposite orientation than the general displacement induced by tectonic loading.
pop-up structure :	structure formed by the meeting in depth of a forward and a backward reverse fault.

CHAPTER 1

Introduction

1.1 Structural geology and geomechanics

The work presented in this thesis lies at the boundary between structural geology, geomechanics and numerical methods. The geological problem represents in the same time the starting point and the ultimate goal of this study. Between them, models (analogue or numerical) are defined to represent an idealisation of the geological reality and to allow the understanding of the assumed phenomenon. Here the choice is made for numerical models in order to solve the geomechanical problem.

As geology is the underlying motivation of this study, some basic geological terminology and concepts which are not usual in civil engineering are recalled. Geology deals with the study of the earth planet, including all its aspects (volcanism, tectonics, oceans, chemistry...). The earth crust (of approximate thickness of 40km for continents) is a part of the tectonic plates, which relative movements (e.g. resulting in plate collision, subduction) have been and still are responsible of the earth topography : mountain belts, sedimentary basins, volcanoes, oceans. Due to tectonic movements (shortening, stretching), parts of the earth crust accommodate deformation by the development of several structures such as folds, faults, and fractures, which can be generated at different scales. For instance, faults size can range between the large scale (several hundreds of km) to the small scale (few cm) on outcrops. Similar features can be described for folds. All these geological objects are studied in the framework of structural geology.

Problems in structural geology are various, ranging from the large to small scale. Most of them resume to obtain a correct interpretation from various available data.

- Regional data, e.g. the orientation of regional major principal stress (σ_1) which can be inferred from major regional tectonic phases and from large to small scale structures (folds, faults). The tectonic framework of the studied area with respect to global plate tectonic context is also part of the regional data.
- Seismic data which are obtained from the development of geophysical methods. For instance, the present day geometry of an oil basin or reservoir can be estimated from seismic (velocity) cross sections highlighting some reflector horizons. Particularly, 3D seismic surveys give the potential to understand the three dimensional geometry of geological structures.
- Borehole data may be available in area of economic or scientific interest : major principal stress orientation (σ_1) as a function of depth inferred from the ovalisation of originally circular well bores (breakout), horizontal stress gradients derived from “leak off” tests (fracturing). Some other information can be obtained from methods used in well bores (diagraphy), e.g. the fracture orientation and density.

The interest of a correct interpretation might be purely academic, but it can also have some very important industrial importance, for instance considering the petroleum industry (discovery of hydrocarbon traps, planning of exploitation) or the mining industry.

In the particular cases which are of interest in this study, several types of problems must be mentioned.

- The validation of geological models on a structural point of view, starting from available data which are sometimes well defined, but which very often only give a part of the information required. For instance, the geological interpretation of particular field cases may be subject to controversy, i.e. several solutions can be put forward. It is often the case for instance with evaporitic rocks.
- The problematic of strain localisation along shear bands, which leads to the genesis of faults. Although this problem raises some fundamental questions (see chapter 2), it is a very important aspect to take into account as the seismic resolution has a lower bound, i.e. this method is blind to small scales structures (several tens of meters, depending on the rock wave propagation velocity).
- The quantitative evaluation of the stress field and the fracture network is of great interest for drilling operations. A major interest comes from the estimation of the well bore stability which depends strongly on in-situ stresses [FJAER et al., 1992]. Obviously, the well bore stability also depends on the occurrence of pre-existing fractures : any rock discontinuity in the rock mass will increase the risk of well collapse by preferential motion along these planes, provided they are correctly oriented with respect to principal stresses. To this respect, the well bore stability may be influenced by the occurrence of shear bands previously mentioned.
- For the oil production phase, the evaluation and quantification of the reservoir fracturation is very important with respect to the final recovering ratio of hydrocarbons. It also has an influence on the oil production method used in reservoir engineering, as the choice is largely conditioned by the characteristics of the fracture network (crack porosity and permeability).
- The interaction or coupling effects between the solid phase of a rock and its saturating fluid which, from field evidences, are known to occur and are supposed to play a key role on the evolution of the geological system (faulting, fracturing).

1.2 Some methods used for the modelling in structural geology

As already mentioned, the high complexity of geological situations and the only partial data which can be obtained from direct or indirect observation has led structural geologists to simulate natural phenomena in order to better understand and predict them. Such modelling process requires to simplify the observed or interpreted phenomena and consists in trying to reproduce them by some appropriate method.

The first method which has been used for simulating geological processes is the so-called analogue modelling. Based on similarity rules between the three fundamental physical units (M: mass, L: length, T: time) [HUBBERT, 1937], it is possible to define models at reduced geometric and time scales. Such models behave in an analogue way than their corresponding idealised reality, thus they allow to apprehend physical processes at reasonable scales. Analogue materials are usually sand, clays or silicons. [PELTZER et al., 1982] reproduce the

indentation of India into Asia using plasticine analogue. Study of the basement induced faulting using sand as analogue has been presented by [RICHARD et al., 1991] or using clay materials by [RAYNAUD, 1987]. Lithospheric buckling has been studied using sand models by [MARTINOD, 1991]. [MALAVIEILLE, 1984] simulated the genesis of thrust belts using limestone powder. In all these models, the displacements field is obtained either by direct visualisation (through transparent boundaries), by destructive methods or by X-ray tomography. No information is obtained on the stress field and it is very difficult to perform hydromechanically coupled experiments. However, a very interesting aspect of these models comes from their relatively easy use, their natural finite strain "formulation" and their cheap ability to treat three dimensional problems.

Another type of experiments has been imagined. Although these ones are not properly scaled in the sense of [HUBBERT, 1937], they reproduce often very realistic features observed in the field. For instance, [RIVES et al., 1994] studied the joint distribution in relation with folding using a PVC plate covered by a brittle varnish.

Based only on kinematical constraints, kinematical methods for constructing balanced cross section have also been developed in extensional [GIBBS, 1983] and compressional context [ENDIGNOUX and WOLF, 1990]. These methods allow to reconstruct the initial configuration from the interpreted present day structures, and therefore to validate an interpretation from a geometrical point of view. Despite the high interest of such method, its main drawback lies in the fact that the obtained solution does not necessarily verify mechanical equilibrium.

In order to overcome this deficiency, numerical models which verify the physical equilibrium of the solution have been applied to geological problems. Such modelling has been allowed with the development of approached numerical methods such as the finite element method. This method has originally been developed to solve continuum mechanics problems encountered in aeronautics and civil engineering in the framework of infinitesimal strains. Following this method has been applied to study geological problems such as folding [e.g. PARRISH, 1973; DE BREMAECKER and BECKER, 1978] or petroleum related structural problems [e.g. NIEUWLAND and WALTERS, 1993]. In the eighties, the development of finite element codes with finite strain formulation and contact interfaces has been a major improvement with respect to geological applications, together with the development of re-meshing techniques in order to overcome the limitation of Lagrangian FE codes. Eventually, the recent work carried out on the strain localisation and damage (from a theoretical and practical point of view) must also be mentioned for its direct implications on rock faulting and fracturing.

1.3 Objectives of this research

In the present work, our objectives are the following :

- obtain a correct representation of the frictional behaviour of rocks,
- allow the development of large scale faults and/or folds,
- reproduce analogue experiments in which large displacements and strain occur,

- validate or invalidate the petrological model of anorthosite diapirism,
- evaluate the potential fracturing of geological units, which is particularly interesting for hydrocarbon exploration/production,
- show the potential interactions between the porous rock and the saturating fluid, including the effect of permeability barrier or drains.

In order to be able to study the above mentioned points, the Lagrangian *LAGAMINE* finite element code developed at MSM Department of Civil Engineering of Liege University must fulfil the following requirements :

- include solid finite elements formulated for large strain and displacements problems,
- include contacts finite elements to represent the behaviour of faults as mechanical discontinuities,
- allow the possibility to modify and adapt easily the numerical mesh in cases where either strain localisation or very large distortion occurs and for complex multi-domain geometries,
- include a efficient frictional constitutive law to represent the frictional behaviour of rocks constituting the upper crust,
- include an elastoviscoplastic constitutive law to represent the behaviour of deeper rocks (lower crust),
- include the modelling of the fluid flow behaviour within the porous media,
- take into account the coupling effects between the solid constituent of the porous media and the saturating fluid, including fluid transfer at discontinuities (faults),
- include the computation of indicators or criteria which will allow to evaluate and quantify processes such as strain localisation and potential fracturation.

1.4 Outline of the thesis

In the second chapter, the basics about the finite element formulation (mechanics) used in this work is presented, including finite strain aspects. Special care is given to the formulation of an elastoplastic constitutive relation for frictional material, which leads to the choice of a general yield criterion. An overview is also given on some other laws (elastoviscoplastic and contact laws) which are used in application chapters.

The third chapter deals with the poromechanical formulation required to solve coupled hydromechanical problems. After a brief review of existing infinitesimal poroelasticity and poroplasticity theories, the finite strain formulation used in the *LAGAMINE* code is presented. A simple test case verifies the validity of the method.

In the fourth chapter, the developed automatic re-meshing algorithm is described, with a special attention put on the transfer algorithm.

In the fifth chapter, the effect of the yield criterion formulation presented in chapter 2 is illustrated for geological examples. It is particularly shown that the classical Drucker Prager

yield surface may lead to unrealistic stress state within rock massifs, and therefore that more a elaborated criterion must be preferred (for instance the Van Eekelen criterion detailed in chapter 2).

The simulation of the thrust propagation observed in analogue experiments is presented in the sixth chapter. Such modelling has only been possible thanks to the automatic re-meshing algorithm detailed in chapter 4. Results are analysed in terms of strain localisation in shear bands and evolution of stress field. A parametric study of the basal friction influence is performed in order to compare with numerical results with experimental ones.

In the seventh chapter, the modelling of diapiric phenomenon at crustal scale is presented. It is based on available data and confirm the mechanical relevance of the petrological model of anorthosite diapirism at the considered scales.

In the eight chapter, the study of an hydrocarbon field is carried out, regarding the relevance of the global geological interpretation. Numerous cases are studied in order to define a reasonable interpretation of the structure. The study of strain localisation and also of the potential reservoir fracturation is given a particular interest here.

In the ninth chapter, an very simple example is defined and used to illustrate the potential interest of studying hydromechanical coupled problems in geology. Especially, the interactions between the porous solid and the dual hydraulic behaviour of a fault (either a barrier or a drain) are illustrated.

1.5 Original contributions

In this work, my personal and original contributions are :

- the formulation, the extensive study and the implementation of the *PLASOL* law in the code (section 2.3),
- the method introduced to define an initial state of stress, particularly in models which are not regular (non horizontal topographic surface or layers (section 2.5),
- the formal link between classical poromechanics and the formulation retained in the *LAGAMINE* code for hydromechanical coupled problems (section 3.3) in finite strain context,
- the development (within the "re-meshing team" of the MSM department) of a more generalised re-meshing algorithm able to handle much complex geometries (multi-domain) and with a much higher automation than the pre-existing version available at MSM (chapter 4),
- the development of an original transfer method algorithm detailed in section 4.3.5.2 from an original idea by [AALEAI, 1986],
- the development of the possibility to up-date the initial configuration as a consequence of re-meshing (section 4.4.1) and to add passive markers of finite displacement (section 4.4.2),

- the pedagogic illustration of the influence of the yield criterion choice (Drucker Prager or smoothed Mohr Coulomb) on the obtained stress state in geological models (sections 5.2 and 5.3), and also on the solid/contact interaction in models with frictional interfaces (section 5.4),
- the simulation of models with high strain localisation level carried out with the help of the developed re-meshing algorithm (sections 6.3.2 and 6.3.3.),
- the simulation of the diapirism phenomenon using the re-meshing algorithm and considering in the same time an elastoplastic behaviour (upper part of the upper crust) and an elastoviscoplastic behaviour for (anorthosite and lower crust) using solid mechanics formulation (sections 7.4 and 7.5). Particularly, it has led to the validation of the petrological model of anorthosite diapirism,
- the modelling of an hydrocarbon trap structure (chapter 8). In this case, the results have allowed to validate an structural interpretation, but it has also allowed to obtain interesting conclusions based on mechanical arguments about the age and the potential origin of some faults observed from seismic data and for which the origin was matter to discussion (see in particular sections 8.4.5, 8.4.6, 8.5.3). This point is completely new and has not been mentioned in previous studies carried out on this field case, which is also the case for the three dimensional modelling presented in section 8.6.
- The interpretation of potential reservoir fracturing from Rice criterion (sections 8.4.6 and 8.5.4),
- The interaction between porous media and fault acting in the same time as a mechanical and hydraulical discontinuity (sections 9.2.1 and 9.2.2), although this modelling rose some presently unsolved questions (9.2.1).

CHAPTER 2

Mechanical modelling of geomaterials : finite elements and constitutive laws

2.1 Introduction

In this chapter, the basics of the finite element code used in this work (*LAGAMINE*) are presented. However for an extensive description of the *LAGAMINE* code, the reader should refer to [CHARLIER, 1987; HABRAKEN, 1989; WANG, 1993], and for a more general description of the finite element method he should refer to the numerous textbooks published on the finite element method (e.g. [HUSTON and PASSERELLO, 1984; ZIENKIEWICZ and TAYLOR, 1987]).

In the first section of this chapter, basics of the finite element method are given to introduce some notions which will be required further on. Particularly, the choice of a referential frame, the large strain description of kinematics, the general form of constitutive relations used and the general equilibrium formulation are presented. The finite elements used are also presented, both regarding solid finite elements and contact finite elements. Eventually, the global algorithm of the *LAGAMINE* code for mechanical simulations is summarised.

In the second part of this chapter, great attention is paid to the choice of constitutive elastoplastic models which are relevant for the modelling of frictional geomaterials. First of all, the general elastoplastic formulation is recalled. Following, three elastoplastic laws (namely Mohr Coulomb, Drucker Prager and Van Eekelen) are considered with their respective advantages and drawbacks. The Mohr Coulomb criterion is only briefly presented as its corresponding yield surface expressed in generalised stress space is not easy to implement in finite element context. The Drucker Prager criterion is described more extensively, and its main drawback (no dependence on the third stress invariant) is underlined. Eventually the Van Eekelen criterion which includes a dependence on the third stress invariant is presented extensively, including hardening/softening. This leads to the formulation of the unified elastoplastic law *PLASOL* which has been implemented in the *LAGAMINE* code following an implicit integration scheme.

In the third part, some specific constitutive laws developed and implemented by previous researchers in the code, and which have been used in this work, are presented in a more concise fashion.

In the fourth part, the problem of stress initiation is discussed. In simple cases, it is often possible to initiate a balanced stress field in the initial configuration prior to computation, which avoid the classical numerical subsidence phenomenon. However, if complex geometries are considered, this is not possible in general. In such cases, alternative methods are presented.

Eventually in the last part, several criteria which can be used to indicate strain localisation phenomena or to indicate the potential rock failure are presented, as these criteria will be used in application chapters 6, 7 and 8.

2.2 Large strain finite element formulation for mechanical analysis

2.2.1 Referential, strain and stress

The infinitesimal description of the deformation remains valid as long as the final and the initial configurations are very similar. In this simple case, strains (usually referred as Cauchy strains) are defined as a linear function of displacements.

However, when the final configuration is very different from the initial one, the infinitesimal description does no longer hold as the non-linearity of kinematics becomes important. A large strain description of the kinematics is therefore required, which must account for rigid body motion (large translation and/or rotation) and for large deformation. In this case, an appropriate referential frame must be chosen for the description of kinematics.

The kinematics of a solid can be described using either an Eulerian or a Lagrangian referential. In an Eulerian description, the movement of particles is described through a spatially fixed referential frame. In a Lagrangian description, the particle movement is described using a reference frame which is attached to the body. The later is therefore more suited for solid mechanics description.

In this work, equilibrium is expressed using an updated Lagrangian formulation in the current configuration γ (see figure 2.1). Thus on a finite element point of view, it means that this reference configuration evolves at every step. Implication of this choice regarding re-meshing will be discussed in chapter 4.

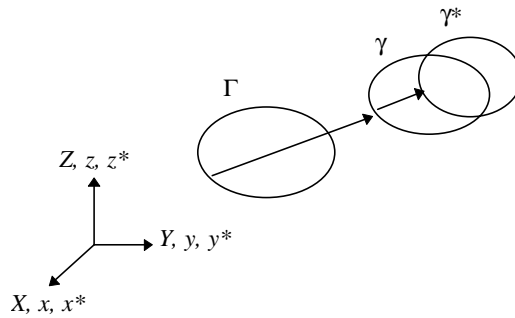


Figure 2.1 Different configurations of a body : Γ (initial configuration), γ (reference configuration), γ^* (deformed configuration).

The Jacobian transformation from the initial to the current configuration which, on a physical point of view, represents here the strain gradient is defined by

$$\mathbf{F} = \frac{\partial \mathbf{x}}{\partial \mathbf{X}} \quad (2.1)$$

The velocity \mathbf{v} of a material point in the current configuration is given by

$$\mathbf{v} = \frac{d\mathbf{x}}{dt} = \dot{\mathbf{x}} \quad (2.2)$$

The velocity gradient \mathbf{L} in the current configuration γ reads

$$\mathbf{L} = \frac{\partial \mathbf{v}}{\partial \mathbf{x}} = \frac{\partial \mathbf{v}}{\partial \mathbf{X}} \frac{\partial \mathbf{X}}{\partial \mathbf{x}} \quad (2.3)$$

which can be decomposed in its symmetrical and anti-symmetrical part

$$\mathbf{L} = \frac{1}{2}(\mathbf{L} + \mathbf{L}^T) + \frac{1}{2}(\mathbf{L} - \mathbf{L}^T) \quad (2.4)$$

The Cauchy strain rate is given as the symmetrical part of the velocity gradient \mathbf{L}

$$\dot{\boldsymbol{\epsilon}} = \frac{1}{2}(\mathbf{L} + \mathbf{L}^T) \quad (2.5)$$

and the spin rate $\boldsymbol{\omega}$ is defined as the anti-symmetrical part of the velocity gradient \mathbf{L}

$$\boldsymbol{\omega} = \frac{1}{2}(\mathbf{L} - \mathbf{L}^T) \quad (2.6)$$

The Cauchy stress tensor $\boldsymbol{\sigma}$, which is symmetrical, is chosen as it is associated with the Cauchy strain rate. The incremental formulation requires to define a stress rate which must be objective (i.e. independent on rigid body rotation). Here the Jaumann objective stress rate is adopted

$$\tilde{\boldsymbol{\sigma}} = \dot{\boldsymbol{\sigma}} - \boldsymbol{\omega}\boldsymbol{\sigma} - \boldsymbol{\sigma}\boldsymbol{\omega}^T \quad (2.7)$$

It must be pointed out that equation (2.5) cannot generally be integrated as it includes a material derivative with respect to the reference configuration γ (which does not remain fixed). Therefore conjugate strains associated with the Cauchy stress tensor do not exist. When strains induced by the whole loading process must be analysed, the natural strain tensor \mathbf{G} can be used

$$\mathbf{G} = \ln \mathbf{U} \quad (2.8)$$

where the stretching tensor \mathbf{U} is obtained by the polar decomposition of the Jacobian \mathbf{F} , \mathbf{R} being the rigid body rotation tensor

$$\mathbf{F} = \mathbf{R}\mathbf{U} \quad (2.9)$$

Note that the strain measure \mathbf{G} coincides with the integral of equation (2.5) in principal axes if they remain unchanged.

2.2.2 Constitutive relations

The constitutive relation between stress rate and strain rate can be written in a general incremental form

$$\tilde{\boldsymbol{\sigma}} = f(\dot{\boldsymbol{\epsilon}}, \boldsymbol{\sigma}, \boldsymbol{\kappa}) \quad (2.10)$$

where $\boldsymbol{\kappa}$ represents some internal variables. The formulation of elastoplastic constitutive relations suitable for geomaterials will be developed in section 2.3.

2.2.3 Equilibrium condition

The general relation for the static equilibrium of an elementary volume is given by

$$\mathbf{div}\boldsymbol{\sigma} + \rho\mathbf{g} = \mathbf{0} \quad (2.11)$$

where ρ : volume mass,

\mathbf{g} : vector of gravity acceleration.

A weak form of this local equilibrium equation can be obtained considering any virtual velocity field $\delta\mathbf{v}$ which is kinematically admissible (i.e. which respects the solid continuity and the boundary conditions). The result is known as the virtual power which expresses the global static equilibrium of the solid

$$\int_V \rho\mathbf{g} \cdot \delta\mathbf{v} \, dV + \int_S \mathbf{t} \cdot \delta\mathbf{v} \, dS = \int_V \boldsymbol{\sigma} : \delta\dot{\boldsymbol{\epsilon}} \, dV \quad (2.12)$$

In this equation, the variables are considered in the current configuration, the right hand side volume integral represents the internal work whereas the two left hand side volume and surface integrals represent the external work (where \mathbf{t} is the vector of surface forces). The virtual work principle states that, for any kinematically compatible virtual velocity field $\delta\mathbf{v}$, the global equilibrium of the solid is verified provided that the external work δW_E is equal to the internal work δW_I

$$\begin{aligned} \delta W_E &= \int_V \rho\mathbf{g} \cdot \delta\mathbf{v} \, dV + \int_S \mathbf{t} \cdot \delta\mathbf{v} \, dS \\ \delta W_I &= \int_V \boldsymbol{\sigma} : \delta\dot{\boldsymbol{\epsilon}} \, dV \end{aligned} \quad (2.13)$$

where $\delta\dot{\boldsymbol{\epsilon}}$ is the virtual strain rate.

2.2.4 Finite element discretisation

Resolution of the equilibrium equation (2.13) requires to discretise the problem, i.e. to divide the domain in elements. Continua are discretised using solid elements and interfaces between bodies are discretised using contact elements.

2.2.4.1 Solid finite elements

2D and 3D isoparametric finite elements of the Serendipity family [ZIENKIEWICZ and TAYLOR, 1987] are used here. For the sake of simplicity, only 2D plane strain elements are described in this section (see figure 2.2). In each element, the co-ordinates \mathbf{x} , the displacement field \mathbf{u} and the velocity field \mathbf{v} are discretised as a function of their nodal values \mathbf{X} , \mathbf{U} , \mathbf{V} using the same interpolation functions Φ

$$\begin{aligned} x_i &= \Phi_L X_{Li} \\ u_i &= \Phi_L U_{Li} \\ v_i &= \Phi_L V_{Li} \end{aligned} \quad (2.14)$$

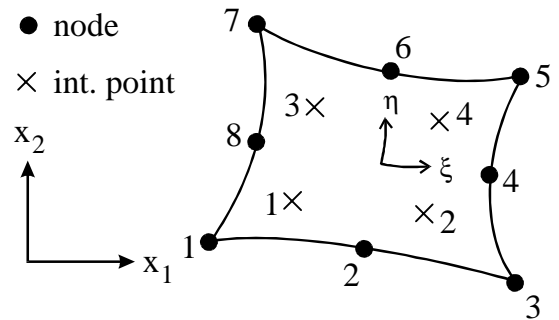


Figure 2.2 Isoparametric plane element.

where the subscript L varies from 1 to the number of nodes of the element. Interpolation functions Φ are defined from the isoparametric co-ordinates (for an exact formulation, refer to [ZIENKIEWICZ and TAYLOR, 1987])

$$\Phi = \Phi(\xi, \eta) \quad (2.15)$$

Considering an element, the internal work reads from relations (2.5) and (2.13)

$$\delta W_I = \int_V \sigma_{ij} \frac{1}{2} \left(\frac{\partial \delta v_i}{\partial x_j} + \frac{\partial \delta v_j}{\partial x_i} \right) dV \quad (2.16)$$

where the virtual velocity gradient

$$\frac{\partial \delta v_i}{\partial x_j} = \frac{\partial \Phi_L}{\partial x_j} \delta V_{Li} \quad (2.17)$$

is function of the spatial derivatives of interpolation function Φ_L in the current configuration

$$\frac{\partial \Phi_L}{\partial x_j} = \frac{\partial \Phi_L}{\partial \xi} \frac{\partial \xi}{\partial x_j} + \frac{\partial \Phi_L}{\partial \eta} \frac{\partial \eta}{\partial x_j} \quad (2.18)$$

The spatial derivatives of local co-ordinates (ξ, η) must be evaluated. For the considered type of element, the Jacobian matrix \mathbf{J} of the transformation from the global co-ordinates (x_1, x_2) to the local co-ordinates (ξ, η) is defined by

$$\mathbf{J} = \begin{bmatrix} \frac{\partial x_1}{\partial \xi} & \frac{\partial x_1}{\partial \eta} \\ \frac{\partial x_2}{\partial \xi} & \frac{\partial x_2}{\partial \eta} \end{bmatrix} \quad (2.19)$$

The Jacobian of the inverse transformation reads

$$\mathbf{J}^{-1} = \begin{bmatrix} \frac{\partial \xi}{\partial x_1} & \frac{\partial \xi}{\partial x_2} \\ \frac{\partial \eta}{\partial x_1} & \frac{\partial \eta}{\partial x_2} \end{bmatrix} = \frac{1}{\det(\mathbf{J})} \begin{bmatrix} \frac{\partial x_2}{\partial \eta} & -\frac{\partial x_1}{\partial \eta} \\ -\frac{\partial x_2}{\partial \xi} & \frac{\partial x_1}{\partial \xi} \end{bmatrix} \quad (2.20)$$

provided that

$$\det(\mathbf{J}) = \frac{\partial x_1}{\partial \xi} \frac{\partial x_2}{\partial \eta} - \frac{\partial x_1}{\partial \eta} \frac{\partial x_2}{\partial \xi} \neq 0 \quad (2.21)$$

Then the internal virtual work equation (2.16) can be expressed as a function of local co-ordinates and integrated using a Gaussian method which gives [CHARLIER, 1987]

$$\delta W_I = \sum_{IP} \left(\sigma_{ij} \frac{1}{2} \left(\frac{\partial \Phi_L}{\partial x_j} \delta V_{Li} + \frac{\partial \Phi_L}{\partial x_i} \delta V_{Lj} \right) t \det(\mathbf{J}) W \right) \quad (2.22)$$

where t is the element thickness (equal to unit for 2D plane elements), IP is the number of integration points and W is the Gauss weight of the integration points. This equation can be re-

arranged to be expressed as a function of the energetically equivalent nodal forces \mathbf{F}_L along global axes 1 and 2

$$\delta W_1 = F_{L1} \delta V_{L1} + F_{L2} \delta V_{L2} \quad (2.23)$$

where

$$\begin{aligned} F_{L1} &= \sum_{IP} \left(\left(\sigma_{11} \frac{\partial \phi_L}{\partial x_1} + \sigma_{12} \frac{\partial \phi_L}{\partial x_2} \right) t \det(\mathbf{J}) W \right) \\ F_{L2} &= \sum_{IP} \left(\left(\sigma_{12} \frac{\partial \phi_L}{\partial x_1} + \sigma_{22} \frac{\partial \phi_L}{\partial x_2} \right) t \det(\mathbf{J}) W \right) \end{aligned} \quad (2.24)$$

These global forces are conjugated with nodal displacements. In the presence of body forces oriented along the vertical axis, the energetically equivalent nodal body forces F_g are given by

$$F_g = \sum_{IP} (\rho g \phi_L t \det(\mathbf{J}) W) \quad (2.25)$$

The specific mass ρ becomes here a state variable due to the mass conservation

$$\rho^\gamma \det(\mathbf{J}^\gamma) = \rho^{\gamma*} \det(\mathbf{J}^{\gamma*}) \quad (2.26)$$

The specific mass is then up-dated incrementally using

$$\rho^{\gamma*} = \rho^\gamma \frac{\det(\mathbf{J}^\gamma)}{\det(\mathbf{J}^{\gamma*})} \quad (2.27)$$

where the superscripts γ and γ^* refer to the current and the incremented configuration, respectively. Thus equation (2.24) reads

$$\begin{aligned} F_{L1} &= \sum_{IP} \left(\left(\sigma_{11} \frac{\partial \phi_L}{\partial x_1} + \sigma_{12} \frac{\partial \phi_L}{\partial x_2} \right) t \det(\mathbf{J}) W \right) \\ F_{L2} &= \sum_{IP} \left(\left(\sigma_{12} \frac{\partial \phi_L}{\partial x_1} + \sigma_{22} \frac{\partial \phi_L}{\partial x_2} - \rho g \phi_L \right) t \det(\mathbf{J}) W \right) \end{aligned} \quad (2.28)$$

It must be pointed out that using equation (2.28), it is possible to compute a balanced initial configuration, i.e. for which $F_{Li} \neq 0$. This is of particular interest for geomechanical models in which body forces resulting from gravity field can be initialised in the initial configuration. It results that such models are already at equilibrium in the initial configuration, thus avoid the classical "numerical subsidence" obtained when no initial lithostatic stress field is initiated.

In the *LAGAMINE* code :

- the corresponding solid finite elements are *PLXLS* (3, 4, 6 or 8 nodes) for two dimensional simulations and *BRILS* (8 or 20 nodes) for three dimensional simulations.
- the initial stress field is computed in the pre-processor *PREPRO* of the *LAGAMINE* code (see section 2.5 for details). Actually, a perfectly balanced initial configuration can only be computed when the geometry of the studied model is simple. If it is not the case, only an approximate initial state of stress can be computed.

2.2.4.2 Contact finite elements

A lot of work has been done by previous researchers to develop efficient contact finite elements (based on penalty method) adapted to large displacements formulation in the *LAGAMINE* code [CHARLIER, 1987; CHARLIER and CESCOTTO, 1988; CESCOTTO and CHARLIER, 1993; HABRAKEN and CESCOTTO, 1996]. As these elements will be used in applications presented further in this work, a brief description is given here.

Consider two deformable solids (or domains) Ω^U and Ω^D with boundaries $\partial\Omega^U$ and $\partial\Omega^D$ (see figure 2.3). They are in perfectly sticking contact through boundaries $\partial\Omega_C^U$ and $\partial\Omega_C^D$.

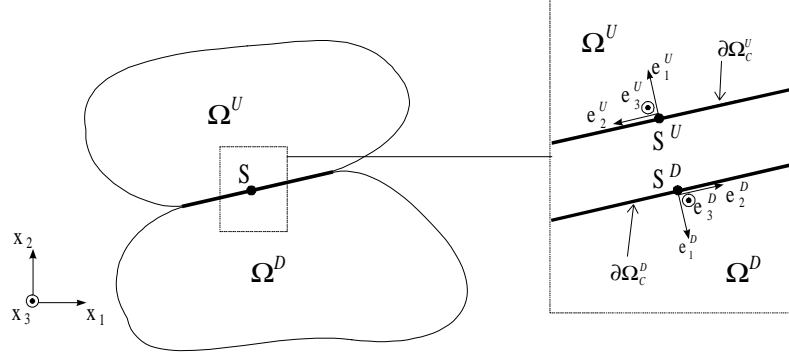


Figure 2.3 Contact between deformable solids.

At any point S of the contact surface, a local triad $(\mathbf{e}_1, \mathbf{e}_2, \mathbf{e}_3)$ can be defined for each solid as indicated on figure 2.3b. The \mathbf{e}_1 axis is normal to the contact whereas the \mathbf{e}_2 and \mathbf{e}_3 axes are tangent. In this local referential, the stress tensor in each solid reduces to the contact stress vector $\boldsymbol{\sigma}_C$ defined by three components

$$\boldsymbol{\sigma}_C = \begin{bmatrix} \sigma_1 \\ \sigma_2 \\ \sigma_3 \end{bmatrix} = \begin{bmatrix} -p \\ \tau_2 \\ \tau_3 \end{bmatrix} \quad (2.29)$$

where p is the pressure and (τ_2, τ_3) are the shear stresses. As this stress vector is defined in a local referential attached to a solid, it is independent of rigid body rotation, i.e. objective [CHARLIER and CESCOTTO, 1988]. The perfectly sticking contact condition is enforced numerically using the classical penalty method which allows a small relative velocity between points S^U and S^D (i.e. a small penetration of the two solids) and a relative sliding between them.

The contact stress vector $\boldsymbol{\sigma}_C$ is associated with the relative displacement velocity $\dot{\mathbf{e}}_C$ (through the contact constitutive law described in section 2.4.3) defined as the time derivative of the distance vector \mathbf{u} between $\partial\Omega_C^U$ and $\partial\Omega_C^D$ (see figure 2.4)

$$\dot{\mathbf{e}}_C = \frac{d\mathbf{u}}{dt} = \mathbf{R} \left(\frac{d\mathbf{x}^D - d\mathbf{x}^U}{dt} \right) + \frac{d\mathbf{R}}{dt} (\mathbf{x}^D - \mathbf{x}^U) \quad (2.30)$$

where the objective distance vector \mathbf{u} is given by

$$\mathbf{u} = \mathbf{R} (\mathbf{x}^D - \mathbf{x}^U) \quad (2.31)$$

and where \mathbf{R} represents the rotation matrix between the triad $(\mathbf{x}_1, \mathbf{x}_2, \mathbf{x}_3)$ and $(\mathbf{e}_1, \mathbf{e}_2, \mathbf{e}_3)$ [CHARLIER and CESCOTTO, 1988]. Note that through the second term of equation (2.30), the relative velocity of the surfaces is function of the rotation rate of the local triad, which preserves objectivity.

The contact side of each body Ω^U and Ω^D can be discretised with contact isoparametric elements which are compatible (same degree and common nodes) with the solid finite elements used to discretise the corresponding body (see figure 2.4). The frictional contact elements used here are based on mixed variational principles [CESCOTTO and CHARLIER, 1993] : contact stresses are computed at contact element integration points whereas displacements of the solid boundary are computed at nodal points. This formulation leads to a smoother contact condition.

The contact condition is simply obtained locally from the geometrical computation of the distance λ_c between the two contact interfaces $\partial\Omega_C^U$ and $\partial\Omega_C^D$ with $\lambda_c = \mathbf{u} \cdot \mathbf{e}_1$

- $\lambda_c < 0$ → no contact (see figure 2.4),
- $\lambda_c \geq 0$ → there is contact.

Computation of λ_c requires to choose temporarily a reference side, for instance $\partial\Omega_C^U$. Consider a contact element U belonging to $\partial\Omega_C^U$ and a contact element D belonging to $\partial\Omega_C^D$. In this case, λ_c^U is computed between an integration point of element U (point D in figure 2.4) and the intersection of the normal to this integration point with element D (point C in figure 2.4).

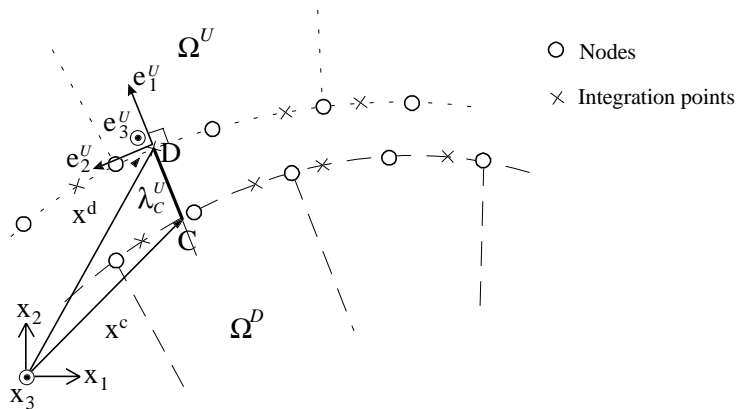


Figure 2.4 Parabolic contact finite elements ($\lambda^U < 0$, i.e. no contact).

The virtual work performed by contact stresses on element U reads

$$\delta W^U = \int_S \boldsymbol{\sigma}_C^U : \delta \dot{\boldsymbol{\epsilon}}_C^U dS \quad (2.32)$$

where S is the contact area of the element and where the superscript U refers to the contact element U . The latter equation can be expressed in term of energetically equivalent nodal forces and virtual displacements [HABRAKEN and CESCOTTO, 1996]

$$\delta W^U = \mathbf{F}^U : \delta \mathbf{u}^U = \left\{ \begin{matrix} (\mathbf{F}_U^U)^T & (\mathbf{F}_D^U)^T \end{matrix} \right\} \left\{ \begin{matrix} \delta \mathbf{u}_U^U \\ \delta \mathbf{u}_D^U \end{matrix} \right\} \quad (2.33)$$

where \mathbf{F}_U^U and \mathbf{F}_D^U represents the equivalent nodal forces acting on the nodes of element U and on the nodes of element D respectively, obtained from the contact stresses computed on element U . Using a classical assembly operator \mathfrak{R} , the contact nodal forces of all the nodes of $\partial\Omega_C^U$ and $\partial\Omega_C^D$ obtained from the contact stresses computed on $\partial\Omega_C^U$ are obtained

$$\begin{aligned}\mathbf{F}_{\partial\Omega_C^U}^{\partial\Omega_C^U} &= \mathfrak{R} \mathbf{F}_U^U \\ \mathbf{F}_{\partial\Omega_C^D}^{\partial\Omega_C^U} &= \mathfrak{R} \mathbf{F}_D^U\end{aligned}\quad (2.34)$$

The same operation can be repeated choosing temporarily $\partial\Omega_C^D$ as the reference side. It will give the contact nodal forces $\mathbf{F}_{\partial\Omega_C^U}^{\partial\Omega_C^D}$ and $\mathbf{F}_{\partial\Omega_C^D}^{\partial\Omega_C^D}$ obtained from the stresses computed on $\partial\Omega_C^D$.

Theoretically, the following equalities should be verified

$$\mathbf{F}_{\partial\Omega_C^U}^{\partial\Omega_C^U} = \mathbf{F}_{\partial\Omega_C^D}^{\partial\Omega_C^U} \quad \text{and} \quad \mathbf{F}_{\partial\Omega_C^D}^{\partial\Omega_C^U} = \mathbf{F}_{\partial\Omega_C^D}^{\partial\Omega_C^D} \quad (2.35)$$

but due to discretisation and numerical integration, they are only approximate. An average contact nodal forces can be computed by

$$\begin{aligned}\mathbf{F}_{\partial\Omega_C^U} &= \alpha \mathbf{F}_{\partial\Omega_C^U}^{\partial\Omega_C^U} + (1-\alpha) \mathbf{F}_{\partial\Omega_C^D}^{\partial\Omega_C^U} \\ \mathbf{F}_{\partial\Omega_C^D} &= \alpha \mathbf{F}_{\partial\Omega_C^D}^{\partial\Omega_C^U} + (1-\alpha) \mathbf{F}_{\partial\Omega_C^D}^{\partial\Omega_C^D}\end{aligned}\quad (2.36)$$

with $0 \leq \alpha \leq 1$. The meaning of parameter α will be explained further. A very interesting aspect of this contact element formulation lies in its quite general description, which can always be particularised afterwards to treat several type of contact.

In the *LAGAMINE* code :

- the reference side $\partial\Omega_C$ on which contact stresses are computed is always referred as the **contact element side** and is discretised using either *CNTCP* (2 dimensional) or *CFI3D* (3 dimensional) contact elements. The parameter *IRIGF* (see *LAGAMINE* code reference manual) defined for the **contact element side** depends on the contact type as explained below.
- the other side on which intersections are looked for is always referred as the **foundation side** and is discretised using *FOUND* elements.

[HABRAKEN and CESCOTTO, 1996] investigated the influence of the parameter α with respect to the accuracy of computation.

2.2.4.2.1 Contact between a deformable solid (Ω^U) and a rigid solid (Ω^D)

In this case, $\partial\Omega_C^U$ must be defined as the **contact element side** (with *IRIGF*=0), whereas $\partial\Omega_C^D$ must be defined as the **foundation side**, i.e. $\alpha=1$. If Ω^D is rigid with imposed motion, there are no degrees of freedom (d.o.f.) associated with it, therefore equation (2.36) reduces here to

$$\mathbf{F}_{\partial\Omega_C^U} = \mathbf{F}_{\partial\Omega_C^U}^{\partial\Omega_C^U} \quad (2.37)$$

If Ω^D is rigid with imposed forces, there are d.o.f. associated with the rigid body modes of Ω^D , therefore equation (2.36) reduces here to

$$\begin{aligned}\mathbf{F}_{\partial\Omega_C^U} &= \mathbf{F}_{\partial\Omega_C^U}^{\partial\Omega_C^U} \\ \mathbf{F}_{\partial\Omega_C^D} &= \mathbf{F}_{\partial\Omega_C^D}^{\partial\Omega_C^D}\end{aligned}\tag{2.38}$$

2.2.4.2.2 Contact between two deformable solids (Ω^U) and (Ω^D)

In this case, there are two possibilities to discretise the contact :

- In the general case, the same importance is given to both sides of the contact. It corresponds to a symmetrical treatment of the contact, i.e. no solid is privileged with respect to the other. In this case, both $\partial\Omega_C^U$ and $\partial\Omega_C^D$ must be defined as a **contact element side** (with $IRIGF=3$) and a **foundation side**. Equation (2.36) applies here with the choice $\alpha=0.5$, which gives

$$\begin{aligned}\mathbf{F}_{\partial\Omega_C^U} &= 0.5 \mathbf{F}_{\partial\Omega_C^U}^{\partial\Omega_C^U} + 0.5 \mathbf{F}_{\partial\Omega_C^D}^{\partial\Omega_C^U} \\ \mathbf{F}_{\partial\Omega_C^D} &= 0.5 \mathbf{F}_{\partial\Omega_C^U}^{\partial\Omega_C^D} + 0.5 \mathbf{F}_{\partial\Omega_C^D}^{\partial\Omega_C^D}\end{aligned}\tag{2.39}$$

This symmetrical treatment of contact gives the best results when the deformability and the mesh density of both solids is comparable [HABRAKEN and CESCOTTO, 1996].

- In some cases, it might be interesting to privilege one side of the contact with respect to the other in order to decrease the number of elements : bodies with very different rigidities or with a different discretisation accuracy. It corresponds to a non-symmetrical treatment of contact. For instance if solid Ω^U is privileged, only $\partial\Omega_C^U$ is defined as the **contact element side** (with $IRIGF=2$) and $\partial\Omega_C^D$ is defined as the **foundation side**. This case corresponds to the choice $\alpha=1$ in equation (2.36) which reduces then to equation (2.38). Conversely if solid Ω^D is privileged, then $\alpha=0$ in equation (2.36)

$$\begin{aligned}\mathbf{F}_{\partial\Omega_C^U} &= \mathbf{F}_{\partial\Omega_C^D}^{\partial\Omega_C^U} \\ \mathbf{F}_{\partial\Omega_C^D} &= \mathbf{F}_{\partial\Omega_C^D}^{\partial\Omega_C^D}\end{aligned}\tag{2.40}$$

However, when the two bodies do not have the same discretisation accuracy, the **contact element side** must refer to the body with the more refined mesh, and the **foundation side** must refer to the body with the coarser mesh. In this case, this non-symmetrical treatment of contact also gives good results [HABRAKEN and CESCOTTO, 1996].

2.2.5 General algorithm of the LAGAMINE code for mechanical analysis

Variables in the present configuration (step beginning, which verifies equilibrium) are noted with the superscript ^A, and variables in the up-dated configuration (step end, which is unknown) are noted with the superscript ^B. The global unknowns to be solved are the nodal co-ordinates \mathbf{x}^B in the incremented configuration. The implicit algorithm used can be summarised as follow (see also figure 2.5).

1. Consider a finite time step increment Δt .

2. For all the nodes :

- compute the up-dated nodal co-ordinates \mathbf{x}^B from the initial nodal co-ordinates \mathbf{x}^A and from the nodal velocities \mathbf{v}^A at the beginning of the time step

$$\mathbf{x}^B = \mathbf{x}^A + \mathbf{v}^A \Delta t \quad (2.41)$$

- at any stage the virtual velocity field must be kinematically compatible, i.e. must verify the mesh degrees of freedom.

3. For every element :

- compute the strain rate gradient from the velocity gradient using equation (2.5),
- integrate over time the constitutive equation to obtain stresses and internal variables at step end,
- compute the energetically equivalent nodal forces using equation (2.28),
- compute the element stiffness matrix \mathbf{k} , which represents the derivative of nodal forces with respect to displacements

$$\mathbf{k} = \frac{\partial \mathbf{F}_L}{\partial \mathbf{u}} \quad (2.42)$$

It is obtained by taking into account the compliance matrix (computed using perturbations of the velocity gradient \mathbf{L}), which integrates the effects of the integration path [CHARLIER, 1987].

4. A norm of the out of balance nodal forces is computed.

5. The global stiffness matrix \mathbf{K} is assembled (from element stiffness matrixes \mathbf{k}) and inverted. A correction on nodal displacements is computed using

$$\Delta \mathbf{u} = \mathbf{K}^{-1} : \mathbf{F}_L \quad (2.43)$$

6. Nodal displacements and velocities are updated.

7. Convergence on a norm of out of balance forces and on a norm of nodal displacements is checked :

- if a given precision (prescribed by the user) is reached for the two norms, then the equilibrium is approximately reached by virtue of the virtual power principle; nodal co-ordinates and velocities are updated and the step terminates,
- else equilibrium is not reached. If the allowed number of iteration $Maxit$ is not reached, then a correction is made on displacements and velocities and a new solution is computed starting from 3, else the step size is reduced and the loop goes back to step 1.

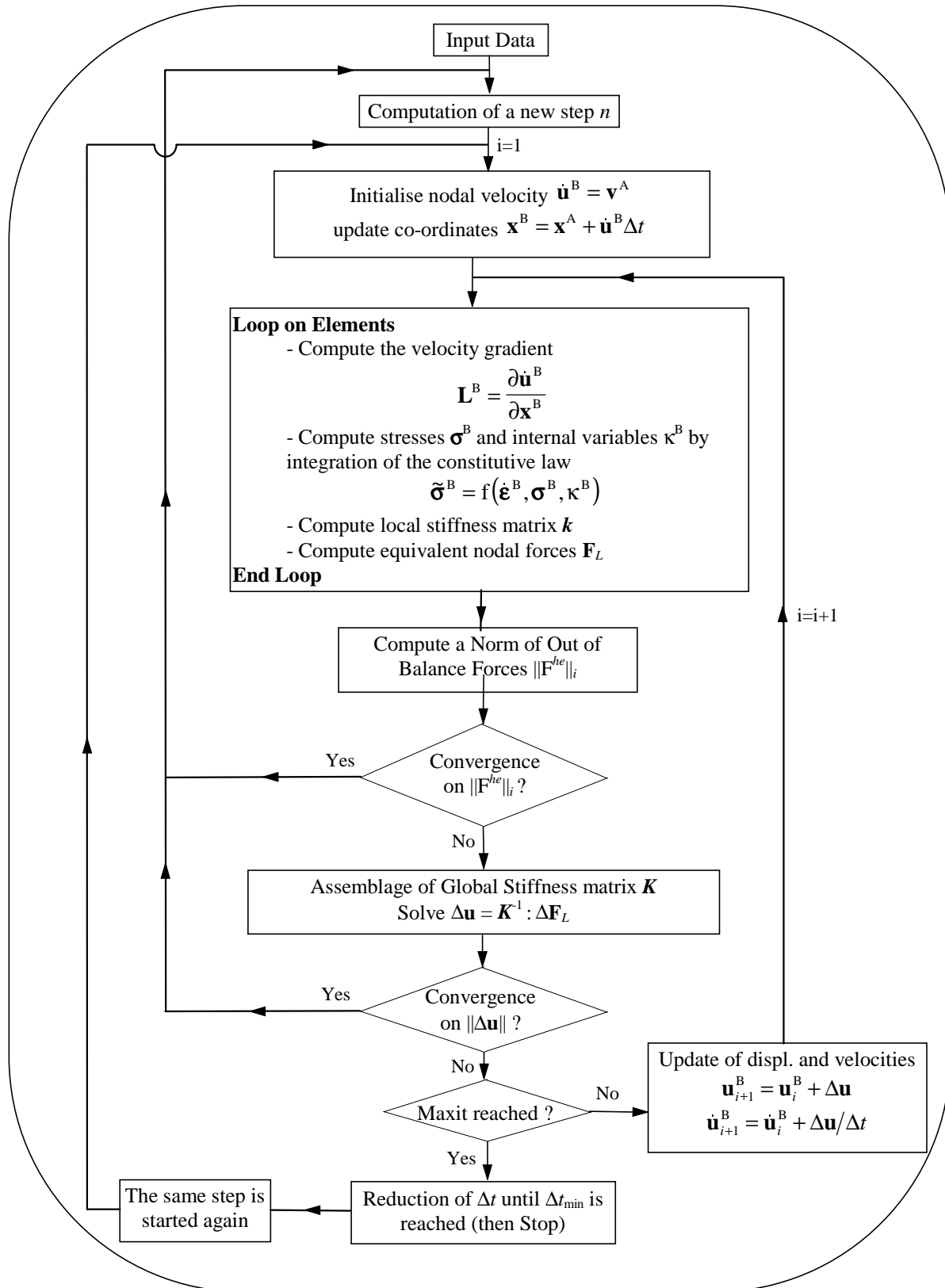


Figure 2.5 General finite element algorithm of the *LAGAMINE* code for mechanical static analysis.

2.3 Frictional elastoplastic constitutive laws for geomaterials

2.3.1 Incremental general elastoplastic formulation

The general elastoplastic relations are formulated in their rate form. The sign convention of solid mechanics is used, i.e. compression is counted negative and traction positive. The strain rate is partitioned in an elastic and a plastic component

$$\dot{\epsilon}_{ij} = \dot{\epsilon}_{ij}^e + \dot{\epsilon}_{ij}^p \quad (2.44)$$

The elastic part is linked to the stress tensor following Hooke law

$$\tilde{\sigma}_{ij} = C_{ijkl}^e \dot{\epsilon}_{kl}^e \quad (2.45)$$

where the compliance elastic tensor is defined by

$$C_{ijkl}^e = \frac{E}{1+\nu} \delta_{ik} \delta_{jl} + \frac{E\nu}{(1+\nu)(1-2\nu)} \delta_{ij} \delta_{kl} \quad (2.46)$$

and where $\tilde{\sigma}$ is the Jaumann objective stress rate defined in equation (2.7).

Using the definition of the compressibility modulus K and the shear modulus G

$$K = \frac{E}{3(1-2\nu)}, \quad G = \frac{E}{2(1+\nu)} \quad (2.47)$$

the constitutive elastic tensor can be written

$$C_{ijkl}^e = 2G\delta_{ik}\delta_{jl} + \left(K - \frac{2}{3}G \right) \delta_{ij}\delta_{kl} \quad (2.48)$$

The limit between the elastic and plastic domain is represented by a yield surface in the principal stress space. This surface is described using the yield function f . If a stress state verifies $f < 0$, then this stress state is elastic. If $f = 0$, the stress state is plastic. In classical (or associated) plasticity, the rate of plastic flow is perpendicular to the yield surface and its intensity is proportional to the so called plastic multiplier $\dot{\lambda}$. During plastic flow, the stress state must remain on the yield surface, i.e. $f = 0$ ($f > 0$ is impossible).

Here the more general framework of non-associated plasticity is considered in order to limit dilatancy, that is the rate of plastic flow is perpendicular to a plastic potential g (however one can obtain an associated law substituting g by f in subsequent equations)

$$\dot{\epsilon}_{ij}^p = \dot{\lambda} \frac{\partial g}{\partial \sigma_{ij}} \quad (2.49)$$

In the last equation, the plastic potential g is defined in an identical fashion than the yield surface but assuming no cohesion. Combining equations (2.44) and (2.49) together gives

$$\dot{\epsilon}_{ij} = \dot{\epsilon}_{ij}^e + \dot{\lambda} \frac{\partial g}{\partial \sigma_{ij}} \quad (2.50)$$

The value of $\dot{\lambda}$ is obtained from the consistency condition which states that during plastic flow, the stress state stays on the limit surface. For a perfectly plastic law this condition yields

$$\dot{f} = \frac{\partial f}{\partial \sigma_{ij}} \tilde{\sigma}_{ij} = 0 \quad (2.51)$$

Considering a general plastic law with hardening/softening of the internal variable κ , the consistency condition can be formulated

$$\dot{f} = \frac{\partial f}{\partial \sigma_{ij}} \tilde{\sigma}_{ij} + \frac{\partial f}{\partial \kappa} \dot{\kappa} = 0 \quad (2.52)$$

In the models developed further (sections 2.3.2.2 to 2.3.2.4), the plastic flow is assumed to induce hardening/softening of the limit surface, which is introduced via an hyperbolic variation of the internal variables (the friction angles ϕ_C and ϕ_E , see section 2.3.2.2 for meaning, and the cohesion c) as a function of the Von Mises equivalent plastic strain ϵ_{eq}^p

$$\begin{aligned} \phi_C &= \phi_{C0} + \frac{(\phi_{Cf} - \phi_{C0}) \epsilon_{eq}^p}{B_p + \epsilon_{eq}^p} \\ \phi_E &= \phi_{E0} + \frac{(\phi_{Ef} - \phi_{E0}) \epsilon_{eq}^p}{B_p + \epsilon_{eq}^p} \\ c &= c_0 + \frac{(c_f - c_0) \epsilon_{eq}^p}{B_c + \epsilon_{eq}^p} \end{aligned} \quad (2.53)$$

where the Von Mises equivalent plastic strain is obtained by integration of the Von Mises equivalent plastic strain rate $\dot{\epsilon}_{eq}^p$

$$\epsilon_{eq}^p = \int_0^t \dot{\epsilon}_{eq}^p dt \quad (2.54)$$

$$\dot{\epsilon}_{eq}^p = \sqrt{\frac{2}{3} \dot{\epsilon}_{ij}^p \dot{\epsilon}_{ij}^p} \quad (2.55)$$

Coefficients B_p and B_c represent respectively the values of equivalent plastic strain for which half of the hardening/softening on friction angle and cohesion is achieved (see figure 2.6). The plastic flow may also induce a modification of the flow surface. In such a case, the rule proposed by Taylor is used [TAYLOR, 1948]

$$\phi - \psi = cste \quad (2.56)$$

Based on experimental evidences, it states that the difference between the friction and dilatancy angle is constant, then any modification of the friction angle will affect the dilatancy angle.

Thus the consistency condition (equation (2.52)) reads

$$\dot{f} = \frac{\partial f}{\partial \sigma_{ij}} \tilde{\sigma}_{ij} + \frac{\partial f}{\partial \phi_C} \dot{\phi}_C + \frac{\partial f}{\partial \phi_E} \dot{\phi}_E + \frac{\partial f}{\partial c} \dot{c} = 0 \quad (2.57)$$

where the derivatives of internal variables ϕ_C , ϕ_E and c with respect to time are given by

$$\dot{\phi}_C = \frac{d\phi_C}{d\varepsilon_{eq}^p} \dot{\varepsilon}_{eq}^p, \quad \dot{\phi}_E = \frac{d\phi_E}{d\varepsilon_{eq}^p} \dot{\varepsilon}_{eq}^p, \quad \dot{c} = \frac{dc}{d\varepsilon_{eq}^p} \dot{\varepsilon}_{eq}^p \quad (2.58)$$

The relation between the plastic multiplier and the Von Mises equivalent strain rate can be obtained combining together equations (2.49) and (2.55)

$$\dot{\varepsilon}_{eq}^p = Val \dot{\lambda} \quad (2.59)$$

where

$$Val = \sqrt{\frac{2}{3} \left(\frac{\partial g}{\partial \sigma_{ij}} \frac{\partial g}{\partial \sigma_{ij}} - \frac{1}{3} \frac{\partial g}{\partial \sigma_{kk}} \frac{\partial g}{\partial \sigma_{ll}} \right)} \quad (2.60)$$

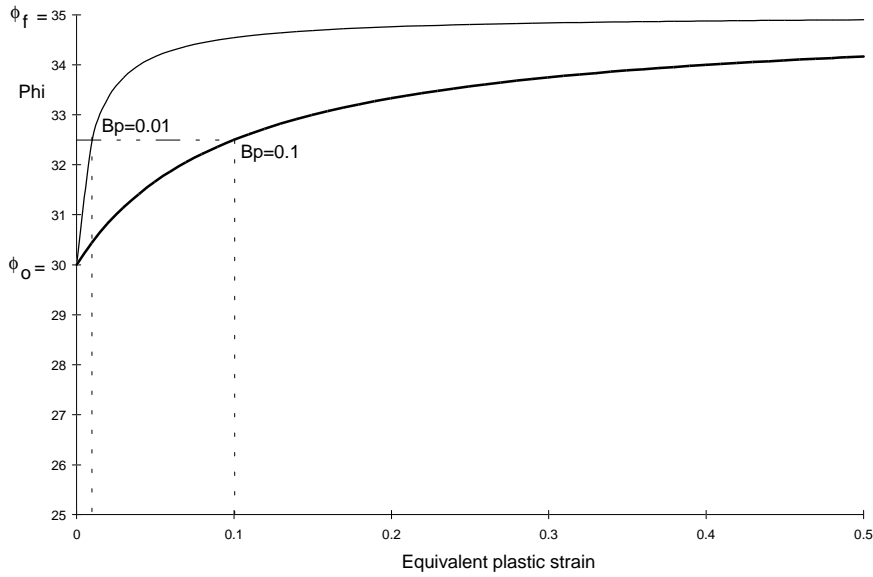


Figure 2.6 Hardening hyperbolic relation for 2 values of coefficient B_p (with $\phi_0=30^\circ$, $\phi_f=35^\circ$).

Thus the general consistency condition (equation (2.57)) becomes

$$\dot{f} = \frac{\partial f}{\partial \sigma_{ij}} \tilde{\sigma}_{ij} + Val \dot{\lambda} \left(\frac{\partial f}{\partial \phi_C} \frac{d\phi_C}{d\varepsilon_{eq}^p} + \frac{\partial f}{\partial \phi_E} \frac{d\phi_E}{d\varepsilon_{eq}^p} + \frac{\partial f}{\partial c} \frac{dc}{d\varepsilon_{eq}^p} \right) = 0 \quad (2.61)$$

Combining together equations (2.45) and (2.50) together gives

$$\tilde{\sigma}_{ij} = C_{ijkl}^e \left(\dot{\varepsilon}_{kl} - \dot{\lambda} \frac{\partial g}{\partial \sigma_{kl}} \right) \quad (2.62)$$

The value of the scalar $\dot{\lambda}$ is then obtained incorporating equation (2.62) into equation (2.61)

$$\dot{\lambda} = \frac{\frac{\partial f}{\partial \sigma_{ij}} C_{ijkl}^e \dot{\varepsilon}_{kl}}{\frac{\partial f}{\partial \sigma_{mn}} C_{mnop}^e \frac{\partial g}{\partial \sigma_{op}} - Val \left(\frac{\partial f}{\partial \phi_C} \frac{d\phi_C}{d\varepsilon_{eq}^p} + \frac{\partial f}{\partial \phi_E} \frac{d\phi_E}{d\varepsilon_{eq}^p} + \frac{\partial f}{\partial c} \frac{dc}{d\varepsilon_{eq}^p} \right)} \quad (2.63)$$

Now the full constitutive incremental elastoplastic relation can be written reporting equation (2.63) into (2.62)

$$\tilde{\sigma}_{ij} = (C_{ijkl}^e - C_{ijkl}^p) \dot{\epsilon}_{kl} \quad (2.64)$$

where the plastic constitutive tensor is

$$C_{ijkl}^p = \frac{\frac{\partial f}{\partial \sigma_{ab}} C_{abkl}^e C_{ijcd}^e \frac{\partial g}{\partial \sigma_{cd}}}{\frac{\partial f}{\partial \sigma_{mn}} C_{mnop}^e \frac{\partial g}{\partial \sigma_{op}} - Val \left(\frac{\partial f}{\partial \phi_C} \frac{d\phi_C}{d\epsilon_{eq}^p} + \frac{\partial f}{\partial \phi_E} \frac{d\phi_E}{d\epsilon_{eq}^p} + \frac{\partial f}{\partial c} \frac{dc}{d\epsilon_{eq}^p} \right)} \quad (2.65)$$

It must be pointed out that, in this general elastoplasticity framework, derivatives of yield surface f and flow surface g with respect to stresses are required. Thus the choice of f and g as continuously derivable functions with respect to stresses is particularly suited for this formulation.

2.3.2 Yield surfaces for frictional behaviour of geomaterials

Geomechanical modelling requires to take into account the plastic behaviour of materials of different rock types (sand, sandstones, limestones, shales). The plastic behaviour is usually based on the concept of yield surface.

Experimentally, the existence of the yield surface expresses the loss of the linear stress-strain relation. The yield surface represents a bound in the stress space which cannot be overcome. As far as frictional materials are concerned, it has been observed from triaxial experiments that a linear relation exists between tangential stresses τ and normal stresses σ_N , which led to the formulation of the so-called Mohr-Coulomb yield criterion (described in the next section). This linearity is not only valid in the Coulomb plane (τ, σ_N) but also in the (p, q) plane. However, the shape of the yield surface in the deviatoric plane has been investigated experimentally much later [LANIER, 1988], see figure 2.7.

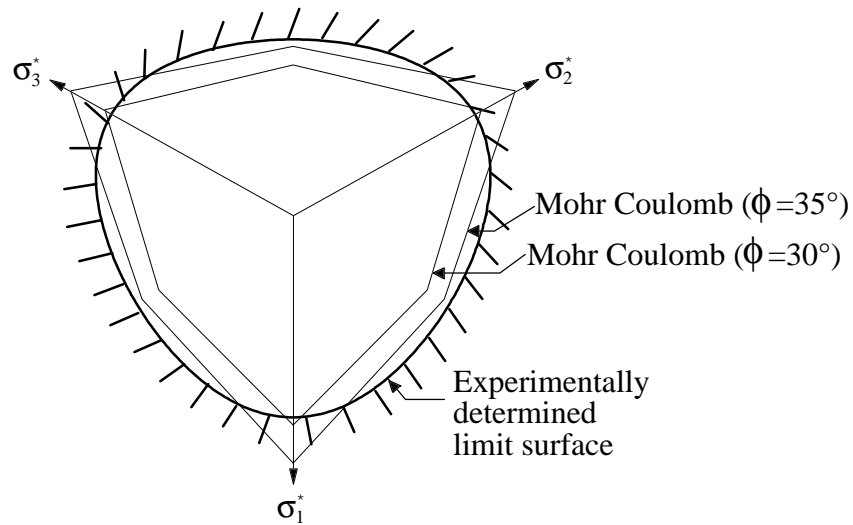


Figure 2.7 Experimental limit surface for Hostun sand, modified from [LANIER, 1988].

As it will be presented in the next section, the more simple model (namely Mohr Coulomb) only considers the frictional properties of those materials as a function of the minimum and maximum principal stress. However, this model is not convenient to use in numerical simulation as the plasticity surface exhibits geometric singularities in the principal stress space. This problem is usually solved using an approximation of the Mohr Coulomb criterion, namely the Drucker Prager criterion. However, this criterion has other main disadvantages which in some cases make doubtful the results obtained. A more sophisticated model can be chosen to approximate the Mohr Coulomb criterion more accurately (e.g. Matsuoka-Nakai [MATSUOKA and NAKAI, 1982], Van Eekelen [VAN EEKELEN, 1980]).

The Mohr Coulomb (MC) model is briefly presented here as this criterion is not implemented in the *LAGAMINE* code. The two other criteria, i.e. the Drucker Prager (DP) and Van Eekelen (VE) criteria, are described in this section. Their full elastoplastic formulation is given including isotropic hardening/softening of friction angles and cohesion. Similarities and differences between them are outlined, which leads to a unified formulation in which the Drucker Prager criterion represents a limit case of the more general Van Eekelen one.

2.3.2.1 Stress invariants and stress space

I_σ , $II_{\hat{\sigma}}$, $III_{\hat{\sigma}}$ and β represent the first stress tensor invariant, the second deviatoric stress tensor invariant, the third deviatoric stress tensor invariant and the Lode angle, respectively

$$I_\sigma = \sigma_{ii} \quad (2.66)$$

$$II_{\hat{\sigma}} = \sqrt{\frac{1}{2} \hat{\sigma}_{ij} \hat{\sigma}_{ij}} \quad (2.67)$$

$$\hat{\sigma}_{ij} = \sigma_{ij} - \frac{I_\sigma}{3} \delta_{ij} \quad (2.68)$$

$$\beta = -\frac{1}{3} \sin^{-1} \left(\frac{3\sqrt{3}}{2} \frac{III_{\hat{\sigma}}}{II_{\hat{\sigma}}^3} \right), \text{ with } III_{\hat{\sigma}} = \frac{1}{3} \hat{\sigma}_{ij} \hat{\sigma}_{jk} \hat{\sigma}_{ki} \quad (2.69)$$

The three invariants I_σ , $II_{\hat{\sigma}}$ and β define a cylindrical referential around the I_σ axis. In this referential, $II_{\hat{\sigma}}$ represents the distance between a stress state p and the I_σ axis, the Lode angle β represents the angular position of p with respect to the pure shear line (see figure 2.8a-b), with $\beta \in [-30^\circ, +30^\circ]$. σ_1^* , σ_2^* and σ_3^* represent the projection of the principal stress axes on the deviatoric (or Π) plane.

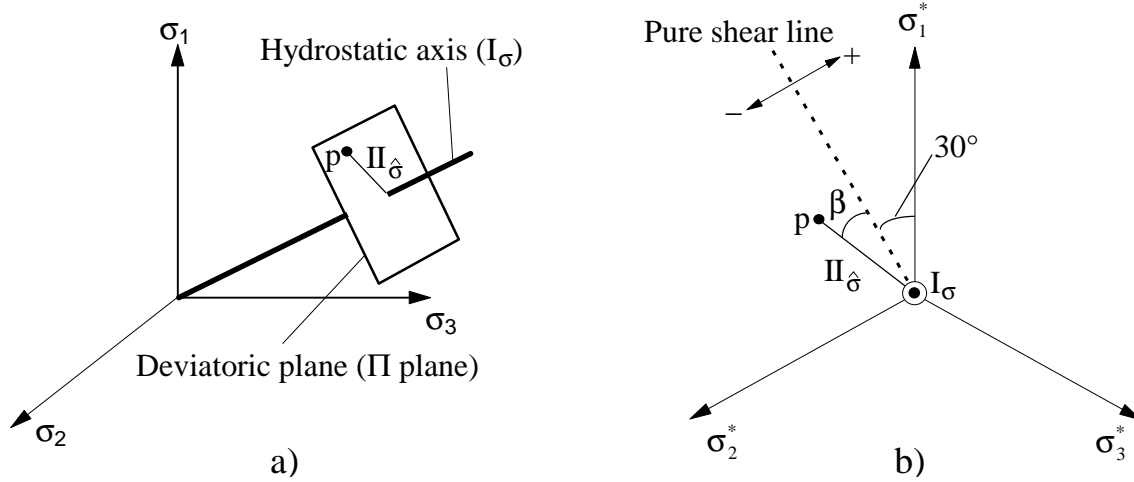


Figure 2.8 a) representation of the principal stress space, b) deviatoric plane.

2.3.2.2 Mohr Coulomb criterion (MC)

The Mohr-Coulomb failure criterion is an intrinsic curve criterion. It expresses a linear relationship between the shear stress τ and the normal stress σ_N acting on a failure plane

$$\tau = c + \sigma_N \tan \phi \quad (2.70)$$

where c is the cohesion and ϕ the friction angle. This criterion can be expressed in a more general fashion in term of principal stresses by the relation

$$f = \frac{I_\sigma}{3} \sin \phi + II_{\hat{\sigma}} \cos \beta - \frac{II_{\hat{\sigma}}}{\sqrt{3}} \sin \beta \sin \phi - c \cos \phi = 0 \quad (2.71)$$

This criterion predicts identical friction angles under triaxial compression paths (referred as ϕ_C) and triaxial extension paths (ϕ_E), thus $\phi_C = \phi_E$ in relation (2.71). Let us recall that starting from an isotropic stress state, the triaxial compression path corresponds to an increase of axial stress whereas the triaxial extension path corresponds to a decrease of the axial stress which however still remains compressive. Therefore, compression and extension refer here to paths in stress and strain space; they do not have any link with the usual geological meaning of compression and extension which then refer to compressive and tensile stresses or to tectonic regimes (i.e. function of the principal stress component which is vertical).

Geometric representation of this criterion in the principal stress space ($\sigma_1, \sigma_2, \sigma_3$) is an irregular hexagonal pyramid (see figure 2.9). As previously mentioned, this model is not convenient to implement in a classical plasticity framework as the gradient of this yield surface is undefined on the hexagon corners. Therefore it is required to develop more complex integration schemes [CRISFIELD, 1987]. More continuously derivable yield surfaces are usually preferred.

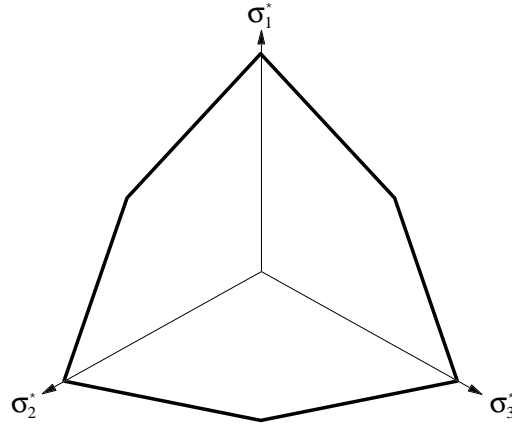


Figure 2.9 Limit surface for Mohr-Coulomb criterion in the deviatoric plane for $\phi=35^\circ$.

2.3.2.3 Drucker Prager criterion (DP)

An alternative solution to overcome this difficulty has been proposed by [DRÜCKER and PRAGER, 1952] who defined the yield function f using a linear relationship between the first stress tensor invariant and the second deviatoric stress tensor invariant

$$f = II_{\sigma} + mI_{\sigma} - k = 0 \quad (2.72)$$

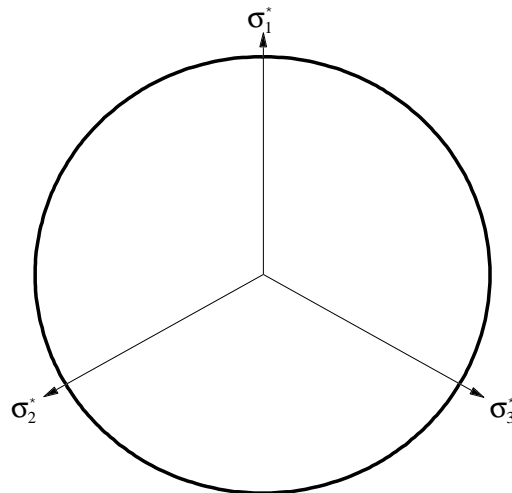


Figure 2.10 Limit surface for Drucker Prager criterion in the deviatoric plane for $\phi=35^\circ$.

In the principal stress space, the plasticity surface becomes a cone which is much easier to use in numerical algorithms. The trace of this plasticity surface on the Π plane is then a circle (see figure 2.10).

Although this simple criterion is widely used in geomechanics to represent frictional material, it does not incorporate a dependence on the third stress invariant and thus on the Lode angle β . As it will be shown further, this characteristic represents a main drawback of this model.

Identification of parameters m and k on the Mohr envelop as a function of internal friction angle in compression ϕ_c and cohesion c leads [DESAI and al, 1984], if the compression cone is chosen (i.e. if the DP circle is circumscribed to the MC hexagon), to

$$m = \frac{2 \sin \phi_C}{\sqrt{3}(3 - \sin \phi_C)} \quad (2.73)$$

$$k = \frac{6c \cos \phi_C}{\sqrt{3}(3 - \sin \phi_C)} \quad (2.74)$$

Then the Drucker Prager criterion can be formulated as

$$f = II_{\dot{\sigma}} + m \left(I_{\sigma} - \frac{3c}{\tan \phi_C} \right) = 0 \quad (2.75)$$

With the definition of reduced radius r

$$r = \frac{II_{\dot{\sigma}}}{I_{\sigma}} \quad (2.76)$$

expressions of the reduced radius in compression (r_C) and in extension (r_E) for triaxial tests can be deduced from Mohr circle and intrinsic curve, leading to

$$r_C = \frac{1}{\sqrt{3}} \left(\frac{2 \sin \phi_C}{3 - \sin \phi_C} \right) \quad (2.77)$$

$$r_E = \frac{1}{\sqrt{3}} \left(\frac{2 \sin \phi_E}{3 + \sin \phi_E} \right) \quad (2.78)$$

which, putting $r_E=r_C$ as the radius is constant in the Drucker Prager model, gives a relation between ϕ_C and ϕ_E . Combining equation (2.77) and (2.78) together reads

$$\phi_E = \sin^{-1} \left(\frac{\frac{3 \sin \phi_C}{3 - \sin \phi_C}}{1 - \left(\frac{\sin \phi_C}{3 - \sin \phi_C} \right)} \right) \quad (2.79)$$

A plot of ϕ_C versus ϕ_E computed from equation (2.79) is given in figure 2.11 and shows that ϕ_E does not increase linearly with ϕ_C . There is a limit value of $\phi_E=90^\circ$ for $\phi_C \approx 36.87^\circ$.

In the principal stress space, the Drucker Prager conical limit surface makes an angle θ

$$\theta = \tan^{-1} \left(\sqrt{2} \frac{2 \sin \phi_C}{3 - \sin \phi_C} \right) \quad (2.80)$$

with respect to the hydrostatic axis ($\sigma_1=\sigma_2=\sigma_3$).

For the Drucker Prager criterion the plastic criterion f is given by equation (2.75) and the plastic potential g is defined in a similar fashion by

$$g = II_{\dot{\sigma}} + m' I_{\sigma} = 0 \quad (2.81)$$

with

$$m' = \frac{2 \sin \psi}{\sqrt{3}(3 - \sin \psi)} \quad (2.82)$$

where ψ is the dilatancy angle.

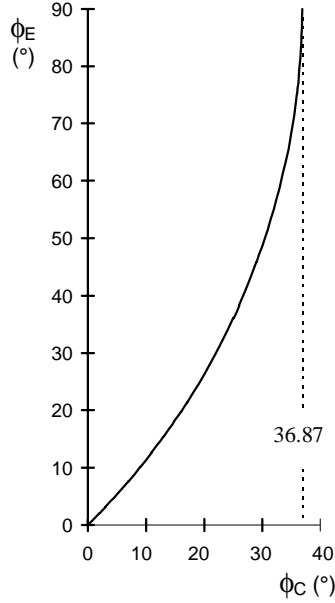


Figure 2.11 ϕ_E versus ϕ_C for Drucker Prager criterion.

In order to achieve the general elastoplastic relation obtained in the previous section, the derivatives of the limit surface f and plastic potential g with respect to stresses are required

$$\frac{\partial f}{\partial \sigma_{ij}} = \frac{\partial f}{\partial I_\sigma} \frac{\partial I_\sigma}{\partial \sigma_{ij}} + \frac{\partial f}{\partial II_{\hat{\sigma}}} \frac{\partial II_{\hat{\sigma}}}{\partial \sigma_{ij}} \quad (2.83)$$

with

$$\frac{\partial f}{\partial I_\sigma} = m \quad (2.84)$$

$$\frac{\partial I_\sigma}{\partial \sigma_{ij}} = \delta_{ij} \quad (2.85)$$

$$\frac{\partial f}{\partial II_{\hat{\sigma}}} = 1 \quad (2.86)$$

$$\frac{\partial II_{\hat{\sigma}}}{\partial \sigma_{ij}} = \frac{\hat{\sigma}_{ij}}{2II_{\hat{\sigma}}} \quad (2.87)$$

Thus, for the Drucker Prager surface, the derivative of f with respect to stresses is

$$\frac{\partial f}{\partial \sigma_{ij}} = m\delta_{ij} + \frac{\hat{\sigma}_{ij}}{2II_{\hat{\sigma}}} \quad (2.88)$$

and by similarity the derivative of g with respect to stresses is

$$\frac{\partial g}{\partial \sigma_{ij}} = m' \delta_{ij} + \frac{\hat{\sigma}_{ij}}{2II_{\hat{\sigma}}} \quad (2.89)$$

In this case the scalar Val which gives the relation between the equivalent plastic strain and the plastic multiplier (see equation (2.60)) simplifies to

$$Val = \frac{\sqrt{3}}{3} \quad (2.90)$$

There are only two independent hardening variables in the DP model considered here, namely the compression friction angle ϕ_c and the cohesion c . The following derivatives are required

$$\frac{\partial f}{\partial \phi_c} = \frac{2I_{\sigma}}{\sqrt{3}} \left(\frac{\cos \phi_c}{3 - \sin \phi_c} + \frac{\cos \phi_c \sin \phi_c}{(3 - \sin \phi_c)^2} \right) - \frac{6c}{\sqrt{3}} \left(\frac{\sin \phi_c}{3 - \sin \phi_c} + \frac{\cos^2 \phi_c}{(3 - \sin \phi_c)^2} \right) \quad (2.91)$$

$$\frac{\partial f}{\partial c} = -\frac{3m}{\tan \phi_c} \quad (2.92)$$

$$\frac{d\phi_c}{d\varepsilon_{eq}} = \frac{\phi_{cf} - \phi_{c0}}{B_p + \varepsilon_{eq}} - \varepsilon_{eq} \frac{\phi_{cf} - \phi_{c0}}{(B_p + \varepsilon_{eq})^2} \quad (2.93)$$

$$\frac{dc}{d\varepsilon_{eq}} = \frac{c_f - c_0}{B_c + \varepsilon_{eq}} - \varepsilon_{eq} \frac{c_f - c_0}{(B_c + \varepsilon_{eq})^2} \quad (2.94)$$

Using the derivatives with respect to stresses of f and g defined above, the left hand term in the denominator of equation (2.65) simplifies to the scalar relation

$$\frac{\partial f}{\partial \sigma_{mn}} C_{mnop}^e \frac{\partial g}{\partial \sigma_{op}} = 9mm' \chi + G \quad (2.95)$$

2.3.2.4 Van Eekelen criterion (VE)

A more sophisticated model can be built from the Drucker Prager cone by introduction of a dependence on the Lode angle β in order to match more closely Mohr Coulomb criterion. It consists of a smoothing of the Mohr Coulomb plasticity surface. The formulation proposed by [VAN EEKELLEN, 1980] is adopted, and it can be written in a very similar fashion than for the Drucker Prager criterion (see equations 2.73 and 2.75)

$$f = II_{\hat{\sigma}} + m \left(I_{\sigma} - \frac{3c}{\tan \phi_c} \right) = 0 \quad (2.96)$$

but here the coefficient m is defined by

$$m = a(1 + b \sin 3\beta)^n \quad (2.97)$$

The only difference between DP and VE criteria comes from the coefficient m which is constant for DP whereas it is a function of the Lode angle for VE. In equation (2.97), $\sin 3\beta$ is derived from equation (2.69)

$$\sin 3\beta = -\left(\frac{3\sqrt{3}}{2} \frac{III_{\sigma}}{II_{\sigma}^3}\right) \quad (2.98)$$

and the three parameters a , b and n must verify the following conditions [VAN EEKELLEN, 1980]

$$\begin{aligned} a &> 0, \\ bn &> 0, \\ -1 &< b < 1 \end{aligned} \quad (2.99)$$

Coefficients a and b allow an independent choice for ϕ_C and ϕ_E

$$b = \frac{\left(\frac{r_C}{r_E}\right)^{\frac{1}{n}} - 1}{\left(\frac{r_C}{r_E}\right)^{\frac{1}{n}} + 1} \quad (2.100)$$

$$a = \frac{r_C}{(1+b)^n} \quad (2.101)$$

where r_C and r_E are given by equations (2.77) and (2.78). The exponent n actually controls the convexity of the yield surface which is required by Drucker's postulate. Following the conclusion of [VAN EEKELLEN, 1980], the default value $n=-0.229$ has been chosen, however the more general convexity condition will be discussed later in this chapter.

The trace of this plasticity surface in the Π plane is shown on figure 2.12. Such a model is actually a smoothing of the Mohr-Coulomb hexagon (see figure 2.9 for comparison), but it fits much better the Mohr-Coulomb criterion than the Drucker Prager failure criterion for high friction angles.

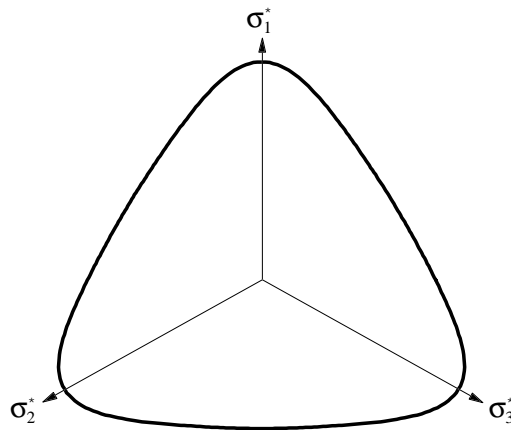


Figure 2.12 Limit surface for Van Eekelen criterion in the deviatoric plane for $\phi=35^\circ$.

In the principal stress space, two angles θ_C and θ_E can be defined

$$\theta_C = \theta = \tan^{-1}\left(\sqrt{2} \frac{2 \sin \phi_C}{3 - \sin \phi_C}\right) \quad (2.102)$$

$$\theta_E = \tan^{-1} \left(\sqrt{2} \frac{2 \sin \phi_C}{3 + \sin \phi_C} \right) \quad (2.103)$$

between the hydrostatic axis ($\sigma_1 = \sigma_2 = \sigma_3$) and the irregular conical limit surface, θ_C corresponding to the compression opening angle and θ_E corresponding to the extension opening angle of the irregular cone.

The plastic potential g for Van Eekelen criterion is defined similarly to f introducing again two dilatancy angles ψ_C and ψ_E .

In order to achieve the general elastoplastic relation obtained in the previous section, the derivatives of the limit surface f with respect to stresses must be defined

$$\frac{\partial f}{\partial \sigma_{ij}} = \frac{\partial f}{\partial I_\sigma} \frac{\partial I_\sigma}{\partial \sigma_{ij}} + \frac{\partial f}{\partial II_{\hat{\sigma}}} \frac{\partial II_{\hat{\sigma}}}{\partial \sigma_{ij}} + \frac{\partial f}{\partial \sin 3\beta} \frac{\partial \sin 3\beta}{\partial \sigma_{ij}} \quad (2.104)$$

$\frac{\partial f}{\partial I_\sigma}, \frac{\partial I_\sigma}{\partial \sigma_{ij}}, \frac{\partial f}{\partial II_{\hat{\sigma}}}, \frac{\partial II_{\hat{\sigma}}}{\partial \sigma_{ij}}$ have already been given for Drucker Prager criterion (see equations (2.84) to (2.87)).

$$\frac{\partial f}{\partial \sin 3\beta} = abn(1 + b \sin 3\beta)^{n-1} \left(I_\sigma - \frac{3c}{\tan \phi_C} \right) \quad (2.105)$$

$$\frac{\partial \sin 3\beta}{\partial \sigma_{ij}} = -\frac{3\sqrt{3}}{2II_{\hat{\sigma}}^3} \left(\hat{\sigma}_{ik} \hat{\sigma}_{kj} - \frac{2}{3} II_{\hat{\sigma}}^2 \delta_{ij} - \frac{3III_{\hat{\sigma}}}{II_{\hat{\sigma}}} \frac{\partial II_{\hat{\sigma}}}{\partial \sigma_{ij}} \right) \quad (2.106)$$

In this case, the scalar Val which gives the relation between the equivalent plastic strain and the plastic multiplier must be computed from equation (2.60).

For this criterion, there are now three independent hardening variables, namely the compressive friction angle ϕ_C , the extensive friction angle ϕ_E and the cohesion c . The derivatives of friction angles and cohesion with respect to equivalent plastic strain are identical than for Drucker Prager criterion (see equations (2.93) and (2.94)). The derivative of f with respect to cohesion gives

$$\frac{\partial f}{\partial c} = -\frac{3a(1 + b \sin 3\beta)^n}{\tan \phi_C} \quad (2.107)$$

and the derivatives with respect to the two independent friction angles simplify to

$$\frac{\partial f}{\partial \phi_C} = \frac{Num_1}{Deno_1} \quad (2.108)$$

$$\frac{\partial f}{\partial \phi_E} = \frac{Num_2}{Deno_2} \quad (2.109)$$

with

$$Num_1 = \frac{\sqrt{3}}{\sin \phi_C} \left(1 + \frac{\sin 3\beta(Pol-1)}{1+Pol} \right)^n (A_1 + Pol A_2) \quad (2.110)$$

$$Den_1 = 2^n (\sin \phi_C - 3)^2 \left(\frac{Pol}{1+Pol} \right)^n (1 - \sin 3\beta + Pol(1 + \sin 3\beta)) \quad (2.111)$$

$$Num_2 = 2\sqrt{3} \frac{(\sin 3\beta - 1)}{\tan \phi_E} (I_\sigma \sin \phi_C - 3c \cos \phi_C) \left(1 + \frac{\sin 3\beta(Pol-1)}{1+Pol} \right)^n \quad (2.112)$$

$$Den_2 = 2^n (\sin \phi_C - 3)(\sin \phi_E + 3) \left(\frac{Pol}{1+Pol} \right)^n (1 - \sin 3\beta + Pol(\sin 3\beta + 1)) \quad (2.113)$$

where

$$Pol = \left(\frac{\sin \phi_C (3 + \sin \phi_E)}{\sin \phi_E (3 - \sin \phi_C)} \right)^{\frac{1}{n}} \quad (2.114)$$

$$A_1 = (6c - 2c \sin \phi_C)(1 - \sin 3\beta) \quad (2.115)$$

$$A_2 = 3c(1 + \sin 3\beta - \cos 2\phi_C - \sin 3\beta \cos 2\phi_C) - 2c \sin \phi_C (\sin 3\beta + 1) + I_\sigma \sin 2\phi_C (1 + \sin 3\beta) \quad (2.116)$$

With such derivatives of f with respect to friction angles, the hardening of the VE model becomes different from the DP one. The initial and final values of friction angles are identical for the two criteria, and so are the intermediate values of the compressive friction angles ϕ_C during hardening. However the extensive friction angles ϕ_E are different during hardening for the two criteria : for DP the variation of ϕ_E is related to the variation of ϕ_C whereas for VE the variation of ϕ_E is related to the equivalent plastic strain via the hyperbolic relation (2.53).

The flow potential g is expressed using a similar formulation than the yield function f

$$g = II_{\dot{\sigma}} + m' \left(I_\sigma - \frac{3c}{\tan \phi_C} \right) = 0 \quad (2.117)$$

where the coefficient m' is obtained in an identical way than m (equations (2.97), (2.100), (2.101), (2.77) and (2.78)) replacing the two friction angles ϕ_C and ϕ_E by the two dilatancy angles ψ_C and ψ_E . Derivatives of the flow potential g with respect to stresses are described with the same relations than those obtained for the yield surface f (equations (2.104) to (2.116)). It is worth pointing out that, unlike for DP criterion, the expression of the flow potential must include the cohesion term as it appears in the derivative of g with respect to stresses (see equation (2.105)).

2.3.2.5 Convexity condition for the Van Eekelen surface

In classical plasticity framework, the maximum plastic work rule is always verified when the flow rule is associated and when the yield criterion is convex. Note that from experimental work on geomaterials, the plasticity is usually found to be non-associated (non-standard materials) with a convex potential (LANIER, 1988; HAMMAD, 1991).

When the Van Eekelen criterion is used, the convexity of the yield surface is not generally ensured. Then special care must be paid when choosing parameters of this criterion. Its convexity depends on three parameters which are examined below.

2.3.2.5.1 Exponent n

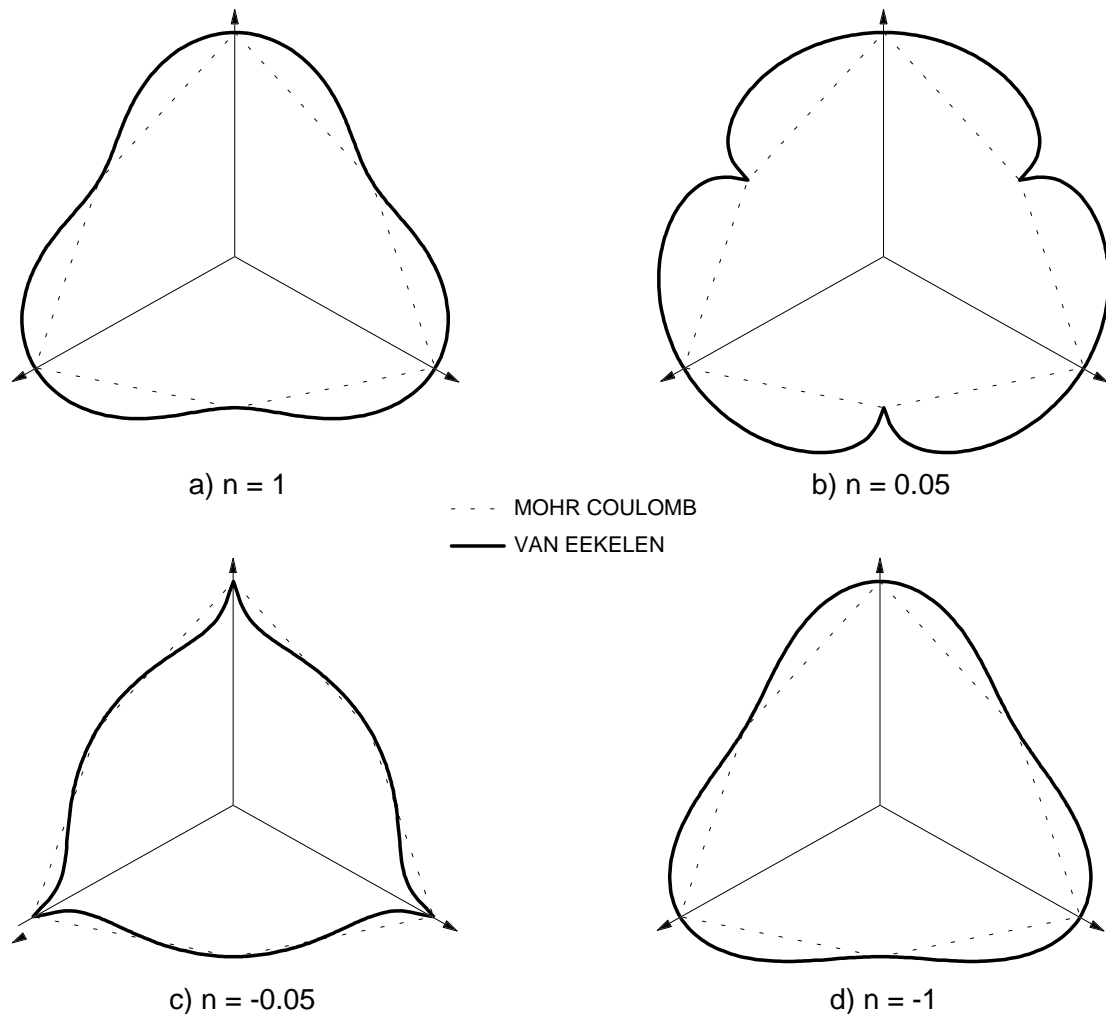


Figure 2.13 Influence of the exponent value on the Van Eekelen yield surface for $\phi_C = \phi_E = 35^\circ$.

The exponent n in equations (2.97), (2.100) and (2.101) directly controls the transition between the extension and compression reduced radii. The trace of VE criterion in the Π plane for $\phi_C = \phi_E = 35^\circ$ and for different values of exponent n is shown on figure 2.13. Note that for all the exponent values displayed, the resulting criteria are no longer convex. VAN EEKELEN [1980] showed that the convexity is usually verified for $n = -0.229$ provided that $\phi_E \geq \phi_C$.

2.3.2.5.2 Friction angle values

This condition holds true as long as friction angles are lower than 50° . Above this value, the Mohr Coulomb criterion shape becomes close to a triangle, then it becomes impossible to obtain a smoothed MC surface which remains convex. This point is illustrated on figure 2.14 for friction angles equal to 70° ($n=-0.229$). In this case, one could obtain a convex yield surface increasing the friction angle for extension paths.

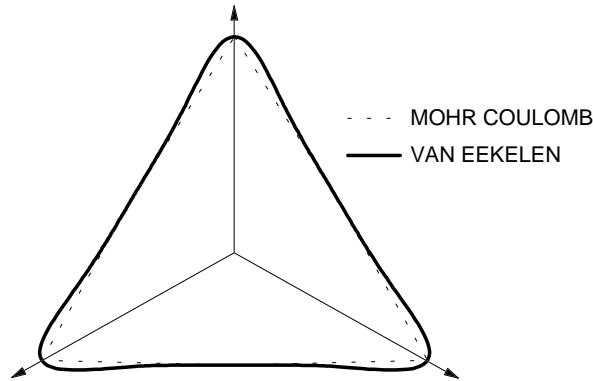


Figure 2.14 Limit surface for Van Eekelen criterion ($n=-0.229$) in the Π plane for $\phi_C=\phi_E=70^\circ$.

2.3.2.5.3 The ratio between ϕ_C and ϕ_E

As ϕ_E becomes smaller than ϕ_C , the yield surface convexity loss occurs for smaller values of friction angles. On the opposite as ϕ_E becomes larger than ϕ_C , the surface tends to be convex for higher friction angle values (the limit case being represented here by the Drucker Prager criterion).

2.3.2.5.4 Conclusion on the convexity condition

As shown in the previous sections, the convexity of the Van Eekelen surface is not ensured for any set of parameters. However, we are mainly concerned here with geomechanical simulations, i.e. with materials for which friction angles higher to 50° are unrealistic. Current friction angles for geomaterials range usually between 0° and $35-40^\circ$, which is the range in which no convexity loss occurs for $n=-0.229$.

Then for such classical material, this standard exponent value $n=-0.229$ will lead in any case to a convex surface. Only in some special cases the convexity might not be reached with the standard n exponent.

In order to avoid the use of a non convex set of parameters, a test of the yield surface convexity has been incorporated in the constitutive law subroutine. It is based on a numerical and approximate evaluation of the surface convexity. For symmetry reasons only a sixth of the surface has to be studied (solid line from point A to B on figure 2.15). This numerical test computes, from the angle $\alpha=0^\circ$ to $\alpha=60^\circ$ (i.e. for Lode angles $\in [-30^\circ; +30^\circ]$), the distance h between the point D and the line AC (see figure 2.15). If this distance h is always positive definite and if it increases as the angle α increases from 0 to 60° , then the Van Eekelen surface is convex. All the other cases represent non convex surfaces. Then the convexity condition is formulated as

$$\text{if } \begin{cases} h \geq 0 \\ h \uparrow \text{ as } \alpha \uparrow \text{ from } 0 \text{ to } 60^\circ \end{cases} \text{ then surface is convex} \quad (2.118)$$

else surface is not convex

This numerical test is performed only once in the pre-processor with initial or initial and final parameter values, depending whether there is hardening/softening or not.

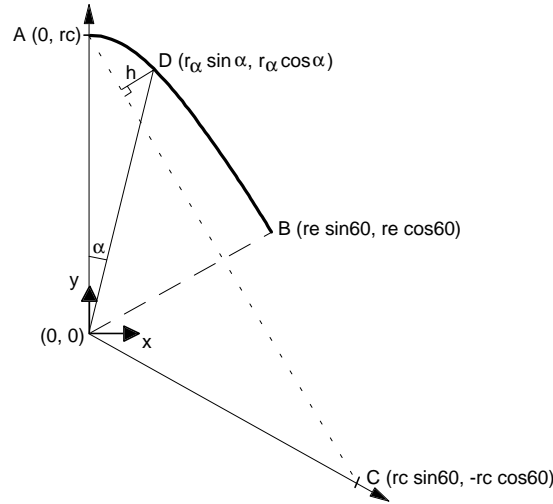


Figure 2.15 Geometrical interpretation of the convexity condition for Van Eekelen criterion.

2.3.2.6 Comparison between MC, DP and VE yield criteria

The traces of the three yield surfaces are plotted on figure 2.16 for low ($\phi_C=5^\circ$) to high friction angles values ($\phi_C=45^\circ$), with $\phi_E=\phi_C$ for Van Eekelen one. At very low friction angles the 3 criteria are pretty much similar (see figure 2.16a). It is clear that the differences between the DP criterion on one hand and the MC or VE criteria on the other hand increases as friction angle gets larger. This is directly related to the relation between ϕ_C and ϕ_E (see equation (2.79) and figure 2.11). From equation (2.79) it is found that, for $\phi_C=20^\circ$, then $\phi_E=26^\circ$. However as friction angle ϕ_C gets closer to the limit value 36.89° , the corresponding angle ϕ_E approaches 90° . Therefore if low friction angles are considered (let say below 20°), the 3 criteria will give approximately the same results. However above this value of 20° , some significant differences can be expected between the DP criterion on one hand and the MC or VE criteria on the other hand. These 3 criteria can also be compared against experimental determination of the limit surface shape in the Π plane obtained on sand by [LANIER, 1988] and given in section 2.3.2. The VE model is the best fit of these experimental results both regarding the yield surface shape and regarding the slight difference observed between the friction angle for triaxial compression and triaxial extension stress paths.

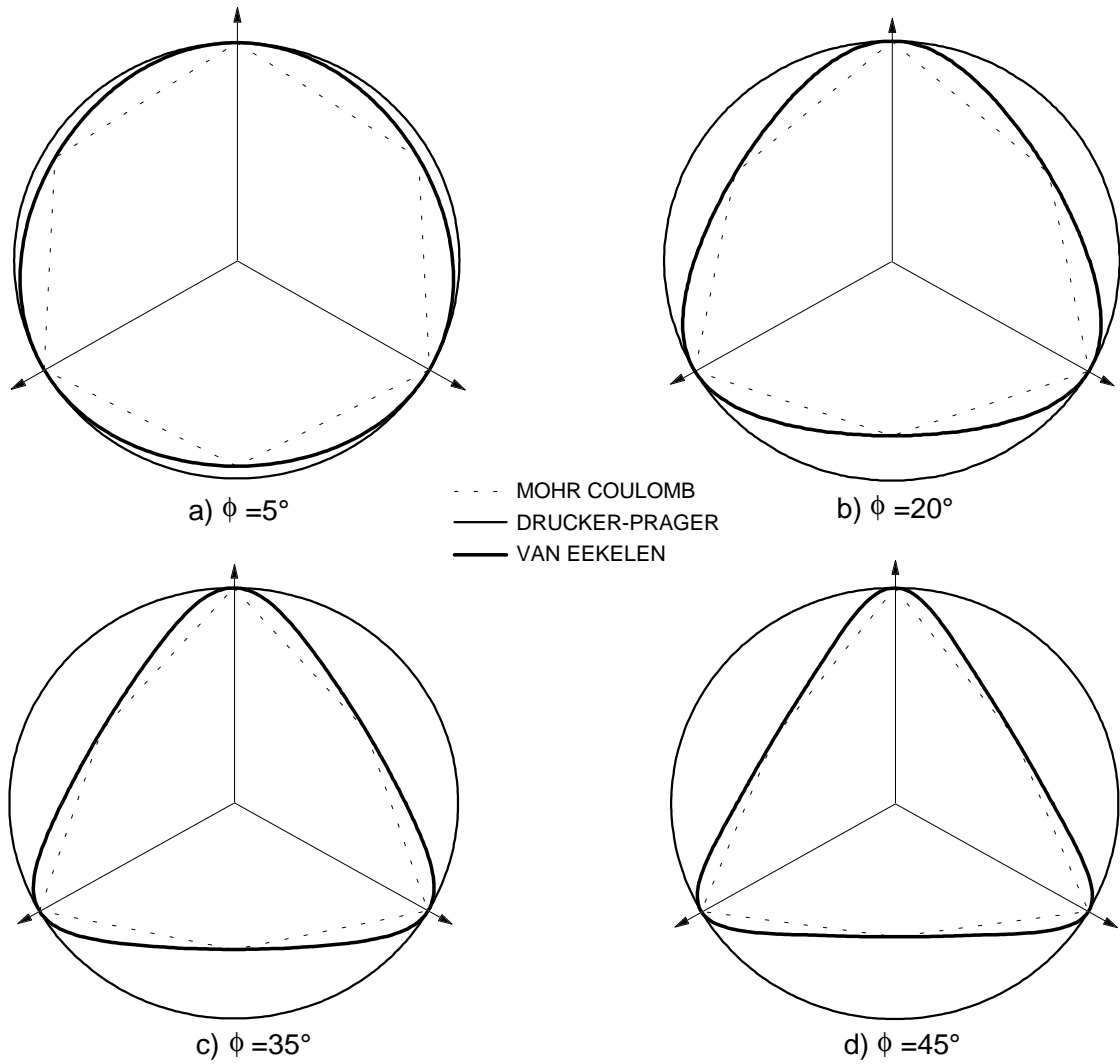


Figure 2.16 Limit surfaces for Mohr-Coulomb, Drucker Prager and Van Eekelen criteria in the deviatoric plane for different friction angle values: a) $\phi=5^\circ$, b) $\phi=20^\circ$, c) $\phi=35^\circ$, d) $\phi=45^\circ$.

2.3.2.7 Frictionless behaviour

If the friction angle is nil ($\phi_c=0$), the equation (2.75) used for the DP yield surface can no longer be used as it includes a division by zero. However, combining equations (2.75) and (2.73) simplifies to the well-posed equation

$$f = II_{\sigma} - \frac{2c}{\sqrt{3}} = 0 \quad (2.119)$$

This is the equation of a cylinder whose axis is the hydrostatic axis, thus the yield surface becomes in this case a Von Mises plastic surface provided that there is some cohesion c .

The VE criterion can no longer be computed when the friction angle is nil as the reduced radius defined by equations (2.77) and (2.78) becomes nil; then computation of coefficient b (equation (2.100)) becomes impossible for this criterion. However, in this case the reduced radii in extension and compression are equal, thus the VE criterion reduces also to a frictionless DP surface (equation (2.119)) provided that there is some cohesion, i.e. a Von Mises plastic surface.

Thus as the friction angles becomes nil, both DP and VE criteria reduce to a Von Mises like surface for which all the derivatives required in the formulation have already been given for the DP criterion. Of course these considerations can also be applied to plastic potential surfaces.

2.3.2.8 Traction behaviour (apex regime)

Provided that $\phi_c \neq 0$, the DP and VE criteria become conical like surfaces with their apex located on the hydrostatic axis at the value

$$I_\sigma = \frac{3c}{\tan \phi_c} \quad (2.120)$$

This point represents a singularity in the yield surface as it is the only location where the yield surface can no longer be derived. Thus although the traction behaviour is not a major concern in this work, it is important for numerical robustness of the stress integration algorithm to take a special care of those ultimate traction state in order to avoid either numerical divergence and unrealistic traction stresses.

For every trial stress state which will overcome some traction stress value, the plasticity will not anymore be described with the classical DP or VE criteria. For such stress states, a new yield surface which states that during plastic flow the stress state is mapped back onto the traction limit point given by equation (2.120). Thus the yield surface reduces to this point and therefore the yield criterion for the apex regime is given by

$$f = I_\sigma - \frac{3c}{\tan \phi_c} = 0 \quad (2.121)$$

Now it is required to evaluate for every trial stress state whether the classical yield criterion (DP or VE) or the apex one should be used. For this purpose, let us consider an elastic stress increment $\Delta\sigma$ applied to a stress state σ^A . Then a trial stress state σ^E is defined (see figure 2.17).

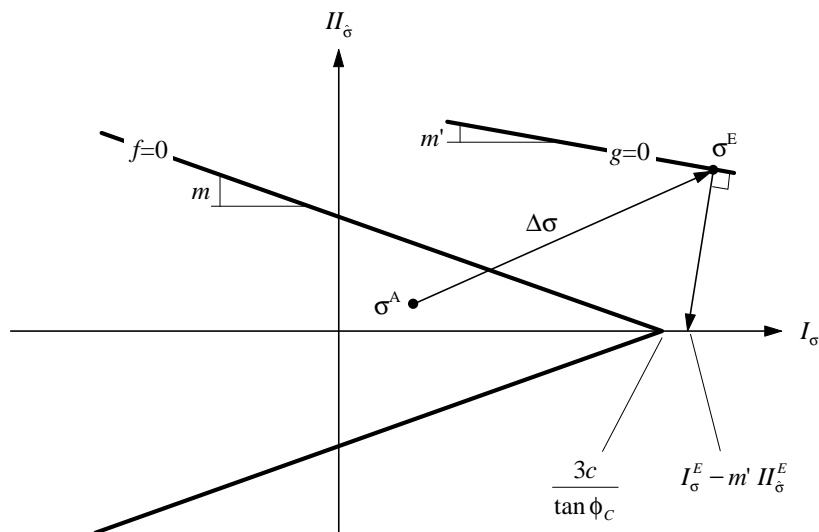


Figure 2.17 Traction regime and projection of the trial state on the hydrostatic axis.

Using the projection of the stress state σ^E onto the hydrostatic axis following the normal to the plastic potential g (see figure 2.17), then the apex criterion (equation (2.121)) must be used if the inequality

$$I_{\sigma}^E - m' II_{\sigma}^E > \frac{3c}{\tan \phi_C} \quad (2.122)$$

is verified. In order to achieve the apex criterion description, the following derivatives are required

$$\frac{\partial f}{\partial \sigma_{ij}} = \frac{\partial g}{\partial \sigma_{ij}} = \delta_{ij} \quad (2.123)$$

Using these derivatives, the left hand term in the denominator of equation (2.65) simplifies to

$$\frac{\partial f}{\partial \sigma_{mn}} C_{mnop}^e \frac{\partial g}{\partial \sigma_{op}} = 9\chi \quad (2.124)$$

At last, the hardening/softening must be introduced in the apex criterion in the same way than for the classical plastic criteria as a function of the Von Mises equivalent plastic strain. However, the equation (2.59) between the plastic strain rate and the plastic multiplier rate becomes equal to zero in this case, then no equivalent plastic strain is associated to apex regime plasticity

$$\dot{\epsilon}_{eq}^p = 0 \quad (2.125)$$

and therefore no hardening/softening occurs.

2.3.3 Integration of the elastoplastic constitutive relation

The general rate constitutive elastoplastic relation has been obtained in the previous section (equation (2.64)). Integration over time of this equation leads to the incremental form

$$\Delta \sigma_{ij} = (C_{ijkl}^e - C_{ijkl}^p) \Delta \epsilon_{kl} \quad (2.126)$$

A detailed analysis of the different methods used for the integration of different stress-strain relations has been presented in [CHARLIER, 1987]. The method used here is based on the operator split methodology [SIMO and TAYLOR, 1985] which consists in computing an elastic predictor/plastic corrector.

2.3.3.1 Elastic predictor

From a given stress state σ^A at beginning of the step, the stress increment $\Delta \sigma^e$ corresponding to a purely elastic response is computed with

$$\Delta \sigma_{ij}^e = C_{ijkl}^e \Delta \epsilon_{kl} \quad (2.127)$$

which defines a trial stress state σ^E at point E

$$\sigma_{ij}^E = \sigma_{ij}^A + \Delta \sigma_{ij}^e \quad (2.128)$$

If the stress state σ^E does not violate the yield criterion (i.e. $f(\sigma^E, \kappa^A) \leq 0$), then the step is fully elastic. If the trial stress state at point E overcomes the yield criterion i.e. $f(\sigma^E, \kappa^A) > 0$ (see figure 2.18), then a plastic correction must be computed to map back the stress state onto the yield surface. Note that the stress point corresponding to the entry in plastic regime lies at σ^C .

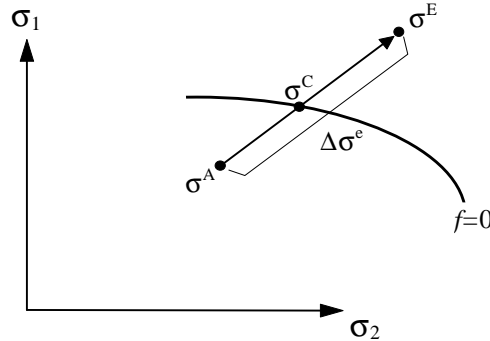


Figure 2.18 Evaluation of the trial stress state at point E.

2.3.3.2 Plastic corrector

In this phase, the plastic strain increment $\Delta \epsilon^p$, the plastic stress increment $\Delta \sigma^p$ (opposite sign to $\Delta \sigma^e$) and the hardening/softening increment $\Delta \kappa$ must be determined.

In the classical framework of non-associated plasticity, the plastic strain increment $\Delta \epsilon^p$ is defined by its direction and intensity (see equation (2.49)). The plastic strain increment direction is given by the normal \mathbf{n} of the plastic flow potential g , i.e.

$$\mathbf{n} = \frac{\partial g}{\partial \sigma} \quad (2.129)$$

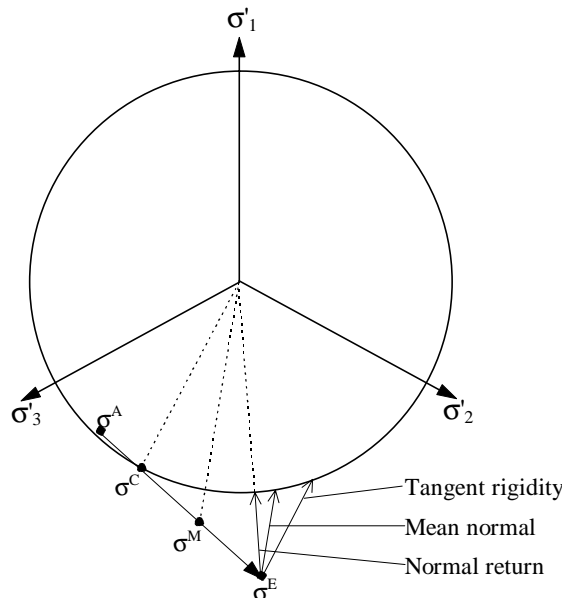


Figure 2.19 Choice of the normal : comparison between three possible directions for a Von Mises type criterion (modified from [CHARLIER, 1987]).

Several choices can be made regarding the choice of the normal \mathbf{n} ([CHARLIER, 1987], see figure 2.19) :

- beginning of the step, i.e. at point C (tangent rigidity), and in this case the method is fully explicit,
- middle of the step, i.e. at point M (mean normal), in this case the method is semi-implicit,
- end of the step, i.e. at point E and in this case the method is fully implicit. This choice corresponds to a radial return for Von Mises type of surfaces in deviatoric plane. However, for non circular surfaces like the Van Eekelen one, this choice does not coincide with a radial return. A radial return can be obtained combining a Van Eekelen yield criterion and a Drucker Prager flow surface.

The explicit method is only stable for small time increments whereas the semi-implicit and fully implicit method are unconditionally stable. Moreover, the explicit and the semi-implicit method require the computation of stresses at point C for which a simple relationship can be derived for the Drucker Prager criterion [CHARLIER, 1987]. However, in the more complex case of the Van Eekelen criterion, such simple relation does not exist and an iterative method must be used to compute the solution at point C, which requires extra computation time.

Therefore a fully implicit backward Euler scheme has been adopted here to integrate the constitutive relation (see figure 2.20), i.e. all the variables are computed at point B, and the solution is obtained using Newton-Raphson iterative method. A first order Taylor development of the plasticity criterion f around the stress state at point B yields

$$f(\sigma_{ij}^B + \Delta\sigma_{ij}^p, \kappa^B + \Delta\kappa) = f(\sigma_{ij}^B, \kappa^B) + \frac{\partial f}{\partial \sigma_{ij}^B} \Delta\sigma_{ij}^p + \frac{\partial f}{\partial \kappa^B} \Delta\kappa \quad (2.130)$$

with

$$\Delta\sigma_{ij}^p = -C_{ijkl}^e \Delta\varepsilon_{kl}^p \quad (2.131)$$

$$\Delta\kappa = \frac{d\kappa}{d\varepsilon_{eq}^p} Val \Delta\lambda \quad (2.132)$$

Thus equation (2.130) can be re-written

$$f = f(\sigma_{ij}^B, \kappa^B) - \frac{\partial f}{\partial \sigma_{ij}^B} C_{ijkl}^e \Delta\lambda \frac{\partial g}{\partial \sigma_{kl}^B} + Val \frac{\partial f}{\partial \kappa^B} \frac{d\kappa}{d\varepsilon_{eq}^p} \Delta\lambda \quad (2.133)$$

Using the consistency condition $f=0$, the increment of plastic strain is obtained

$$\Delta\lambda = \frac{f(\sigma_{ij}^B, \kappa^B)}{\frac{\partial f}{\partial \sigma_{ij}^B} C_{ijkl}^e \frac{\partial g}{\partial \sigma_{kl}^B} - Val \frac{\partial f}{\partial \kappa^B} \frac{d\kappa}{d\varepsilon_{eq}^p}} \quad (2.134)$$

and the corrected stress state σ^B is obtained from

$$\sigma_{ij}^B = \sigma_{ij}^B - \Delta\lambda C_{ijkl}^e \frac{\partial g}{\partial \sigma_{kl}^B} \quad (2.135)$$

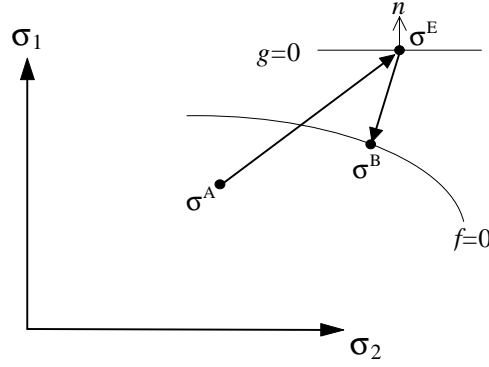


Figure 2.20 Fully implicit scheme : stress space representation for perfect plasticity.

On a practical point of view, the values used at the first iteration are the one known at point E (σ^E, κ^E). For further iterations, those values are corrected by the ones obtained at the previous iteration.

For perfectly plastic circular criterion (DP or Von Mises), a coherent stress state at point B such that $f(\sigma^B, \kappa^B) \approx 0$ is reached after one iteration (one step return algorithm). But in a more general case of a non-circular criterion, some iterations are required to obtain a stress state at point B such that $f(\sigma^B, \kappa^B) \approx 0$. If there is hardening/softening, some iterations are also required to integrate κ^B over the step. The global integration algorithm is summarised on figure 2.21.

The convergence condition

$$f(\sigma^B, \kappa^B) \approx 0 \quad (2.136)$$

of this integration algorithm has been adapted to numerical handling. The convergence criterion is written in terms of the stress increments ratio between the $n-1^{\text{th}}$ iteration and n^{th} iteration following

$$1 - Prec < \max \left| \frac{\Delta \sigma_{ij}^n}{\Delta \sigma_{ij}^{n-1}} \right| < 1 + Prec \quad (2.137)$$

A value $Prec=10^{-3}$ has been chosen, thus convergence is achieved when the maximum stress variation between 2 iterations is smaller than 0.1%. The interest of such convergence criterion is that it is dimensionless, i.e. independent of the problem and unit system chosen.

Beginning of constitutive law integration

$n=0$

1. Compute elastic predictor σ^E

$$\sigma_{ij}^E = \sigma_{ij}^A + C_{ijkl}^e \Delta \varepsilon_{kl}$$

If $f(\sigma^E, \kappa^A) \leq 0$ Then

$$\sigma_{ij}^B = \sigma_{ij}^E, \quad \kappa^B = \kappa^A \quad (\text{elastic stress state})$$

Else

Initialise stresses and internal variables :

$$\sigma_{ij}^B = \sigma_{ij}^E, \quad \kappa^B = \kappa^A$$

2. Iteration $n=n+1$

Compute $\Delta \lambda$

$$\Delta \lambda = \frac{f(\sigma_{ij}^B, \kappa^B)}{\frac{\partial f}{\partial \sigma_{ij}^B} C_{ijkl}^e \frac{\partial g}{\partial \sigma_{kl}^B} - Val \frac{\partial f}{\partial \kappa^B} \frac{d\kappa}{d\varepsilon_{eq}^p}}$$

3. up-date equivalent plastic strain

$$\varepsilon_{eq}^p = \varepsilon_{eq}^p + Val \Delta \lambda$$

4. If (Hardening/Softening) up-date of κ^B

5. Compute new stresses at σ^B

$$\sigma_{ij}^B = \sigma_{ij}^B - \Delta \lambda C_{ijkl}^e \frac{\partial g}{\partial \sigma_{kl}^B}$$

6. Test on yield condition $f(\sigma^B, \kappa^B) \approx 0$:

If $(1 - \text{Prec} < \max|\Delta \sigma^n / \Delta \sigma^{n-1}| < 1 + \text{Prec})$ Then

Solution has converged

Goto **End**

Else

Goto **2**

End If

Figure 2.21 Implicit backward Euler integration algorithm implemented in the elastoplastic constitutive law *PLASOL*.

2.3.3.3 Test of the integration algorithm

The global efficiency of this integration algorithm has been checked numerically. Separate runs considering different stress paths in a given deviatoric plane have been performed : considering the deviatoric plane at $I_\sigma=1$, the stress range in Cartesian co-ordinates $x \in [-10r_C, 10r_C]$, $y \in [-10r_C, 10r_C]$ and $z=1$ has been chosen, with an increment of $0.25r_C$ in both directions (r_C is given in equation (2.77)). Thus, for each test a set of 6561 stress points has been computed. This procedure requires to transform stress tensors expressed in Cartesian co-ordinates $\mathbf{X}_{/xyz}$ into stress tensors expressed in deviatoric plane $\mathbf{X}_{/123}$ co-ordinates using

$$\mathbf{X}_{/123} = \mathbf{R}\mathbf{X}_{/xyz} \quad (2.138)$$

with the definition of the transformation matrix \mathbf{R}

$$\mathbf{R} = \begin{bmatrix} \frac{2}{\sqrt{6}} & 0 & \frac{1}{\sqrt{3}} \\ \frac{1}{\sqrt{6}} & \frac{1}{\sqrt{2}} & \frac{1}{\sqrt{3}} \\ -\frac{1}{\sqrt{6}} & \frac{1}{\sqrt{2}} & \frac{1}{\sqrt{3}} \\ -\frac{1}{\sqrt{6}} & -\frac{1}{\sqrt{2}} & \frac{1}{\sqrt{3}} \end{bmatrix} \quad (2.139)$$

Only the Van Eekelen criterion is studied, considering a non-associated plastic law without dilatancy ($\psi=0^\circ$) and an associated law ($\psi=\phi$). Friction angles of 50° , 35° , 20° and 5° have been considered. In all these cases, the number of iterations required to map the trial stress state back onto the yield surface falls in the range [2;4]. When the dilatancy is nil, the stress return (which then is a radial return) is performed in two iterations for all the considered angles values. On the opposite when associated law are chosen, the stress return is no longer a radial return and some additional iterations are required. Figure 2.22 displays the contour map of the total number of iterations required to map the stress state onto the yield surface.

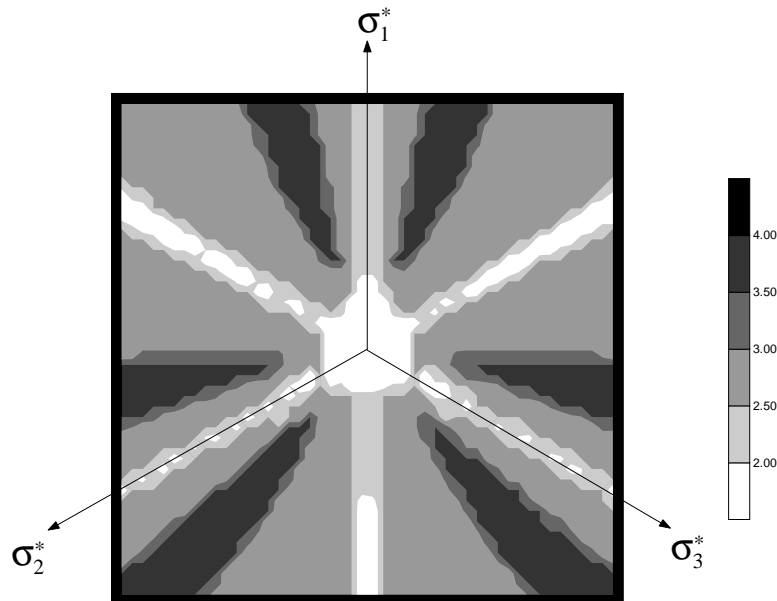


Figure 2.22 Isovalues map of the number of iterations required to map back a trial state, with $x \in [-10r_C, 10r_C]$, $y \in [-10r_C, 10r_C]$ and for $\phi_C=\phi_E=\psi_C=\psi_E=50^\circ$.

2.3.3.4 Sub-step integration

In order to decrease the computation time, loading steps Δt as large as possible are required. However for such large steps, the stress integration must remain as accurate as possible. This can be achieved performing a sub-step integration which is a classical procedure used in the *LAGAMINE* code. The time increment Δt is divided in $Nintv$ sub-intervals δt defined by

$$\delta t = \frac{\Delta t}{Nintv} \quad (2.140)$$

The number of sub-intervals $Nintv$ can be fixed to a given value (let say 10 or 20). However, a better choice consists in computing an adaptive value of $Nintv$ as a function of deformation [WANG, 1993] at integration point level

$$Nintv = \min \left\{ 1 + \frac{\dot{\epsilon}_N \Delta t}{Div}, 100 \right\} \quad (2.141)$$

where a strain norm rate is defined by

$$\dot{\epsilon}_N = \sqrt{\dot{\epsilon}_{ij} \dot{\epsilon}_{ij}} \quad (2.142)$$

As a result, for every iteration the number of sub-intervals is adapted at each integration point as a function of strain : the larger the strain at one integration point, the larger the number of sub-intervals and then the better the stress integration accuracy. On the opposite, for integration points where strain is low, then the number of sub-intervals is low. Of course, the choice of the parameter Div is somehow arbitrary [WANG, 1993], but experience has shown that a default value of $Div \approx 5.10^{-3}$ usually gives satisfactory adaptive values for $Nintv$.

2.3.3.5 Implementation in the *LAGAMINE* code

Three yield surfaces, namely the Von Mises, the Drucker Prager and the Van Eekelen criteria have been implemented in the *LAGAMINE* finite element code under the generic law name *PLASOL*. A two dimensional (plane strain and axisymmetric cases, subroutine *PLA2EA*) and three dimensional version (subroutine *PLA3D*) of *PLASOL* law are available. These 2 main subroutines call the following subroutines : *PLAINV* (computation of stress invariants), *PLANOR* (stress normalisation), *PLAINT* (time integration) and *PLADER* (computation of derivatives). The organisation of these routines is described in the diagram below.

PLA2EA or *PLA3D*

→ call *PLAINV*

→ call *PLANOR*

→ call *PLAINT*

→ call *PLADER*

→ call *PLAINV*

→ call *PLANOR*

2.4 Some other constitutive laws for geomaterials

2.4.1 An elastoviscoplastic law

The non-linear elastoviscoplastic law *IRSID* was originally developed for metals, its extensive description can be found in [CHARLIER, 1987]. Such law can also represent the behaviour of some specific rocks (rocks under high temperature, evaporitic rocks). This law will be used in chapter 7 to represent the behaviour of anorthositic rocks.

A Von Mises plastic surface $f=II_{\hat{\sigma}}-H=0$ is chosen to separate the elastic domain ($f<0$) from the viscoplastic domain ($f\geq 0$), where H is the initial yield limit corresponding to the radius of the Von Mises cylinder in the principal stress space. In this case, the yield surface is not a limit surface, i.e. there is no consistency condition. The viscoplastic strain rate is defined by

$$\dot{\mathbf{\epsilon}}^{vp} = \dot{\lambda} \frac{\partial f}{\partial \hat{\boldsymbol{\sigma}}} = \dot{\lambda} \hat{\boldsymbol{\sigma}} \quad (2.143)$$

As in associated plasticity, the viscoplastic strain direction is normal to a plastic potential. However its intensity $\dot{\lambda}$ cannot be defined from the consistency condition. It is function here of the distance $d=II_{\hat{\sigma}}-H$ between the plastic criterion and the stress deviator (usually referred as the overstress), provided that the condition $d>0$ is verified (otherwise the state is elastic). Equation (2.143) reads

$$\dot{\mathbf{\epsilon}}^{vp} = B \left(\frac{II_{\hat{\sigma}}}{H} \right)^n \frac{\hat{\boldsymbol{\sigma}}}{II_{\hat{\sigma}}} \quad (2.144)$$

If a linear behaviour is considered ($n=1$) and provided that H is small compared to $\hat{\boldsymbol{\sigma}}$, equation (2.144) represents a linear viscoelastic behaviour in which the term B/H is equivalent to the inverse of viscosity $1/\eta$.

2.4.2 Contact laws

The contact elements presented in section 2.2.4.2 require the use of a particular constitutive relation which links the contact stress rate to the contact strain rate.

2.4.2.1 Coulomb frictional model

For contact, the Coulomb frictional law (equation (2.70)) can be written

$$f = \sqrt{(\tau_2)^2 + (\tau_3)^2} - (c + \mu p) \quad (2.145)$$

where $\mu=\tan\phi$ is the friction coefficient and p is the contact pressure. In this relation, f can be considered as a yield surface in the $(p, \sqrt{(\tau_2)^2 + (\tau_3)^2})$ plane which defines three zones (see figure 2.23) :

- $f<0$ is the domain of sticking contact,
- $f=0$ is the domain of sliding contact,
- $f>0$ is impossible.

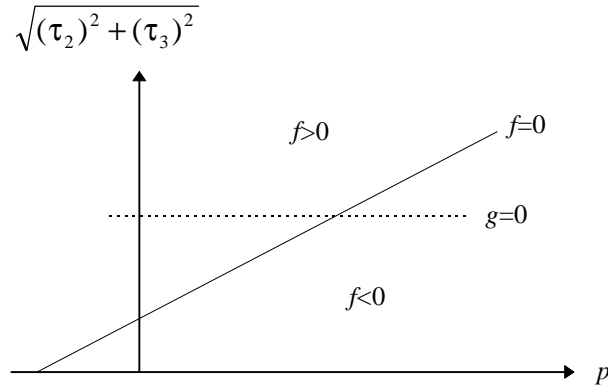


Figure 2.23 Coulomb contact law.

If there is sticking contact ($f < 0$), the contact strain rate must be nil ($\dot{\epsilon}_c = 0$). However, as mentioned in section 2.2.4.2, this condition is relaxed using a penalty method.

The sticking contact stress rate can be computed from

$$\dot{\sigma}_c = \mathbf{K}_c \dot{\epsilon}_c \quad (2.146)$$

or

$$\begin{Bmatrix} \dot{p} \\ \dot{\tau}_2 \\ \dot{\tau}_3 \end{Bmatrix} = \begin{bmatrix} K_p & 0 & 0 \\ 0 & K_\tau & 0 \\ 0 & 0 & K_\tau \end{bmatrix} \begin{Bmatrix} \dot{\epsilon}_{c1} \\ \dot{\epsilon}_{c2} \\ \dot{\epsilon}_{c3} \end{Bmatrix} \quad (2.147)$$

where \mathbf{K}_c is the penalty matrix. The penalty coefficients K_p and K_τ controls the tolerated penetration d_1 and the relative sliding d_2 through the approximate formulas

$$K_p \approx \frac{p}{d_1}, \quad K_\tau \approx \frac{\tau_2}{d_2} \approx \frac{\tau_3}{d_2} \quad (2.148)$$

On a practical point of view, these penalty coefficients (see the *COU2DC-COU3DC* contact laws in the *LAGAMINE* reference manual) should be as large as possible in order to prevent significant penetration and relative sliding between the two bodies. However, too high values generally leads to convergence difficulties of the iterative resolution method. Therefore, although equation (2.148) usually gives reasonable values, some practice is usually required to choose an acceptable set of values for K_p and K_τ .

If there is sliding contact ($f = 0$), a classical elastoplastic development can be applied [CHARLIER and CESCOTTO, 1988] in a similar fashion than the one developed in section 2.3.1. Here a non-associated flow surface g is used

$$g = \sqrt{(\tau_2)^2 + (\tau_3)^2} \quad (2.149)$$

which corresponds to isochoric plasticity, i.e. with dilatancy $\psi = 0$.

2.4.2.2 Other laws

The elastoplastic constitutive relations formulated for solid elements can be adapted for the use with contact finite elements [CHARLIER and PIERRY, 1993] in order to account for

dilatancy and/or hardening/softening phenomena. Plane strain state is considered. With the interface thickness noted e , the strain rate tensor $\dot{\boldsymbol{\epsilon}}_{Cs}$ for the material lying inside the interface and expressed in local axes $(\mathbf{e}_1, \mathbf{e}_2, \mathbf{e}_3)$ reads

$$\dot{\boldsymbol{\epsilon}}_{Cs} = \frac{1}{e} \begin{bmatrix} \dot{u}_1 & \dot{u}_2/2 & 0 \\ \dot{u}_2/2 & 0 & 0 \\ 0 & 0 & 0 \end{bmatrix} \quad (2.150)$$

where the components \dot{u}_1 and \dot{u}_2 have already be defined in equation (2.30). In this case the contact stress tensor $\boldsymbol{\sigma}_{Cs}$ expressed in the local axes $(\mathbf{e}_1, \mathbf{e}_2, \mathbf{e}_3)$

$$\boldsymbol{\sigma}_{Cs} = \begin{bmatrix} \sigma_{C11} & \sigma_{C12} & 0 \\ \sigma_{C12} & \sigma_{C22} & 0 \\ 0 & 0 & \sigma_{C33} \end{bmatrix} \quad (2.151)$$

is linked to the global stress tensor $\boldsymbol{\sigma}$ expressed in the global axes $(\mathbf{x}_1, \mathbf{x}_2, \mathbf{x}_3)$ by the relations

$$\begin{aligned} \sigma_{C11} &= \sigma_{11} \cos^2 \alpha + \sigma_{22} \sin^2 \alpha + \sigma_{12} \sin 2\alpha \\ \sigma_{C12} &= \frac{1}{2} (\sigma_{22} - \sigma_{11}) \sin 2\alpha - \sigma_{12} \cos 2\alpha \\ \sigma_{C22} &= \sigma_{11} \cos^2 \left(\alpha - \frac{\pi}{2} \right) + \sigma_{22} \sin^2 \left(\alpha - \frac{\pi}{2} \right) + \sigma_{12} \sin 2\alpha \\ \sigma_{C33} &= \sigma_{33} \end{aligned} \quad (2.152)$$

where the angle α is the angle between the \mathbf{x}_1 axis and the normal to the contact \mathbf{e}_1 (see figure 2.24).

Then the general form of the constitutive relation can be used

$$\dot{\boldsymbol{\sigma}}_{Cs} = \frac{1}{e} \mathbf{C} : \dot{\boldsymbol{\epsilon}}_{Cs} \quad (2.153)$$

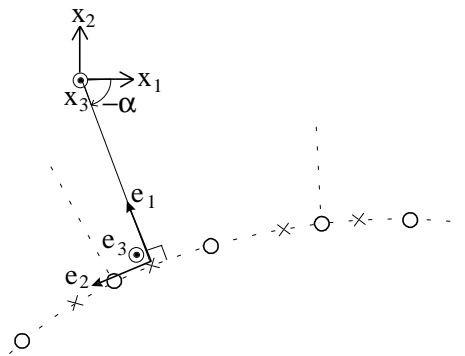


Figure 2.24 Angle between the contact element and the global axes \mathbf{x} .

For an elastic behaviour, this equation is similar to equation (2.148) with the penalty matrix \mathbf{K}_C defined by

$$\mathbf{K}_C = \frac{1}{e} \mathbf{C} \quad (2.154)$$

2.5 Initiation of the stress state

As mentioned earlier in this chapter, when a computation is performed from a virgin (i.e. nil) state of stress ($\sigma=0$ in every integration point of the solid domains) under gravity forces, a global subsidence of the model is usually observed in the first step. This comes from the compressibility (mainly elastic) of the materials which are submitted to a gravity field from a nil state of stress.

In order to avoid partially this problem, it is possible in simple cases to compute analytically a balanced initial state of stress which verifies the equilibrium equation (2.11). In general, this is the case when the geometry of the model is simple (quadrilateral) and when its boundaries coincide with the chosen referential. In such a case, equilibrium along the vertical direction yields the relation for vertical stress by integration of (2.11)

$$\sigma_v = -\rho gh \quad (2.155)$$

In geomechanics, the horizontal stress component is usually defined from

$$\sigma_h = K_0 \sigma_v \quad (2.156)$$

where the coefficient K_0 remains to be defined.

If a linear elastic behaviour is considered, equilibrium is independent of K_0 , thus any value can be chosen for K_0 . Let us recall the definition of the elastic oedometric stress state

$$K_0 = \frac{\nu}{1-\nu} \quad (2.157)$$

where ν is the Poisson ratio.

If a Mohr Coulomb plastic behaviour is considered, the yield criterion (2.70) can be written considering either the vertical stress as the minor or major principal stress. Solving each case for K_0 gives the plastically admissible range for K_0

$$\frac{1-\sin\phi}{1+\sin\phi} - \frac{2c\cos\phi}{\sigma_v(1+\sin\phi)} \leq K_0 \leq \frac{1+\sin\phi}{1-\sin\phi} + \frac{2c\cos\phi}{\sigma_v(1-\sin\phi)} \quad (2.158)$$

which corresponds to the range for which $f \leq 0$. Note that if there is cohesion, the limit values of K_0 depend on the vertical co-ordinates through σ_v .

If a viscous behaviour is considered, the stress isotropy implies that

$$K_0 = 1 \quad (2.159)$$

In the *LAGAMINE* code, the stress initialisation is usually defined in the element section of the input file (see the parameter *INSIG* in the *LAGAMINE* reference manual). When *INSIG*=1, the initial vertical stresses are computed automatically from (considering 2D cases)

$$\sigma_v = \sigma_y = \sigma_{y0} + y \, dsig \quad (2.160)$$

in which

$$|dsig| = \rho g \quad (2.161)$$

and σ_{y0} is the vertical stress value at depth $y=0$. A modified version disables the possibility to generate traction state of stress ($INSIG=2$) using (considering 2D cases)

$$\sigma_v = \sigma_y = \min(\sigma_{y0} + y \, dsig ; 0) \quad (2.162)$$

In any cases, horizontal stresses are also computed automatically from (2.156). Of course similar reasoning can be applied to three-dimensional models for which the parameter $INSIG$ is also available.

However, the initial geometry may be more complex : free surface is not flat, layer boundaries do not coincide with referential axes, difference of specific mass between the materials... It then becomes impossible to define analytically an initial balanced stress field.

As the main interest of the initial stress computation is to avoid large vertical displacements due to gravity loading, it is still possible to compute an approximation of the vertical stress component using equations (2.155) and (2.156). If several layers with different specific masses are present, an average or a lower bound specific mass can be chosen. When there is a non-horizontal free surface, there are two possibilities to choose the value of σ_{y0} (see figure 2.25). The first one consists in computing its value from the topographic highest point and the second one from the lowest point. The first case results in an excess of stress everywhere but at the highest point, which will induce an artificial uplifting. The second case induces a lack of vertical stress every where but at lowest point, resulting in an artificial subsidence (in this case, the parameter $INSIG=2$ must be chosen to avoid initial traction states).

It must be pointed out that although this simple method is only approximate in simple cases, it generally allows to obtain quite small amount of numerical subsidence resulting from the initial equilibrium computation.

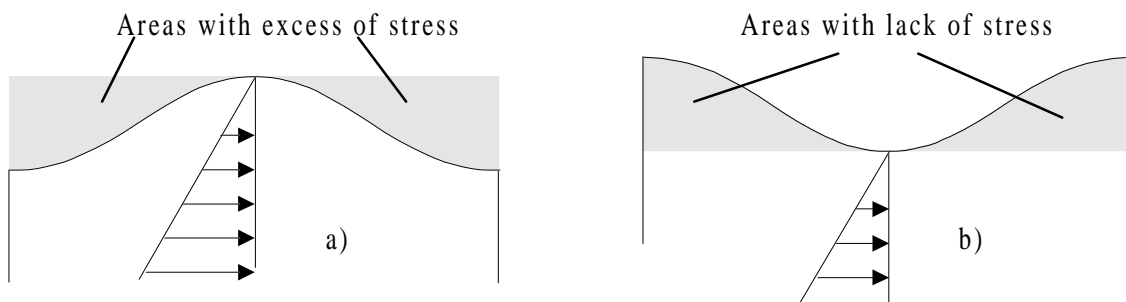


Figure 2.25 Stress initialisation for models with non-horizontal free surface : a) from the highest topographic point, b) from the lowest topographic point.

In the *LAGAMINE* code, the contact element formulation is based on the computation of the distance between the two sides of the contact area (see section 2.2.4.2). In the initial configuration, either a small interpenetration of the contact sides or initial stresses must be introduced in order to compute reactions on contact nodes and therefore a correct stiffness matrix. It is straightforward to initialise contact stresses (pressure and tangential stress) following a similar method than the one presented above for solid domains.

2.6 Predictive models for strain localisation and failure

In the classical elastoplastic framework, the irreversible behaviour of rocks is characterised by the change of stress regime from elasticity to plasticity, which is defined by a stress bound (yield criterion) in the stress space. Strain localisation may result from such type of models.

Rock failure can also be viewed as a bifurcation or change in the response of a model to a given loading condition. Diffuse modes of bifurcation or localised modes of bifurcation can exist. A diffuse mode can be represented by the buckling response of a laminated medium submitted to compression [BIOT, 1961]. In localised mode of deformation, the strain concentrates along elongated zones (or bands) with a given length and thickness. In this case, the localisation phenomenon comes from the change of the governing equations type (loss of ellipticity). This results in the indetermination of the band thickness, in the result's mesh dependence and in the questionable representation of post-bifurcation behaviour, unless high order continua (Cosserat media [COSSERAT, 1909], gradient plasticity [DE BORST, 1992; PAMIN, 1994] or non-local plasticity [LI and CESCOTTO, 1996]) are used. However, use of these continua lacks the experimental determination of the internal length parameters and a clear definition and meaning of boundary conditions. Sometime quite important modifications of the resolution algorithm are also required. These are the reasons why such enhanced continua have not been used in the practical examples studied further in this work.

In the damage theory, rock failure can also be viewed as the degradation of the tangent modulus with strain [ZHU, 1993; PEERLINGS et al., 1996]. This aspect has not been considered in the present work.

In the application chapters 6, 7, 8 and 9, several criteria and indicators will be used to visualise the strain localisation and to predict the *potential* failure of rock masses. They are reviewed in this section. These indicators actually must answer the following questions :

- when does failure or strain localisation occur?
- where does its occur?
- and how does it occur (direction, mode)?

2.6.1 Scalar indicators of strain localisation estimated from plasticity theory

Analysis of the strain field can show strain localisation along bands. The simplest analysis of the generation of a shear band is based on the visualisation of the Von Mises cumulated equivalent strain ε_{eq} map

$$\varepsilon_{eq} = \sqrt{\frac{3}{2} \hat{\mathbf{G}} : \hat{\mathbf{G}}} \quad (2.163)$$

where the strain tensor \mathbf{G} is computed with equation (2.8) in which the stretching tensor \mathbf{U} is computed between the initial configuration and the deformed configuration. Although \mathbf{G} represents the total strain tensor, it comes mainly from the plastic part of the strain. Isovalues maps of this scalar ε_{eq} show well achieved shear bands when localisation has strongly developed, but does not give the possibility to detect early stages of localisation.

In order to overcome this deficiency, a kinematic scalar indicator α can be defined, based on [VILOTTE et al., 1990]

$$\alpha = \frac{\Delta \dot{\epsilon}_{eq} \Delta t}{\epsilon_{eq}} \quad (2.164)$$

where Δt is the numerical time step increment and $\Delta \dot{\epsilon}_{eq}$ is the incremental deviatoric strain rate. This indicator represents the incremental equivalent strain related to cumulated equivalent strain. It allows to detect shear band localisation much earlier than relation (2.163) [BARNICHON and CHARLIER, 1996; CHARLIER et al., 1997; PIERRY, 1997].

In cases where the deformation reaches high value, it may be interesting to compute a "local" Von Mises cumulated equivalent strain $\epsilon_{eq(l)}$, which is computed in the same way than ϵ_{eq} but here the stretching tensor \mathbf{U} is computed between an intermediate configuration and the deformed configuration. Interest of this indicator will be illustrated in chapter 6.

These three criteria can be used to indicate the existence and the development of strain localisation, and particularly to detect strain localisation along shear bands.

2.6.2 Directions of failure estimated from plasticity theory

The Coulomb failure angle θ_C corresponds to the maximum shear stress at failure. It gives the directions of preferred failure plane with respect to the maximum compressive stress (soil mechanics sign convention)

$$\theta_C = \frac{\pi}{4} - \frac{\phi}{2} \quad (2.165)$$

where ϕ is the Coulomb friction angle. [ARTHUR et al., 1977] introduced the influence of the dilatancy angle, leading to the failure angle θ_A

$$\theta_A = \frac{\pi}{4} - \frac{\phi + \psi}{4} \quad (2.166)$$

Therefore, the theoretical failure angle θ for plasticity can be estimated from

$$\theta_C \leq \theta \leq \theta_A \quad (2.167)$$

The preferential failure directions can then be evaluated from the principal stress directions which can either be visualised using stress crosses or isostatic lines (as in chapter 6).

2.6.3 Rice bifurcation criterion

The Rice criterion [RICE, 1976] analyses the stress state and investigates the possibility of a bifurcation by formation of a shear band in the stress and strain paths. The theoretical scheme of a shear band is presented on figure 2.26. The development and the implementation of this criterion in the *LAGAMINE* code in large strain context has been achieved by [WANG, 1993] in which an extensive presentation can be found. Basics of its formulation are recalled here.

This criterion is based on a kinematic condition, a static condition and on the constitutive equation. The superscript ⁰ denotes variables outside the band and the superscript ¹ denotes variables inside the band.

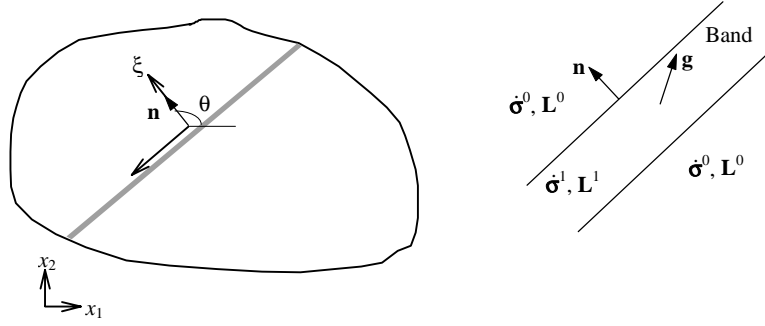


Figure 2.26 Theoretical scheme of a shear band.

The static condition expresses the surface equilibrium at the interface between the inner and outer band

$$\mathbf{n}(\dot{\boldsymbol{\sigma}}^1 - \dot{\boldsymbol{\sigma}}^0) = 0 \quad (2.168)$$

The kinematic condition expresses the strain jump across the band interface by a dilatant strain jump and a shear strain jump, but without any longitudinal strain jump

$$\mathbf{L}^1 = \mathbf{L}^0 + \mathbf{g} \otimes \mathbf{n} \quad (2.169)$$

where \mathbf{L} is the velocity gradient defined by equation (2.3), \mathbf{n} is the vector normal to the band, and \mathbf{g} is a vector describing the band mode.

The third equation introduced in the Rice criterion is the constitutive law. For an elastoplastic or an elastic law, one has

$$\dot{\boldsymbol{\sigma}} = \mathbf{C}:\mathbf{L} \quad (2.170)$$

where \mathbf{C} is the constitutive tangent tensor. For an elastoplastic law, this equation becomes

$$\dot{\boldsymbol{\sigma}} = \mathbf{C}^{ep}:\frac{1}{2}(\mathbf{L} + \mathbf{L}^T) + \boldsymbol{\sigma} \frac{1}{2}(\mathbf{L} - \mathbf{L}^T)^T + \frac{1}{2}(\mathbf{L} - \mathbf{L}^T)\boldsymbol{\sigma} \quad (2.171)$$

Introducing (2.171) into (2.168) and (2.169) gives a third order equation system which unknowns are the components of the \mathbf{g} vector.

$$\mathbf{n} \cdot (\mathbf{C}^1:(\mathbf{L}^0 + \mathbf{g} \otimes \mathbf{n}) - \mathbf{C}^0:\mathbf{L}^0) = 0 \quad (2.172)$$

The trivial solution $\mathbf{g}=0$ is always possible but means that not shear band can appear. The condition $\mathbf{g} \neq 0$ can be transformed in a fourth order equation in $\tan(\theta)=t$, with θ being the angle between \mathbf{n} and the x -axis

$$at^4 + bt^3 + ct^2 + dt + e = 0 \quad (2.173)$$

At the beginning of loading, this equation does not have any real solution. After some load steps, the first real solution is a double one [WANG, 1993], which then gives two bifurcation directions. The vector \mathbf{g} which describes the additional strain gradient normal to the band can be obtained for each solution. [WANG, 1993] introduced the parameter S

$$S = \frac{\mathbf{g}}{\|\mathbf{g}\|} \cdot \mathbf{n} \quad (2.174)$$

which can be used to distinguish between the nature or mode of the shear band (see table 2.1).

It is important to recall that the Rice bifurcation criterion indicates the possibility of a shear band appearance from a continuum mechanics point of view, but it does not imply their existence. On a practical point of view, this criterion is computed at every step for all integration points.

Table 2.1 Significance of the S parameter of Rice bifurcation criterion, from [WANG, 1993].

S	-1]-1;0[0]0;1[1
Band type	pure closing mode	Intermediate mode	Pure Shear mode	Intermediate mode	Pure opening mode
Mode	-I	-I \leftrightarrow II	II	II \leftrightarrow I	I

2.6.4 Wallace-Bott shape ratio of the stress tensor

For geological applications, it is useful to characterise the stress tensor by defining a scalar which indicates the type of stress tensor [GUIRAUD et al., 1989; RITZ and TABOADA, 1993; SASSI and FAURE, 1997]. The proposition of [SASSI and FAURE, 1997] has been retained

$$R^* = \frac{\sigma_2 - \sigma_1}{\sigma_3 - \sigma_1}, \text{ with } R^* \in [0;1] \quad (2.175)$$

This ratio then describes, for non-isotropic stress tensors, the relative value of the intermediate stress with respect the major and minor stress components (see figure 2.27).

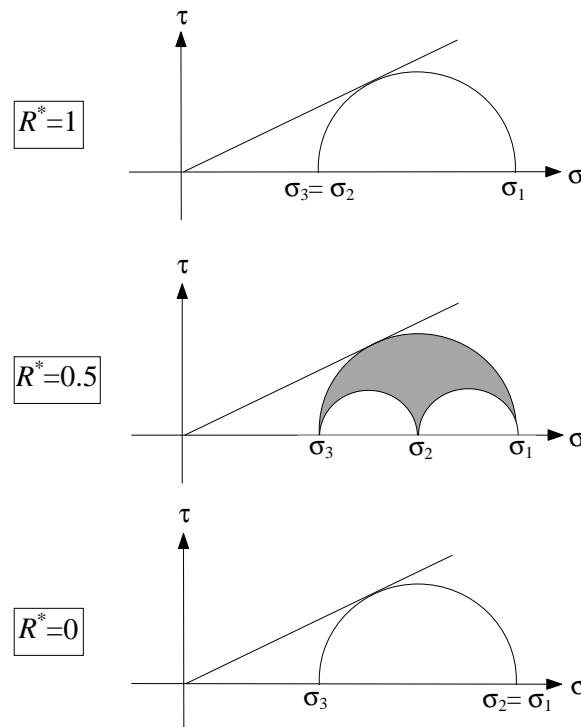


Figure 2.27 Interpretation of the stress shape ratio R^* in the Mohr plane.

Taking advantage that, in geological models, the vertical stress is close to one of the principal stress component, [WALLACE, 1951] and [BOTT, 1959] generalised the classification of tectonic faulting. Then a modified parameter R (referred as Wallace-Bott stress shape ratio in the application chapters) can be defined

$$R = 1 - R^*, \text{ with } R \in [0;1] \quad (2.176)$$

and by adding an information about the tectonic regime (based on which principal stress is closer to the vertical) :- if $\sigma_v = \sigma_1 \rightarrow$ extension tectonic regime, $R \in [0;1]$

- if $\sigma_v = \sigma_2 \rightarrow$ strike-slip tectonic regime, $R \in [1;0]$

- if $\sigma_v = \sigma_3 \rightarrow$ compression tectonic regime, $R \in [0;1]$

As a consequence, R varies continuously from 0 to 1 in the extension tectonic regime, from 1 to 0 in the strike slip tectonic regime and from 0 to 1 in the compression tectonic one. As mentioned by [SASSI and FAURE, 1997], the transition of tectonic regime is accompanied by a rotation of tectonic direction : for instance there is a continuous transition between east-west oriented extension to north-south oriented compression. It is possible to correlate the value of parameter R with the different types of faulting figure 2.28. It must be pointed out that such an interpretation of a stress state in term of *potential* faulting for geological models is not based on a continuum mechanics description, but on the comparison with field observations.

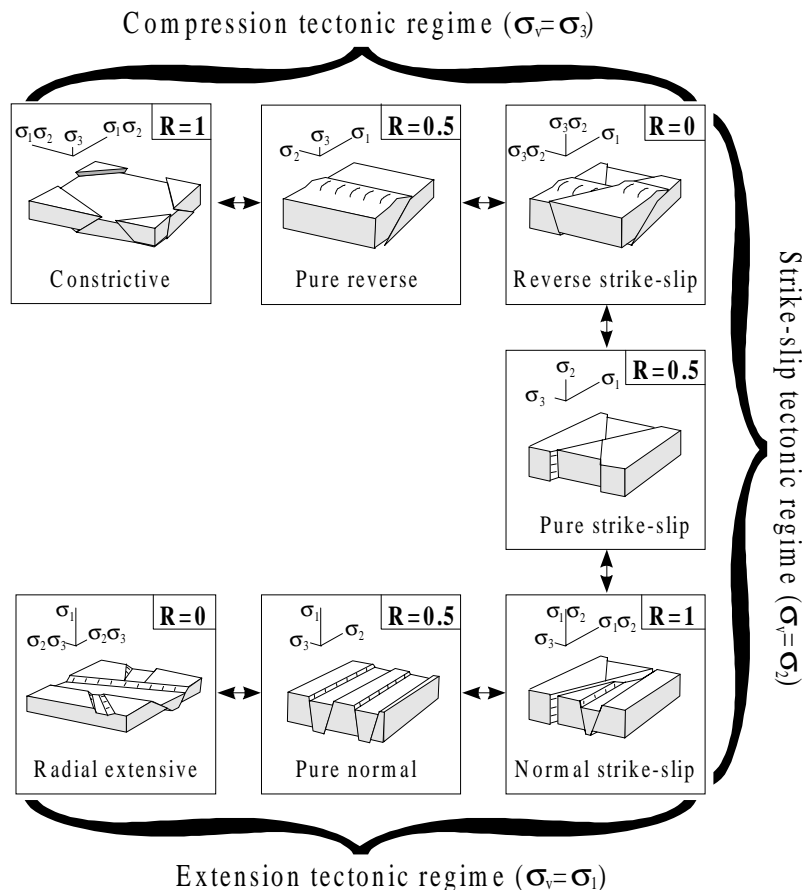


Figure 2.28 Geometry of faulted block diagrams characterising the different theoretical types of deformation as a function of stress ratio R and stress orientation, adapted from [GUIRAUD et al., 1989] : there is a continuous variation of stress ratio R between the compression and the extension tectonic regime.

2.7 Conclusion

After the presentation of some basics about the finite element method used throughout this work, special attention has been paid to the elastoplastic formulation of the constitutive relation which links the stress tensor to the strain tensor. It has led to the full definition of the general elastoplasticity relations including hardening/softening of state variables.

The Drucker Prager and the Van Eekelen yield surfaces have been presented in details including the particular plastic regime encountered in the apex zone. Extension of these two yield surfaces to the simple Von Mises surface has also been given. The implicit algorithm used to integrate the constitutive relation has been detailed, its convergence efficiency and reliability have been verified. Implementation has been achieved in the law *PLASOL*, in which the Drucker Prager criterion represents a limit case of the more general Van Eekelen one.

Similarities between the Drucker Prager and the Van Eekelen formulation have been outlined as well as differences, with their respective advantages and drawbacks. The major disadvantage of the Drucker Prager criterion comes from the dependence of the friction angle for extensive triaxial paths ϕ_E on the friction angle ϕ_C for compressive triaxial paths (see figure 2.11) : the use of this criterion instead of a Mohr Coulomb type can lead to a subsequent stress overestimation as the friction angle gets closer to 36.87° . At this limit value $\phi_C=36.87^\circ$, the associated friction angle ϕ_E for extension paths becomes equal to 90° . This main disadvantage is also verified from experimental results where it is clear that the DP criterion is only a poor representation of the frictional material behaviour in the deviatoric plane.

This main disadvantage of the Drucker Prager criterion results in a unbounded admissible stress space for friction angles higher than 36.87° whereas the stress space remains bounded for Mohr Coulomb and Van Eekelen criteria. Thus an overestimated stress field can be obtained when using the Drucker Prager criterion. Therefore, it can be concluded that in order to obtain reliable stress magnitude when average to high friction angles are used (i.e. greater than 20°), a criterion which includes the third stress invariant must necessarily be used (e.g. Mohr Coulomb, Van Eekelen or any similar criterion). This is especially true for geomechanical simulations in which σ_v is the minor principal stress. This will be illustrated in two application cases presented in chapter 5.

Additional laws used further on have also been presented briefly : the elastoviscoplastic law *IRSID* and some contact laws.

A simple method to avoid or reduce the numerical subsidence resulting from gravity loading has been presented.

Eventually, several criteria (not based on enhanced continua) which will be used to analyse rock failure and strain localisation (directions, mode) in application chapters have been detailed.

CHAPTER 3

Coupled hydromechanical behaviour of porous geomaterials : finite elements and constitutive laws

3.1 Introduction

In the previous chapter, the formulation of the mechanical behaviour of a solid medium has been presented, based on an up-dated Lagrangian description of kinematics and considering finite strains. In this chapter, this formulation is extended to saturated porous media.

In this first part of this chapter, a review of poromechanics developments is presented, based on recent works by [DETOURNAY and CHENG, 1991; COUSSY, 1995; BOURGEOIS and DORMIEUX, 1996]. The basic concepts are recalled : kinematical description of the porous medium, variation in fluid mass content, flow behaviour of the fluid phase, fluid mass conservation, relationships between the poroelastic parameters. Eventually, the coupled behaviour of the porous medium is given considering an isotropic linear elastic for the solid phase, which corresponds to the so-called poroelastic behaviour. The concepts of elastic and plastic effective stress tensors are also recalled with their underlying assumptions.

In the second part of this chapter, the coupled hydromechanical behaviour as formulated in the *LAGAMINE* code is presented. It is based on the solid phase (grains) incompressibility assumption, which ensures the validity of the effective stress (both regarding elastic and plastic behaviour) concept. Extension of the formulation to finite strains is made through the up-date of porosity, apparent specific mass and permeability.

Eventually, a validation of the hydromechanical formulation implemented in the code is carried out by comparing analytical and FE results on the well-known consolidation problem (in infinitesimal transformation).

3.2 Classical poromechanics

Most of the concepts presented hereafter have been compiled and summarised from general textbooks on mechanics of porous media, see e.g. [DETOURNAY and CHENG, 1991; COUSSY, 1995].

3.2.1 Definition of the granular porous medium, hypotheses

At the microscopic scale, an elementary volume $d\Omega$ of a granular porous medium can be defined as the juxtaposition of two constituents (see figure 3.1) :

- the granular solid constituent, which is an arrangement of grains and which is continuous. The volume $d\Omega_s$ of this medium is equal to the volume of the grains. The specific mass of the grains is noted ρ_s . It must be pointed out that the mechanical behaviour of the grains is rather different from the mechanical behaviour of the grain arrangement (skeleton) for which strains are based on slip between grains.
- the void medium of volume $d\Omega_v$, which is filled by some fluid phase of specific mass ρ_f . On the one hand, the porous medium can be fully saturated by one fluid, i.e. all the void medium is filled by this fluid (e.g. water). On the other hand, the void medium may be filled by a fluid and a gas, in this case the porous medium is referred as a partially saturated one.

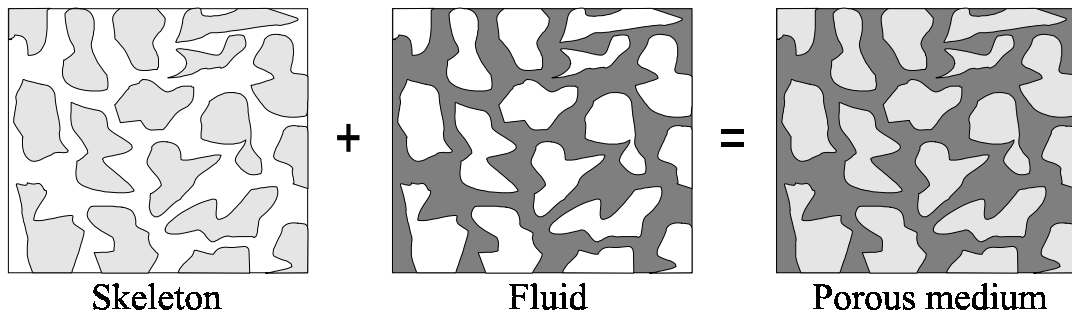


Figure 3.1 Microscopic description of a saturated porous medium.

Homogenisation at the macroscopic scale of the porous medium allows to define the continuous porous medium as the superposition of the fluid phase and the skeleton, considering that at any geometrical point a skeleton and fluid particle coincide. For the sake of simplicity, non-connective pores are not considered. The porosity n is defined by

$$n = \frac{\Omega_v}{\Omega} = \frac{\Omega_v}{\Omega_s + \Omega_v} \quad \text{with } n \in [0;1] \quad (3.1)$$

The void ratio e can also be defined by

$$e = \frac{\Omega_v}{\Omega_s} \quad (3.2)$$

In the following, the subscript $_v$ refers to the void medium, $_f$ to the fluid phase (which may be different from water) and $_s$ to the solid grains.

3.2.2 Problem formulation

3.2.2.1 Kinematics of the porous medium

As mentioned previously, the porous medium can be separated in a solid phase and a fluid phase.

Kinematics of the skeleton (solid phase) can be described in a similar fashion than for classical continua. Therefore, the up-dated Lagrangian formulation described in chapter 2 is suited to describe the skeleton kinematics (see equations (2.1) to (2.9)), in which the referential is attached to the skeleton materials and up-dated at each step. Also, the static equilibrium condition given in equation (2.11) can be applied to express the skeleton equilibrium.

Regarding the fluid phase, there is obviously no equivalent in classical mechanics, thus the kinematics of the fluid phase must now be considered. There is a very important difference between classical continua and porous continua. Classical continua are closed, i.e. any elementary volume $d\Omega$ does not exchange any material with the outer world. On the opposite, porous continua are open ones as any elementary volume $d\Omega$ may exchange some fluid with the outer world. They are therefore referred as thermodynamically open continua [COUSSY, 1995].

3.2.2.1.1 Eulerian description of the fluid kinematics

Following [COUSSY, 1995; BOURGEOIS and DORMIEUX, 1996], the transformation of the fluid can be described by the Eulerian relative flow of fluid mass vector \mathbf{w} . Let us consider an infinitesimal surface da with normal \mathbf{n} . At time t and per unit of time, a fluid mass J_f^m flows through this surface da defined by

$$J_f^m = \mathbf{w} \cdot \mathbf{n} da \quad (3.3)$$

in which the vector \mathbf{w} is defined by

$$\mathbf{w} = \rho_f n \mathbf{v}^r = \rho_f \mathbf{v}^d \quad (3.4)$$

In the later relation, the vector \mathbf{v}^r represents the effective relative velocity between the fluid particle and the skeleton at the same geometrical point, which is linked to Darcy velocity (\mathbf{v}^d) following $\mathbf{v}^r = \mathbf{v}^d / n$ (BURGER et al., 1985).

3.2.2.1.2 Lagrangian description of the fluid kinematics

The equivalent of \mathbf{w} expressed in Lagrangian variables is the fluid mass vector \mathbf{M} defined by

$$J_f^m = \mathbf{M} \cdot \mathbf{N} dA \quad (3.5)$$

where the surface dA with normal \mathbf{N} in the reference configuration corresponds to the surface da in the deformed configuration.

3.2.2.2 Variation in fluid mass content, fluid mass conservation

Let us consider the elementary volume in its initial (or reference) configuration A at t^A where it occupies a volume $d\Omega^A$. The porous space with porosity n^A is filled by a fluid of specific mass ρ_f^A . The fluid mass at t^A in the elementary volume is equal to $\rho_f^A n^A d\Omega^A$. Let us assume that at time t^B , the elementary volume is in a deformed configuration B where it occupies a volume

$d\Omega^B$, with a porosity n^B and a fluid specific mass ρ_f^B . The fluid mass at t^B is then equal to $\rho_f^B n^B d\Omega^B$, but it can also be expressed as $\rho_f^A n^A d\Omega^A + md\Omega^A$ where $md\Omega^A$ represents the fluid mass exchanged between t^A and t^B by the elementary volume $d\Omega^A$. Then the change in fluid mass content m with respect to configuration A is defined by [BIOT, 1977]

$$m = J \rho_f^B n^B - \rho_f^A n^A \quad (3.6)$$

where J is defined as the determinant of the Jacobian transformation \mathbf{F} given in equation (2.1), i.e. J corresponds to the volume ratio between the deformed and the initial configuration

$$J = \det(\mathbf{F}) = \det\left(\frac{\partial \mathbf{x}}{\partial \mathbf{x}_0}\right) = \frac{d\Omega^B}{d\Omega^A} \quad (3.7)$$

Equation (3.6) includes two contributions on the change in fluid mass : the effect of the variation of fluid specific mass ρ_f (if compressible) and the effect of volume change of the grains and pores.

The overall fluid mass conservation reads [BOURGEOIS and DORMIEUX, 1996]

$$\dot{m} d\Omega^A + d\Omega^B \operatorname{div} \mathbf{w} = 0 \quad (3.8)$$

where the divergence operator is relative to Eulerian co-ordinates, i.e. to the deformed configuration γ . Using (3.7), the latter equation can be written

$$\dot{m} + J \operatorname{div} \mathbf{w} = 0 \quad (3.9)$$

It is also useful to express the fluid mass conservation using only Lagrangian variables which then writes [COUSSY, 1995]

$$\dot{m} + \operatorname{div} \mathbf{M} = 0 \quad (3.10)$$

If the assumption of small skeleton displacement is made (i.e. displacements which are much smaller than the fluid velocity), vectors \mathbf{M} and \mathbf{w} become equivalent, i.e. the following particular form of the fluid mass conservation is obtained

$$\dot{m} + \operatorname{div} \mathbf{w} = 0 \quad (3.11)$$

and J can be identified to

$$J = 1 + \varepsilon_v \quad (3.12)$$

where $\varepsilon_v = \operatorname{tr} \boldsymbol{\varepsilon} = \varepsilon_{ii}$ represents the volumetric strain.

3.2.3 Constitutive laws

3.2.3.1 Linearised fluid state equation

Considering an isotherm evolution, the fluid state equation relates its specific mass ρ_f to its pressure p_f . Considering a linear elastic behaviour for the fluid yields the following relation between the volume V_f and the pressure variation of the fluid

$$\frac{\Delta V_f}{V_f} = \frac{-\Delta p_f}{K_f} \quad (3.13)$$

where K_f represents the fluid bulk modulus. Using the mass conservation law $\rho_f^A V_f^A = \rho_f^B V_f^B$, the following linearised fluid state equation is obtained [BURGER et al., 1985]

$$\rho_f^B = \rho_f^A \left(1 + \frac{p_f^B - p_f^A}{K_f} \right) \quad (3.14)$$

3.2.3.2 Flow behaviour

The general Darcy flow law, which is valid for low Reynolds numbers, defines the Darcy fluid velocity \mathbf{v}^d as a linear function of permeability, the gradient of fluid pressure p_f ,

$$\mathbf{v}^d = -\frac{\mathbf{K}}{\rho_f g} \cdot (\nabla p_f + \rho_f g \nabla z) \quad (3.15)$$

where $\nabla z = [0 \ 0 \ -1]^T$ and where the permeability tensor \mathbf{K} (unit $[LT^{-1}]$) is defined

$$\mathbf{K} = \begin{bmatrix} K_{11} & K_{12} & K_{13} \\ K_{21} & K_{22} & K_{23} \\ K_{31} & K_{32} & K_{33} \end{bmatrix} \quad (3.16)$$

If isotropic permeability is considered, relation (3.15) reduces to

$$\mathbf{v}^d = -\frac{K}{\rho_f g} (\nabla p_f + \rho_f g \nabla z) \quad (3.17)$$

where K is the isotropic permeability coefficient (unit $[LT^{-1}]$).

The relation between the intrinsic permeability k (unit $[L^2]$) and the permeability coefficient K is given by

$$k = K \frac{\mu_f}{\rho_f g} \quad (3.18)$$

where μ_f (unit $[ML^{-1}T^{-1}]$) is the fluid dynamic viscosity (equal to 10^{-3} Pa.s for water at 20°C).

3.2.3.3 Linear poroelastic behaviour in infinitesimal transformation

Although theoretical developments have been made for thermoporoelasticity [COUSSY, 1995], only the specific case of linear poroelasticity in infinitesimal transformation is recalled here. The linear poroelastic behaviour is characterised by a zero intrinsic dissipation. This behaviour is described by the relations

$$\boldsymbol{\sigma}^B - \boldsymbol{\sigma}^A = \mathbf{C} : \boldsymbol{\varepsilon} - M \mathbf{B} \frac{m}{\rho_f^A} \quad (3.19)$$

$$p_f^B - p_f^A = M \left(-\mathbf{B} : \boldsymbol{\varepsilon} + \frac{m}{\rho_f^A} \right) \quad (3.20)$$

The first equation relates to the skeleton and the second relates to the fluid behaviour (storage law). Equation (3.20) can be rewritten

$$M\mathbf{B} \frac{m}{\rho_f^A} = \mathbf{B}(p_f^B - p_f^A) + M\mathbf{B} \otimes \mathbf{B} : \boldsymbol{\varepsilon} \quad (3.21)$$

Then the poroelastic constitutive relation can be obtained from (3.19) which gives

$$\boldsymbol{\sigma}^B - \boldsymbol{\sigma}^A = \mathbf{C}' : \boldsymbol{\varepsilon} - \mathbf{B}(p_f^B - p_f^A) \quad (3.22)$$

where the effective tangent operator \mathbf{C}' is defined by

$$\mathbf{C}' = \mathbf{C} - M\mathbf{B} \otimes \mathbf{B} \quad (3.23)$$

Using Biot's effective stress definition, the elastic effective stress tensor writes

$$\boldsymbol{\sigma}' = \boldsymbol{\sigma} + \mathbf{B}p_f \quad (3.24)$$

Then relation (3.21) can be re-written in an identical form than for classical elasticity but where the effective stress tensor is linked to the strain tensor by the effective tangent operator \mathbf{C}'

$$\boldsymbol{\sigma}'^B - \boldsymbol{\sigma}'^A = \mathbf{C}' : \boldsymbol{\varepsilon} \quad (3.25)$$

The previous relation is the linear elastic relation expressed in effective stresses.

If isotropic linear elastic behaviour is considered, equations (3.19), (3.22) and (3.20) simplify to

$$\boldsymbol{\sigma}^B - \boldsymbol{\sigma}^A = \left(K - \frac{2G}{3} \right) \boldsymbol{\varepsilon}_v \mathbf{I} + 2G\boldsymbol{\varepsilon} - bM \frac{m}{\rho_f^A} \mathbf{I} \quad (3.26)$$

$$\boldsymbol{\sigma}^B - \boldsymbol{\sigma}^A = \left(K' - \frac{2G}{3} \right) \boldsymbol{\varepsilon}_v \mathbf{I} + 2G\boldsymbol{\varepsilon} - b(p_f^B - p_f^A) \mathbf{I} \quad (3.27)$$

$$p_f^B - p_f^A = M \left(-b \boldsymbol{\varepsilon}_v + \frac{m}{\rho_f^A} \right) \quad (3.28)$$

where \mathbf{I} is the unit tensor. In the latter relations, K' and K represent the drained and undrained bulk modulus, G is the classical elastic shear modulus and b is the Biot coefficient. Let us point out that equation (3.28) can be written

$$m = \rho_f^A \left(\frac{p_f^B - p_f^A}{M} + b \boldsymbol{\varepsilon}_v \right) \quad (3.29)$$

which then represents the storage law of the porous medium. Similarly to equation (3.24), the elastic effective stress tensor then reads

$$\boldsymbol{\sigma}' = \boldsymbol{\sigma} + bp_f \mathbf{I} \quad (3.30)$$

Several parameters can be used to define the poroelastic behaviour, and the different relations between them can be summarised [BOUTECA and SARDA, 1994] :

- the elastic drained coefficients (noted with prime)

$$\begin{aligned} E' &= G \frac{3\lambda' + 2G}{\lambda' + G}, & \nu' &= \frac{\lambda'}{2(\lambda' + G)}, & 3K' &= 3\lambda' + 2G \\ \lambda' &= \frac{E'\nu'}{(1+\nu')(1-2\nu')}, & G &= \frac{E'}{2(1+\nu')}, & 3K' &= \frac{E'}{1-2\nu'} \end{aligned} \quad (3.31)$$

- the elastic undrained coefficients

$$\begin{aligned} E &= G \frac{3\lambda + 2G}{\lambda + G}, & \nu &= \frac{\lambda}{2(\lambda + G)}, & 3K &= 3\lambda + 2G \\ \lambda &= \frac{E\nu}{(1+\nu)(1-2\nu)}, & G &= \frac{E}{2(1+\nu)}, & 3K &= \frac{E}{1-2\nu} \end{aligned} \quad (3.32)$$

- the coefficients linking the drained and undrained elastic coefficients

$$\begin{aligned} \text{a) } K' &= K - b^2 M, & \text{b) } B_s &= \frac{Mb}{K} \\ \text{c) } b &= \frac{1}{B_s} \left(1 - \frac{K'}{K} \right), & \text{d) } M &= B_s^2 \frac{K^2}{K - K'} \end{aligned} \quad (3.33)$$

where the Skempton coefficient B_s represents the ratio between the pore pressure and the mean stress in an undrained experiment (i.e. $B_s = -\Delta p_f / \Delta \sigma_m$). Between all these parameters, only four of them are independent, and thus required to define the poroelastic behaviour.

- the relationship between the characteristics of the poroelastic medium and its constituents [BOUTECA and SARDA, 1994]

$$\text{a) } b = 1 - \frac{K'}{K_s}, \quad \text{b) } \frac{1}{M} = \frac{b - n_0}{K_s} + \frac{n_0}{K_f} \quad (3.34)$$

where it is recalled that the subscripts $_s$ and $_f$ refer to the grains and the fluid, respectively, and n_0 represents the reference porosity in the initial state at $t=0$.

There may be a relation which links the Biot coefficient b with some state variables. Based on experimental data, [BOUTECA et al., 1991; SCHNEIDER et al., 1993] proposed a relationship between the porosity and Biot's coefficient for carbonates

$$b = \frac{n}{n + a[n_0 - n]} \quad (3.35)$$

where the parameter a must be identified from experiments. From a theoretical point of view, it can be seen from equation (3.34a) that the Biot coefficient b becomes equal to 1 when the grains are incompressible ($K_s \rightarrow \infty$). Then from (3.34b) the Biot modulus M becomes equal to K_f/n_0 . Reporting this value into equation (3.33a) gives the undrained bulk modulus of the porous medium

$$K = K' + \frac{K_f}{n_0} \quad (3.36)$$

In this case, it must be pointed out that the elastic effective stress tensor corresponds to Terzaghi definition of effective stresses

$$\boldsymbol{\sigma}' = \boldsymbol{\sigma} + p_f \mathbf{I} \quad (3.37)$$

and that the storage law (3.29) reduces to

$$m = \rho_f^A \left(\frac{p_f^B - p_f^A}{K_f / n_0} + \varepsilon_v \right) \quad (3.38)$$

A general poroelastic problem can be separated in three distinct phases, namely the short term state, the transient phase and the long term state.

During the short term (or instantaneous) phase, there is no fluid movement, i.e. the change in fluid mass content m is nil [COUSSY, 1995]

$$\dot{m} = 0 \quad (3.39)$$

The short term solution of a poroelastic evolution problem is identical to the solution the elastic problem in which the undrained elastic parameters have been considered.

The transient phase cannot generally be solved analytically, although it is sometimes possible in simple cases. In this phase, there is usually in the same time an evolution of the pore pressure (following the diffusion equation) and the displacement fields.

When the long term (or asymptotic) phase is reached, the pore pressure generated at short term has dissipated. A balanced state is reached in which the pore pressure remains constant, i.e.

$$\dot{p}_f = 0 \quad (3.40)$$

The long term solution of a poroelastic evolution problem is identical to the solution the elastic problem in which the drained elastic parameters have been considered.

3.2.3.4 Poroplastic behaviour in infinitesimal transformation

In poroelasticity, the skeleton deformation is reversible. As soon as it is no longer the case, the behaviour of the porous solid becomes poroplastic. As in classical plasticity, the strain of the skeleton is then partitioned in an elastic (reversible) component and an irreversible (plastic) one

$$\boldsymbol{\varepsilon} = \boldsymbol{\varepsilon}^e + \boldsymbol{\varepsilon}^p \quad (3.41)$$

The skeleton plastic volumetric strain ε_v^p is linked to the plastic porosity n^p through [COUSSY, 1995]

$$\varepsilon_v^p = n^p + (1 - n_0) \varepsilon_s^p \quad (3.42)$$

where n_0 is the initial porosity and ε_s^p is the plastic volumetric strain of the grains referred to the initial configuration at $t=0$. This relation highlights the two origins of the irreversible changes in volume of the skeleton : a first part comes from the plastic porosity variation (mainly slips between grains) and a second one from the grain volume changes.

Similarly, the change in fluid mass content m is partitioned in an elastic and a plastic part

$$m = m^e + m^p \quad (3.43)$$

The general yield criterion for a poroplastic material reads

$$f(\boldsymbol{\sigma}, p_f, \kappa) = 0 \quad (3.44)$$

It can be shown that, similarly to the elastic effective stress tensor defined in equation (3.23), a plastic effective stress tensor $\boldsymbol{\sigma}^p$ is defined by [COUSSY, 1995]

$$\boldsymbol{\sigma}^p = \boldsymbol{\sigma} + \mathbf{B}^p p_f \quad (3.45)$$

in which the tensor \mathbf{B}^p verifies the relation

$$dn^p = \mathbf{B}^p : d\boldsymbol{\varepsilon}^p \quad (3.46)$$

In the general case, there is no reason for \mathbf{B} to coincide with \mathbf{B}^p , thus there is no reason for the elastic effective stress $\boldsymbol{\sigma}^{\text{el}}$ to be equivalent to the plastic one $\boldsymbol{\sigma}^p$. It results in an effective stress discontinuity at the elastic-plastic transition, which is not admissible. However, in some cases it is possible to have equality between \mathbf{B} and \mathbf{B}^p .

Secondly, in the particular case where the grains are incompressible, i.e. $\varepsilon_s^p = 0$, equation (3.42) simplifies to

$$\varepsilon_v^p = n^p \quad (3.47)$$

i.e. the irreversible volumetric strain corresponds to the change in plastic porosity. Then equation (3.46) implies

$$\mathbf{B}^p = \mathbf{I} \quad (3.48)$$

Thus, when the grains are elastically and plastically incompressible, the Biot elastic and plastic effective stress tensors coincide and are equal to the Terzaghi effective stress tensor

$$\boldsymbol{\sigma}^{\text{el}} = \boldsymbol{\sigma}^p = \boldsymbol{\sigma} + p_f \mathbf{I} \quad (3.49)$$

This result, which holds both for a plastically incompressible ($\psi=0$) and compressible skeleton ($\psi \neq 0$), has been extended to finite deformation by [BOURGEOIS and DORMIEUX, 1996]. They demonstrated that for standard materials (i.e. materials for which the flow potential corresponds to the yield function), the yield criterion (3.44) can be written equivalently

$$f(\boldsymbol{\sigma}', \kappa) = 0 \quad (3.50)$$

Such an effective stress formulation is very convenient to use in finite element models as any mechanical law can be used to represent the skeleton behaviour (in hydromechanical simulations) almost without modifications.

3.3 Poromechanical formulation in the LAGAMINE code in finite strain

The basic assumption of elastic and plastic incompressibility of the grains is made. It implies the validity of relation (3.48), i.e. the unique existence of the Terzaghi effective stress tensor (both for elasticity and plasticity). This simplification allows to separate the two constituents of the saturated porous medium.

As in the purely mechanical case, an up-dated Lagrangian formulation is used in which the reference configuration A is up-dated at each step, the deformed configuration is noted B. The additional effects of finite strains (specific mass changes, porosity (i.e. volume) changes, permeability changes) must be taken into account.

Such poromechanical behaviour has been implemented in the LAGAMINE code in the CSOL2B and CSOL3B finite elements for two and three dimensional analyses, respectively.

3.3.1 Formulation for the solid phase

3.3.1.1 Mechanical law

The skeleton, for which the incremental stress-strain relation (see chapter 2) relates now the Jaumann derivative of the effective stress rate tensor to the strain rate tensor

$$\tilde{\sigma}' = \tilde{\sigma} + \dot{p}_f \mathbf{I} = \mathbf{C} : \dot{\epsilon} \quad (3.51)$$

This relation actually expresses the influence or coupling of flow (p_f) onto mechanics (σ). Any classical mechanical constitutive relation of the LAGAMINE code can be used.

If a linear elastic law is considered, the matrix \mathbf{C} corresponds to the drained elastic matrix \mathbf{C}' obtained from the drained elastic parameters (E', ν'). It then accounts for the long term behaviour of the porous medium.

If an elastoplastic behaviour is considered, the yield criterion is based on this effective stress tensor following equation (3.49), and the volumetric plastic strain corresponds to the change in plastic porosity. Integration of the constitutive relation (see chapter 2) over the time step gives finally the stress tensor σ^B in the deformed configuration.

3.3.1.2 Apparent specific mass up-date

In the weak form of the equilibrium relation (see equation 2.12) which is computed in the deformed configuration B, the specific mass is required to correctly compute body forces. In the framework used, it corresponds to the apparent specific mass ρ_a^B , which refers to the specific mass of the porous medium made up of a mixture between the solid and the fluid phase in the deformed configuration. It is obtained from the relation

$$\rho_a^B = (1 - n^B) \rho_s + n^B \rho_f^B \quad (3.52)$$

where ρ_s refers to the constant specific mass of the grains given in the mechanical law of the skeleton (see LAGAMINE user's manual). In this relation, the porosity n^B in the deformed configuration is required.

3.3.1.3 Porosity up-date

Consider the elementary volume $d\Omega^A$ with porosity n^A in the reference configuration A. In A, the fluid mass in the elementary volume is equal to $\rho_f^A n^A d\Omega^A$. In the deformed configuration B, the elementary volume occupies a volume $d\Omega^B$ with porosity n^B . Taking advantage of the grain incompressibility and using the definition (3.1), porosities in the two configurations can be written

$$n^A = \frac{d\Omega_v^A}{d\Omega_s + d\Omega_v^A} \quad (3.53)$$

$$n^B = \frac{d\Omega_v^B}{d\Omega_s + d\Omega_v^B} \quad (3.54)$$

From definition (3.9) of J, the global volume variation between A and B reads

$$J = \frac{d\Omega^B}{d\Omega^A} = \frac{d\Omega_s + d\Omega_v^B}{d\Omega_s + d\Omega_v^A} \quad (3.55)$$

which gives the following expression for the porous volume in B

$$d\Omega_v^B = J(d\Omega_s + d\Omega_v^A) - d\Omega_s \quad (3.56)$$

The later equation can be re-arranged

$$d\Omega_v^B = d\Omega^A (J - (1 - n^A)) \quad (3.57)$$

Introducing equation (3.57) into (3.54) yields, after simplification, the relation for the up-date of porosity between A and B

$$n^B = 1 - \frac{1 - n^A}{J} \quad (3.58)$$

This relation gives the porosity evolution during one time step taking into account large strain effects. The porosity evolution affects some other properties of the porous medium, such as the apparent specific mass and the permeability.

3.3.1.4 Equilibrium

Global equilibrium of the solid phase is expressed in the deformed configuration B in term of total stresses by the weak form of the local static equilibrium relation, see equation (2.12). The classical stiffness matrix k_{m-m} is computed following

$$k_{m-m} = \frac{\partial \mathbf{F}_m}{\partial \mathbf{x}_m} \quad (3.59)$$

where \mathbf{F}_m represents the nodal mechanical forces and \mathbf{x}_m the nodal displacements.

3.3.2 Formulation for the fluid phase

This constitutive relation for fluid flow is implemented in the flow law *ECO* (see *LAGAMINE* user manual for details).

3.3.2.1 Flow law

The fluid mass flow is described by the Darcy flow law. Considering the intrinsic isotropic permeability k , Darcy velocity vector for the fluid reads

$$\mathbf{v}^d = -\frac{k}{\mu_f} (\nabla p_f + \rho_f g \nabla z) \quad (3.60)$$

It must be recalled that the Darcy velocity represents the relative velocity of the fluid particle with respect the skeleton, i.e. it does not depend on rigid body displacement.

3.3.2.2 Storage law

The evolution of the fluid phase specific mass is considered to follow the linearised state equation given in equation (3.7) according to its bulk modulus K_f . The variation of fluid mass content m during one time step can be evaluated from equation (3.6). After manipulations (see appendix 1 for exact derivation), the following storage law is obtained

$$m = \rho_f^A ((J-1) + n^A) \frac{p_f^B - p_f^A}{K_f} + \rho_f^A (J-1) \quad (3.61)$$

Note that compared to the infinitesimal storage law given in equation (3.38), a large strain effect is introduced in the porosity term : n_0 is replaced here by $(J-1)+n^A$. The storage rate is then $\dot{m} \approx m/\Delta t$. In this relation, the coupling effect of the mechanics ($\boldsymbol{\sigma}$) onto the flow (p_f) is incorporated through the volumetric strain $(J-1)$.

3.3.2.3 Permeability up-date

The modification of the porous medium porosity affects the apparent specific mass of the medium, but it also affects its permeability. As a limit case, if the actual porosity tends towards zero, the permeability should also tend towards zero. The formulation proposed by Kozeny-Carman has been chosen, which reads

$$k^B = ck_0 \frac{(n^B)^s}{(1-n^B)^r} \quad (3.62)$$

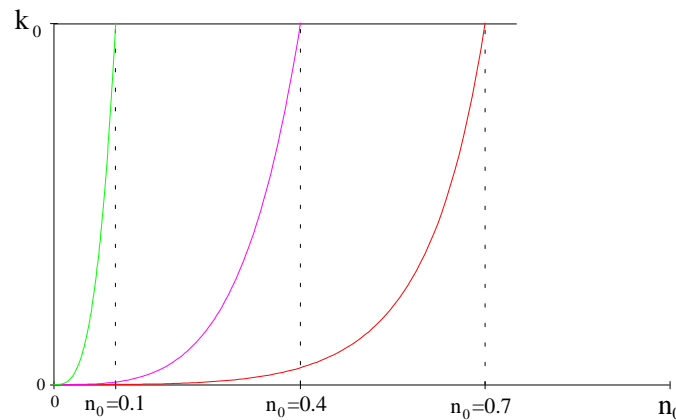


Figure 3.2 Kozeny-Carman relation for permeability-porosity dependence ($r=2$, $s=3$).

where the constant ck_0 is determined from the initial (reference) values of intrinsic permeability k_0 and porosity n_0 , and where exponents r and s are constant parameters.

$$ck_0 = k_0 \frac{(1-n_0)^s}{n_0^s} \quad (3.63)$$

The evolution of k^B with respect to n^B is presented on figure 3.2 for different values of initial porosity.

3.3.2.4 Equilibrium

Equilibrium of the fluid phase is expressed through the weak form of the fluid mass conservation equation (3.9) which reads

$$\int_V Q \delta p_f dV + \int_A q \delta p_f dA = \int_V (\dot{m} \delta p_f - \mathbf{w} \cdot \nabla \delta p_f) dV \quad (3.64)$$

where δp_f is the virtual fluid pressure increment, Q and q are imposed volume and surface fluxes. It is also expressed in the deformed configuration B.

The flow stiffness matrix \mathbf{k}_{f-f} is computed following

$$\mathbf{k}_{f-f} = \frac{\partial \mathbf{F}_f}{\partial \mathbf{x}_f} \quad (3.65)$$

where \mathbf{F}_f represents the nodal fluxes and \mathbf{x}_f the nodal pressures.

3.3.3 Coupling stiffness matrixes

In the global Newton-Raphson iterative resolution, the coupling is taken into account by the computation of the coupling matrixes \mathbf{k}_{m-f} and \mathbf{k}_{f-m} which represent the coupling of mechanics onto flow and flow onto mechanics, respectively

$$\mathbf{k}_{m-f} = \frac{\partial \mathbf{F}_f}{\partial \mathbf{x}_m} \quad \text{and} \quad \mathbf{k}_{f-m} = \frac{\partial \mathbf{F}_m}{\partial \mathbf{x}_f} \quad (3.66)$$

3.3.4 Summary

The parameters required to define entirely the poromechanical model in the *LAGAMINE* code are summarised on figure 3.3. Only the explicit parameters must be specified in the user file.

The drained behaviour relates to the skeleton whereas the undrained behaviour relates to the fluid. The effective stress computation must be specified using the parameter *ISOL* in the mechanical constitutive law (see the *LAGAMINE* reference manual for description).

Let us point out that if stresses are initiated following the procedure detailed in section 2.5, it must be based on the effective stress field. Therefore the vertical stress gradient $dsig$ used in equation (2.161) must be computed from

$$|dsig| = (\rho_a - \rho_f)g \quad (3.67)$$

where ρ_a has been defined in relation (3.52).

If contact elements *CNTCP* are defined in the *LAGAMINE* user file, the Coulomb contact law should be expressed in effective pressure, i.e. $p'-\tau$, with $p'=p-p_f$ (see the parameter *ISOL* in the Coulomb law).

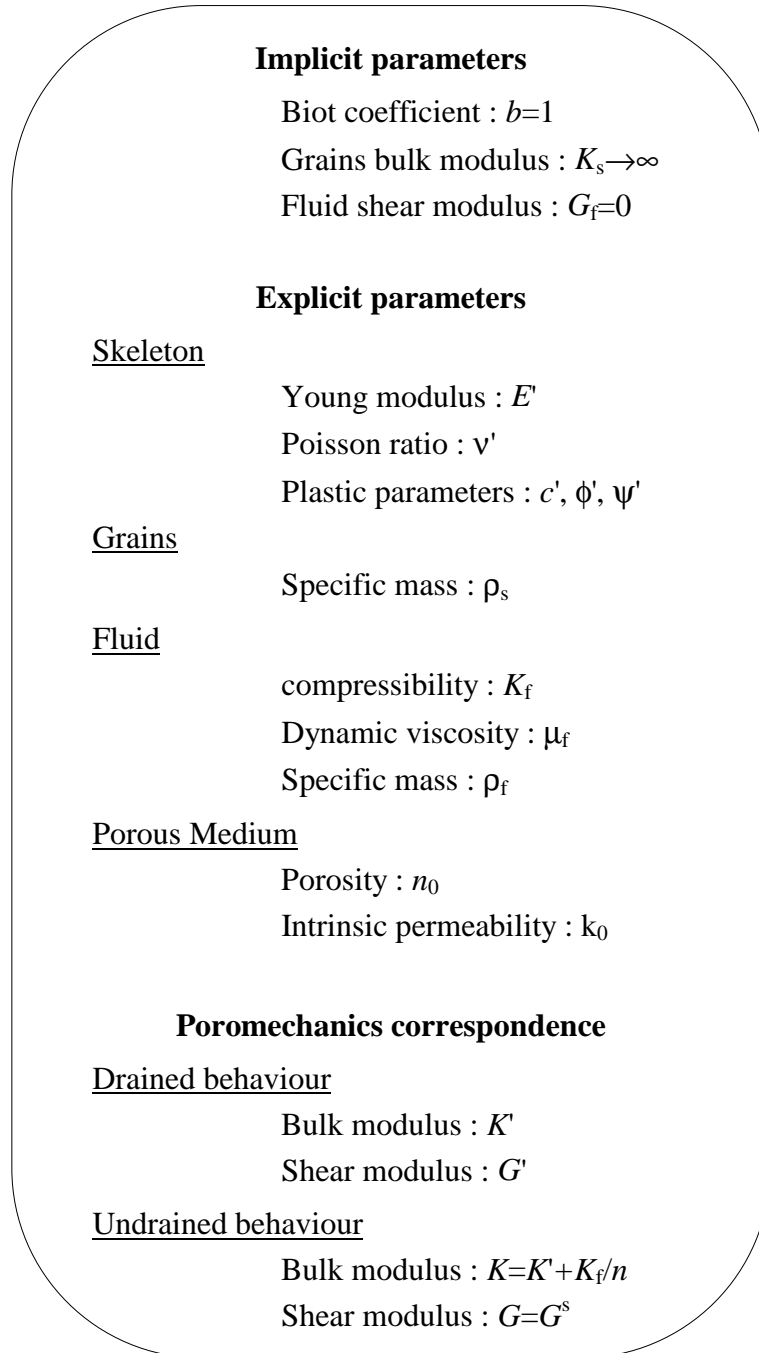


Figure 3.3 Parameters required to define the poromechanical simulation in the *LAGAMINE* FE code.

3.4 Consolidation of a soil layer in infinitesimal transformation

Let us assume an initially horizontal layer of saturated porous soil under gravity forces, which is resting on a horizontally flat impervious substratum (see figure 3.4a). The top surface is drained, i.e. $p_f = p_{atm}$ at $y=h$. The horizontal extent of the medium is infinite.

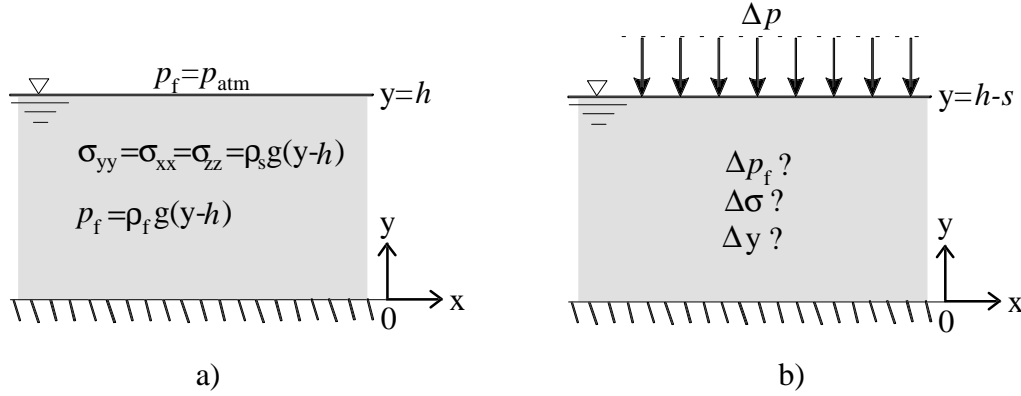


Figure 3.4 The consolidation problem.

At time $t=0$, an overload Δp is applied instantaneously at the top free surface (figure 3.4b). It will then result in a variation of the fluid pressure, of the stress field and of the vertical displacements (settlement). These fields will vary through time until the long term equilibrium is reached.

3.4.1 Analytical solution

Owing to the superposition theorem, only the variations of stresses, displacements and fluid pressure need to be analysed. Since the soil is homogeneous, the displacement field is only function of y . It follows that the total stress and strain increment tensor will have the form

$$\Delta \boldsymbol{\sigma}(t) = \begin{bmatrix} \Delta \sigma_{xx} & 0 & 0 \\ 0 & \Delta \sigma_{yy} & 0 \\ 0 & 0 & \Delta \sigma_{zz} \end{bmatrix}, \quad \Delta \boldsymbol{\varepsilon}(t) = \begin{bmatrix} 0 & 0 & 0 \\ 0 & \Delta \varepsilon_{yy} & 0 \\ 0 & 0 & 0 \end{bmatrix} \quad (3.68)$$

where $\Delta \sigma_{yy} = -\Delta p$ and $\Delta \varepsilon_{yy} = -\Delta y/h$. As mentioned in section 3.2.3.3, the resolution of a poroelastic boundary value problem must distinguish between the undrained solution ($\dot{m} = 0$), the transient phase and the drained solution ($\dot{p}_f = 0$).

The short term (or instantaneous at $t=0^+$) solution for the mechanical part is obtained from the classical elastic relation with undrained coefficients

$$\Delta \varepsilon_{ij} = \frac{1}{E} \left[(1 + \nu) \Delta \sigma_{ij} - \nu \Delta \sigma_{kk} \delta_{ij} \right] \quad (3.69)$$

which gives

$$\Delta y(t = 0^+) = -h \Delta p \frac{1 - \nu - 2\nu^2}{E(1 - \nu)} \quad (3.70)$$

$$\Delta \sigma_{xx}(t = 0^+) = \Delta \sigma_{zz} = -\Delta p \frac{\nu}{1 - \nu}$$

The instantaneous fluid pressure can be obtained from the definition of Skempton coefficient

$$\Delta p_f(t = 0^+) = -B_s \Delta \sigma_m \quad (3.71)$$

Similarly the drained (or long term at $t = \infty$) solution is obtained replacing the undrained coefficients E and ν in (3.69) by the drained ones E' and ν' . The fluid pressure has then dissipated, i.e. $\Delta p_f(t = \infty) = 0$.

In the transient phase, the decrease of fluid pressure and the increase of settlement is function of time (see e.g. [COUSSY, 1995] for the solution).

3.4.2 Finite element representation

As the consolidation problem is a one dimensional problem, a simple finite element discretisation (see figure 3.5) has been used, which is made up of 153 nodes and 30 quadrilaterals (with 8 nodes).

The following set of parameters has been chosen :

$$h = 10\text{m},$$

$$E' = 10^9\text{Pa}, \nu' = 0.35, \rho_s = 2400\text{kg.m}^{-3},$$

$$K_f = 3.10^9\text{Pa}, \rho_f = 1000\text{kg.m}^{-3},$$

$$n = 0.4, k = 10^{-15}\text{m}^2,$$

$$\Delta p = 10^5\text{Pa}.$$

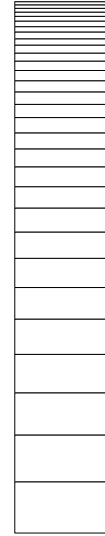


Figure 3.5 FE mesh for the consolidation test.

3.4.3 Comparison between analytical and finite element solution

The comparison between the analytical solution and the *LAGAMINE* solution is presented on figure 3.6. The dissipation of the fluid pressure profile with time is illustrated on figures 3.6a and 3.6b for the analytical and *LAGAMINE* solution respectively. A very good agreement is found between them, which is also the case when comparing the evolution of settlement with time (see figure 3.6c).

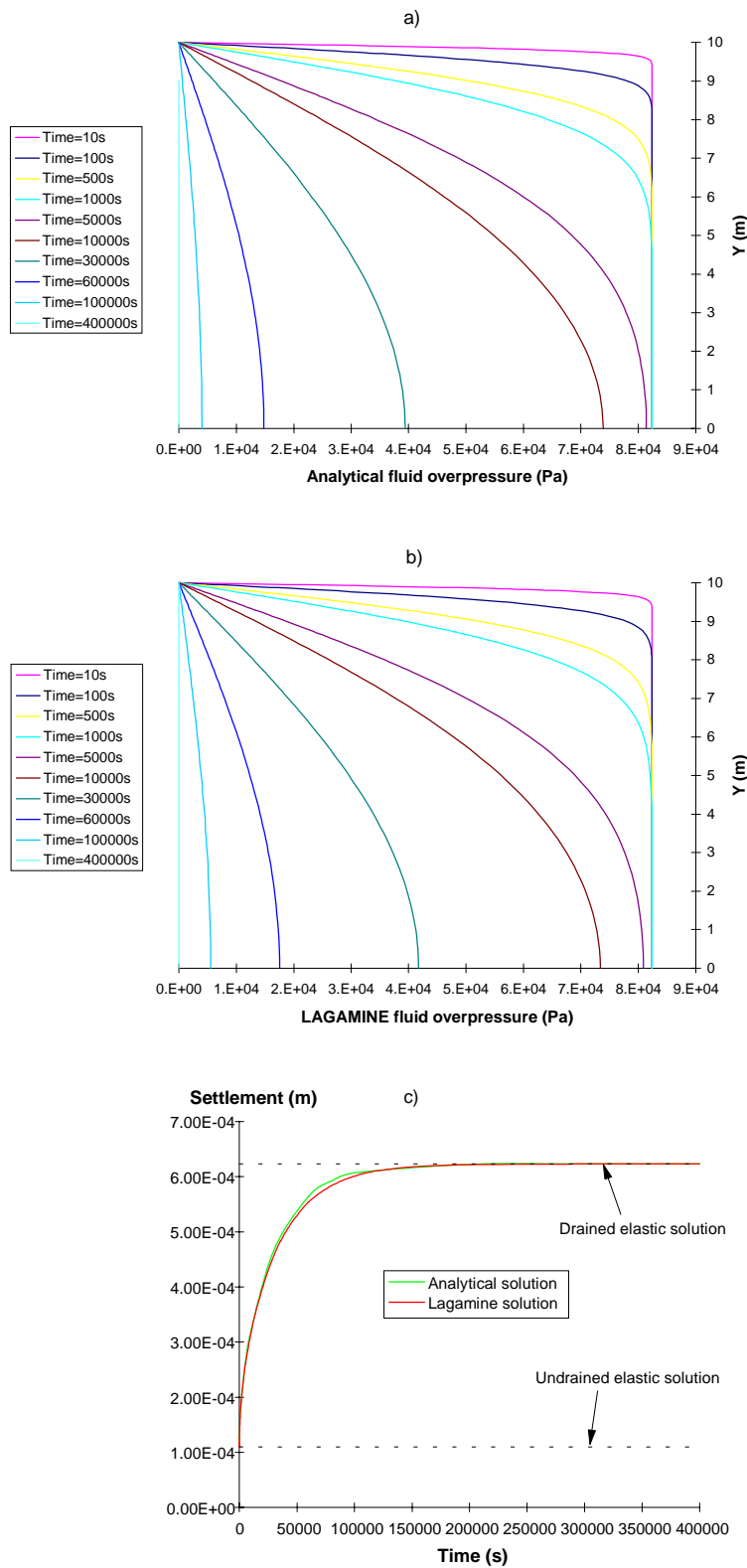


Figure 3.6 Comparison between the analytical and the *LAGAMINE* solution for the consolidation test : a) analytical evolution of the fluid pressure profile with time, b) *LAGAMINE* solution of the evolution of the fluid pressure profile with time, c) evolution of settlement with time.

3.5 Conclusion

In this chapter, the coupled hydromechanical behaviour of porous media has been recalled briefly described.

Following, the formulation used in the *LAGAMINE* finite element code has been presented, based on the restrictive assumption of grain incompressibility. Following, the behaviour of both constituents (skeleton and fluid) is defined separately. The grain incompressibility assumption allows to treat the mechanical problem (i.e. related to skeleton) from the effective stress tensor concept which represents the coupling of flow onto mechanics, and the flow problem (i.e. related to fluid) from the classical Darcy flow law. The coupling of the mechanics onto flow is incorporated through the change of fluid mass content m in the fluid mass conservation law. In the general iterative resolution scheme, it follows that coupling terms appears in the stiffness matrix, which results in the formulation of monolithic finite elements.

The validation of the method has been verified by comparing the analytical and numerical results obtained on the classical consolidation problem.

In finite strains context, the up-date of porosity, permeability and actualised specific mass is consistent. An example of hydromechanical simulation including finite strain effects is presented in chapter 9. Eventually, let us mention some examples of coupled simulations carried out with the *LAGAMINE* code [RADU and CHARLIER, 1994; CHARLIER et al., 1997] in slightly different domains than the one which is presented in chapter 9.

CHAPTER 4

Adaptive re-meshing strategy

4.1 Introduction

When simulating geological like objects, the problems of large displacements and strain localisation (shear strain localisation and/or mode I fracture) arises quite naturally. The difficulty of addressing correctly the localisation phenomenon on a computing numerical point of view is not yet fully solved because its very fundamentals are still matter to discussion. Several methodologies have been developed which all lead to a regularisation of the problem at the onset of bifurcation by introduction of an internal length scale. Several methods have been proposed : the gradient plasticity [e.g. DE BORST, 1992; PAMIN, 1994], the non local plasticity [LI and CESCOTTO, 1996], the Cosserat media [e.g. DE BORST and SLUYS, 1991; DE BORST, 1993], interface band elements [CHARLIER and PIERRY, 1993; CHAMBON and CROCHEPEYRE, 1997].

In this work, the problem is tackle from a more practical point of view. Once strain localisation is detected, the model must allow for such highly non-homogeneous displacement field. Recent work has been made on the development of efficient re-meshing algorithms in order to allow large displacements resulting from localisation phenomenon. Four main types of re-meshing algorithms can be found in the literature :

- the r-version : no new elements are defined, the nodal co-ordinated of already existing elements are redistributed in the domain,
- p-version : no new elements are defined, but the interpolation functions are modified using higher order polynomials,
- h-version : only some elements of the pre-existing mesh are refined,
- independent re-meshing, i.e. a completely new mesh is build without keep any elements of the pre-existing one.

In the present work the choice of an independent re-meshing algorithm has been made as it allows the full control on the new mesh to be created. Originally, a re-meshing algorithm dedicated to *LAGAMINE* FE code had been developed by [HABRAKEN, 1989; HABRAKEN and CESCOTTO, 1990]. However, this algorithm was suffering very important limitations which were limiting drastically its applicability for geomechanical simulations. The model was designed to work extremely well in some specific configurations, e.g. models with only one solid domain. Unfortunately, geomechanical simulations frequently deal with geometries incorporating several domains. Moreover, the regeneration of data and especially boundary conditions was not automated in an optimal manner as the user had to specify them explicitly.

Thus it appeared that, taking advantage of the previous re-meshing algorithm, a new one had to be designed which would be able to deal with much more complex simulations such has multi-domains with complex boundary conditions. Such an algorithm also had to be user friendly and fully automatic in order to spent no engineering time to this task. All this has been made possible by developing an algorithm based on an efficient analysis of the model topology. Additionally, as the Lagrangian mesh changes during re-meshing phases, the possibility to introduce passive markers which are kept through re-meshing phases has been introduced in order to visualise easily finite displacements.

4.2 Re-meshing decision

The re-meshing decision must answer the following two questions : when re-meshing must be performed (i.e. when the global error is too high) and where the mesh size should be modified (i.e. where the local error is concentrated)? Answering these questions is not straightforward, as they can be related to the finite element induced error [ZIENKIEWICZ and HUANG, 1995; DYDUCH, 1996; GALLIMARD et al., 1996], to bifurcation phenomena (e.g. Rice criterion, see [PIERRY, 1997]) or to geometric criteria [HABRAKEN, 1989]. An overview of two methods is presented below.

4.2.1 Error estimation

An amount of error is associated with the finite element discretisation. Generally, it can be estimated from the computed finite element fields which are only kinematically admissible. [DYDUCH, 1996] proposed to compute two types of error :

- a global error ζ_{Ω}^{glo} on each solid domain Ω

$$\zeta_{\Omega}^{glo} = \frac{\int_{\Omega} \|\boldsymbol{\sigma}^* - \boldsymbol{\sigma}\| d\Omega}{\int_{\Omega} \|\boldsymbol{\sigma}\| d\Omega} \quad (4.1)$$

based on the stress field and where $\boldsymbol{\sigma}$ is the stress field obtained by finite element, $\boldsymbol{\sigma}^*$ is the improved stress field which can be estimated by different methods (e.g. finite differences on arbitrary grids, see [DYDUCH, 1996]).

- a local error $\zeta_{\Omega e}^{loc}$ on each element Ωe

$$\zeta_{\Omega e}^{loc} = \frac{\int_{\Omega e} \|\dot{\boldsymbol{\epsilon}}^* - \dot{\boldsymbol{\epsilon}}\| d\Omega e}{\overline{\zeta}^{loc}} \quad (4.2)$$

where $\dot{\boldsymbol{\epsilon}}$ is the computed strain rate, $\dot{\boldsymbol{\epsilon}}^*$ is the improved strain rate and $\overline{\zeta}^{loc}$ is the mean value of the local error for each element i.e.

$$\overline{\zeta}^{loc} = \frac{\sum_{iele=1}^{nele} \zeta_{\Omega e}^{loc}}{nele} \quad (4.3)$$

with $nele$ being the number of solid elements.

Such an error estimation can be used as a basis for re-meshing decision : [DYDUCH, 1996] presented metal forming simulations in which the global error was used to decide when the re-meshing had to be performed, whereas the local error was used to indicate locations where the mesh should be refined/coarsened. Although this criterion has not been used in this work, some remarks will be formulated on its potential use in chapter 6.

4.2.2 Distortion criterion

[AELAAI, 1986] and [HABRAKEN, 1989] have proposed several criteria to evaluate the distortion of finite elements. Most of them are based on the definition of the relative change of

some parameters between the undeformed and the deformed element which cannot exceed a threshold value :

- the criterion for triangles : quadrilateral elements can be divided in four elementary triangles as represented on figure 4.1a; this criterion is defined as the relative change of the surface of each elementary triangles,
- the criterion of angles, defined as the relative variation of the four corner angles (see figure 4.1b) of quadrilaterals,
- the criterion of Jacobian determinant based on the relative change in volume,
- and the criterion of slenderness based on the ratio between the shortest and the longest characteristic distance.

The following one is not based on any threshold value :

- Criterion of the central third which is equivalent to say that middle node of each side must stay in the central third of the side, as figured on figure 4.1c.

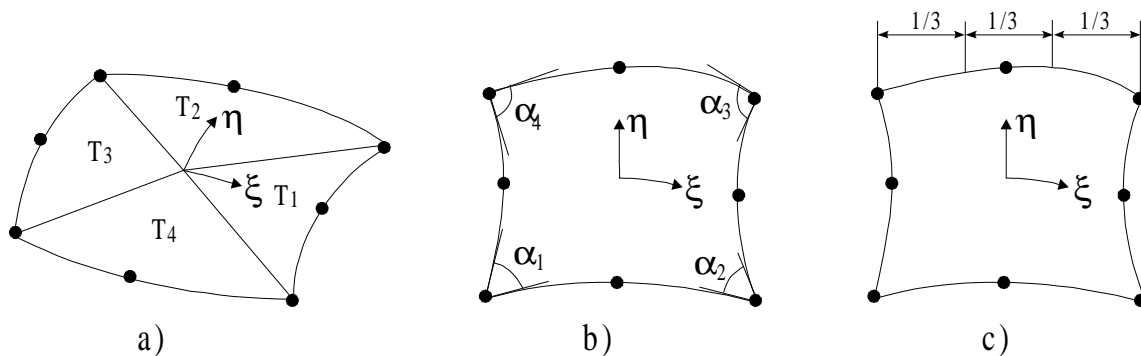


Figure 4.1 Illustration of some geometric criteria : a) triangle criterion, b) angle criterion, c) central third criterion.

As soon as one of these criteria is verified for an element, this element is considered to be an "unaccurate" element. When a relative percentage of "unaccurate" elements is reached, re-meshing must be performed.

These geometric criteria have been used in simulations presented in chapter 7. In chapter 6, the re-meshing decision has been based more heuristically on convergence difficulties or user's choice.

4.3 Re-meshing strategy

4.3.1 Overview

Let us consider the configuration C^F of a system, which is defined by :

- one or several solid domains Ω^F with boundary $\partial\Omega^F$, each domain Ω^F having a unique constitutive relation, i.e. corresponding to a rheological domain,
- a given mesh M^F , i.e. a discrete representation of Ω^F and $\partial\Omega^F$,
- a given set of boundary conditions B^F on boundaries $\partial\Omega^F$,
- and several discrete fields which are the solution of the discrete problem $(\mathbf{v}^F, p_f^F, \boldsymbol{\sigma}^F)$ and its related state variables $(\boldsymbol{\kappa}^F)$, where p_f^F is the fluid pressure in case of coupled hydromechanical simulations.

Let us assume that, from an error criterion or element distortion criterion, it is known that the obtained solution $(\mathbf{v}^F, p_f^F, \boldsymbol{\sigma}^F)$ of the problem becomes less accurate. The main issue of re-meshing aims at building a new configuration C^S which must be as close as possible to C^F but for which the solution $(\mathbf{v}^S, p_f^S, \boldsymbol{\sigma}^S)$ is hoped to improve (the superscript F refers to father and S to son). The global strategy of the developed re-meshing algorithm consists in four phases :

- the first phase of the re-meshing algorithm aims to analyse the current topology of C^F , i.e. to define Ω^F , its boundaries $\partial\Omega^F$ with its related boundary conditions B^F . Such analysis allows to build the data required to create the new mesh M^S , and also the data required to re-build the boundary conditions,
- the second phase consists in the generation of the mesh M^S itself,
- the third phase aims to re-generate the boundary conditions B^S in the new mesh, the constitutive laws and control data,
- the fourth and last phase consists in the transfer of the nodal information (\mathbf{v}^F, p_f^F) and Gauss point information $(\boldsymbol{\sigma}^F, \boldsymbol{\kappa}^F)$ computed on M^F in the new mesh M^S . This phase is crucial for the accuracy of the whole re-meshing procedure.

These four phases have naturally been separated in four programs which are detailed in the following sections.

4.3.2 Analysis of the current configuration (program *CRECOU*)

Any solid domain Ω , which is closed, is defined by n boundaries $\partial\Omega$, with $n \geq 1$. When $n=1$, the domain is defined by a unique external boundary $\partial\Omega_e$. If $n > 1$, the domain is then defined by one external boundary $\partial\Omega_e$ and by $n-1$ internal boundaries $\partial\Omega_i$, that is this domain has $n-1$ holes. In each case the external boundary $\partial\Omega_e$ is unique. On a practical point of view, in the *LAGAMINE* code, the finite elements are anticlockwise defined, i.e. the order of definition of each element nodes is anticlockwise. It results that external boundaries $\partial\Omega_e$ are naturally anticlockwise defined whereas the internal boundaries $\partial\Omega_i$ are clockwise defined.

Let us consider a mesh M^F which discretises the configuration C^F made up of one solid domain Ω^F . The domain Ω^F is itself defined by a unique boundary $\partial\Omega^F$ on which boundary

conditions B^F are defined. Each element side (es) which is defined by $nnode$ nodal points ($nnode=2$ for linear elements, $nnode=3$ for parabolic elements) is stored in the matrix $s_{i,j}^F$, where the subscript i refers to the segment number and j varies between 1 and $nnode$. Removing all the es which are shared by several elements gives the es which describe the boundary $\partial\Omega^F$ of the domain Ω^F . Ordering these es between them such that the last node ($nnode$) of the i^{th} es is equal to the first node of the $i+1^{th}$ es

$$s_{i+1,1}^F = s_{i,nnode}^F \quad (4.4)$$

defines the boundary $\partial\Omega^F$ in an ordered manner. It is considered that boundary conditions B^F are only applied on $\partial\Omega^F$, i.e. boundary conditions relate to the element sides $s_{i,j}^F$. Five types of boundary conditions have been distinguished, related to five types of es s^F :

- free boundary or es s^{Ff} , i.e. a side which does not represent an interface with an other domain, and which is free of any loading, prescribed displacement or pressure,
- solid/solid boundary or es s^{Fs} representing an interface with an other domain for which nodes are common to the two sub-domains; this boundary is always perfectly adherent,
- contact boundary or es s^{Fc} , on which a contact element *CNTCP* or *FOUND* is defined,
- pressure boundary or es s^{Fp} , on which a pressure element *LICHA* is defined,
- prescribed displacement boundary (including zero or non-zero values) or es s^{Fd} , on which constant displacements are imposed.

Based on these properties of the es , ns boundary segments $\partial\omega^F$ can be defined which regroup several es : each boundary segment $\partial\omega^F$ is continuous, and properties of all of its es are identical. Consequently, $\partial\Omega^F$ can be defined as the sum of the contiguous ns boundary segments $\partial\omega_i^F$.

$$\partial\Omega^F = \sum_{i=1}^{ns} \partial\omega_i^F \quad (4.5)$$

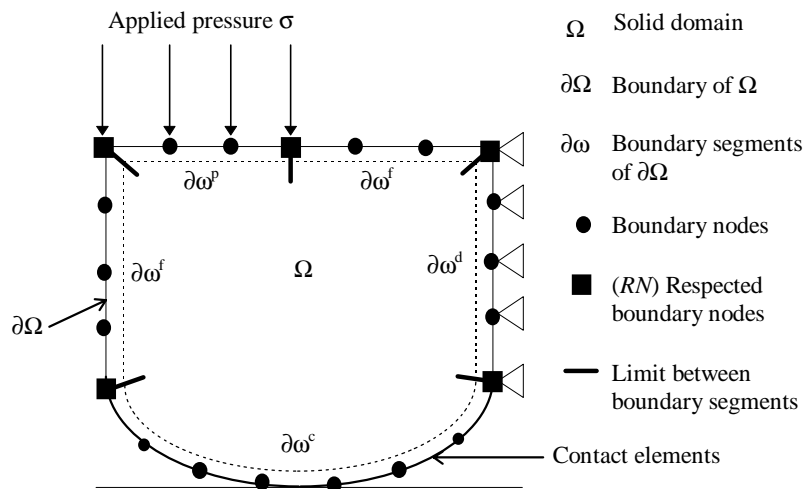


Figure 4.2 Illustration of the analysis of a model.

An example is presented on figure 4.2 to illustrate these definitions.

The closeness condition of $\partial\Omega^F$ implies that, considering a given starting point, there is a unique way to describe $\partial\Omega^F$ in an ordered manner. Then the boundary $\partial\Omega^F$ is defined univocally by the arrangement of ordered segments $\partial\omega_i^F$ which are themselves ordered and which moreover have a unique property (free, solid/solid, contact, pressure or prescribed).

For each $\partial\omega_i^F$, the first and the last point (corresponding to nodes in M^F) represent locations in M^F where the boundary conditions change. As in the new mesh M^S , the boundary conditions must remain identical, it follows that every first and last point of each $\partial\omega_i^F$ must be present in M^S . These particular points (which are nodes in M^F) are referred as respected nodes RN^F , i.e. nodes of M^F which will correspond to nodes in M^S (see figure 4.2 for an illustration). In addition, another type of particular nodal points in M^F must be respected in M^S : the nodes for which the angle between two sides is lower than a limit angle are considered as corner nodes and must also be respected in the new mesh. If in the father configuration C^F there are more than one solid domain, the same type of operation is repeated for each solid domain Ω^F .

At the end of this algorithm, a file is created for the mesh generator. This file contains all the required information on M^F , regarding the definition of each solid domain Ω^F , i.e. $\partial\Omega^F$, $\partial\omega_i^F$, and RN^F . Note that all boundary conditions are contained in $\partial\omega_i^F$. If required, density points can be defined in order to generate a mesh with variable density. These density points can be attributed to bifurcated points (in the sense of Rice, see e.g. [PIERRY, 1997]) or to local error estimator (see e.g. [DYDUCH, 1996]).

4.3.3 Generation of the new mesh for the solid domain (program *GMAILL*)

The mesh generator has been developed in parallel to the global re-meshing algorithm. It is based on a frontal meshing algorithm which can manage multi-domain topology with internal boundaries [GODINAS, 1995]. Only a brief description of the algorithm is given here. The meshing phase of solid domain Ω^S is divided into three parts :

- Definition of a relative density field : from density points analysed in the previous phase, a relative density field is defined on the whole model. Note that this density field is unique on internal domain interfaces $\partial\Omega_i$, which will result in an identical distribution of nodes on these interfaces.
- Meshing of the boundaries $\partial\Omega^S$ of the solid domain Ω^S : the RN^F respected nodes which have been defined in the previous phase are defined as boundaries of temporary contour segments $\partial\omega_i$ (without properties). Based on the global density field previously defined, the new nodes located on the domain boundary $\partial\Omega^S$ are defined with the constraint that they must belong to the element sides $s_{i,j}^F$, in order to respect as close as possible the father boundary $\partial\Omega^F$. Although $\partial\Omega^F$ is not perfectly respected in the son mesh due to its approximation by segments, the error on the external boundary representation is very small.
- Meshing of the solid domain Ω^S : starting from the boundary $\partial\Omega^S$, the mesh is then built from the outer part of the domain towards its centre. Each domain is divided repeatedly in order to obtain triangles with maximised angles (closest to 60°) which verify the relative density function over the domain. First (linear) or second order (parabolic) triangles are

directly generated. First or second order quadrangles are built afterwards by merging initial triangles by couples. After some nodal co-ordinates rearrangements which aim to get angles as close as possible to 60° for triangles and 90° for quadrangles, the final mesh M^S of the solid domain Ω^S is obtained.

Finally, as the following conditions

$$\begin{aligned} RN^S &\cong RN^F \\ \partial\Omega^S &\cong \partial\Omega^F \end{aligned} \quad (4.6)$$

have been verified, it follows that the definition of the solid domain in the son and father configuration are almost identical, i.e.

$$\Omega^S \cong \Omega^F \quad (4.7)$$

4.3.4 Reconstruction of boundary conditions and global data (program *CREDAT*)

This phase consists in building the new data file from the mesh given by the mesh generator. Classical control data are straightforward to re-build (i.e. laws parameters, type of analysis) as these ones do not change between C^F and C^S .

In an similar way than for M^F , the solid element sides are stored in the matrix s_{ij}^S , the ones which belong to $\partial\Omega^S$ are kept and ordered. The respected nodes RN^S in the son mesh M^S are found from the RN^F , which allows to re-arrange the new boundary $\partial\Omega^S$ in the same fashion than $\partial\Omega^F$. Finally, the new boundary segments $\partial\omega^S$ can be identified together with their respective properties. From the definition and properties of all the boundary segments $\partial\omega^S$, it is then straightforward to regenerate to corresponding boundary conditions and thus the new data file corresponding to M^S . As the condition

$$\partial\omega_i^S \cong \partial\omega_i^F \quad (4.8)$$

is verified, it follows that the discretisation in the son and father configuration (including boundary conditions) are very similar, i.e.

$$M^S \cong M^F \quad (4.9)$$

It must be pointed out that, in case of hydromechanical coupled simulation, the fluid pressure d.o.f. is transferred from M^F to M^S during this phase following the same procedure than for nodal velocities (see next section for description).

4.3.5 Transfer of the solution and state variable fields (program *INTERP*)

All the information available at the final step in the father mesh M^F , i.e. nodal values (velocities \mathbf{v}^F and pressure p_f^F) and integration point values (stresses $\boldsymbol{\sigma}^F$ and internal variables κ^F) must be transferred to the new mesh ($\mathbf{v}^S, p_f^S, \boldsymbol{\sigma}^S, \kappa^S$). This is a very important task as the new fields obtained should be as close as possible equivalent to the old ones in order to induce very small perturbation of the physical system, i.e.

$$\begin{aligned}
 \mathbf{v}^S(\mathbf{x}) &\cong \mathbf{v}^F(\mathbf{x}) \\
 p_f^S(\mathbf{x}) &\cong p_f^F(\mathbf{x}) \\
 \boldsymbol{\sigma}^S(\mathbf{x}) &\cong \boldsymbol{\sigma}^F(\mathbf{x}) \\
 \kappa^S(\mathbf{x}) &\cong \kappa^F(\mathbf{x})
 \end{aligned} \tag{4.10}$$

The transfer method which was originally available is presented. As this method generally gave poor results in the geomechanical simulations presented in chapter 6, another transfer method has been developed and implemented.

4.3.5.1 Original transfer method

In the transfer method originally developed in an earlier version of the re-meshing algorithm [HABRAKEN, 1989] and referred as the $1/r^p$ method, the value of a field $a(\mathbf{x})$ at any point Q is obtained by the average of the values at the surrounding points R which are weighted by the distance r to point Q following the relation

$$a^Q(\mathbf{x}) = \begin{cases} a^R(\mathbf{x}) & \text{if } r \leq r_0 \\ \frac{\sum a^R(\mathbf{x})}{\sum r^p} & \text{if } r > r_0 \\ \frac{1}{\sum \frac{1}{r^p}} & \end{cases} \tag{4.11}$$

where the summation sign indicates a summation over all points R . The distance between point Q and point R is r , p is the order of interpolation and r_0 is the minimum distance under which points Q and R are considered similar.

With this transfer method, a continuous smoothed field is obtained in any case. This algorithm can be used for the transfer of the nodal velocity field as well as for the stress and internal variable fields.

Several reasons have motivated the implementation of a different transfer method :

- The data defined at integration points ($\boldsymbol{\sigma}^F, \kappa^F$) must be distinguished from the ones defined at nodes (\mathbf{v}^F, p_f^F). On the one hand, the continuity condition implies naturally that the nodal velocity field $\mathbf{v}^F(\mathbf{x})$ and the fluid pressure field $p_f^F(\mathbf{x})$ are continuous over Ω^F . On the other hand, the stresses $\boldsymbol{\sigma}^F$ and the state variables κ^F are only known at integration points without any constraint on the global fields $\boldsymbol{\sigma}^F(\mathbf{x})$ and $\kappa^F(\mathbf{x})$. It can be assumed that these fields are continuous over each element but not between them, thus $\boldsymbol{\sigma}^F(\mathbf{x})$ and $\kappa^F(\mathbf{x})$ are only continuous by parts. As mentioned earlier, this later feature of the stress and state variable fields is related to the finite element formulation used in which the main unknowns are the nodal values, i.e. the solution is a kinematically admissible one. As a consequence, there is no reason to use the same algorithm for the transfer of the continuous fields and for the transfer of the Gauss points fields.
- It is straightforward to show that, for constant gradient fields, the $1/r^p$ transfer method is quite poor on the domain boundary $\partial\Omega^S$, due to the averaging of the field resulting from equation (4.11). Let us consider a scalar field $b(x)$ in the one-dimensional space x , which is continuous and monotonic on the interval $[x_0; x_n]$ and with a constant gradient (see figure

4.3). Assume that $b(x)$ is only known at discrete points x_1, x_2, x_3, x_4 and x_5 . If the value of b is evaluated using equation (4.11) on the boundaries x_0 and x_n , it is obvious that the following conditions will be obtained

$$\begin{aligned} b(x_0) &\in]b(x_1); b(x_5)[\\ b(x_n) &\in]b(x_1); b(x_5)[\end{aligned} \quad (4.12)$$

whereas, for the considered example given in figure 4.3, the true values of b at the boundaries should verify

$$\begin{aligned} b(x_0) &< b(x_1) \\ b(x_n) &> b(x_5) \end{aligned} \quad (4.13)$$

The poor representation of the field $b(x)$ on boundaries using the $1/r^p$ method is also true considering non linear fields for which the gradient is not constant.

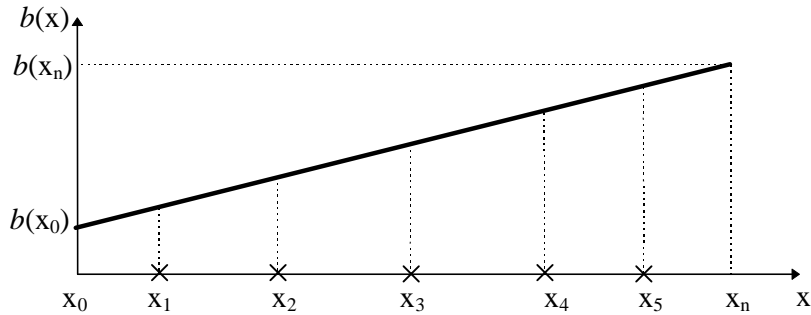


Figure 4.3 Representation of a scalar field with constant gradient.

This feature is of particularly importance for the transfer of integration point values from M^F to M^S .

- We are mainly interested here in simulations where body forces are taken into account. As a first approximation, body forces will result in a stress field with a constant vertical gradient for the vertical stress component σ_v^F . The poor representation of σ_v^F close to the upper and vertical boundaries will lead globally to an underestimation of σ_v^S in the son mesh, which may result in non-negligible perturbations of the configuration C^S compared to C^F .
- Moreover, the numerical examples carried out in chapter 6 showed that computed fields frequently exhibit high gradient variations (regarding stresses, strains and state variables) in relation with boundary conditions. In such cases, the poor representation of these fields close to boundaries may lead to modify the physical problem. This may become non-negligible when state variables such as specific mass, friction angle and cohesion are poorly transferred.

For all the previously mentioned reasons, a new transfer method has been developed and is presented in the next section.

4.3.5.2 Developed transfer method

This method separates the transfer of nodal quantities (\mathbf{v}^F, p_f^F) from the transfer of Gauss points quantities ($\boldsymbol{\sigma}^F, \kappa^F$). As already mentioned, the nodal fields are already continuous over Ω^F which is not the case for the Gauss points fields.

In a first step, all the fields defined at Gauss points are transferred to the nodal points in order to obtain continuous fields. For this transfer, an extrapolation method has been preferred to an averaging method (i.e. the $1/r^p$ method) in order to limit the smoothing effect close to boundaries, which is inherent to such method (see previous section). In a second step, interpolation of all the information which is now continuously known at nodes of M^F to integration points of M^S is performed using the isoparametric formulation of the elements. Details about these procedures are given in the next two sections.

4.3.5.2.1 Nodal extrapolation of integration point values (in the old mesh)

For every element of M^F , each value known at integration points is extrapolated linearly to the nodes. For linear elements this operation is straightforward as there is either one integration point or the same number of nodes than integration points. For quadratic elements with reduced integration, there are more integration points than nodes, for instance 8 and 4 considering quadrilaterals with reduced integration. In this case, a linear extrapolation is made at the corner nodes as for linear elements. Mid-side nodes values are extrapolated linearly from the corner nodes values. On a numerical point of view, the nodal extrapolation is managed using extrapolation functions which are build in an identical fashion than interpolation ones, but here local co-ordinates of integration points are $(\pm 1, \pm 1)$.

This nodal extrapolation is carried out for all the elements of M^F . Finally, for each node which is shared by nel elements, any variable a^F is defined at this node by nel values a_i^F , where i vary between 1 and nel . Then for each node of M^F , the averaged variable a^{F*} is obtained from

$$a^{F*} = \frac{\sum_{i=1}^{nel} a_i^F}{nel} \quad (4.14)$$

Repeating this operation for all the nodes of M^F gives the continuous fields $\boldsymbol{\sigma}^{F*}(\mathbf{x})$ and $\kappa^{F*}(\mathbf{x})$.

4.3.5.2.2 Interpolation of nodal fields of M^F to points (nodes or integration points) of M^S

Let us consider a point P^S (which can be a node or an integration point) of M^S with global co-ordinates (\mathbf{x}^p) . At this point we want to compute, using an isoparametric formulation, the component a^S from the continuous field $a^F(\mathbf{x})$ defined at the nodes of M^F . The general problem is to find in which solid element E^F of M^F the point P^S is located, and to find the local co-ordinates $\boldsymbol{\xi}$

$$\boldsymbol{\xi} = \begin{bmatrix} \xi \\ \eta \end{bmatrix} \quad (4.15)$$

and associated interpolation functions $\Phi(\boldsymbol{\xi})$ of P^S in E^F . As there is no explicit solution for this problem, a numerical computation of the solution must be carried out, e.g. using Newton-Raphson method. Let us starts from the isoparametric description

$$\mathbf{x}_i^p = \Phi_L(\boldsymbol{\xi})\mathbf{x}_{Li}^F \quad (4.16)$$

where \mathbf{x}_{Li}^F represents the co-ordinates of the L nodes of E^F . A first order Taylor development of equation (4.16) yields

$$\mathbf{x}_i^p = \mathbf{x}_i^{p0} + \mathbf{J}_{ij}\Delta\xi_j \quad (4.17)$$

where \mathbf{J} represents the jacobian of the transformation from \mathbf{x} to $\boldsymbol{\xi}$

$$\mathbf{J}_{ij} = \frac{\partial \mathbf{x}_i^p}{\partial \xi_j} = \frac{\partial \Phi_L}{\partial \xi_j} \mathbf{x}_{Li}^F \quad (4.18)$$

Solving for $\Delta\xi$ gives the correction to be applied on local co-ordinates

$$\Delta\xi_j = \mathbf{J}_{ij}^{-1}(\mathbf{x}_i^p - \mathbf{x}_i^{p0}) \quad (4.19)$$

provided that the following condition is verified

$$\det(\mathbf{J}) > 0 \quad (4.20)$$

Using the previous relations, the isoparametric co-ordinates of P^S can be computed using the iterative algorithm presented in figure 4.4. Newton iterations are performed within two nested loops (loop 1 and 2 on figure 4.4) for each element, in order to verify if P^S is located inside this element. Usually less than five iterations are required to converge to the precision $prec=10^{-4}$ on $\Delta\xi$. It is more economical to perform these iterations only for neighbour elements to P^S , i.e. elements for which co-ordinates of P^S verifies the conditions

$$\begin{aligned} x_{\min} < x^P < x_{\max} \\ y_{\min} < y^P < y_{\max} \end{aligned} \quad (4.21)$$

where x_{\min} , x_{\max} , y_{\min} , and y_{\max} are defined on figure 4.5.

Once the element of M^S containing P^S is found, i.e. $\Delta\xi$, it is then straightforward to interpolate the value of the field $a^S(\mathbf{x})$ at P^S using

$$a_i^S = \Phi_L a_{Li}^F \quad (4.22)$$

Repeating this operation for all the integration points of M^S gives the continuous fields $\mathbf{v}^S(\mathbf{x})$, $p_i^S(\mathbf{x})$, $\boldsymbol{\sigma}^S(\mathbf{x})$ and $\kappa^S(\mathbf{x})$ in the son mesh from the continuous fields in the father mesh $\mathbf{v}^F(\mathbf{x})$, $p_i^F(\mathbf{x})$, $\boldsymbol{\sigma}^F(\mathbf{x})$ and $\kappa^F(\mathbf{x})$.

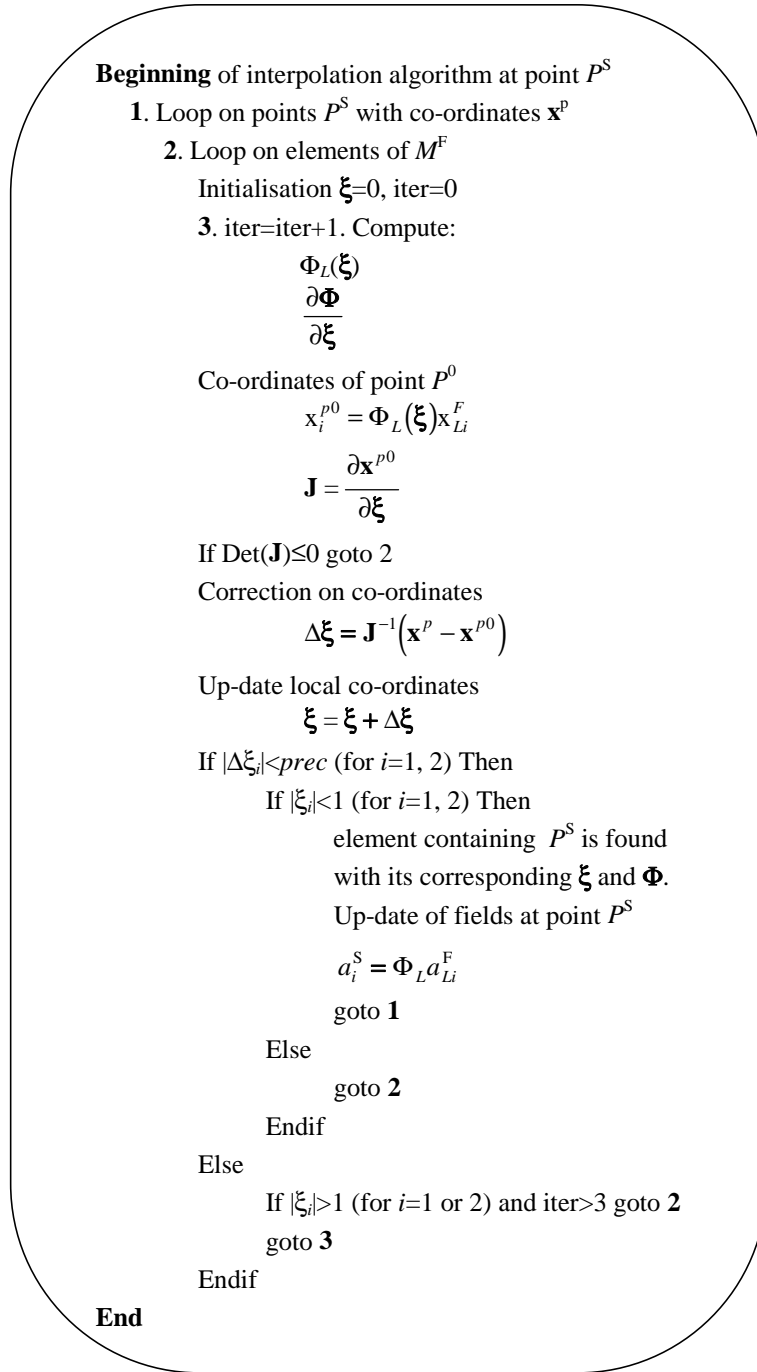


Figure 4.4 Algorithm of interpolation of a field at points P^S in a mesh M^F .

There has also been some work done to find the best method to transfer tensors, for instance transferring its eigenvalues and eigenvectors or its global components, see [AELAAI, 1986] and [HABRAKEN, 1989]. As it does not seem that one method is very much better than the other, the tensors have been transferred using their global co-ordinates expression.

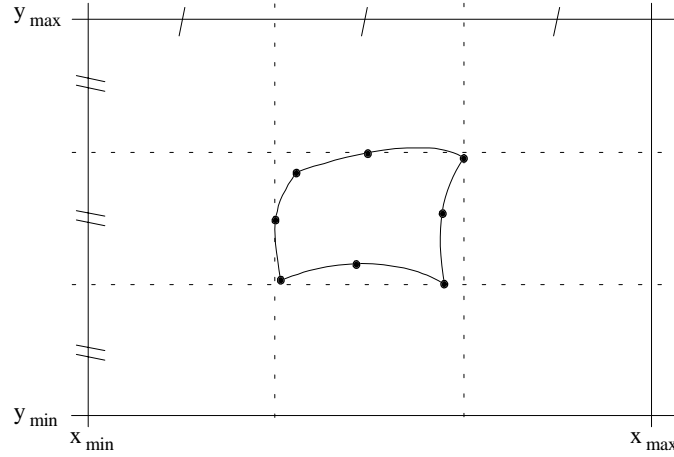


Figure 4.5 Definition of the window $(x_{\min}; x_{\max}; y_{\min}; y_{\max})$ in which P^S must be located for computing its local co-ordinates.

4.3.5.3 Transfer of contact data

If the configuration includes boundary segments with contact properties (i.e. with CNTCP and FOUND elements), the contact fields (pressure, hydraulic flux) must also be transferred from M^F to M^S . This is performed by :

- a linear extrapolation from contact elements Gauss points to nodes of M^F ,
- an average at contact nodes of M^F ,
- a linear interpolation from M^F to the new contact integration points of M^S .

Such a transfer of contact variables is consistent with the transfer of solid domain variables, it usually improves the convergence after re-meshing [HABRAKEN, 1989], i.e. decreases the global disequilibrium of C^S .

4.3.6 Plastic admissibility

As mentioned in the previous section, some error has been generated in the transfer of the stress and field variable fields. Here we have chosen to transfer the stress tensor in global co-ordinates. Considering a general elastoplastic constitutive relation integrated using the implicit algorithm presented in section 2.3.3, then for each Gauss points of the father mesh, the stress tensor σ^F (if coupled hydromechanical problems are considered, σ^F is replaced by the effective stress tensor σ^{1F} in this section) and the state variables κ^F verify the condition

$$f(\sigma^F, \kappa^F) \leq 0 \quad (4.23)$$

In the new mesh, some error (though small) has been generated during the transfer of the stress and state variable. It implies that, in the new mesh some integration points may violate the yield criterion, i.e.

$$f(\sigma^S, \kappa^S) > 0 \quad (4.24)$$

Such stress states are not plastically admissible, thus a correction must be applied such that the yield condition is no violated. Assuming that these points are in plastic state, they should verify the yield function

$$f(\boldsymbol{\sigma}^S, \kappa^S) = 0 \quad (4.25)$$

In order to restore this condition, two methods are possible:

- the yield surface can be brought onto the stress state performing an up-date of the state variables, without modification of the stress state $\boldsymbol{\sigma}^S$,
- the stress state can be brought back onto the yield surface, without modification of the states variables κ^S .

The second possibility has been chosen here, i.e. the stress state is mapped back onto the yield surface without modification of the pressure. For integration points which verify equation (4.24), we want to evaluate the modified stress state $\boldsymbol{\sigma}^{S*}$ for which the condition

$$f(\boldsymbol{\sigma}^{S*}) = 0 \quad (4.26)$$

is verified, where $\boldsymbol{\sigma}^{S*}$ is defined by

$$\boldsymbol{\sigma}^{S*} = \boldsymbol{\sigma}^S + \Delta\boldsymbol{\sigma} \quad (4.27)$$

The stress increment $\Delta\boldsymbol{\sigma}$ represents the correction applied to the stress state. Similarly to plasticity algorithm, it is chosen normal to a modified flow potential g^* with $\psi^*=0$ (non-dilatant path) in order to keep the same pressure during the correction, i.e.

$$\Delta\boldsymbol{\sigma} = \lambda^* \frac{\partial g^*}{\partial \boldsymbol{\sigma}^S} \quad (4.28)$$

where λ^* represents a pseudo plastic multiplier. A first order Taylor development of f around $\boldsymbol{\sigma}^{S*}$ yields

$$f(\boldsymbol{\sigma}^{S*}) = f(\boldsymbol{\sigma}^S) + \frac{\partial f}{\partial \boldsymbol{\sigma}^S} \Delta\boldsymbol{\sigma} \quad (4.29)$$

incorporating equation (4.28) into (4.29) and solving for λ^* which gives

$$\lambda^* = - \frac{f(\boldsymbol{\sigma}^S)}{\frac{\partial f}{\partial \boldsymbol{\sigma}^S} \frac{\partial g^*}{\partial \boldsymbol{\sigma}^S}} \quad (4.30)$$

Then $\boldsymbol{\sigma}^{S*}$ is up-dated using equations (4.27), (4.28) and (4.30). For similar reasons than the ones invoked in section 2.3.3.2, an implicit algorithm is used to ensure that the consistency condition is verified very accurately. The algorithm used is summarised on figure 4.6. It is a modified version of the general integration algorithm given in figure 2.20.

4.3.7 Equilibrium of the initial state

Using the transfer method described in the previous section, the obtained fields $\mathbf{v}^S(\mathbf{x})$ and $p_f^S(\mathbf{x})$ are consistent with the initial fields $\mathbf{v}^F(\mathbf{x})$ and $p_f^F(\mathbf{x})$ because the later were continuous and have been interpolated using the isoparametric formulation, i.e. the following relations are verified

$$\begin{aligned} \mathbf{v}^S(\mathbf{x}) &\cong \mathbf{v}^F(\mathbf{x}) \\ p_f^S(\mathbf{x}) &\cong p_f^F(\mathbf{x}) \end{aligned} \quad (4.31)$$

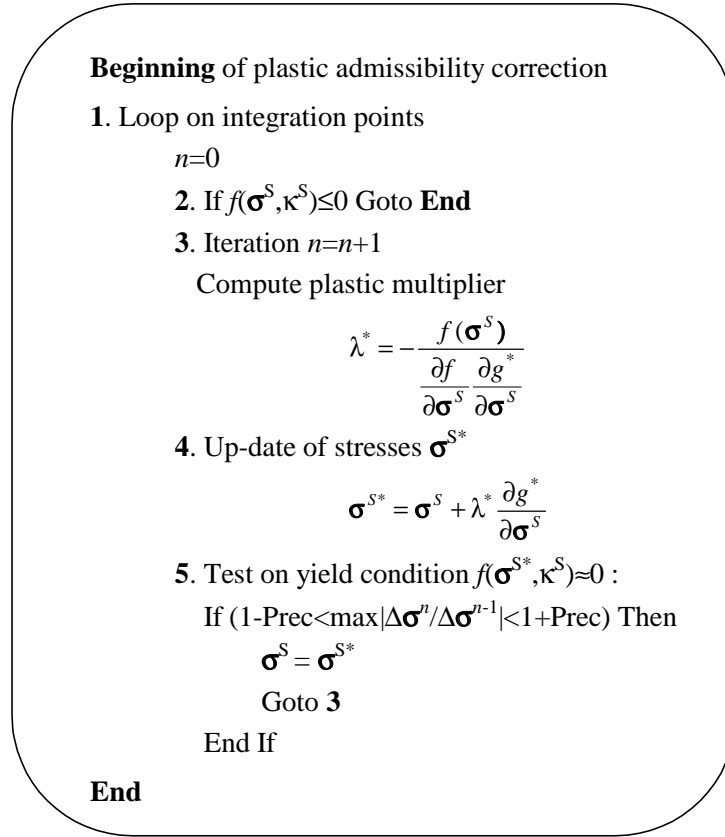


Figure 4.6 Algorithm used for plastic admissibility correction.

As mentioned previously, the transfer of the discontinuous fields $\boldsymbol{\sigma}^F(\mathbf{x})$ and $\kappa^F(\mathbf{x})$ to the new mesh has generated some error resulting from :

- the nodal extrapolation,
- the smoothing of the fields which has been carried out to obtain continuous fields (equation 4.14),
- the plastic admissibility correction.

Such error is mainly related to the error associated with the finite element mesh. Therefore, it must be minimised using a mesh adapted to the problem and to its evolution, see for instance [DYDUCH, 1996]. As a result, the stress and state variable fields are close but not identical between the father and the son mesh, i.e.

$$\begin{aligned} \boldsymbol{\sigma}^S(\mathbf{x}) &\cong \boldsymbol{\sigma}^F(\mathbf{x}) \\ \kappa^S(\mathbf{x}) &\cong \kappa^F(\mathbf{x}) \end{aligned} \quad (4.32)$$

Then, the weak form of the local equilibrium equation (2.12) is generally not verified, i.e.

$$\int_V \rho \mathbf{g} \cdot \delta \mathbf{u} \, dV + \int_S \mathbf{t} \cdot \delta \mathbf{u} \, dS \neq \int_V \boldsymbol{\sigma} : \delta \dot{\boldsymbol{\epsilon}} \, dV \quad (4.33)$$

For time-independent problems, it is always possible to perform iterations without any additional loading in order to compute a balanced initial configuration C^{S0} .

4.4 Additional improvements

The re-meshing algorithm has two main effects on the general finite element formulation, which are presented below.

4.4.1 Update of the initial configuration

The initial configuration at $t=0$ is lost through re-meshing procedure. This has no direct effects on the finite element formulation as an up-dated Lagrangian referential is used to express equilibrium (see section 2.2.1). The initial configuration is only required in post-processing phases (post-processor *SELECT*) in order to compute the natural strain tensor (see equation 2.8). Thus, an image of the current mesh in configuration at $t=0$ should be computed during the re-meshing phase.

Let us note \mathbf{x}^{F0} the co-ordinates of the father mesh M^{F0} at $t=0$, \mathbf{x}^F the co-ordinates of the father mesh M^F at t for which re-meshing is performed, and \mathbf{x}^S the co-ordinates of the son mesh M^S at t for which re-meshing is performed. All these co-ordinates are known during re-meshing. The problem is now to compute the co-ordinates \mathbf{x}^{S0} , i.e. the co-ordinates of the son mesh M^{S0} in the initial configuration at $t=0$. This can be solved by computing the local co-ordinates of every nodes of M^S in M^F using a similar algorithm than the one given in figure 4.4. Then using the property that local co-ordinates of any point P belonging to the father mesh will not vary between M^F and M^{F0} , i.e.

$$\xi^{P(F0)} = \xi^{P(F)} \quad (4.34)$$

the co-ordinates \mathbf{x}^{S0} are further obtained from

$$x_i^{P(S0)} = \Phi_L(\xi^{P(F)})_{x_{Li}^{P(F)}} \quad (4.35)$$

The up-date is performed automatically during the re-meshing in the program *CREDAT*. The initial configuration \mathbf{x}^{S0} is saved on a file with extension *.cin and is read afterward on user's choice in the post-processor *SELECT*.

4.4.2 Introduction of passive markers of the finite displacement

In classical simulations without re-meshing, the Lagrangian mesh can be used to visualise directly the finite displacement field. However, it is no longer the case when re-meshing is performed. Such problem can be overcome by introducing in the initial mesh M^{F0} at $t=0$ some artificial points which will be kept through re-meshing procedure. This has been achieved by writing of two programs : passive markers are generated in the program *GENMKP* and stored on file *.mkp, the passive markers up-date is made either during re-meshing or in post-treatment using the program *MARKPA*. It is based on very similar properties than the ones used to up-date the initial configuration. The up-dated co-ordinates \mathbf{x}^P of point P are obtained following

$$x_i^{P(F)} = \Phi_L(\xi^{P(F0)})_{x_{Li}^{P(F)}} \quad (4.36)$$

in which $\Phi_L(\xi^{P(F0)})$ has been obtained from the algorithm given in figure 4.4.

4.5 Conclusion

The developed automatic re-meshing algorithm has been detailed in this chapter. It is based on a comprehensive analysis of the topology of the father mesh, including multi-domains, domain boundaries, boundary segments with their respective properties and respected nodes.

Such an analysis allows to regenerate a new mesh with identical boundary conditions in a quite general framework. Many types of boundary conditions are included, with possible complex combinations between them. An interesting point lies in the full automation of the re-meshing procedure which can always be performed without any user control. Of course experienced users can have control on several re-meshing procedures, e.g. the choice of the transfer method... This results in a very user friendly algorithm which then can be run very quickly and easily. The decision of re-meshing is either based on error criterion, distortion criterion or user choice.

The introduction of the initial configuration up-date together with passive markers is also valuable when analysing results, due to very large amount of strains and displacements which can be simulated using the re-meshing procedure. This will be particularly illustrated in application examples presented in chapters 6 and 7.

CHAPTER 5

Influence of the limit surface shape on the stress state in geomechanical simulations

5.1 Introduction

In chapter 2, differences between the Drucker-Prager criterion and the Van Eekelen criterion have been detailed.

Especially, it has been shown that, as far as large friction angles are concerned, the use of the Drucker Prager criterion could lead to an important stress overestimation compared to a Mohr Coulomb or a Van Eekelen criterion. It has then been demonstrated that this effect results directly from the independence of the Drucker Prager criterion with respect to Lode angle, which is against experimental evidences [see e.g. LANIER, 1988]. Eventually, it has also been noticed that such effect can also be invoked for other types of constitutive models such as models from the critical state family [GENS and POTTS, 1988].

In this chapter, specificities of the geological stress fields are examined and their implications in term of yield criterion and allowed stress paths are detailed. Especially, it is shown that general yield criteria can be reduced to two-dimensional ones. In such case, the differences between the three yield criteria presented in chapter 2 appear very clearly.

The concepts presented in this chapter are illustrated through two simple application cases.

In the first one, a quantitative study of this stress overestimation is carried out for an anticline structure model, considering the two elastoplastic criteria (DP and VE) implemented in the *PLASOL* law of *LAGAMINE*. The influence on plastic dilatancy is also investigated.

In the second application case, the effect of the yield criterion is illustrated in the particular case where both an elastoplastic solid and a contact interface are present.

5.2 Particularities of geological stress fields, implications for geomechanical simulations

In geological context, the stress field exhibits a particularity, i.e. the vertical stress σ_v is actually a problem data as it approximately derives from the lithostatic weight induced by gravity forces

$$\sigma_v \approx -\rho g z \quad (5.1)$$

where z is the depth from the topographic surface.

Depending on the regional tectonic regime, one may found :

- $\sigma_v = \sigma_1$ in extensive regime,
- $\sigma_v = \sigma_2$ in strike slip regime,
- $\sigma_v = \sigma_3$ in compressive regime.

Those three limit stress states correspond with the three typical Andersonian states of stress [ANDERSON, 1951] represented on figure 5.1.

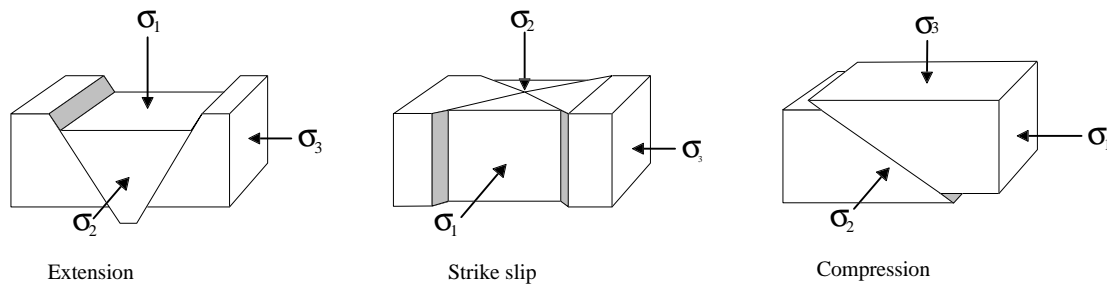


Figure 5.1 The three typical Andersonian state of stress.

Let us consider a given material point M located at depth z which is submitted to a given tectonic regime. Assume for instance a compression regime which results approximately in $\sigma_3 = \sigma_v = \text{constant}$ and assume here that this relation is perfectly verified. Then for point M , the 3D yield criterion reduces to a 2D- $\sigma_3 = c^{\text{st}}$ one, which actually represents a cross section of the 3D criterion at $\sigma_3 = \sigma_v$. Such 2D yield criterion can be generalised to any material point of the model provided that the model includes gravity forces.

This concept is illustrated in figures 5.2 and 5.3, where the 3D and corresponding 2D- $\sigma_3 = c^{\text{st}}$ Drucker Prager, Van Eekelen and Mohr Coulomb criteria are presented for $\phi_C = 20^\circ$ and 35° , respectively. Note that for a given ϕ_C value, the plot scale is identical for the 3 criteria.

Differences between the yield surfaces are clearly underlined :

- if $\phi_C = 20^\circ$, the maximum values for σ_1 and σ_2 are quite similar between these 3 criteria (see figure 5.2),
- as ϕ_C increases, the difference between the DP criterion and the two others becomes more and more pronounced (see figure 5.3 for $\phi_C = 35^\circ$). Denoting σ^{MAX} as the yield stress value for which $\sigma_1 = \sigma_2$, then σ^{MAX} is much higher for the Drucker Prager model than for the Van Eekelen and Mohr Coulomb ones. It is worth mentioning that σ^{MAX} for Van Eekelen and Mohr Coulomb criteria are equal, provided $\phi_C = \phi_E$ in VE.

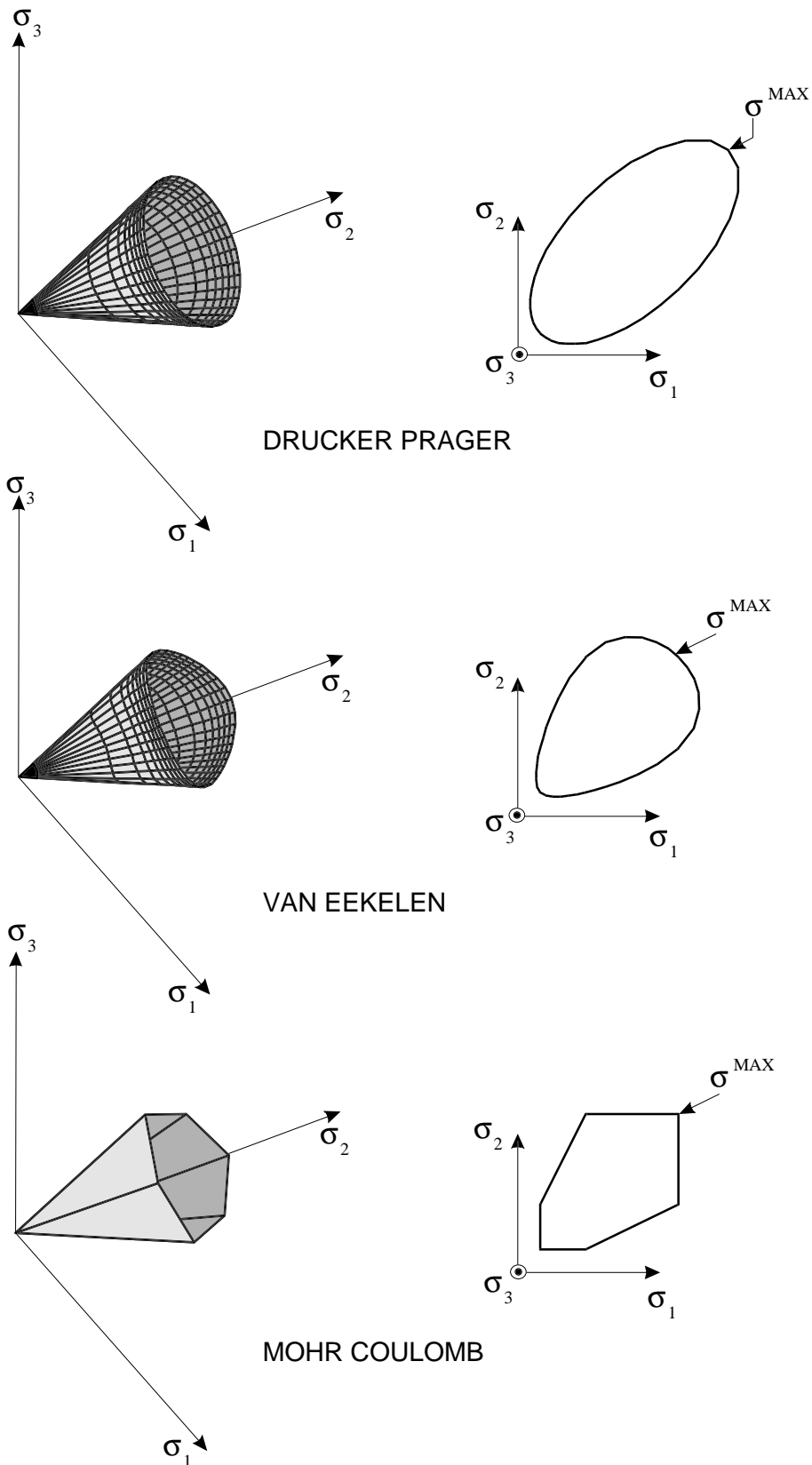


Figure 5.2 Three dimensional and corresponding two dimensional ($\sigma_3=c^{st}$) yield surfaces for plastic criteria with $\phi=20^\circ$, $c=0$.

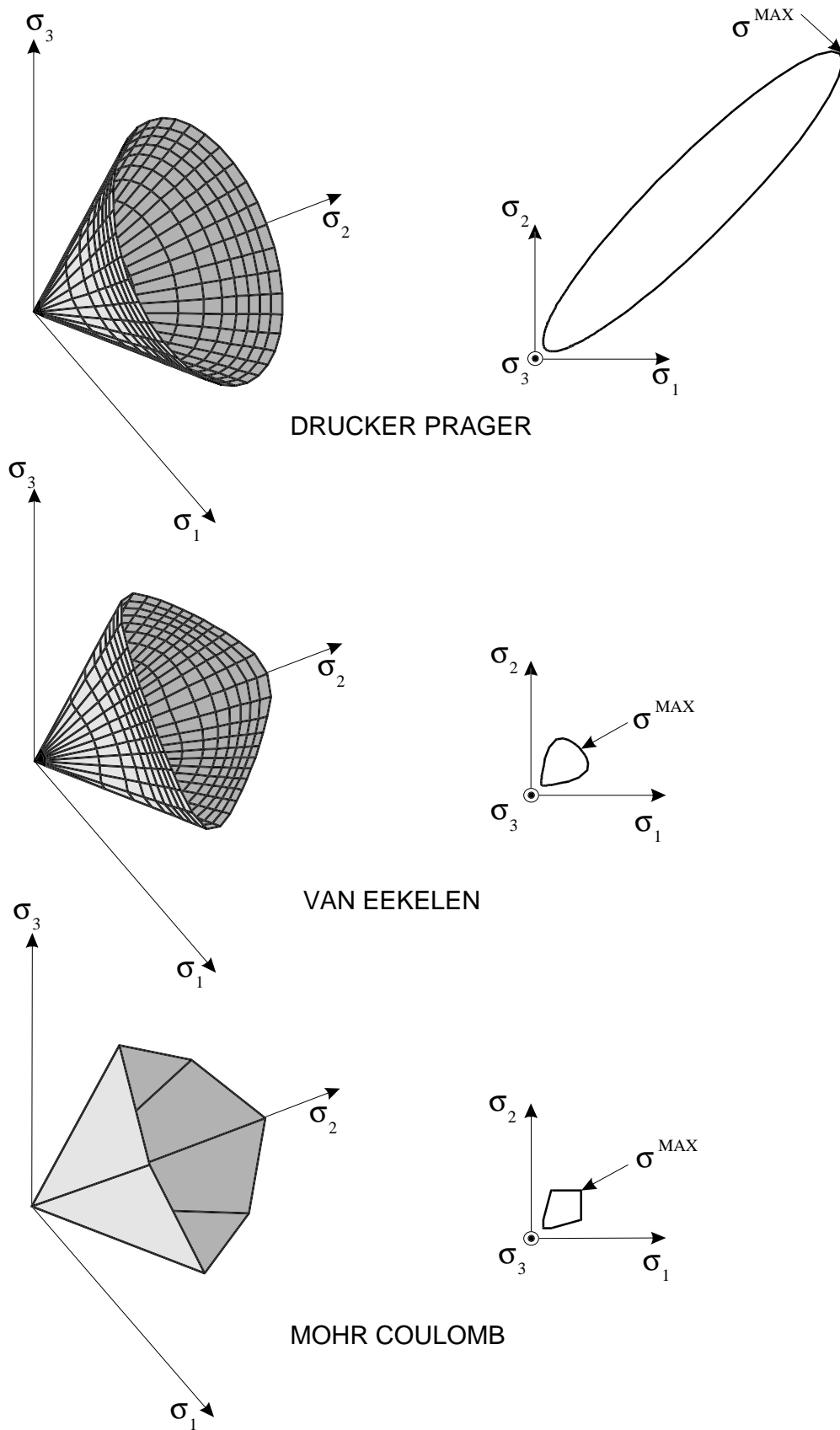


Figure 5.3 Three dimensional and corresponding two dimensional ($\sigma_3=c^{st}$) yield surfaces for plastic criteria with $\phi=35^\circ$, $c=0$.

For the two cases previously presented ($\phi_C=20^\circ$ and 35°) the yield surfaces are closed, i.e. there is a lower and an upper bound for stresses in the (σ_1, σ_2) plane. This is the case as long as the yield surface does not intersect the $(\sigma_1, \sigma_2, \sigma_3=0)$ plane (considering $c=0$). Let us define α as the angle between the hydrostatic axis and the (σ_1, σ_2) plane, and the angles θ_C , θ_E as shown on figure 5.4a. Then in global stress axes, the angle α is given by

$$\alpha = \tan^{-1}\left(\frac{1}{\sqrt{2}}\right) \approx 35.26^\circ \quad (5.2)$$

Using the previous definition of θ_C and θ_E , it follows that the Drucker Prager yield surface is no longer closed in any (σ_1, σ_2) plane (i.e. there is no upper bound for stresses in the (σ_1, σ_2) plane) if θ_C or θ_E is larger than α . From equation (2.80), it is found that this limit value for $\theta_C=\alpha$ corresponds to $\phi_C=36.87^\circ$, which is also the limit value for obtained $\phi_E=90^\circ$ from equation (2.79).

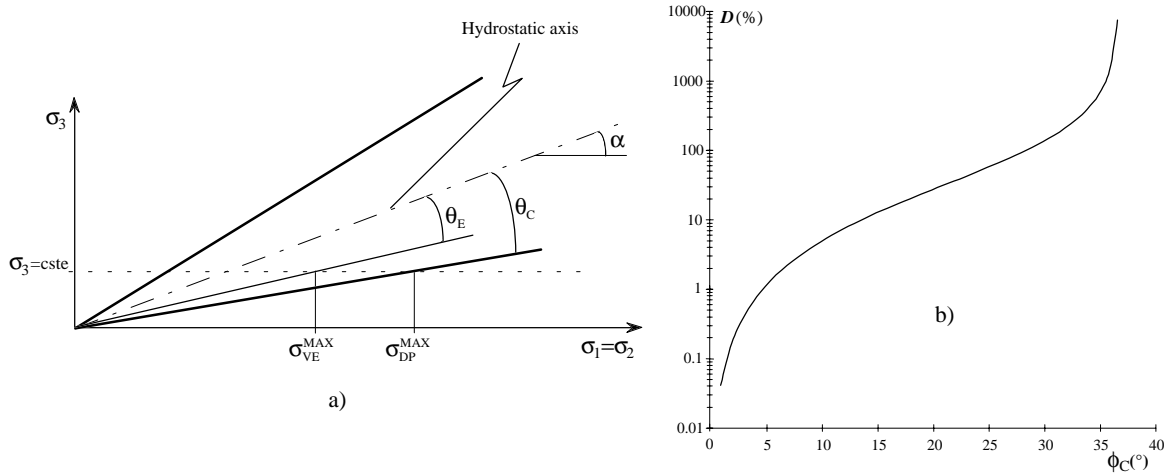


Figure 5.4 a) Graphical interpretation of σ^{MAX} , b) D plotted versus ϕ_C .

This lack of upper bound on σ^{MAX} stresses for $\phi_C > 36.87^\circ$ can lead to an infinite overestimation of stresses in the (σ_1, σ_2) plane! It can also be interpreted as a linear purely elastic behaviour in a triaxial lateral compression test in which the axial stress σ_A (i.e. σ_3) is constant and the confining stress σ_L (i.e. $\sigma_1=\sigma_2$) increases (with $\sigma_A < \sigma_L$). In any case, there is no limit for the stress deviator which then can reach infinitely high values either following elastic or plastic paths.

For θ values smaller than α , the error on σ^{MAX} induced by the use of Drucker Prager criterion compared to a Mohr Coulomb or Van Eekelen one can be expressed by the ratio D

$$\begin{aligned} D &= 100 \frac{\sigma_{\text{DP}}^{\text{MAX}} - \sigma_{\text{VE}}^{\text{MAX}}}{\sigma_{\text{VE}}^{\text{MAX}}} \\ &= 100 \frac{\tan(\alpha - \theta_E) - \tan(\alpha - \theta_C)}{\tan(\alpha - \theta_C)} \end{aligned} \quad (5.3)$$

A plot of equation (5.3) versus ϕ_c displays the evolution of the error D and shows that (see figure 5.4b) :

- for $\phi_c < 20^\circ$, the error on σ^{MAX} is lower than 27%,
- for $20^\circ < \phi_c < 36.87^\circ$, the error D on σ^{MAX} increases quite quickly and becomes infinite as ϕ_c approaches 36.87° .

Thus, it can be concluded that for geomechanical simulation taking into account body forces, then for low friction angle values (let say $0^\circ < \phi_c < 20^\circ$), it may be reasonable to approximate the Mohr Coulomb criterion by a circumscribed Drucker Prager criterion as the maximum error on stresses will be about 27%. However, as friction angle approaches $\phi_c = 36.87^\circ$, the approximation of a circumscribed Drucker Prager criterion becomes poor and can result in an important overestimation of stresses compared to a classical Mohr Coulomb model. Thus, a more sophisticated yield criterion including the third stress invariant must be used. If $\phi_c > 36.87^\circ$, choice of the Drucker Prager criterion :

- may result in an elastic behaviour for some stress paths,
- and results always in an unbounded stress space ($\sigma_1, \sigma_2, \sigma_3 = \text{cst}$) which can induce infinitely high values of the stress deviator, at least from a theoretical point of view. Thus again, a more elaborated criterion must be used.

These conclusions are of course only valid if the choice of a Drucker Prager criterion circumscribed to the Mohr Coulomb one is made. One could argue that a better choice could be to fit the DP criterion in order to minimise the discrepancy between the 2 models (i.e. choosing either an inscribed or intermediate DP criterion). However, none of these choices is fully satisfactory as there will always be Lode angle values for which the approximation will be poor [SCHWEIGER, 1994]. For instance, considering the extension Drucker Prager cone would lead to a good fit with Mohr Coulomb for extension stress paths, but to an underestimation of stresses for compressive stress paths.

Therefore, as the stress path followed by any point of the solid is not known a priori, either a proper Mohr Coulomb or a smoothed version (e.g. Van Eekelen) must be used to guarantee a correct representation of the geomaterials behaviour.

5.3 Application case 1 : simulation of the stress state in an anticline structure

5.3.1 Initial model

The anticline structure studied here represents a potential oil trap. The model (see the cross section on figure 5.5) consists of 4 sub-horizontal layers. The total thickness of the model is 8 km and its length is 30 km. From the top, the second and third layer represent major rheological discontinuities as their friction angle is 20° and 36° respectively whereas friction angle is 30° in the cover and basement. The second layer could represent a shale layer and the third layer a sandstone one. No shear stresses are assumed on lateral and basal boundaries. The loading consists of a horizontal displacement u applied to the left lateral boundary. The initial stress field consists of vertical stresses σ_v given by equation (5.1) and of horizontal stresses σ_h defined with the ratio $K_0=0.8$ (see equation (2.156)).

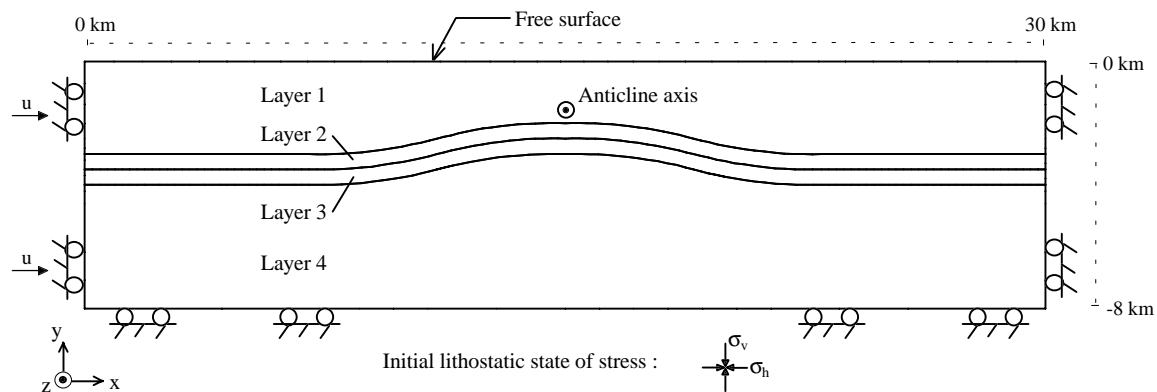


Figure 5.5 Geometry and boundary conditions of the anticline model.

Discretisation of this model consists of 1214 elements and 1263 nodes (see figure 5.6).

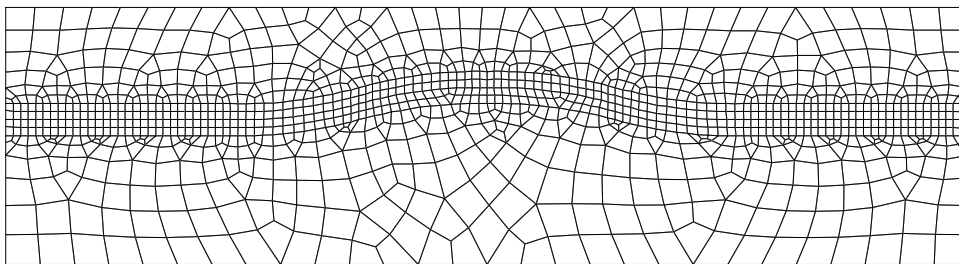


Figure 5.6 Mesh of the anticline model.

The stress field evaluation of such a structure might be important for instance regarding drilling operations. One can get an estimation of the present in situ stress field considering the last loading phase which in this simple case is represented by the horizontal displacement u , which is perpendicular to the anticline axis (out of plane in figure 5.5). Plane strain 2D simulations with non associated DP and VE criteria have been performed. The mechanical characteristics are reported in table 5.1. For each criterion, 2 values of dilatancy angle have been considered : in a first set of computations, dilatancy angles are nil, whereas in the second set dilatancy angles are equal to half the corresponding friction angles (see table 5.2).

Table 5.1 Physical parameters.

Layer	E (GPa)	ν	c (MPa)	ϕ_C (°)	ϕ_E DP (°)	ϕ_E VE (°)	ρ (kg/m ³)
1	10	0.25	2	30	48.6	30	2500
2	2	0.25	1	20	26.3	20	2500
3	20	0.25	2	36	75.1	36	2500
4	10	0.25	2	30	48.6	30	2500

Table 5.2 Dilatancy angle values.

Layer	Plasticity without dilatancy ψ (°)	Plasticity with dilatancy ψ (°)
1	0	15
2	0	10
3	0	18
4	0	15

5.3.2 Results

Results of these simulations will be analysed using vertical profiles at the centre of the structure, i.e. at $x=15000m$. Profiles of mobilised friction angles and stresses (vertical and horizontal) are presented for horizontal displacements $u=750m$ (2.5% global shortening) and $u=1500$ (5% global shortening). The influence of plastic dilatancy is also studied.

5.3.2.1 Coulomb's mobilised friction angle profiles

The Coulomb's mobilised friction angle represents the friction angle which is effectively mobilised in the Mohr plane (σ_n, τ) by any stress state (σ_1, σ_3). Graphically, it is given by the tangent line to the Mohr circle which also passes through the fixed origin point $a=c/\tan\phi$ (see figure 5.7). Then, the Coulomb's mobilised friction angle reads

$$\phi_m = \sin^{-1} \left(\frac{\frac{\sigma_1 - \sigma_3}{2}}{\frac{\sigma_1 + \sigma_3}{2} + \frac{c}{\tan \phi}} \right) \quad (5.4)$$

The mobilised friction angle profiles are displayed on figure 5.8 for the computations without dilatancy. For VE criterion, ϕ_m is stable (as the plasticity is reached) down to $-3500m$ depth for the 2 loading steps considered. Below this depth, this plasticity is not reached at $u=750m$ but is reached at $u=1500m$. For DP criterion, ϕ_m is no longer stable between the 2 steps, it increases rather unrealistically ($\phi_m \approx 50^\circ$ in the sandstone layer for which the prescribed friction angle is 36°) even when the plasticity is reached (see the 2 upper layers). These high values of mobilised friction angle, which range between ϕ_C and ϕ_E (see figure 5.8), are entirely induced by the DP plastic criterion.

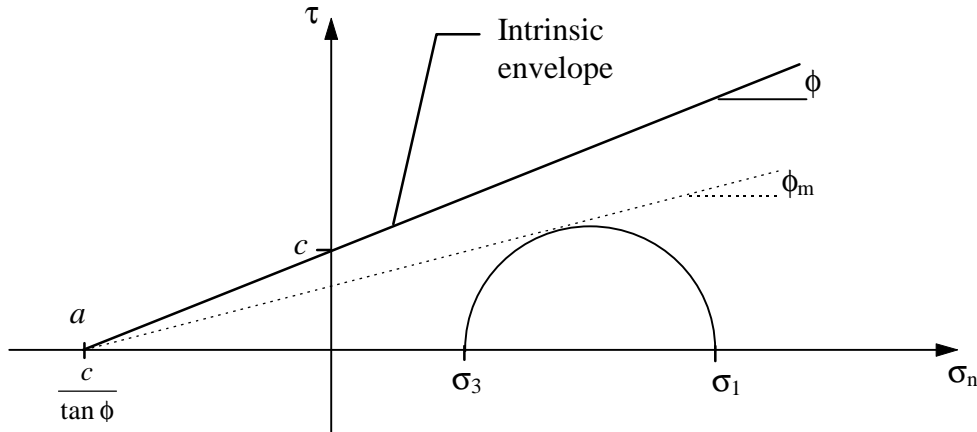


Figure 5.7 Graphical interpretation of the mobilised friction angle ϕ_m in the Mohr plane.

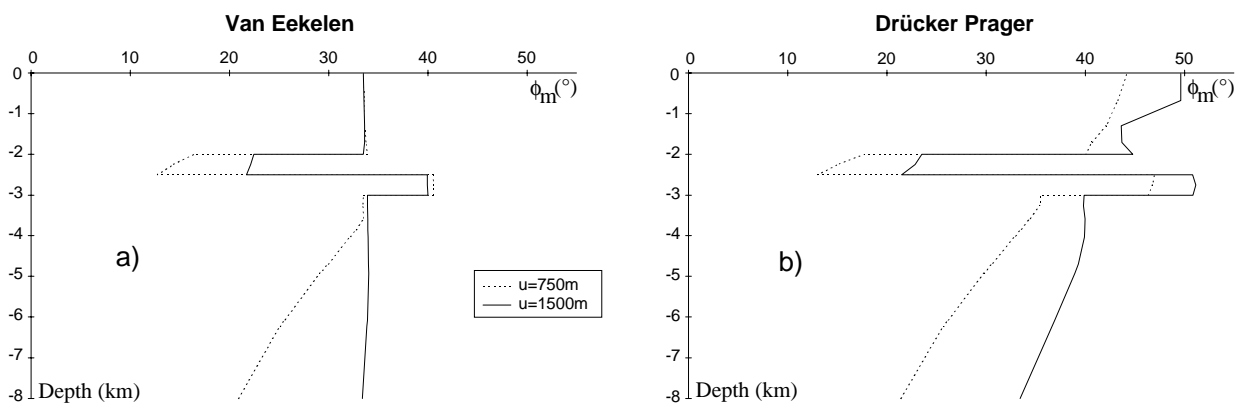


Figure 5.8 Plasticity without dilatancy - Mobilised friction angle profiles (in $^{\circ}$) at $x=15000m$ versus depth, for 2 values of loading.

5.3.2.2 Stress profiles

At the initial state, stress profiles are given by equations (5.1) and (5.4). The vertical stress coincides with the maximum principal stress σ_1 and the other two principal stresses are equal and horizontal (see figure 5.9). In figures 5.10a-b-c-d, the profile of vertical stress $\sigma_v = \sigma_y$ is represented with dotted lines : it remains approximately constant throughout the simulation as it results from the lithostatic weight and therefore is not dependant on the plastic criterion.

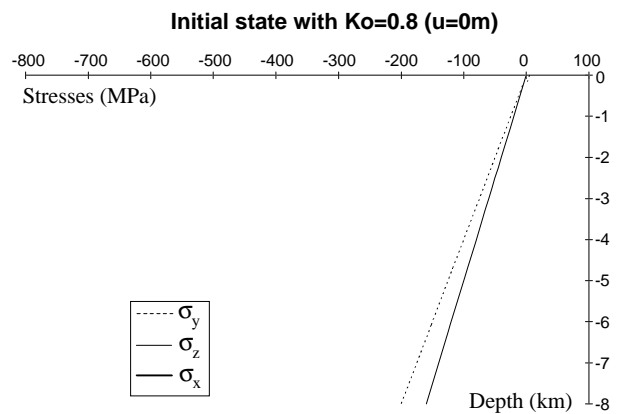


Figure 5.9 Initial stress profiles (in Pa) at $x=15000m$.

Let us define the concept of stress saturation as the tendency of stress variation in response to a monotonic loading increment : an important stress variation traduces a low stress saturation whereas a small stress variation traduces a high stress saturation. Obviously the stress saturation is directly linked with the shape of the criterion and the friction angle value as it results from the existence of upper bound in the stress space (see figures 5.2 and 5.3).

For VE criterion, the stress profiles in the upper 3 layers (i.e. for depth down to -3500m) are pretty much similar regardless of the loading value (see figures 5.10a-c). It underlines the high stress saturation at the loading value $u=750\text{m}$ of this model for the considered depth. However, in deeper layers (-3500 to -8000m), this is no longer the case as the σ_x and σ_z stresses increase between $u=750$ and $u=1500\text{m}$.

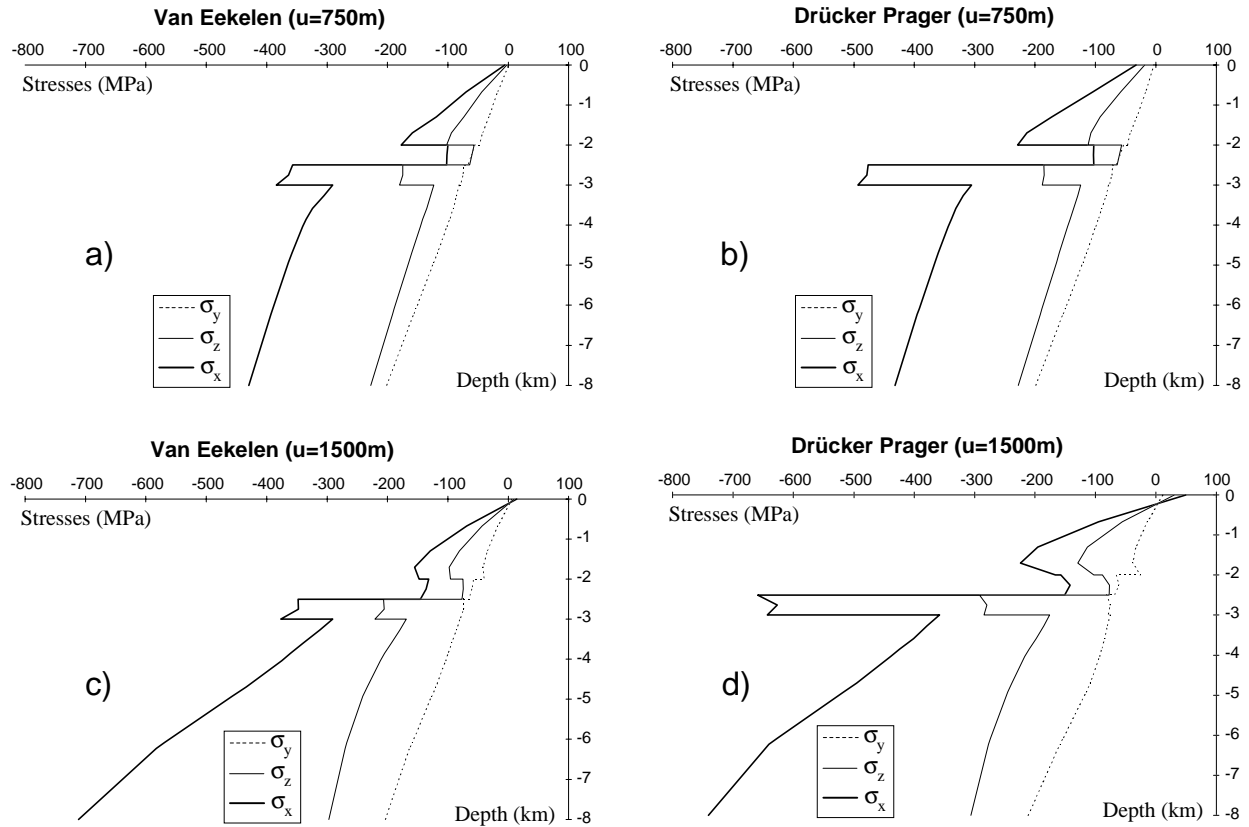


Figure 5.10 Plasticity without dilatancy - Stress profiles (in Pa) at $x=15000\text{m}$: a) $u=750\text{m}$ with VE, b) $u=750\text{m}$ with DP, c) $u=1500\text{m}$ with VE, d) $u=1500\text{m}$ with DP.

For DP criterion, the stress saturation is much lower than for VE one, especially in the third layer with high friction angle : there is a 200MPa stress jump between $u=750$ and 1500m whereas none exists with the VE criterion for this layer.

5.3.2.3 Dilatancy influence

The influence of plastic dilatancy has been investigated in a second set of computation considering the dilatancy angles reported in table 5.2.

Results are presented on figures 5.11a-b-c-d. Qualitatively, the same remarks than for the computation without dilatancy can be made. On a quantitative point of view, it must be noticed that the stress increase for the dilatant DP model is even larger here (from 500 to 800MPa, see figures 5.11b-d) compared with the non-dilatant one (from 500 to 650MPa, see figures 5.10b-d).

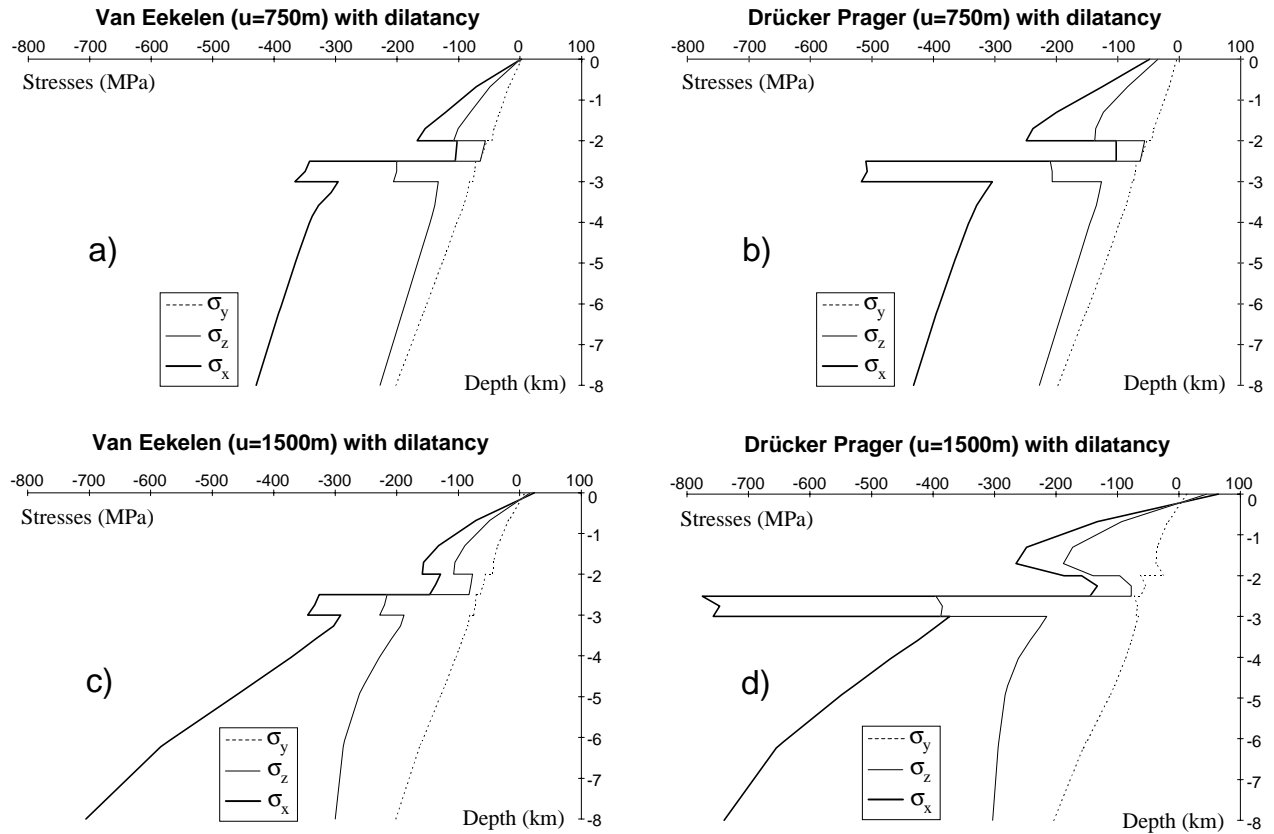


Figure 5.11 Plasticity with dilatancy - Stress profiles (in Pa) at $x=15000\text{m}$: a) $u=750\text{m}$ with VE, b) $u=750\text{m}$ with DP, c) $u=1500\text{m}$ with VE, d) $u=1500\text{m}$ with DP.

5.3.2.4 Stress overestimation

The overestimation of σ_x obtained using DP criterion with respect to stresses obtained using VE criterion is presented on figure 5.12a-b.

According to relation (2.79), no σ_x overestimation appears in the "weak" layer, i.e. the second layer (with a friction angle of 20°).

Considering the non-dilatant computation, the stress overestimation of the σ_x component is approximately equal to 50MPa in the upper and bottom layer and approximately equal to 300MPa in the third layer (with friction angle of 36°).

Considering the dilatant computation, the stress overestimation of the σ_x component is approximately equal to 100MPa in the upper and bottom layer, and approximately equal to 450MPa in the third layer.

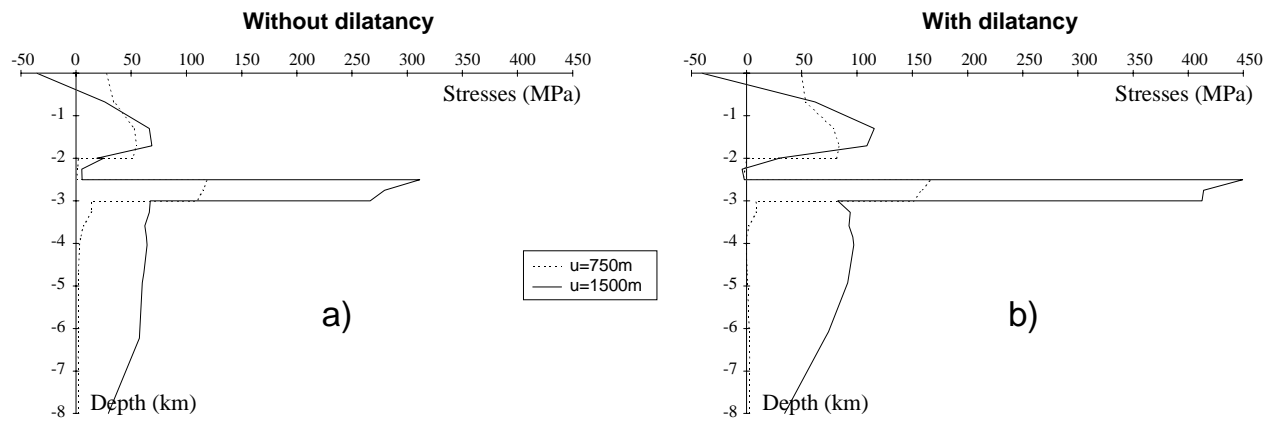


Figure 5.12 σ_x overestimation (in Pa) induced by DP criterion.

5.4 Application case 2 : modelling with frictional interfaces

As it has been mentioned in chapter 2 and illustrated in the previous section, the shape of the limit surface in the deviatoric plane plays an important role on the Coulomb's mobilised friction angle ϕ_m within the solid. If a part of the solid boundary is in frictional contact with another solid (rigid or deformable), it also has an influence on the behaviour of the solid+interface model.

For this purpose, consider a rigid body in perfect contact on an horizontal plane. Assuming that the contact surface is planar, the Coulomb definition of frictional contact gives a relation between the contact pressure p and the tangential stress τ following the relation (2.70)

$$\tau = c + \mu p \quad (5.5)$$

Consider now that the solid is not perfectly rigid and exhibits a frictional behaviour. In such case, there is generally a competition between the frictional resistance within the solid and on the contact interface. On the one hand, the contact frictional resistance results from the friction coefficient μ of the Coulomb law. On the other hand, the solid frictional resistance comes from the friction angle ϕ of the solid constitutive relation, and also from the shape of the yield surface in the deviatoric plane as detailed in chapter 2. Therefore, the representation of the solid frictional behaviour will play a non-negligible role on the solid/contact interaction. This is illustrated on the example presented below.

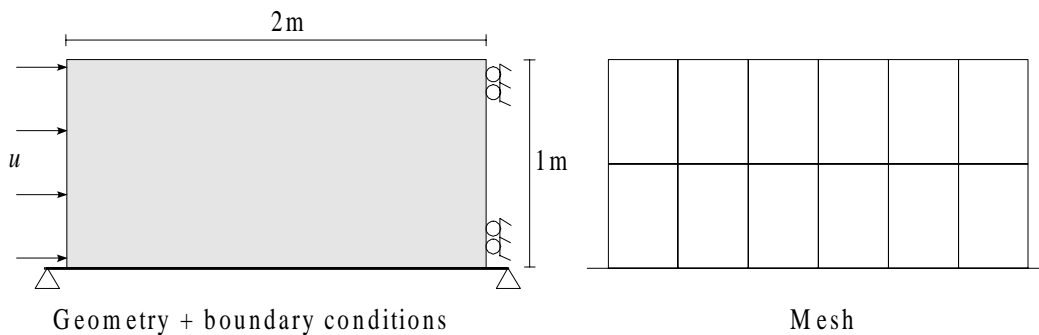


Figure 5.13 Geometry, boundary conditions and mesh of the contact test model.

A solid is considered to rest on an horizontal rigid plate with boundary conditions as mentioned on figure 5.13. The contact between the plate and the solid is frictional, with a friction coefficient μ equal to 0.7 (corresponding to a friction angle of 35°). The loading consists of gravity forces and of an applied displacement on the left side of the solid. An elastoplastic behaviour is chosen for the solid, with an internal friction angle equal to 35° . In a first model, this frictional behaviour is represented using the Drucker-Prager (DP) yield criterion, i.e. for which $\phi_C = \phi = 35^\circ$. The corresponding friction angle for extension paths ϕ_E can be deduced from equation (2.79) which here gives $\phi_E \approx 68^\circ$. In a second model, the frictional behaviour is represented using the Van Eekelen (VE) yield criterion, i.e. for which $\phi_C = \phi_E = \phi = 35^\circ$. Results are presented for these two models on figure 5.14 for a given loading value.

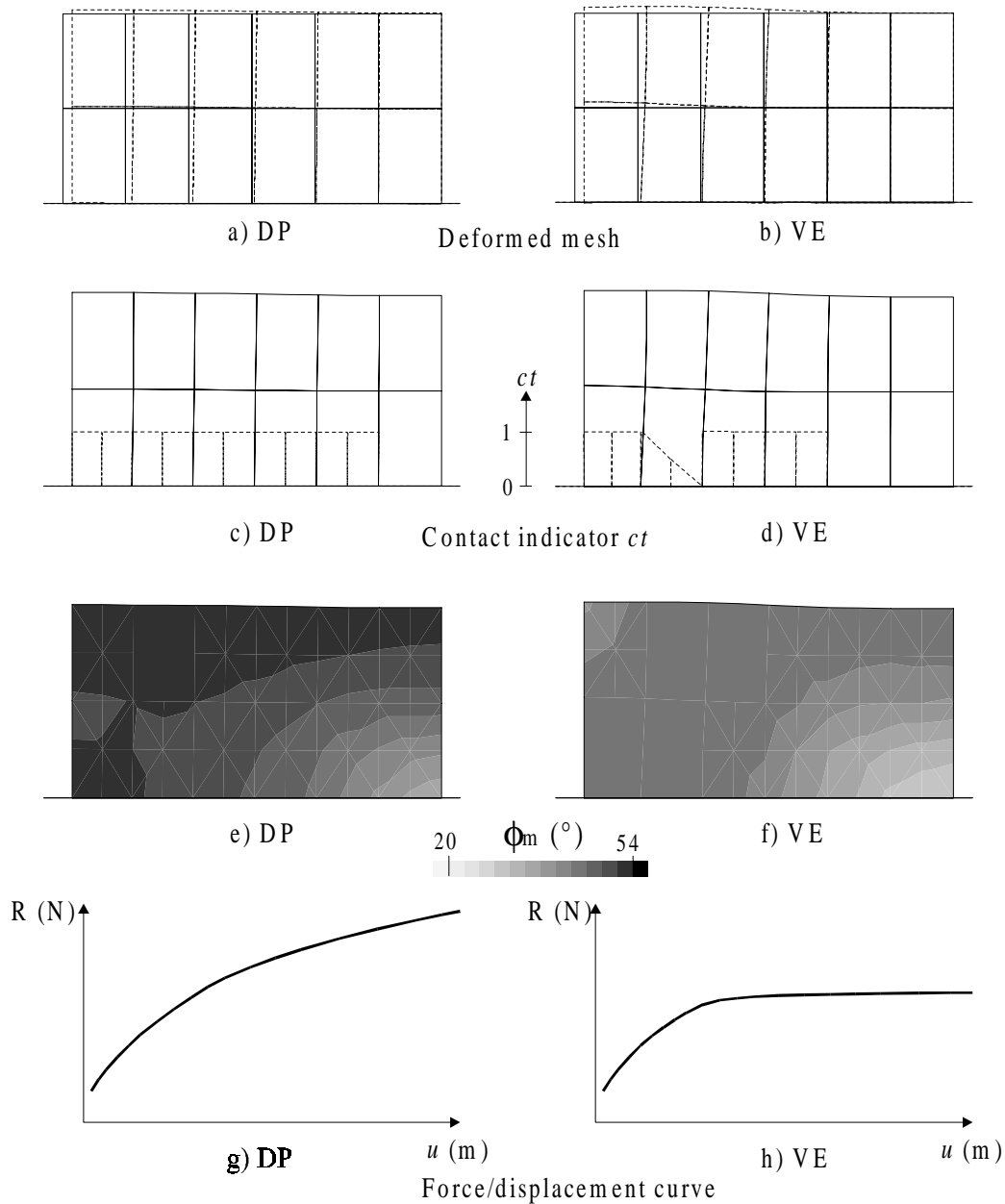


Figure 5.14 Results of the contact test model.

The sliding along the interface is more important in the DP model than in the VE one, as attested by the deformed meshes shown on figures 5.14a,b and by the contact indicator ct ($ct=0$: no sliding, $ct=1$: sliding) shown on figures 5.14c,d. It seems that the contact is less resistant in the DP than in the VE model. Obviously, it is not the case as μ is the same for both models. Actually, the difference comes from the larger resistance (almost multiplied by 2 at the ultimate loading value) of the elastoplastic solid in the DP model compared to the VE one (see the force/displacement diagram on figures 5.14g,h). This larger resistance of the DP model comes entirely from the inaccurate approximation of the frictional behaviour which leads to unrealistic values of Coulomb's mobilised friction angles ϕ_m within the solid (see figures 5.14e,f) : ϕ_m reaches a maximum value 53° in the DP model compared to 39° in the VE model.

5.5 Conclusion

In geomechanical simulations, the general three-dimensional yield criteria reduce approximately to two-dimensional ones considering that, at any point, the vertical stress component remains almost constant.

When the main disadvantage (no influence of the third stress invariant) of the Drucker Prager criterion is particularised to the case of geomechanical simulations including gravity forces, it results in a unbounded admissible stress space for friction angles higher than 36.87° whereas the stress space remains bounded for Mohr Coulomb and Van Eekelen criteria. As a consequence, it can result in an overestimated stress field when the Drucker Prager criterion is used.

Computations of an anticline structure presented as the first application case showed that this stress overestimation can reach 300MPa at 3000m depth for isochoric plasticity. Considering plastic dilatancy, the stress overestimation can even get larger in the studied example (450MPa at 3000m depth).

In the second application case, the choice of the yield criterion is also shown to have a drastic influence when frictional solid and interface coexist. In such case, the choice of a Drucker-Prager yield criterion leads to an overestimation of the solid resistance with respect to the contact one, that is the frictional interface seems less resistant than it really is.

Therefore it can be concluded that, in order to obtain reliable stress magnitude when average to high friction angles are used (i.e. greater than approximately 20°), a criterion which includes the third stress invariant must necessarily be used (e.g. Mohr Coulomb, Van Eekelen or any similar criterion). This is especially true for geomechanical simulations in which σ_v is the minor principal stress (i.e. in compressive tectonic context) and/or when frictional contact is involved.

CHAPTER 6

Simulation of forward thrust propagation in sandbox experiments

6.1 Introduction

Thrust tectonics usually occurs in areas where the global tectonic stress regime is compressive, i.e. the maximum principal stress is horizontally oriented. On a geological point of view, it corresponds to particular locations with respect to plate tectonics where mountain belts have formed. It is often locations which are of interest on a petroleum point of view, which explains the interest manifested by oil companies to understand such complex geological context. In order to reproduce the complexity of tectonic compression areas, geologists have been using for long time experimental models in which analogue materials are used.

In the first part of this chapter, some results obtained from physical experiments carried out on models based on sand material are briefly presented.

In the second part, the initial geometry, boundary conditions and loading of the experimental model are used as a basis to build the corresponding numerical models. Particularly, the influence of the basal friction on the kinematical evolution of the model is investigated. Results are analysed through the evolution of the stress, the deviatoric strain and the displacement fields, and also through the evolution of faulting indicators (Rice bifurcation criterion, Wallace-Bott stress shape ratio, kinematic indicator α).

Eventually, a comparison between the numerical and experimental results is presented in the last part of this chapter. It allows, by inverse analysis, to obtain the real basal friction value in the studied experiment.

6.2 Simulation of thrusting in sandbox experiments

In order to investigate the structures genesis in complex cases, geologists have been using for a long time physical experiments. Using physics similarity principles [HUBBERT, 1937], it is possible to represent at the laboratory scale processes which occur at much larger scales. Laboratory experiments using sand material as an earth crust analogue, referred to as sandbox models, have been performed for quite a long time. Such physical modelling gives access to the displacement field using either destructive methods (usually a set of cross-sections) or non-destructive ones (e.g. X-ray tomography, [COLLETTA et al., 1991]).

Sandbox modelling often gives very realistic geological structures, which is very helpful for the structural interpretation of seismic profiles in the petroleum industry. Rather complex three-dimensional geometries and boundary conditions can be investigated, which represents a very important advantage of this method. However, disadvantages of the method come from the lack of information on the stress field, from the quite limited range of material behaviour which can be investigated, and from the approximate control on the boundary conditions. Also, it is very difficult to perform experiments with interstitial fluid within the sand pores, i.e. the hydromechanical coupling effects cannot be taken into account easily.

In this chapter, the sandbox simulation of thrust propagation under tectonic compression carried out at Institut Français du Pétrole by [COLLETTA et al., 1991] is chosen as a reference case. In these experiments, the use of X-ray tomography allowed to analyse the displacement field in a quasi-continuous way throughout the tectonic loading. The studied model consists of a sand layer ($\approx 28\text{cm}$ length, 1.4cm thick) resting on a fixed rigid platen. Between the sand layer and the rigid platen, a thin layer of glass microbeads was introduced to reduce the basal friction angle to approximately 20° [SASSI et al., 1993]. Shortening is then applied at the left boundary. The tomographic images obtained are presented on figure 6.1 at four displacement (noted u) values $u=0\text{cm}$, $u\approx 3.5\text{cm}$, $u\approx 4.0\text{cm}$ and $u\approx 6.5\text{cm}$, respectively.

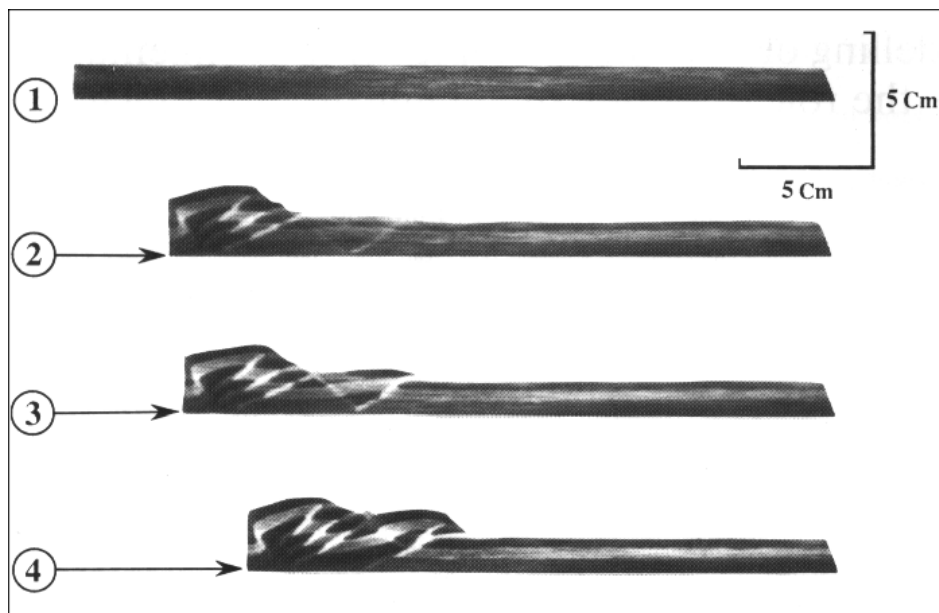


Figure 6.1 Thrust propagation experiments analysed by tomographic images, modified after [SASSI et al., 1993] at $u=0\text{cm}$ (1), $u\approx 3.5\text{cm}$ (2), $u\approx 4.0\text{cm}$ (3) and $u\approx 6.5\text{cm}$ (4).

6.3 Finite element simulation of thrusting propagation

In this section, the finite element modelling of the previously presented analogue experiment is presented. Particularly, the influence of the basal friction coefficient is investigated. Early part of this work has been published in [BARNICHON and CHARLIER, 1996]. A previous study of the similar problem has been presented by [DESEGAULX et al., 1991] using the commercial finite element code *GEOSIM2D* with re-meshing techniques and the classical Drücker-Prager criterion. Here the more realistic Van Eekelen criterion described in chapter 2 is used, coupled with the automatic re-meshing algorithm presented in chapter 4.

6.3.1 Initial geometry, boundary conditions and rheological parameters

The initial model is based on the sandbox experiments presented in [COLLETTA et al., 1991] and in [SASSI et al., 1993], which results are given on figure 6.1. It consists of a 1.4cm thick sand layer resting on a horizontal rigid platen (see figure 6.2). The model length has been reduced in the numerical model (in order to limit the element numbers) to 20cm. Its thickness is equal to 1.4cm. The right hand side of the model is horizontally constrained. In the physical experiment, the thin layer of glass microbeads acts as a de-coupling layer. It is represented in the numerical model by a sliding interface between the bottom sand layer and the horizontal rigid platen (noted HP) which is fixed in both directions. The loading consists of gravitational body forces and of an applied horizontal displacement u imposed to a rigid platen (noted LP) on the left hand side of the model. Contact between the left platen and the sand is frictional.

From the experimental results presented on figure 6.1, it is expected that several zones of shear strain localisation should develop within the sand layer. Such process will require to frequently perform re-meshing of the sand domain in order to avoid a too large distortion of the FE mesh. To this purpose, the re-meshing algorithm presented in chapter 4 has been used, the re-meshing decision being based in this case either on convergence difficulties or on user's estimation of the mesh distortion. In all the cases, the CPU time spent on re-meshing was negligible compared to the global CPU time required for the system resolution (less than few percents). In order to follow displacements throughout re-meshing procedures, four artificial passive markers (initially horizontal) have been introduced in the mesh (see chapter 4 for details about the procedure), as shown on figure 6.4.

Two sets of simulation have been performed. In both sets, the sand behaviour is represented by the frictional elastoplastic Van Eekelen criterion described in chapter 2, see equations (2.96) to (2.101) and implemented in the *PLASOL* law. The classical Drücker Prager yield surface has not been considered here as it has already been shown that it could lead to stress overestimation and wrong prediction of the Wallace-Bott stress shape ratio [BARNICHON and CHARLIER, 1996]. Perfect plasticity is assumed, i.e. there is no hardening and/or softening. Note that plastic dilatancy is introduced through the dilatancy angle which is chosen equal to 10° . The contact behaviour is represented by the Coulomb friction law (*COU2DC* law) described in section 2.4.2.1, with penalty coefficients $K_p=1.10^7\text{Pa}$ and $K_\tau=5.10^6\text{Pa}$ (for significance of these penalty coefficients, see equation (2.147)). No contact cohesion is considered, and two different friction values are considered for the contact between the horizontal platen and the sand, i.e. two set of simulations will be performed. The

difference between the 2 sets of simulations comes from the contact friction of the HP/sand interface : it is equal to 0.466 (corresponding to $\phi=25^\circ$) in the first model and to 0.268 (corresponding to $\phi=15^\circ$) in the second model, thus providing an upper and lower bound of the estimated value of 20° . Differences between these two models will allow to investigate the effect of basal friction on the kinematical evolution of the model. All the mechanical parameters used in the simulations are reported in Table 1. An initial stress state is introduced in the model according to equations (2.155) and (2.156) using a K_0 value of 0.8.

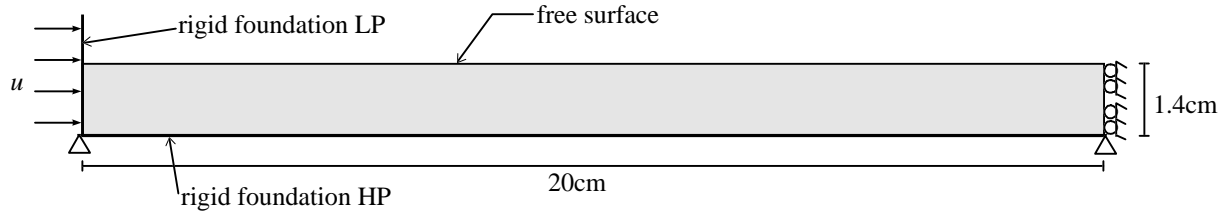


Figure 6.2 Initial geometry and boundary conditions of the thrust model.

The model is discretised by 1350 nodes and 393 quadrilaterals with 8 nodes and 4 integration points (reduced integration), see figure 6.3.

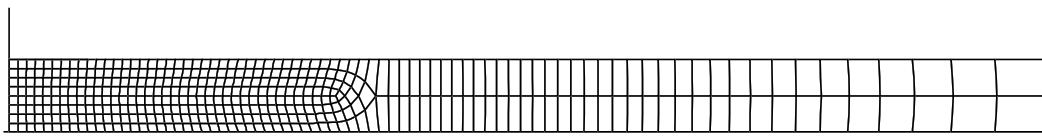


Figure 6.3 Initial mesh of the thrust model (1350 nodes, 393 quadrilaterals with 8 nodes).

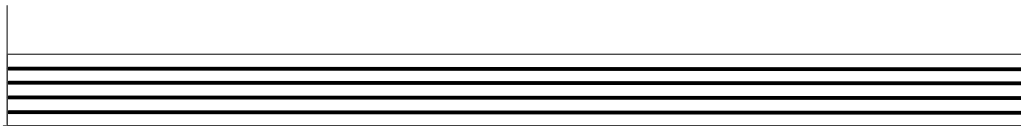


Figure 6.4 Initial passive markers in the thrust model.

Table 6.1 Physical parameters of the thrust model

	Density	E (kPa)	ν	c (Pa)	ϕ ($^\circ$)	ψ ($^\circ$)	μ
Sand	2.2	50	0.20	20	35	10	
LP/sand contact				0	25	0	0.466
HP/sand contact							
model 1				0	25	0	0.466
model 2				0	15	0	0.268

6.3.2 Model 1

This model corresponds to a high basal friction angle of 25° ($\mu=0.466$).

In order to perform this simulation for displacement values ranging from $u=0$ to $u=5.81$ cm, nine re-meshing phases were required. The transfer method presented in section 4.3.5.2 has been used and in this case it led to a smaller disequilibrium compared with the $1/r^p$ method (for which it was sometimes not even possible to re-equilibrate the model just after re-meshing). Results are analysed in terms of in-plane principal stress directions (isostatic lines), Coulomb's mobilised friction angle ϕ_m , Wallace-Bott stress shape ratio R , Rice bifurcation criterion, equivalent strain ϵ_{eq} , kinematic indicator of localisation α , local equivalent strain $\epsilon_{eq(l)}$ (it is the equivalent strain computed using a reference configuration different from the initial one) and passive markers deformation. Results are presented on figures 6.5 to 6.10 for displacements values $u=0.3$ cm, $u=1.5$ cm, $u=2.45$ cm, $u=3.36$ cm, $u=4.5$ cm, and $u=5.81$ cm, respectively, which allows to visualise the evolution of the studied parameters.

At a first stage ($u=0.3$ cm), see figure 6.5, strain localisation occurs in the left part of the model close to the imposed displacement condition. It consists of a set of 2 conjugate reverse shear bands which then delimits a pop-up like structure (see figure 6.5d,e,f,g), corresponding to zones where plasticity is reached (see figure 6.5b). Everywhere but in the shear bands where fault activity is concentrated, there is virtually no strain at all (see deformed passive markers on figure 6.5h). The stress state is in compressional regime in the left part of the model, whereas it remains in extension regime on the right part as attested by figures 6.5a,c (see the principal stress permutation attested by isostatic lines). Such effect results entirely from the basal friction which limits the effect of compression towards the right of the model.

At a second stage ($u=1.5$ cm), see figure 6.6, localisation carried on in a similar fashion than at first stage, inducing a thickening of the pop-up block. Actually, the backward reverse fault is similar than at the first stage but the active forward fault has now moved in the foreland which explains the apparent thickening of this fault. This is clearly attested by looking at Rice direction of bifurcation, α indicator and $\epsilon_{eq(l)}$ which all coincide together on the one hand, and which do not coincide with the total ϵ_{eq} on the other hand. It traduces a forward migration of the forward thrust fault, which results from the thickening of the pop-up. Note that an extension tectonic regime is obtained at the top part of the pop-up as attested by the isostatic lines (principal stress rotation and permutation close to the surface) and by the R ratio.

At a third stage ($u=2.45$), another reverse fault has propagated in the foreland area (see figures 6.7d,e,f,g,h). There is still a tectonic extension zone in the top part of the uplifted zone (figures 6.7a,c).

At a fourth stage ($u=3.36$ cm), see figure 6.8, the pop-up thickening has continued, and a third forward reverse fault has formed. However, the main difference now comes from a completely new pop-up structure which has started to initiate in front of the uplifted wedge. It has started to initiate at the free surface from the point where the first pop-up ended. In other words, it has been reflected onto the free surface (figures 6.8d,e,f,g,h).

At a fifth stage ($u=4.5$ cm), the fault activity is mainly related to the second pop-up development (figures 6.9d,g), which offsets a secondary pop-up structure located between the

2 main ones. An extension tectonic regime develops at the top of the second pop-up (figure 6.9c) whereas most of the model is now in compression regime (figure 6.9a).

At a final stage ($u=5.81\text{cm}$), the forward thrust fault of the second main pop-up has migrated in the foreland, in a similar way than the first pop-up did between stages 1 and 3 (figures 6.10f,g). Note that here there may be some fault activity in the left part of the model as attested by Rice criterion (figure 6.10d). This is interpreted by the effect of the right vertical boundary which now perturbs significantly the stress state by inhibiting horizontal displacements. The whole part of the model is now in tectonic compression regime (except small areas near the pop-up top surface) as shown on figure 6.10c.

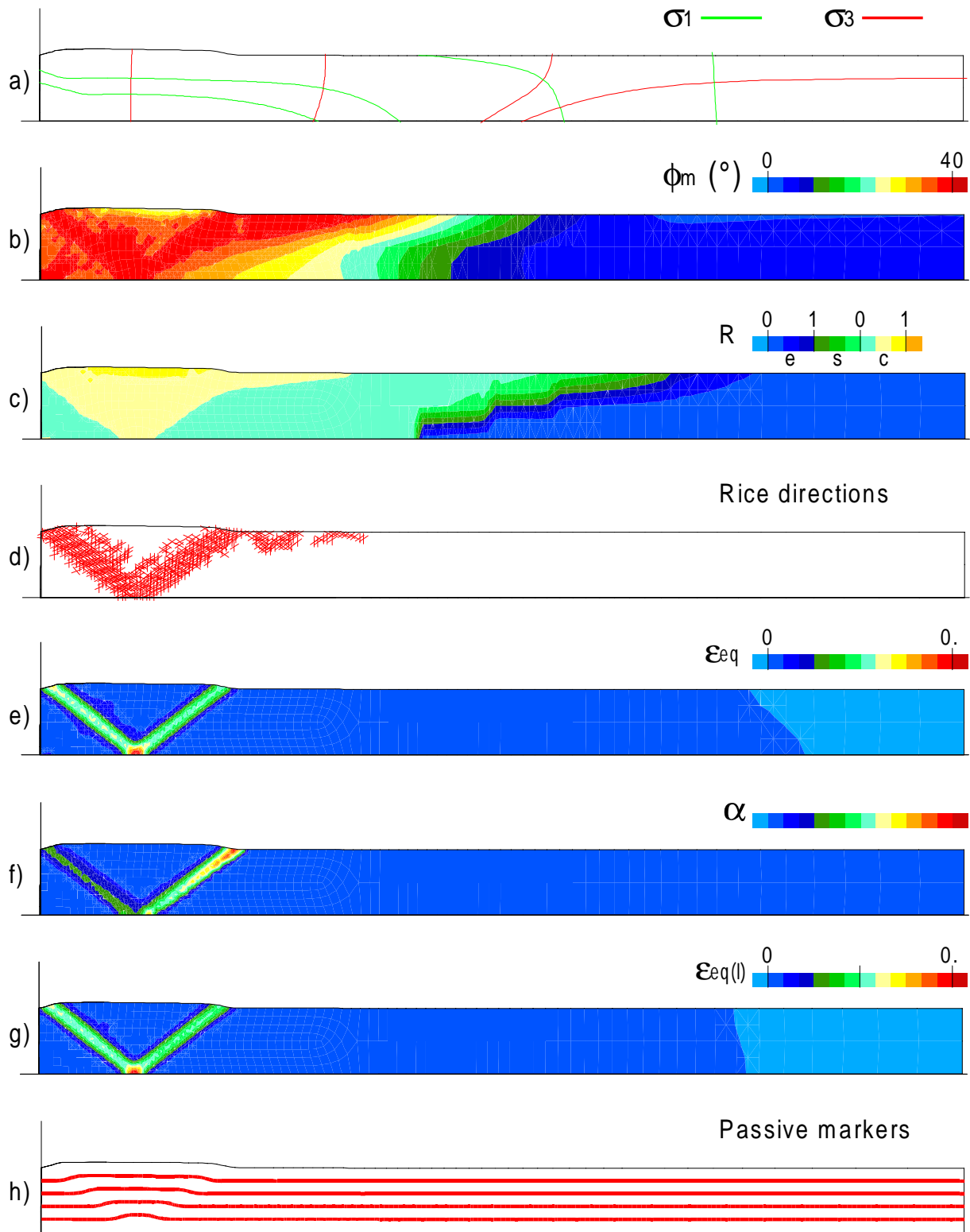


Figure 6.5 Thrust model 1 ($\mu=0.466$) at $u=0.30\text{cm}$: a) principal stress isostatic lines, b) Coulomb's mobilised friction angle, c) Wallace-Bott shape ratio, d) Rice directions of bifurcation, e) equivalent strain, f) kinematic indicator of localisation, g) local equivalent strain, h) deformed passive markers.

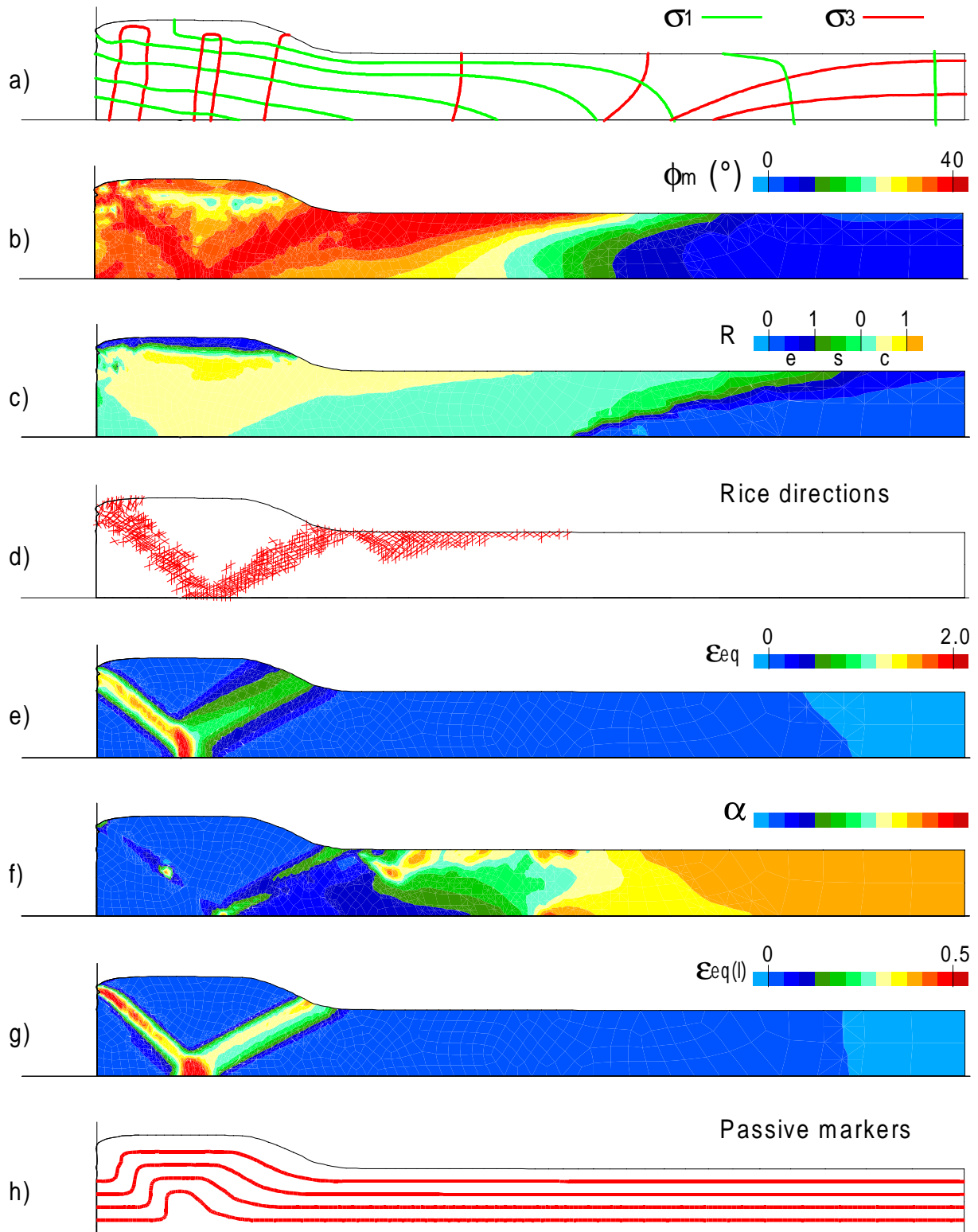


Figure 6.6 Thrust model 1 ($\mu=0.466$) at $u=1.5\text{cm}$: a) principal stress isostatic lines, b) Coulomb's mobilised friction angle, c) Wallace-Bott shape ratio, d) Rice directions of bifurcation, e) equivalent strain, f) kinematic indicator of localisation, g) local equivalent strain, h) deformed passive markers.

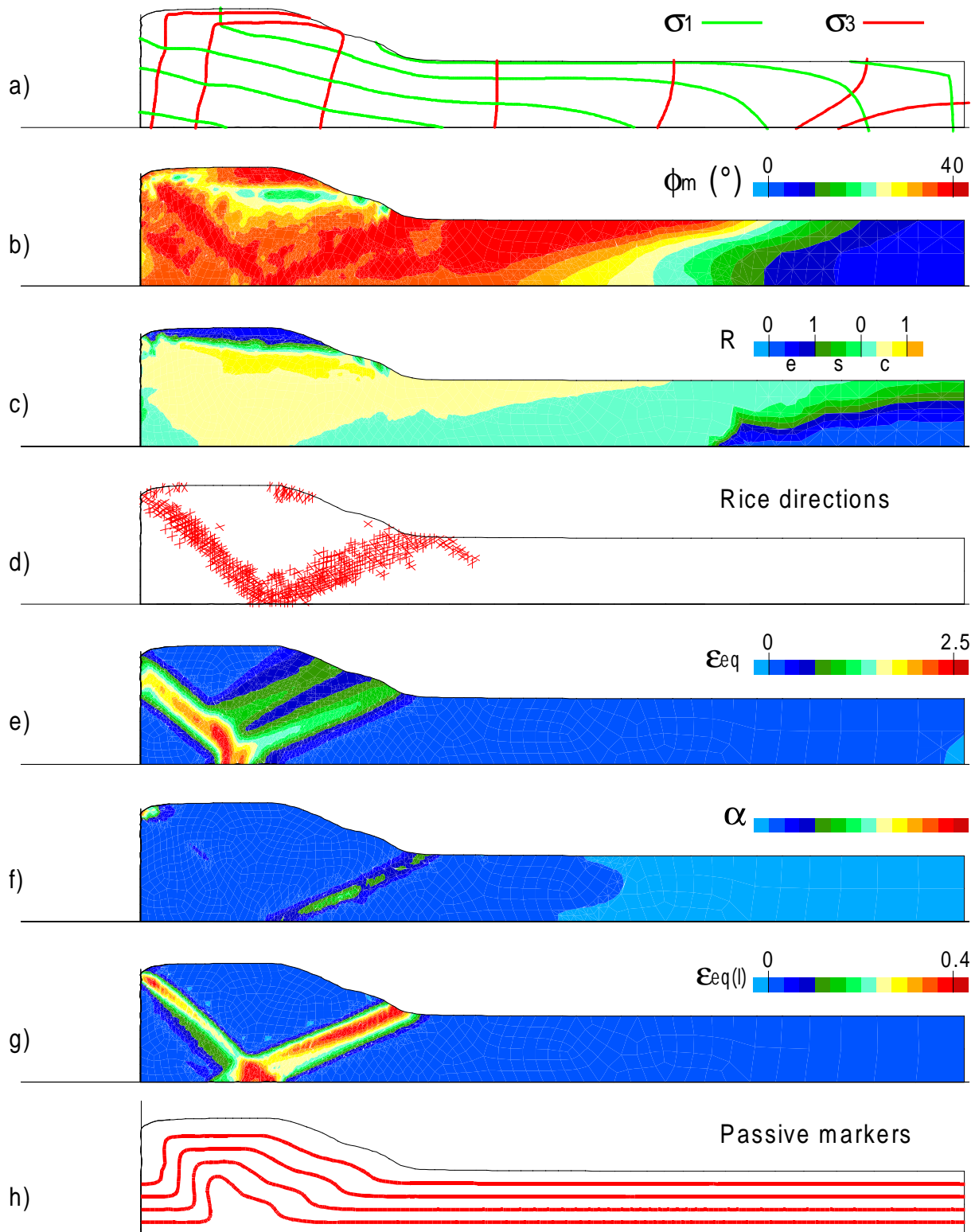


Figure 6.7 Thrust model 1 ($\mu=0.466$) at $u=2.45\text{cm}$: a) principal stress isostatic lines, b) Coulomb's mobilised friction angle, c) Wallace-Bott shape ratio, d) Rice directions of bifurcation, e) equivalent strain, f) kinematic indicator of localisation, g) local equivalent strain, h) deformed passive markers.

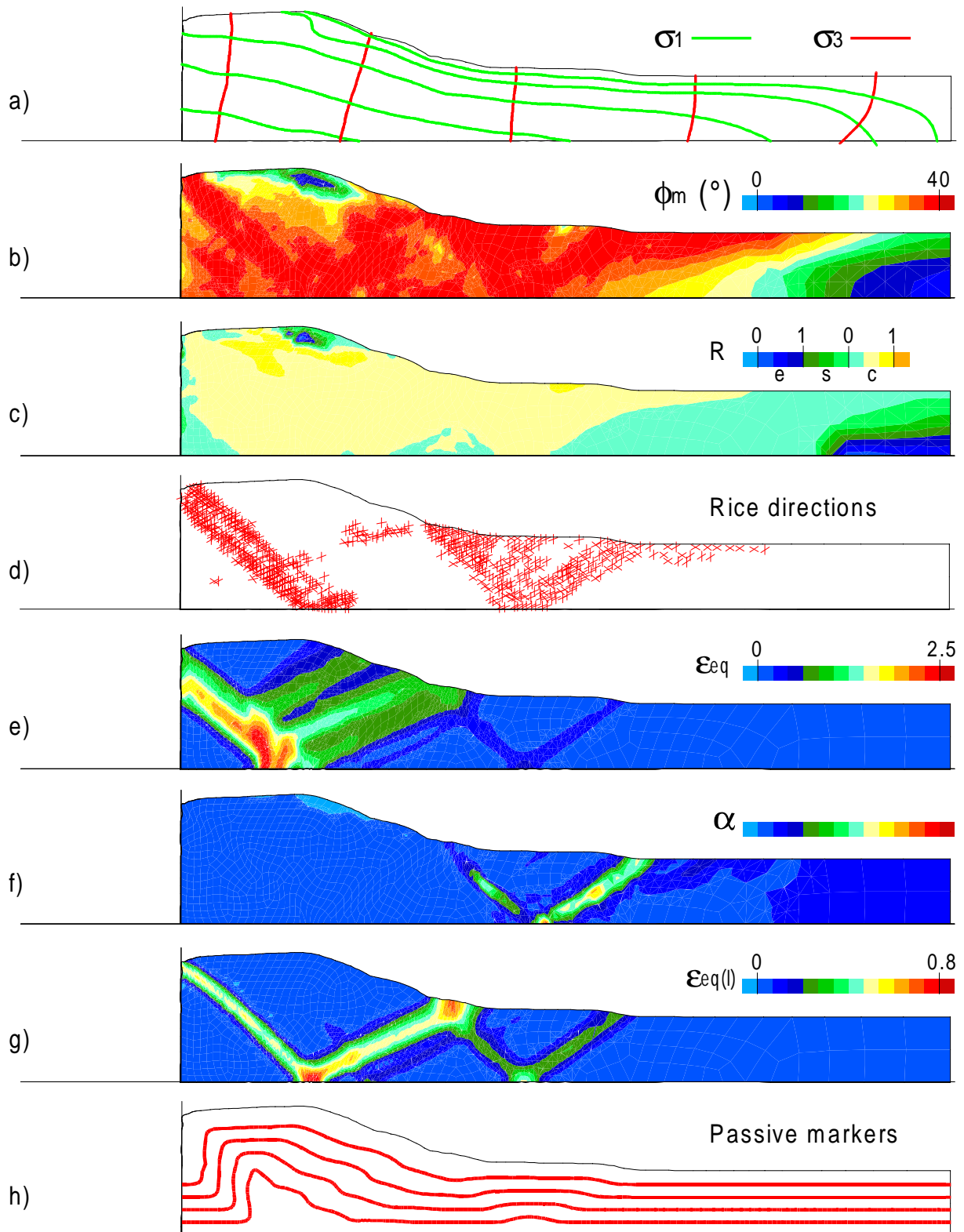


Figure 6.8 Thrust model 1 ($\mu=0.466$) at $u=3.36\text{cm}$: a) principal stress isostatic lines, b) Coulomb's mobilised friction angle, c) Wallace-Bott shape ratio, d) Rice directions of bifurcation, e) equivalent strain, f) kinematic indicator of localisation, g) local equivalent strain, h) deformed passive markers.

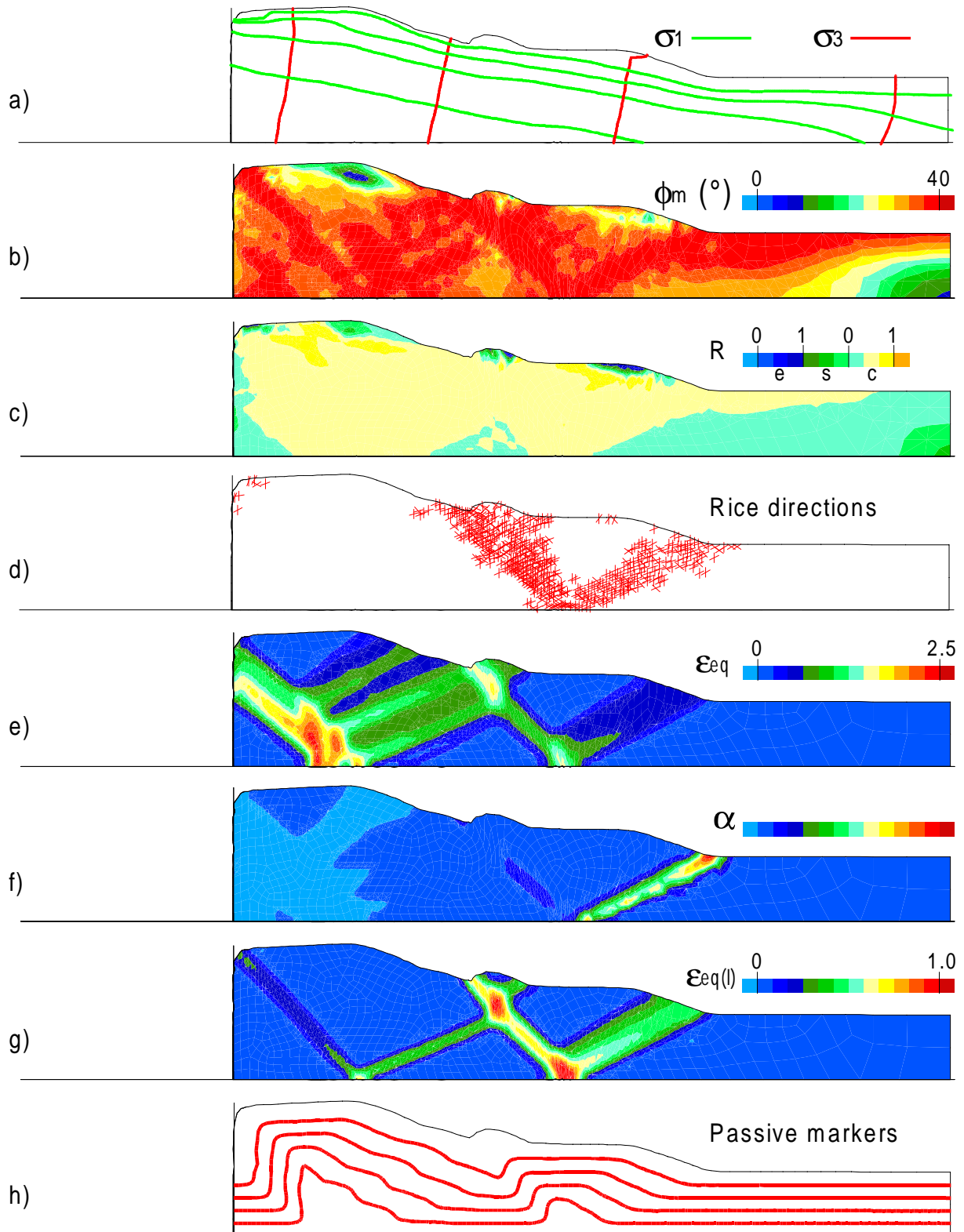


Figure 6.9 Thrust model 1 ($\mu=0.466$) at $u=4.5\text{cm}$: a) principal stress isostatic lines, b) Coulomb's mobilised friction angle, c) Wallace-Bott shape ratio, d) Rice directions of bifurcation, e) equivalent strain, f) kinematic indicator of localisation, g) local equivalent strain, h) deformed passive markers.

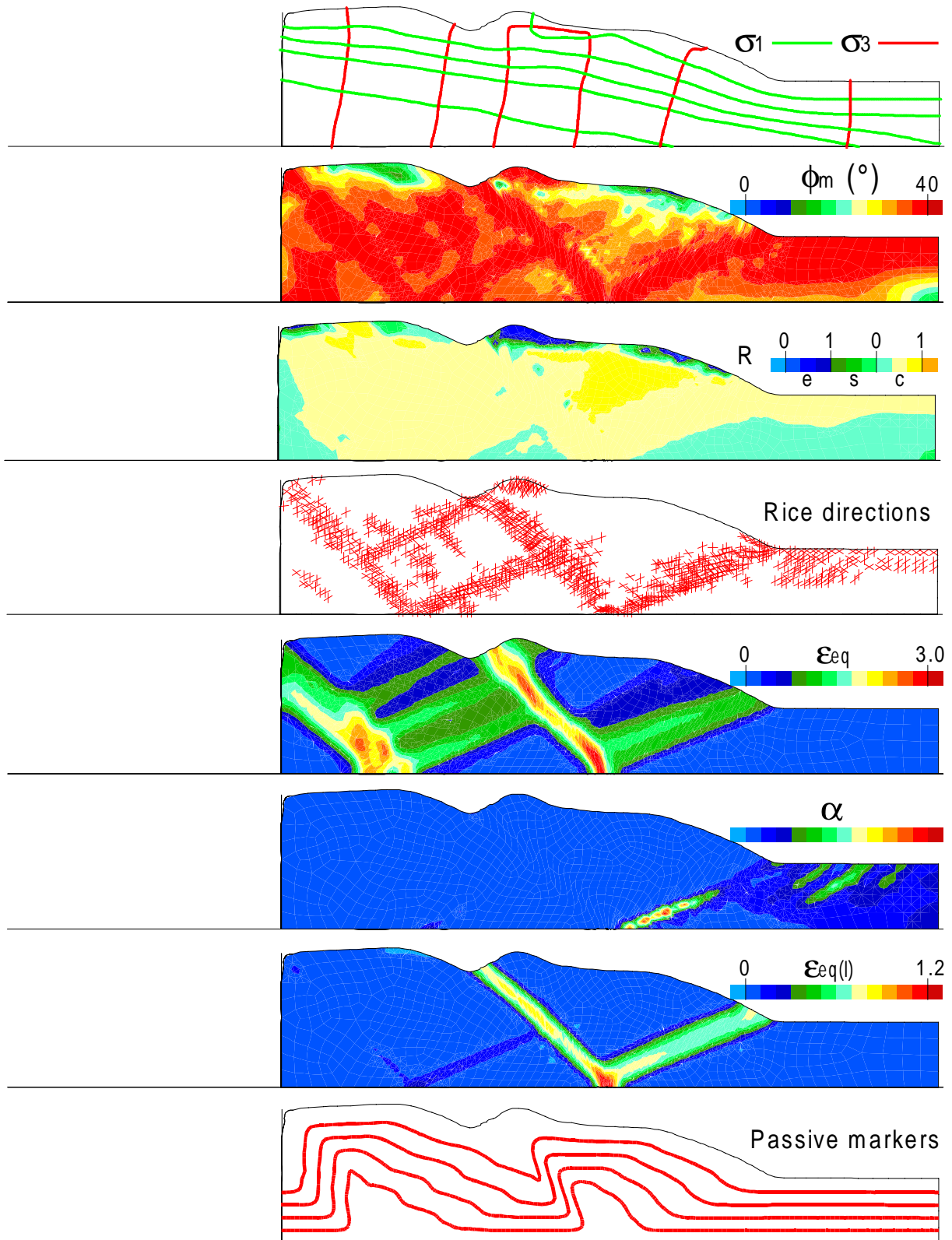


Figure 6.10 Thrust model 1 ($\mu=0.466$) at $u=5.81\text{cm}$: a) principal stress isostatic lines, b) Coulomb's mobilised friction angle, c) Wallace-Bott shape ratio, d) Rice directions of bifurcation, e) equivalent strain, f) kinematic indicator of localisation, g) local equivalent strain, h) deformed passive markers.

6.3.3 Model 2

This model corresponds to a low basal friction angle of 15° ($\mu=0.268$), all the other properties are similar than in model 1.

In order to perform this simulation for displacement values ranging from $u=0$ to $u=5.5\text{cm}$, five re-meshing phases were required. Results are analysed using the same variables than for model 1 and they are presented on figures 6.11 to 6.16 for displacements values $u=0.3\text{cm}$, $u=1.0\text{cm}$, $u=2.0\text{cm}$, $u=3.5\text{cm}$, $u=4.5\text{cm}$, and $u=5.5\text{cm}$, respectively.

At a first stage ($u=0.3\text{cm}$), the results are very similar than in model 1, except the extension of the tectonic regimes. In this case the extension regime is located further in the foreland than in model 1. This results from the lower basal friction in this case ($\mu=0.268$) compared with model 1 ($\mu=0.466$).

At a second stage ($u=1.0\text{cm}$), a second forward thrust has developed (figures 6.12d,f,g) and the top of the pop-up is already in tectonic extension regime. Note that Rice bifurcation indicate potential localisation in the foreland (figure 6.12d). The right part of the model is still in extension regime (figures 6.12a,c).

At a third stage ($u=2.0\text{cm}$), a second pop-up has already developed in front of the first one (figures 6.13d,e,f), and both of them are active synchronously (figure 6.13g) although the second is more active than the first one. Note now that the whole model is in tectonic compression regime even close to the right boundary (figure 6.13a,c).

At a fourth stage ($u=3.5\text{cm}$), main fault localisation has concentrated around the second pop-up structure (figure 6.14g), but a third pop-up has also developed in the foreland in front of the second one (figures 6.14d,g,h).

At a fifth stage ($u=4.5\text{cm}$), mainly the second and the third pop-up have continued to develop (figure 6.15d,e,f,g,h), without many differences compared with the fourth stage.

At a final stage ($u=5.5\text{cm}$), a fourth pop-up has developed in the foreland, crosscutting the third one. This is likely to result from the perturbing effect of the right vertical boundary, thus its observed location is certainly not meaningful.

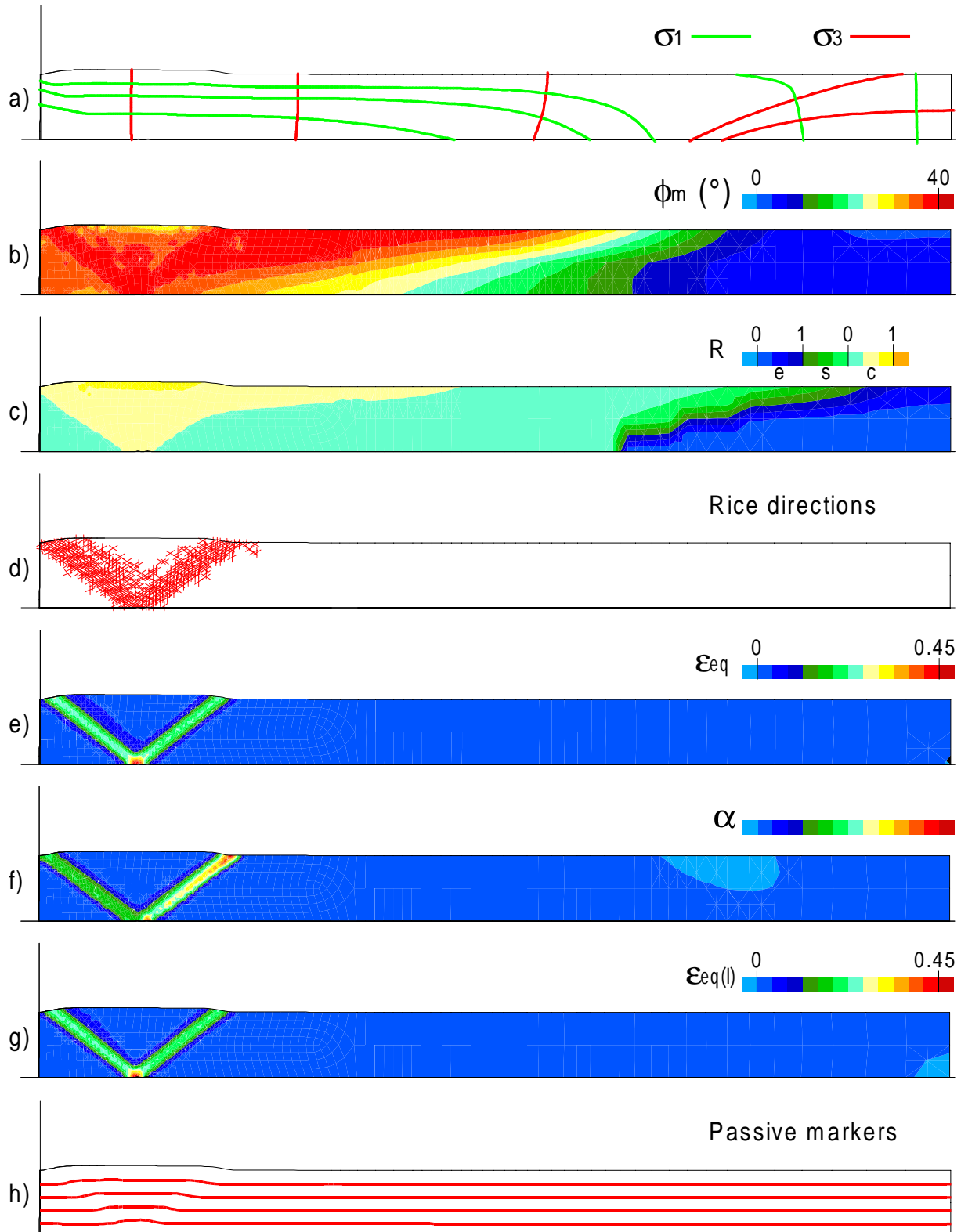


Figure 6.11 Thrust model 2 ($\mu=0.268$) at $u=0.30\text{cm}$: a) principal stress isostatic lines, b) Coulomb's mobilised friction angle, c) Wallace-Bott shape ratio, d) Rice directions of bifurcation, e) total equivalent strain, f) kinematic indicator of localisation, g) local equivalent strain, h) deformed passive markers.

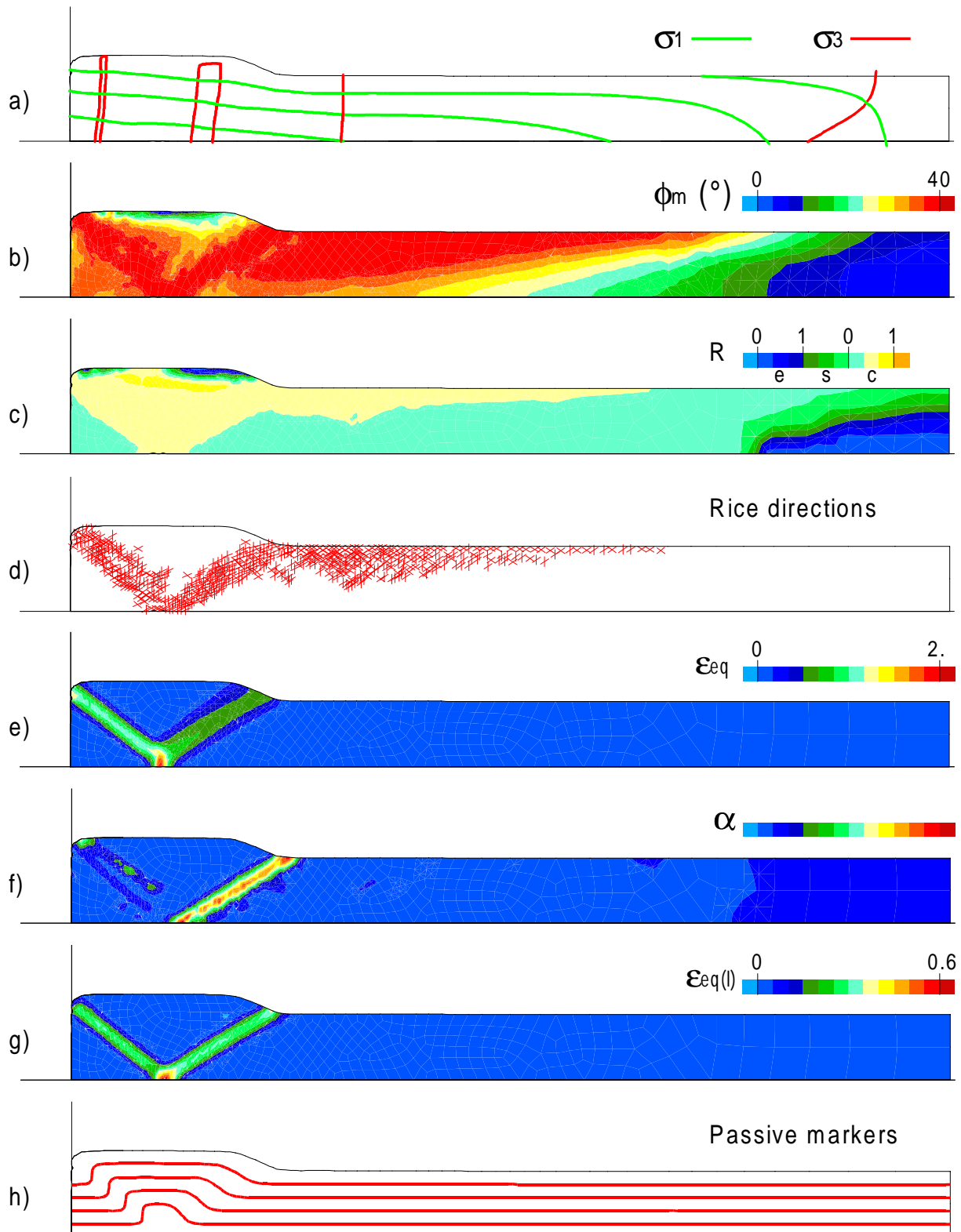


Figure 6.12 Thrust model 2 ($\mu=0.268$) at $u=1.0\text{cm}$: a) principal stress isostatic lines, b) Coulomb's mobilised friction angle, c) Wallace-Bott shape ratio, d) Rice directions of bifurcation, e) total equivalent strain, f) kinematic indicator of localisation, g) local equivalent strain, h) deformed passive markers.

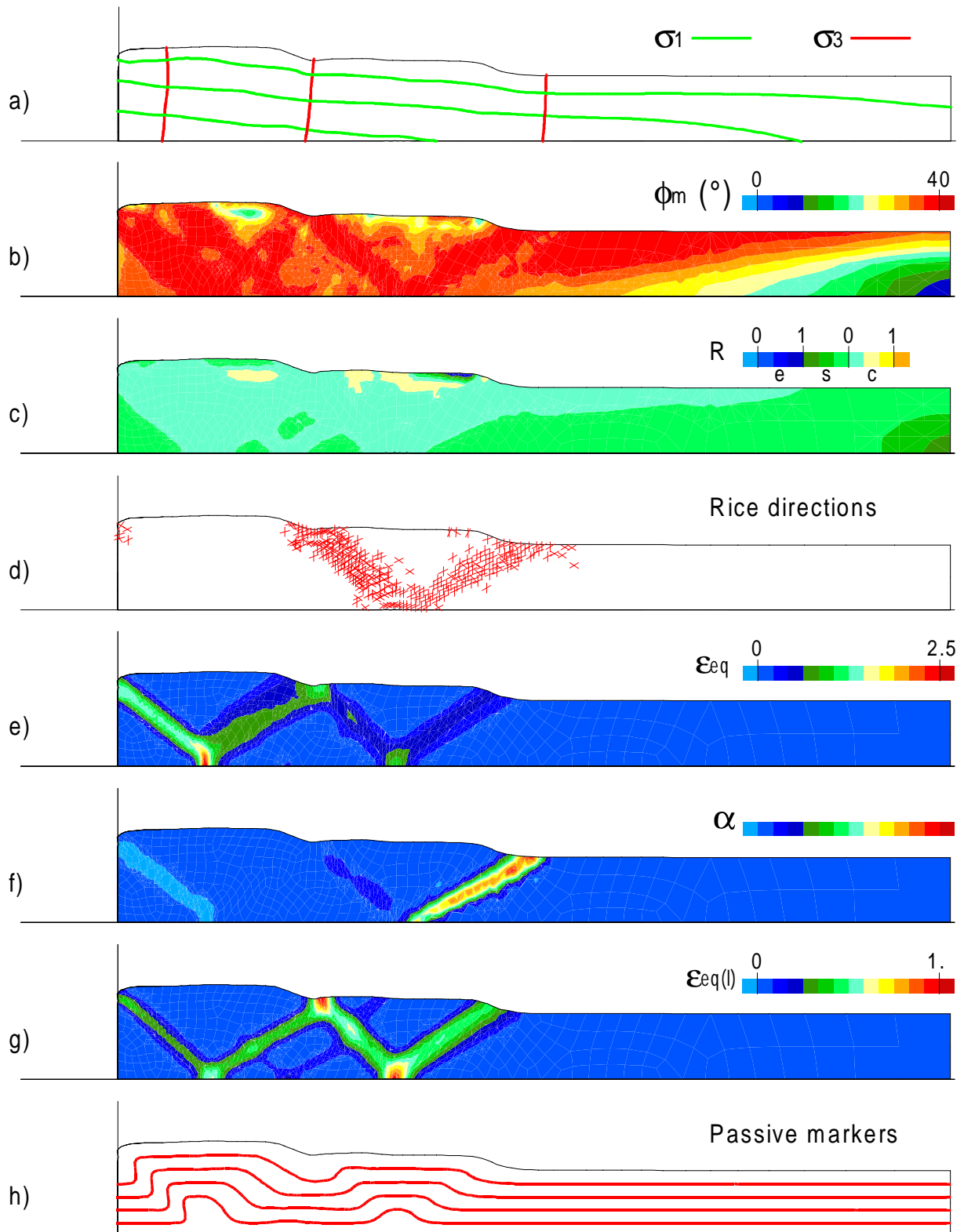


Figure 6.13 Thrust model 2 ($\mu=0.268$) at $u=2.0\text{cm}$: a) principal stress isostatic lines, b) Coulomb's mobilised friction angle, c) Wallace-Bott shape ratio, d) Rice directions of bifurcation, e) total equivalent strain, f) kinematic indicator of localisation, g) local equivalent strain, h) deformed passive markers.

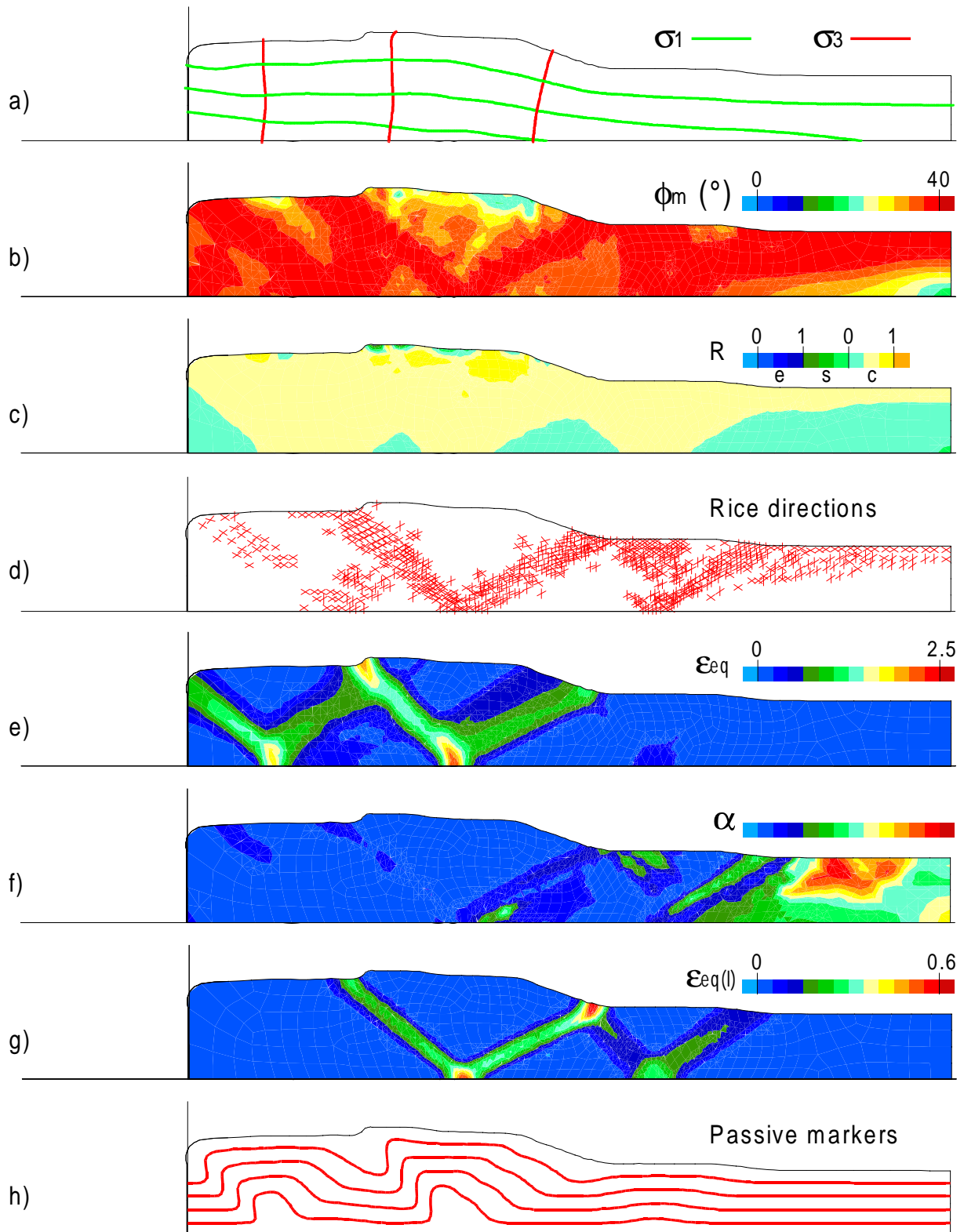


Figure 6.14 Thrust model 2 ($\mu=0.268$) at $u=3.5\text{cm}$: a) principal stress isostatic lines, b) Coulomb's mobilised friction angle, c) Wallace-Bott shape ratio, d) Rice directions of bifurcation, e) total equivalent strain, f) kinematic indicator of localisation, g) local equivalent strain, h) deformed passive markers.

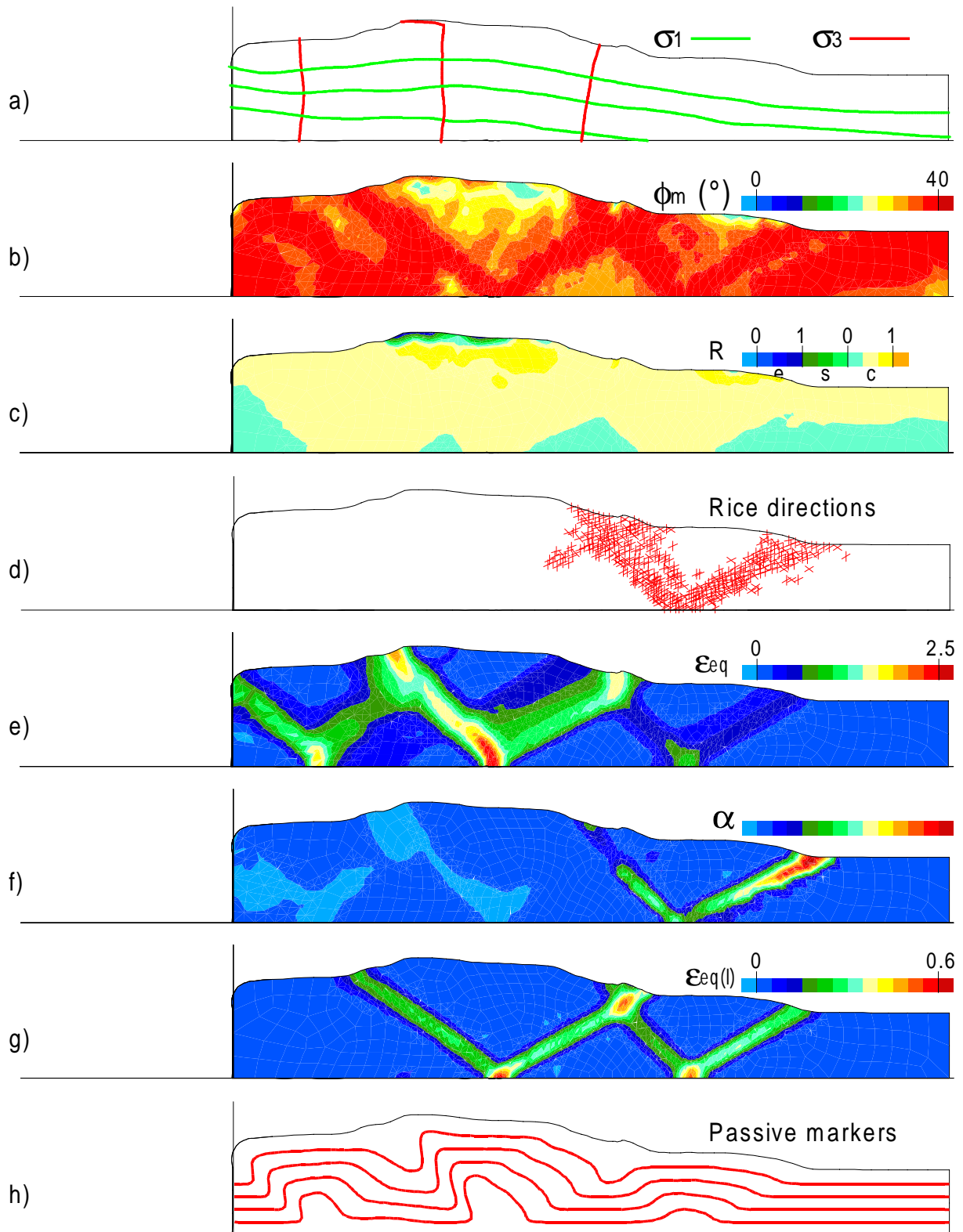


Figure 6.15 Thrust model 2 ($\mu=0.268$) at $u=4.5\text{cm}$: a) principal stress isostatic lines, b) Coulomb's mobilised friction angle, c) Wallace-Bott shape ratio, d) Rice directions of bifurcation, e) total equivalent strain, f) kinematic indicator of localisation, g) local equivalent strain, h) deformed passive markers.

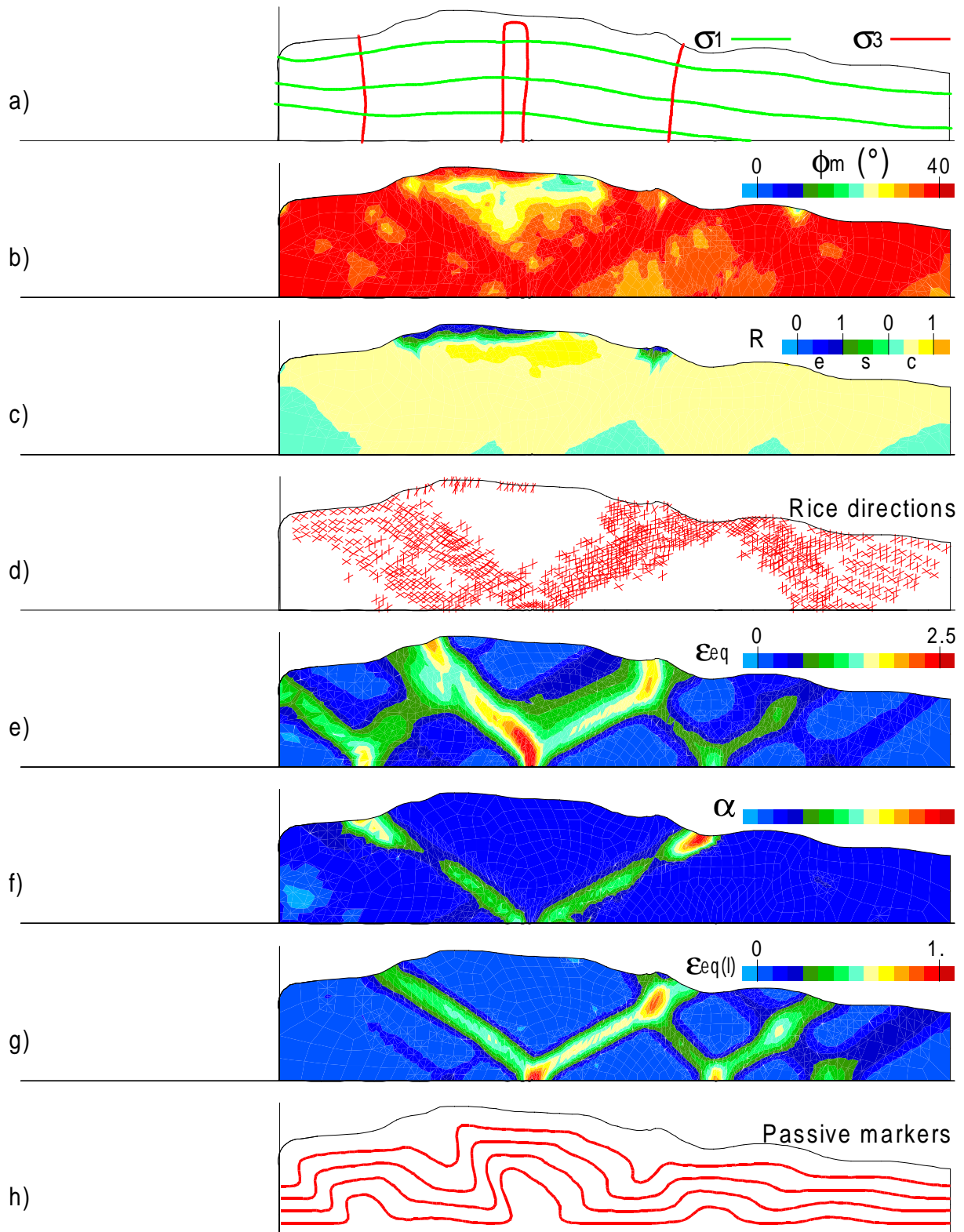


Figure 6.16 Thrust model 2 ($\mu=0.268$) at $u=5.5\text{cm}$: a) principal stress isostatic lines, b) Coulomb's mobilised friction angle, c) Wallace-Bott shape ratio, d) Rice directions of bifurcation, e) total equivalent strain, f) kinematic indicator of localisation, g) local equivalent strain, h) deformed passive markers.

6.3.4 Interpretation and comparison of the results

Based on all the results presented previously, a schematic interpretation of faults for both models 1 and 2 with their relative movement is presented on figure 6.17.

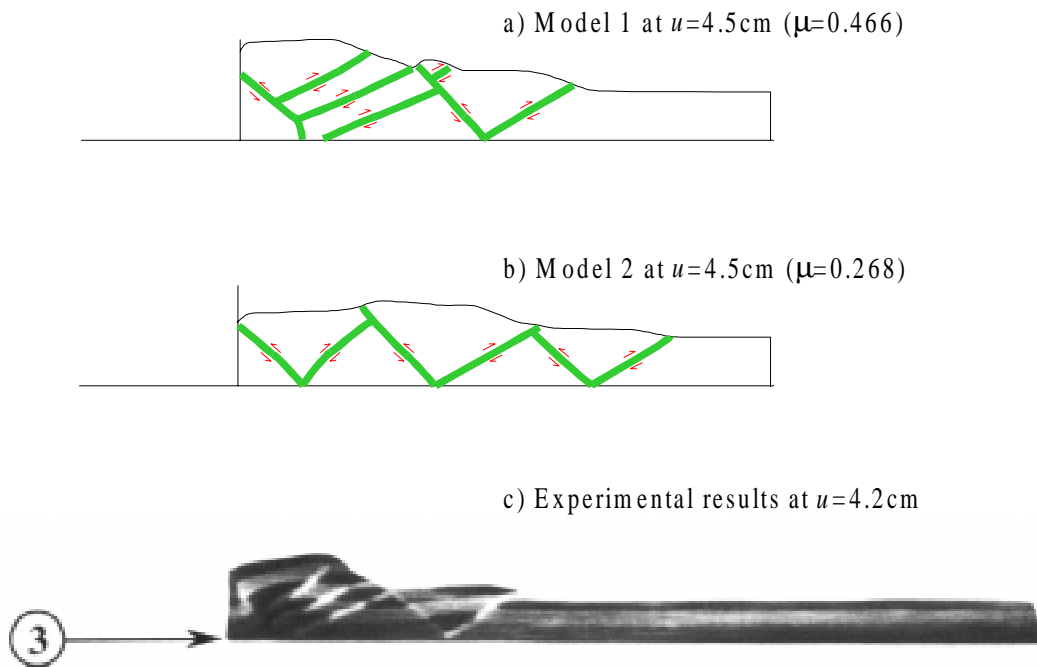


Figure 6.17 Interpretation of the 2 thrust models at $u=4.5$ cm : a) model 1 with high basal friction ($\mu=0.466$), b) model 2 with low basal friction ($\mu=0.268$), c) experimental results from [COLLETTA et al., 1991].

The influence of the basal friction (and thus the existence and properties of the basal decoupling layer) has a very important influence on the faulting pattern within the sand layer.

- If high basal friction is considered (model 1, figure 6.17a), the forward propagation of thrust fault systems is partly inhibited by the basal friction, thus there is a tendency to stack thrust faults one onto the other until a sufficiently large sand wedge forms near to left boundary (see for instance the three forward faults corresponding to the first pop-up structure). Then a new pop-up initiates in the foreland as it becomes easier to reach failure in less confined parts of the model. It follows that in such cases, the foreland tectonic regime can be different from the compressive tectonic regime existing in the wedge.
- If low basal friction is considered (model 2, figure 6.17b), thrust fault systems propagate in the foreland as conjugate thrust sets defining pop-up structures, without stacking forward thrust faults as it occurred for model 1. The propagation of thrusts in the foreland is much more efficient in the present case, and the influence zone of the tectonic compression (in the foreland) has a larger extent than in model 1.

The correlation between the structures reported on figures 6.17a (basal contact friction angle of 25°) and 6.17c of the physical experiment by [COLLETTA and al., 1991] is quite remarkable, which argue for a glass microbead friction angle of about 25° , i.e. slightly higher than the value proposed by [COLLETTA and al., 1991].

6.4 Conclusion

Starting from experimental results for which initial conditions, boundary conditions and deformed states are known quite accurately, numerical simulations have been performed in order to reproduce the experimental observations.

Due to the highly localised mode of deformation occurring in the model, this task could not have been achieved without the help of the re-meshing procedure developed and presented in chapter 4. Especially the transfer method presented in section 4.3.5.2 has proved to be more efficient than the original one as it reduced the out of equilibrium forces induced by the re-meshing procedure.

The comparison between the experimental results obtained by [COLLETTA and al., 1991] and the obtained numerical results showed a remarkable agreement between them. In the same time, this result back-validates the re-meshing procedure developed and used, and moreover it allows to obtain an estimation of the basal friction angle by inverse analysis.

It is worth pointing out that such a very good correlation between experimental and numerical results comes also from the better representativeness of the constitutive model used (Van Eekelen) for frictional material such as sand compared to a classical Drucker Prager one. This allowed to better represent the interaction between the sand medium and the frictional interface, which as shown in section 5.4 would not have been the case if DP model would have been used.

CHAPTER 7

Diapiric emplacement of the Egersund-Ogna anorthosite massif

7.1 Introduction

In this chapter, a finite element simulation of the diapiric emplacement of the Egersund-Ogna (EGOG) anorthosite massif is presented. This work has been initiated in the framework of an engineer degree thesis [HOFFER, 1996]. Most of this chapter has been submitted for publication in [BARNICHON et al., *subm.*].

Emplacement of anorthosite massifs usually occurs in anorogenic conditions and petrological models have long invoked diapirism as the major mechanism of emplacement [ASHWAL, 1993]. However, the cases in which diapirism could be unambiguously demonstrated are actually restricted, either because many anorthosite massifs have been affected after their emplacement by regional deformation which has blurred the original features (e.g. [MARTIGNOLE, 1996]), or because some massifs have not been sufficiently documented from a structural point of view.

Recent geochronological and petrological data on the Egersund-Ogna (EGOG) massif in Rogaland (South Norway) have brought new lights to support a diapir model and provide accurate constraints on the timing, geometry and initial conditions of the phenomenon. The arguments in favour of diapirism of the EGOG massif are summarised in [HAVENITH et al., *subm.*] together with a structural analysis constraining the strain distribution in the inner margin of the intrusion.

A finite element (FE) simulation of the diapiric emplacement of this massif is presented, in which geochronological and petrological data are used to define a reasonable geometry and rheology of the model. The main difficulty in simulating such physical process comes from the very large amount of deformation which takes place during diapirism, leading to unreasonably distorted Lagrangian meshes. Therefore, the finite element modelling has been coupled with the automatic re-meshing algorithm. The algorithm detailed in section 4.3.5.2 has been used for the transfer of fields from the father to son configurations. Also, artificial passive markers have been introduced in order to follow the finite displacement field. Both procedures have been detailed in chapter 4 and they both have been successfully applied here.

Purely mechanical analyses have been carried out, which can be justified by the fact that the diapirism is mechanically driven. Of course the coupling effect of temperature on the mechanical properties such as viscosity cannot be represented in such a framework. However, the first order mechanism of diapirism is satisfactorily represented by such modelling, as it will be shown further.

After recalling the main concept of diapirism, the particular field case of the EGOG massif is described, particularly regarding the available control data. Then, several simulations are performed and their results are mainly analysed in term of strain and displacement fields. Eventually, a comparison with recent available field data obtained from [HAVENITH et al., *subm.*] is given.

7.2 The diapirism : a brief review

7.2.1 Mechanism of diapirism

Diapirism results from the buoyant upwelling of a light viscous liquid when overlain by a heavier one. Such state is in unstable balanced state, i.e. every perturbation of the system will lead to overturn the two liquid layers to reach the stable balanced state where the lighter liquid floats on the heavier one (see figure 7.1). The initial stage of this instability is described analytically by the Rayleigh-Taylor (RT) instability.

In the field, the RT instability is observed both in plutonic and sedimentary environments, from crustal to meter scale [RÖNNLUND, 1989]. It is observed as the intrusion of a sub-spherical body called diapir into surrounding country rocks. Numerous examples of salt diapirism have been described, e.g. in North Germany [TRUSHEIM, 1960], in the Gulf of Mexico or in Texas [e.g. JACKSON and SENI, 1983]. Regarding the plutonic intrusions, some models have generally been accepted, e.g. the diapirism associated with subduction, although there is some controversy about the realism of the model for shallow (10-5km depth) granitic emplacement [e.g. VIGNERESSE, 1995]. The diapirism model for anorthositic rocks is subject to less controversy as the fluid-like behaviour is realistic for considered emplacement depth ($\approx 20\text{km}$).

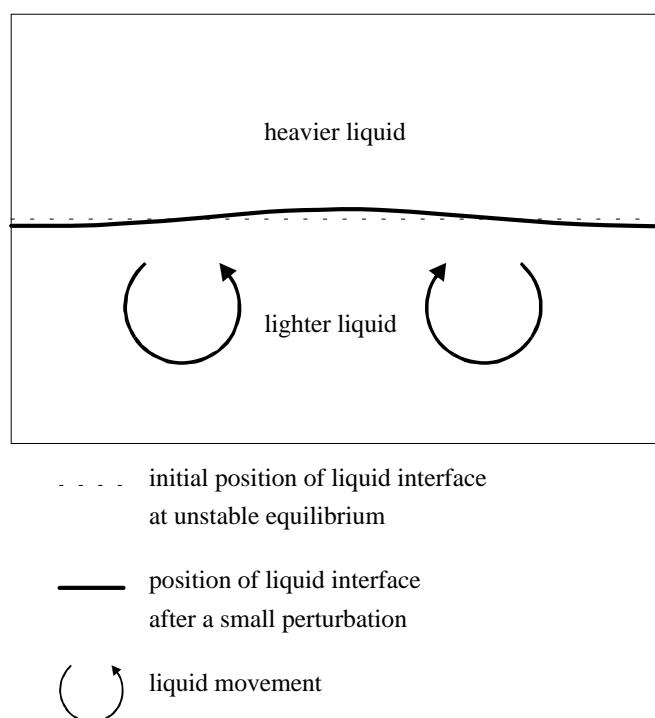


Figure 7.1 Rayleigh-Taylor type of instability, in which the lighter liquid (above) is in an unstable equilibrium.

7.2.2 Modelling, state of the art

A lot of effort has been made to simulate diapirism for its own scientific interest and for the economic interest of the salt diapirism with respect to hydrocarbon exploration. Experimentally, the diapirism has first been studied considering real fluids materials [NETTLETON, 1934; NETTLETON, 1943; KOYI, 1991]. It highlighted the relation between the diapir shape and the viscosity ratio. Later experiments using clays and silicones models submitted to an increased gravity field (using centrifuge apparatus) have been performed by [RAMBERG, 1981] and further authors [e.g. TALBOT et al., 1991]. In these experiments, the analysis is based on the study of the displacement field at the final stage using destructive methods (usually a set of cross sections). These experiments show the three-dimensional geometry of the diapiric phenomenon, which is comparable to a cellular pattern [TALBOT et al., 1991]. Numerous two-dimensional numerical simulations of the diapirism have been performed in past studies, based on fluid mechanics description in which the fluids are considered as incompressible materials [WOIDT, 1978; SCHMELING, 1987; ZALESKI and JULIEN, 1992]. These models have led to similar conclusions about the influence of the viscosity ratio on the finite diapir shape. More recently, simulations based on solid mechanics description have been performed [see e.g. POLIAKOV et al., 1993], most of them assuming a plane strain condition. Recently, a complex modelling of salt diapirism including erosion and sedimentation processes has been presented by [POLIAKOV et al., 1996] and has successfully demonstrated the mechanical relevance of syn-sedimentary diapirism for salt rocks.

The study presented in this chapter aims at testing the diapirism model for the emplacement of the EGOG anorthosite massif. It is based on a purely mechanical analysis using the *LAGAMINE* finite element code, which is coupled with the automatic adaptive re-meshing algorithm and with the use of artificial passive markers. The re-meshing procedure, which avoids large distortion of the Lagrangian mesh, is automatically activated when a given ratio of overdistorted elements is reached, following [HABRAKEN, 1989]. The passive markers allow to follow distortion through re-meshing phases as the up-dated Lagrangian mesh does not allow anymore to visualise the global distortion. Details about these procedures have been presented in chapter 4.

7.3 The Egersund-Ogna anorthosite massif, South Norway

7.3.1 Regional geology

The EGOG anorthosite massif (S. Norway) belongs to the Rogaland anorthosite province which is part of the Precambrian Sveconorwegian crystalline domain (see figure 7.2). The massif, roughly 20km in diameter, is intruded into migmatitic gneisses in granulite facies of noritic and charnockitic composition. In its central part, the EGOG massif is made up of anorthosite (a rock containing more than 90% plagioclase) with some leuconorite (between 10 and 25% orthopyroxene) containing rare but characteristic high-alumina orthopyroxene megacrysts (HAOM), up to 1m long, which form aggregates with megacrysts of plagioclase [DUCHESNE and MAQUIL, 1987]. The rocks have been mildly deformed: the plagioclases are nearly completely granulated and the HAOM are kinked and slightly granulated. The margin of the massif is globally leuconoritic in composition and enriched in HAOM. It has been considerably deformed with formation of a well-defined foliation parallel to the contact with the neighbouring massifs. The HAOM in particular have been extensively (and spectacularly) stretched along the foliation plane. These features and some others developed in the companion paper point to a diapiric emplacement according to classical criteria [ENGLAND, 1990].

In the model generally accepted for the genesis of anorthosite massifs [e.g. ASHWAL, 1993] and which is presented in figure 7.3, a mafic magma intrudes a magma chamber at the base of the crust, close to the Moho discontinuity. Slow crystallisation produces mafic minerals (olivine) which sink at the bottom of the chamber and megacrysts of plagioclase with some HAOM which float at the roof of the chamber. Due to a lower density than that of the surrounding rocks, Rayleigh-Taylor instabilities can initiate the diapiric rise of the anorthosite mush (plagioclases with entrained HAOM). Several diapirs would rise through the lower crust to a level of equilibrium where they expand laterally and coalesce to form anorthosite massifs.

7.3.2 Depth and timing of emplacement, gravity data

It is interesting to note that the anorthosite massifs and particularly EGOG provide good constraints on the geometry and timing of emplacement. The depth of the first magma chamber is constrained by the stability of HAOM whose Al content has been shown experimentally to require about 1.2GPa pressure (≈ 42 km) [LONGHI et al., 1993] and several lines of evidence point to 0.5GPa (≈ 18 km) [VANDER AUWERA and LONGHI, 1994] for the final emplacement pressure of Rogaland anorthosites.

The EGOG massif is separated from the neighbouring massifs by screens of migmatitic rocks (see figure 2). The Håland-Helleren massif is another massif type anorthosite and the Bjerkreim-Sokndal massif is a layered intrusion deformed by a gravity induced process [PALUDAN et al., 1994]. It thus forms as a rim-syncline, produced in response to the diapiric rise of the neighbouring anorthosite plutons [DUCHESNE and SCHÄRER, *subm.*].

Accurate age determination on HAOM indicates that EGOG crystallisation in the deep-seated magma chamber took place at 929 ± 2 Ma and that late undeformed dykes, crosscutting the anorthosites, are also about the same age at 931 ± 5 Ma [SCHÄRER et al., 1996]. It indicates

that the whole emplacement process took place in a very short time interval. It is reasonable to accept a value of 2Ma.

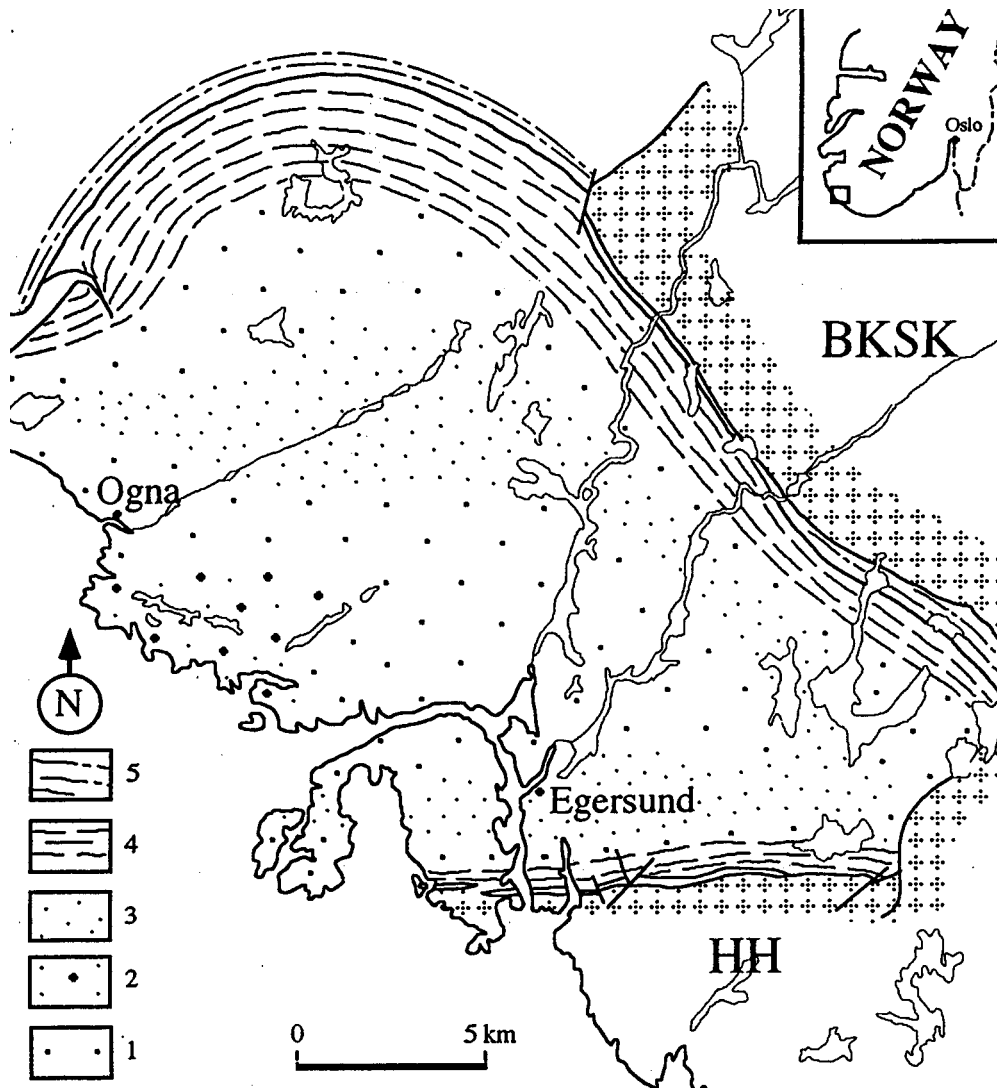


Figure 7.2 Geological map of the Egersund-Ogna anorthosite massif, after [HAVENITH et al., subm.]. Abbreviations: BSKK: Bjerkreim-Sokndal layered intrusion, HH: Håland-Helleren anorthosite massif. Legend: 1: anorthosite; 2: anorthosite rich in HAOM; 3: leuconorite; 4: foliated anorthosite and leuconorite; 5: migmatitic gneiss.

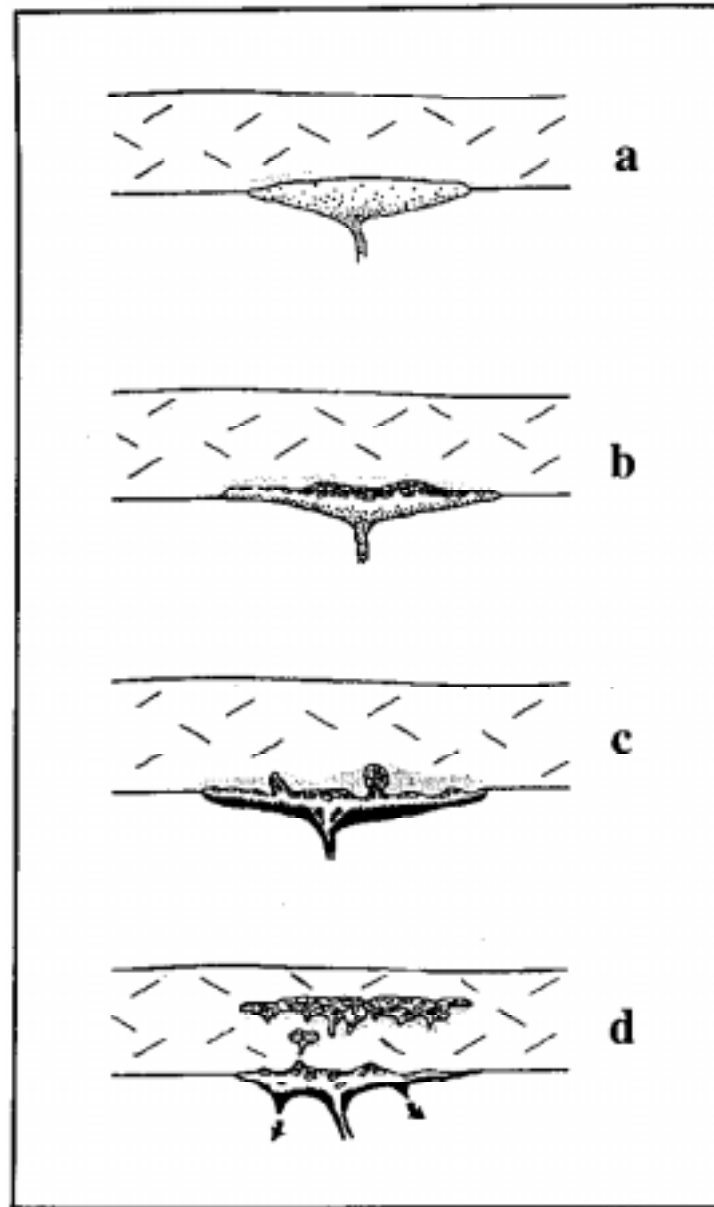


Figure 7.3 The two-stage model for the generation of anorthosite massifs, after [ASHWAL, 1993]. a. a magma chamber develops at the base of the crust in which a basic magma starts crystallising mafic minerals; b. mafic minerals sink and when plagioclase crystallises it floats and accumulates at the top of the magma chamber; c. lumps of plagioclase-rich mush form and rise as diapirs through the lower crust; d. several diapirs coalesce at mid-crustal depth to make up anorthosite massifs. Stippled area: heat from the magma chamber causes partial melting of the crust.

7.3.3 Lithological profile

The considered lithological profile is presented on figure 7.4 with the rock density values. The density of the lower crust falls in the range $3.0 < d < 3.2$ [HALL, 1986] and the density of the plagioclase megacrysts (An₅₀) at 1200°C falls in the range $2.63 < d < 2.65$ [CAMPBELL et al. 1978]. A conservative density value $d=2.75$ has been adopted here for the anorthosite crystal mush, considering that some liquid of higher density can have been entrapped in the mush.

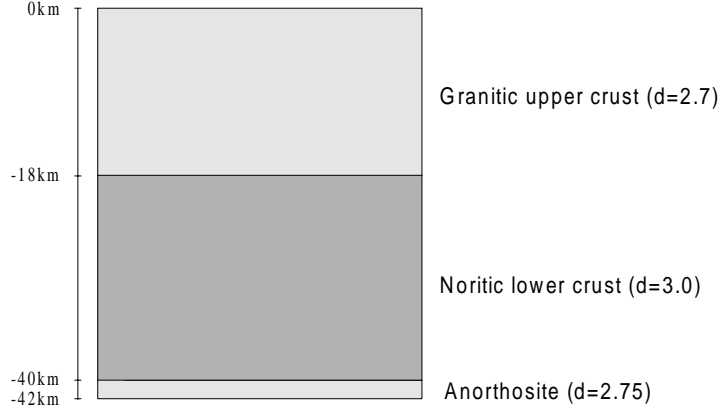


Figure 7.4 Initial lithology for the initial diapir model.

A 2km thick anorthosite layer is considered. The top anorthosite is at 40km depth, which is the average value of the depth at which HAOM started to crystallise. It is assumed that this initial anorthosite layer has a large enough extent to be represented by a horizontal layer. From the available data, it is also assumed that the diapir moved upward across the whole lower crust (noritic composition) and that emplacement stopped at the limit between the upper crust and the lower crust. Therefore, the lower crust extends from 40km to 18km depth and the upper crust (granitic composition) has a thickness of 18km.

7.3.4 Constitutive flow laws for the continental crust

It is required to evaluate the deviatoric behaviour for the previously defined geometry and lithology. Such methodology can be found in [DAVY and COBBOLD, 1991] and has already been used in [BARNICHON, 1994]. Two main flow mechanisms are considered for the deviatoric behaviour of the crust. The first one is a time independent brittle behaviour [BYERLEE, 1978] which is usually considered to follow Coulomb's criterion given in equation (2.70). This plastic flow criterion writes

$$\tau = \sigma_N \tan \phi \quad \text{or} \quad \frac{\sigma_1 - \sigma_3}{2} \cos \phi = c + \left(\frac{\sigma_1 + \sigma_3}{2} - \frac{\sigma_1 - \sigma_3}{2} \sin \phi \right) \tan \phi \quad (7.1)$$

where c is the cohesion and ϕ the friction angle. For such behaviour, the intensity and orientation of plastic strains are computed incrementally following the classical plasticity framework presented in chapter 2. The second behaviour is a time dependent viscous one. Classically, the elastoviscoplastic power law [CARTER and TSENN, 1987] is considered

$$\dot{\hat{\boldsymbol{\epsilon}}} = A \exp\left(-\frac{Q}{RT}\right) \hat{\boldsymbol{\sigma}}^n \quad (7.2)$$

which links the deviatoric stress tensor $\hat{\boldsymbol{\sigma}}$ to the deviatoric strain rate tensor $\dot{\hat{\boldsymbol{\epsilon}}}$. In this relation, Q is the activation energy of creep, R is the gas constant, T is the absolute temperature, A and n are material constants. Such non-linear behaviour is obviously temperature dependent. Values for these parameters for a broad range of minerals and rocks are presented in [CARTER and TSENN, 1987]. If a linear behaviour is assumed, i.e. the exponent $n=1$ in equation (7.1), then equation (7.2) simplifies to the linear Newtonian model

$$\dot{\epsilon} = \frac{\hat{\sigma}}{\eta} \quad (7.3)$$

where the dynamic viscosity η defined by

$$\frac{1}{\eta} = A \exp\left(-\frac{Q}{RT}\right) \quad (7.4)$$

7.3.5 Computation of rheological profiles

From the two flow behaviours presented previously, the corresponding rheological profiles can be computed making additional assumptions : a steady state thermal field is considered, an homogeneous strain rate is assumed throughout the considered domain and a given tectonic regime must be chosen [SIBSON, 1974] to define which of the principal stress components is closer to the vertical. In the present case, the strain value is approximated by assuming that the initially 2km thick anorthosite layer will flow upward over the lower crust (15-20km thickness), which gives an approximate strain value $\epsilon=15/2\approx 7$. Assuming that the emplacement takes place in about 2Ma leads to the strain rate $\dot{\epsilon}$

$$\dot{\epsilon} = \frac{7}{2(3.15 \cdot 10^{13})} \approx 10^{-13} s^{-1} \quad (7.5)$$

Table 7.1 Parameters of the power law, from [CARTER and TSENN, 1987; ORD and HOBBS, 1989].

	<i>Rock or mineral type</i>	<i>n</i>	<i>Q</i> (kJ.mole ⁻¹)	<i>A</i> (MPa ⁻ⁿ s ⁻¹)
Lower bound set	Simpson quartzite	2.72	134	-6.9
	Quartz diorite	2.4	212.	-1.5
	Anorthosite	3.2	239	-3.48
Upper bound set	Westerly granite (dry)	3.3	186.5	-5.7
	Maryland diabase (dry)	3.05	276	-1.2
	Hale albite (dry)	3.9	234.2	-5.63

The anorogenic assumption means that no compression nor extension tectonic phase occurs. Thus it is comparable to an oedometric condition in which the maximum principal stress is vertical, i.e. the K_0 value defined as the ratio of vertical over horizontal stress is lower than one ($K_0 < 1$). It actually corresponds to an extension tectonic regime, although no tectonic extension is assumed. From these assumptions, the following steps are performed :

- Considering a lithological profile, a density profile and a thermal profile, the differential stress ($\sigma_1 - \sigma_3$) is computed for the two criteria (plastic and viscous) as a function of depth. The lithological and density profiles used have already been presented in figure 7.4. For the plastic flow, Coulomb criterion with $\phi=37^\circ$ and cohesion $c=0$ have been considered. Values of rheological parameters for the power law have been chosen from [ORD and HOBBS, 1989] and from the compilation by [CARTER and TSENN, 1987]. They are reported in table 7.1 in which a lower and an upper bound set of parameters have been defined. Granite and quartzite types of rocks have been considered to approximate the upper crust, quartz

diorite and diabase (gabbro) are possible equivalent for the lower crust [HALL, 1986], and albite for the anorthosite mush. The thermal profile has been computed from the model proposed by [CHAPMAN, 1986] using a surface heat flow value $q_0=90\text{mWm}^{-2}$ (see figure 7.5).

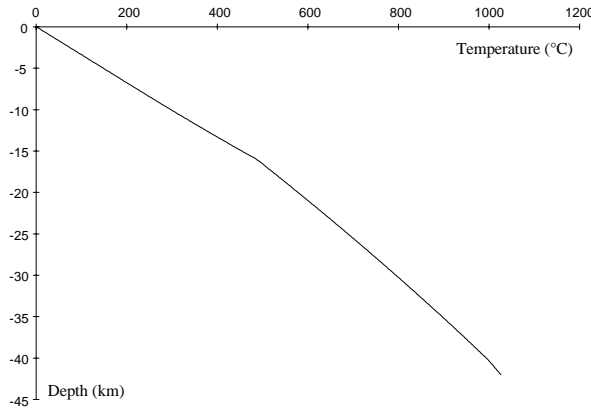


Figure 7.5 Temperature profile.

- The flow law type (plastic or viscous) which minimises the differential stress as a function of depth is determined. Changes in flow law type define the rheological boundaries.
- The $(\sigma_1 - \sigma_3)$ profile obtained is a combination of linear parts (due the plastic flow) and non-linear parts (due to viscous flow). Each non-linear domain can be linearised by integrating the differential stress $(\sigma_1 - \sigma_3)$ over its thickness. The average value of $(\sigma_1 - \sigma_3)^*$ is then obtained dividing the previous integral by the thickness h of the viscous domain [DAVY and COBBOLD, 1991]

$$(\sigma_1 - \sigma_3)^* = \frac{\int_h (\sigma_1 - \sigma_3) dh}{h} \quad (7.6)$$

- From this linearised value, an equivalent linear viscosity η^* can be obtained by

$$\eta^* = \frac{(\sigma_1 - \sigma_3)^*}{\dot{\epsilon}} \quad (7.7)$$

This method for differential stress profile computation has been implemented in the *PROFILE* program [BARNICHON, 1994]. The computed profiles are given on figures 7.6 and 7.7 considering two values of strain rate. The equivalent linear viscosity η^* values estimated from equation (7.7) are given for each rock type in table 7.2. For both considered strain rates, the lower and the upper bound of parameters are displayed. It must be kept in mind that these values only give the order of magnitude of linear viscosities for the EGOG diapiric emplacement, provided that all the underlying assumptions are verified.

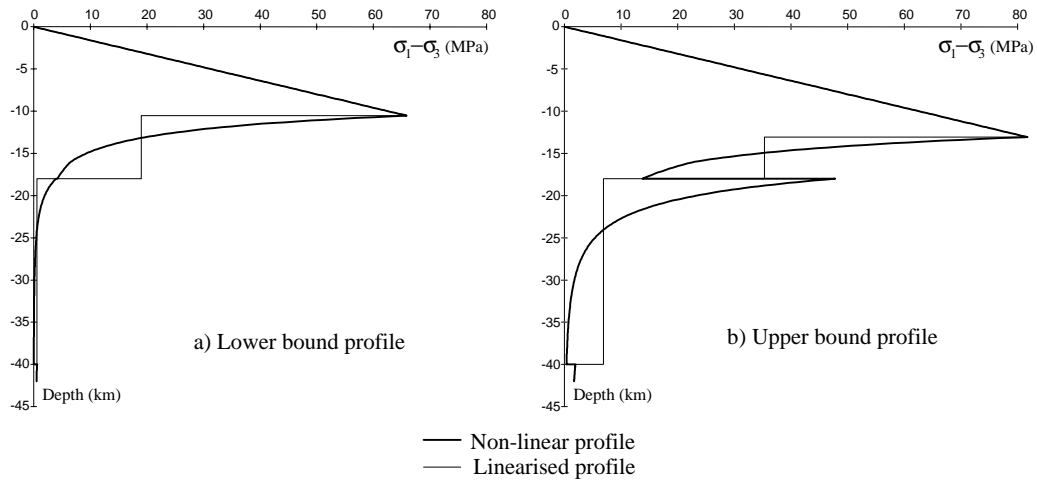


Figure 7.6 Rheological profile for the diapir model computed for $\dot{\epsilon}=10^{-13}\text{s}^{-1}$: a) lower bound profile, b) upper bound profile.

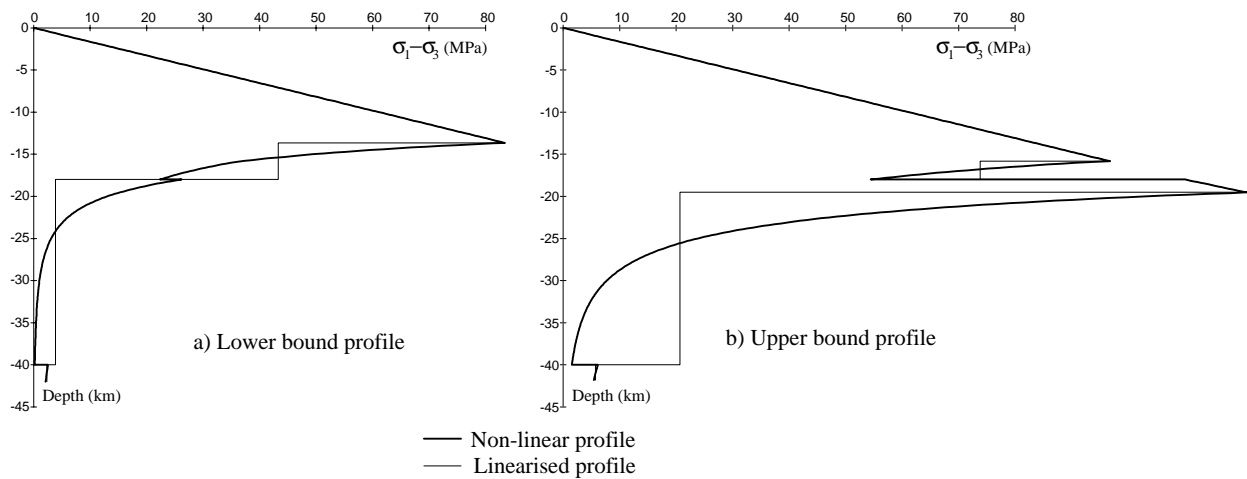


Figure 7.7 Rheological profile for the diapir model computed for $\dot{\epsilon}=10^{-11}\text{s}^{-1}$: a) lower bound profile, b) upper bound profile.

Table 7.2 Rock viscosities obtained for different values of strain rates.

	<i>Rock or mineral type</i>	η^* ($\dot{\epsilon}=10^{-13}\text{s}^{-1}$) (Pa.s)	η^* ($\dot{\epsilon}=10^{-11}\text{s}^{-1}$) (Pa.s)
Lower bound set	Simpson quartzite	$1.9 \cdot 10^{20}$	$4.4 \cdot 10^{18}$
	Quartz diorite	$5.8 \cdot 10^{18}$	$4. \cdot 10^{17}$
	Anorthosite	$5.6 \cdot 10^{18}$	$2.4 \cdot 10^{17}$
Upper bound set	Westerly granite (dry)	$3.5 \cdot 10^{20}$	$7.5 \cdot 10^{18}$
	Maryland diabase (dry)	$6.8 \cdot 10^{19}$	$2.1 \cdot 10^{18}$
	Hale albite (dry)	$1.8 \cdot 10^{19}$	$5.9 \cdot 10^{17}$

The relevance of the linear viscosity values computed from the rheological profile can be assessed by trying to evaluate the duration of diapir emplacement for such values. An approximation can be obtained from Stokes law which describes the upward velocity V of a spherical particle of radius r , viscosity η_b in a viscous medium of viscosity η_f . Provided the sphere is less viscous than the medium, i.e. $\eta_b \ll \eta_f$, the upward velocity of the sphere in the viscous liquid reads [TURCOTTE and SCHUBERT, 1982]

$$V = \frac{1}{3} \frac{r^2 g (\rho_f - \rho_b)}{\eta_f} \quad (7.8)$$

where ρ_f and ρ_b are the specific masses of the medium and the particle, respectively (with $\rho_f > \rho_b$). Of course, this relation does not describes accurately the present diapiric phenomenon as the diapir is not spherical, nor individualised from its source layer. However, it is interesting to test the relevance of the viscosities computing the theoretical upward velocity of a diapir using this relation. The obtained values can be compared to the observed average value of 22km/2Ma, equivalent to 1.1cm.a^{-1} . For an EGOG diapir radius $r=10\text{km}$, values obtained from equation (7.8) are given in of table 7.3 for different strain rates and the upper and lower bound set of parameters. Comparison leads to define the upper bound model with $\dot{\epsilon}=10^{-13}\text{s}^{-1}$ as the more representative with an predicted upward velocity $V=4.6\text{cm.a}^{-1}$, which is within one order of magnitude from the expected value $V=1.1\text{cm.a}^{-1}$.

Table 7.3 Upward velocities computed from Stokes law considering a sphere radius $r=10\text{km}$.

<i>Rheological model</i>	$V (\text{cm.a}^{-1})$
Upper bound with $\dot{\epsilon}=10^{-13}\text{s}^{-1}$	4.6
Lower bound with $\dot{\epsilon}=10^{-13}\text{s}^{-1}$	54.
Upper bound with $\dot{\epsilon}=10^{-11}\text{s}^{-1}$	150.
Lower bound with $\dot{\epsilon}=10^{-11}\text{s}^{-1}$	789.

7.4 Diapir model 1

7.4.1 Initial geometry, boundary conditions

The number of layers and their respective depth (figure 7.8) are defined from the rheological profile presented on figure 7.6b, corresponding to the upper bound model with $\dot{\epsilon}=10^{-13}\text{s}^{-1}$: the granitic upper crust is separated in a plastic part ($-13\text{km}<y<0\text{km}$) and a viscous part ($-18\text{km}<y<-13\text{km}$). The whole lower crust ($-40\text{km}<y<-18\text{km}$) and anorthosite mush ($-42\text{km}<y<-40\text{km}$) are viscous.

The problem is studied in two dimensions under an axisymmetrical state of deformation, i.e. assuming a symmetry of revolution around the future diapir vertical axis (see figure 7.9). The upper surface is a free surface. The frictionless basal boundary condition is considered to be a reasonably good approximation of the deep-seated magma chamber. The lateral boundaries are also frictionless and fixed following the horizontal direction. An initial perturbation is required to trigger the diapirism : a 300m deflection along the vertical direction has been chosen, i.e. the interface between the anorthosite layer and the lower crust is not perfectly flat. The only mechanism considered here is the density inversion, i.e. the loading consists only of body forces applied along the vertical direction. A quasi balanced isotropic lithostatic state of stress is initialised in the model prior computation : at each point stress components are equal to the overlying rock column weight, with $K_0=1$ in equation (2.156). Three horizontal passive markers are introduced in the anorthosite layer and in the lower crust layer (dashed lines on figure 7.9) in order to follow the distortion through re-meshing procedures.

The initial mesh is made up 2152 nodes and 683 quadrilaterals with 8 nodes and 9 integration points (see figure 7.10). Classical 8 nodes elements with reduced integration have not been chosen in this simulation as they exhibited kinematical modes of deformation, i.e. deformation modes which do not require energy.

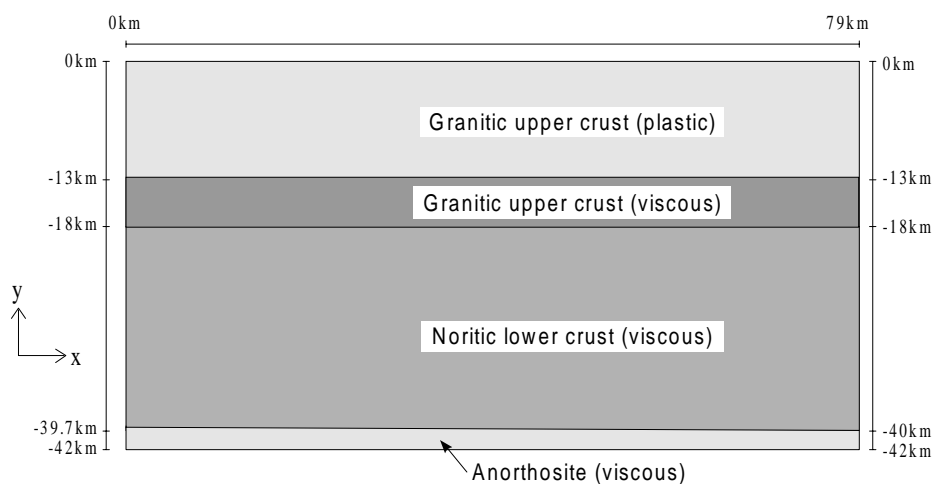


Figure 7.8 Geometry of the diapir model 1.

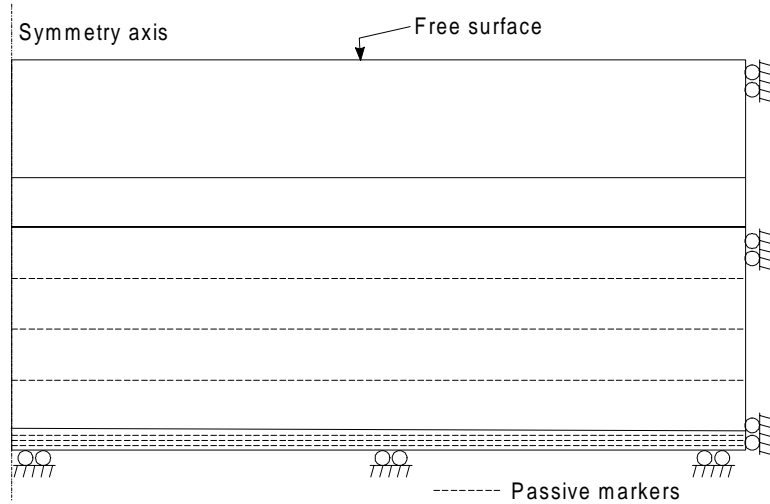


Figure 7.9 Boundary conditions of the diapir model 1.

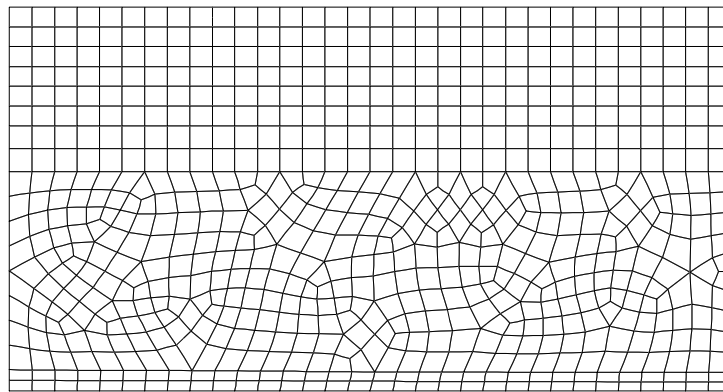


Figure 7.10 Initial mesh of the diapir model 1 (2152 nodes, 683 elements).

7.4.2 Constitutive laws

The plastic behaviour of the upper granitic crust is represented by the perfectly plastic Drucker Prager elastoplastic modified yield surface following [VAN EEKELEN, 1980] implemented in the *PLASOL* law,

$$f = II_{\hat{\sigma}} + m \left(I_{\hat{\sigma}} - \frac{3c}{\tan \phi_c} \right) = 0 \quad (7.9)$$

where coefficient m depends on the third deviatoric stress invariant (see section 2.3.2.4 for details). The viscous behaviour of the other rocks is represented by an elastoviscoplastic law for which the elastic domain is bounded by a Von Mises surface. The viscoplastic strain rate is defined by

$$\dot{\hat{\epsilon}}^{vp} = \frac{B}{H} \hat{\sigma} \quad (7.10)$$

in which the coefficient $B/H=1/\eta$ is equivalent to the inverse of viscosity and H is the yield limit (equivalent to cohesion). Linear viscosity is assumed. For both the elastoplastic and the elastoviscoplastic behaviours, the volumic part follows Hooke's law

$$\dot{\sigma}_m = K\dot{\epsilon}_m \quad (7.11)$$

where K is the elastic compressibility modulus

$$K = \frac{E}{3(1-2\nu)} \quad (7.12)$$

All the rheological parameters used are reported in table 7.4.

Table 7.4 Mechanical parameter for diapir model 1.

<i>Layer</i>	<i>E</i> (GPa)	<i>v</i>	ϕ (°)	<i>c</i> (MPa)	<i>H</i> (Pa)	η (Pa.s)	ρ (kg.m ⁻³)
> Granite	10	0.24	36.9	0			2700
< Granite	10	0.24			100	3.5 10 ²⁰	2700
Norite	10	0.24			100	6.8 10 ¹⁹	3000
Anorthosite	10	0.24			100	1.8 10 ¹⁹	2750

7.4.3 Results

Seven re-meshing phases have been performed to reach the final computed state presented further, i.e. eight meshes have been used successively for this simulation. Each of these meshes is displayed on figure 7.11. The total CPU time is less than 10 hours on an Alpha Dec workstation, in which the CPU time spent for re-meshing phases represents less than 5% which is negligible compare to resolution CPU time.

The evolution of the geometry, the velocity field and the strain field are presented on figures 7.12 to 7.14 for the initiation, the amplification and the damping phases, respectively. Note that for each phase, the strain tensor is computed between the two geometries given in figures 7.12a, 7.13a, 7.14a, and thus represents an incremental strain tensor. The mechanics convention sign is used for strains, i.e. negative values indicate compression whereas positive ones indicate extension.

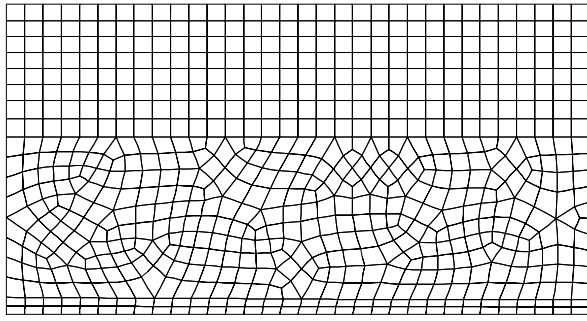
During the initiation phase, a major clockwise "convection" cell develops close to the symmetry axis, as attested by the velocity field at $t=2.02\text{Ma}$ (figure 7.12b). The term "convection" is used by analogy to thermal convection phenomenon, but here it is a mechanical convection induced by the inverse density gradient. It highlights the clockwise movement of the anorthositic material around the axis which has been triggered by the initial geometrical imperfection. The deformed passive markers (figure 7.12c) indicate a quite homogenous displacement field, the upper marker being almost non-deformed. The resulting diapir exhibits a bell shape. Around the diapir axis, the radial strain component ϵ_r and the circumferential strain component ϵ_θ indicates a compression state (figures 7.12d,f), while the vertical strain component ϵ_z attests for an extension state (figure 7.12e). Note that in any point the volumic strain is negligible compared to the deviatoric strain, thus $\epsilon_r + \epsilon_\theta + \epsilon_z \approx 0$. In the lower crust above the diapir, the strain state is inverted for all the components, and its intensity is lower. During this initiation phase, the average rising velocity of the diapir apex reads 0.37cm.a^{-1} .

At the end of the amplification phase ($t=2.39\text{Ma}$), the average rising velocity of the diapir apex reads 2.54cm.a^{-1} , the velocity intensity is multiplied by 3 compared with the end of the

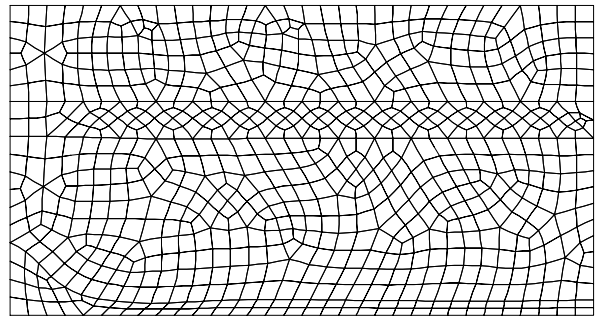
previous phase (figure 7.13). The velocity field (figure 7.13b) shows that the viscous part of the granitic crust is involved in the diapirism and also that a second convection cell is associated with the first one but in an anticlockwise rotation. The deformed passive markers (figure 7.13c) show the large displacement of the material within the diapir, which has generated a rim syncline in the lower crust. Two strain domains can be distinguished (figures 7.13d,e,f). The first one is located within the diapir, near its base : the strain regime is very similar to the one described during the initiation phase. The second strain domain is located around the diapir apex and affects both the anorthosite and its cover : the strain state is inverted compared to the first domain, i.e. ϵ_r and ϵ_θ are in extension whereas ϵ_z is in compression. Such strain state reflects the radial and circumferential expansion of the diapir upper part which is visible on figure 7.13a. Note that, as in the initiation phase, the ϵ_r and ϵ_θ extension values are almost equal near the diapir apex.

In the damping phase at $t=2.81\text{Ma}$ (figure 7.14), the average rising velocity of the diapir apex decreases to 0.47cm.a^{-1} . The velocity field (figure 7.14b) gives the explanation for the development of two diapir-like structures located in the middle and on the right boundary of the model : they are generated by additional convection cells and corresponds to the location of new diapirs. The axisymmetric assumption is no longer valid for these new diapirs as they have the meaning of ring-diapirs and not isolated ones. However, the first diapir can still be studied accurately. Within the lower crust, the rim syncline is more pronounced (figure 7.14c), and the viscous part of the granitic crust is involved in the diapirism. Inside the diapir, the two strain domains defined are still present (figures 7.14d,e,f). The second domain, which is induced by the radial and circumferential expansion of the diapir, is now centred around the diapir bulb. A major difference between this damping phase and the previous ones lies in the fact that the circumferential extension is now larger than the radial extension, i.e. $\epsilon_\theta > \epsilon_r$, whereas in the initiation and amplification phases, these components were quite similar.

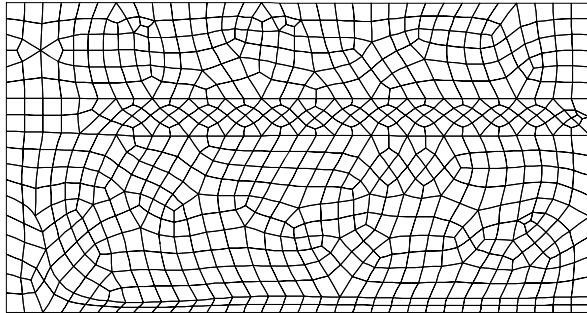
As expected, the brittle upper crust is not involved in the diapirism and remains almost non-deformed. It must be pointed out that, above the diapir, there is a diffuse zone in which the brittle upper crust reaches plasticity, but without plastic strain localisation, i.e. without fault generation.



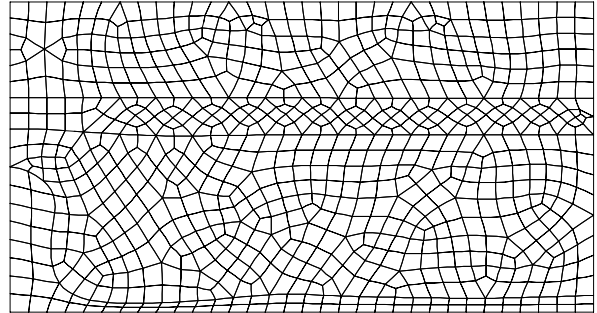
Mesh 1



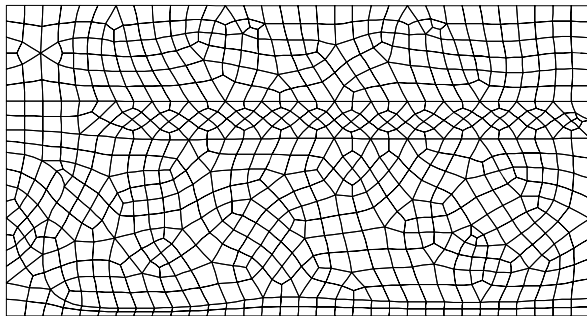
Mesh 2



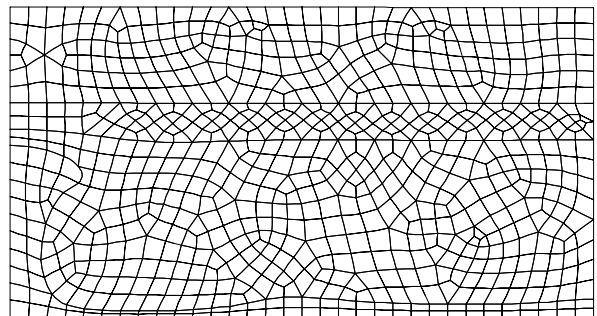
Mesh 3



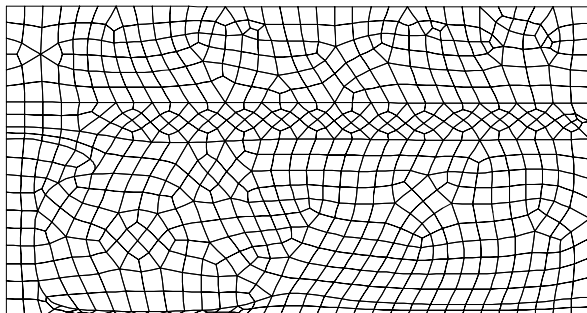
Mesh 4



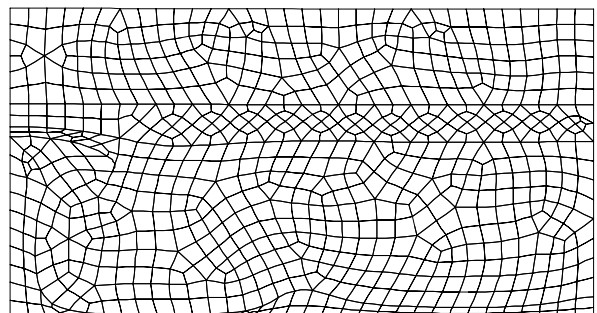
Mesh 5



Mesh 6



Mesh 7



Mesh 8

Figure 7.11 Successive meshes generated by the re-meshing algorithm used for the diapir model 1.

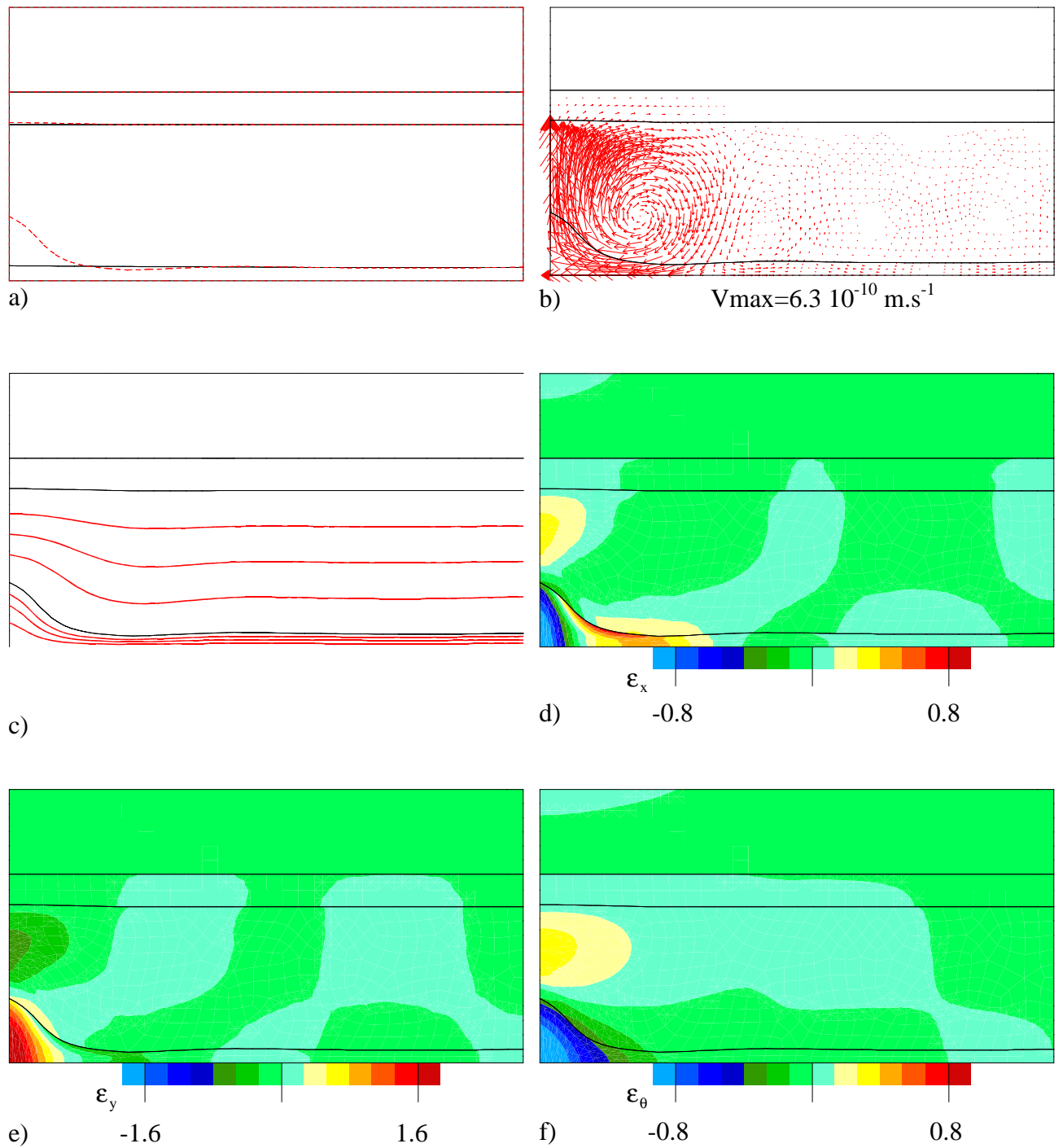


Figure 7.12 Diapir model 1 initiation phase : a) deformed geometry at $t=0\text{Ma}$ (full line) and $t=2.02\text{Ma}$ (dashed line), b) velocities at $t=2.02\text{Ma}$, c) passive markers (thick lines) at $t=2.02\text{Ma}$, d, e, f) horizontal, vertical and circumferential components of the strain tensor computed for the time range $0\text{Ma} < t < 2.02\text{Ma}$.

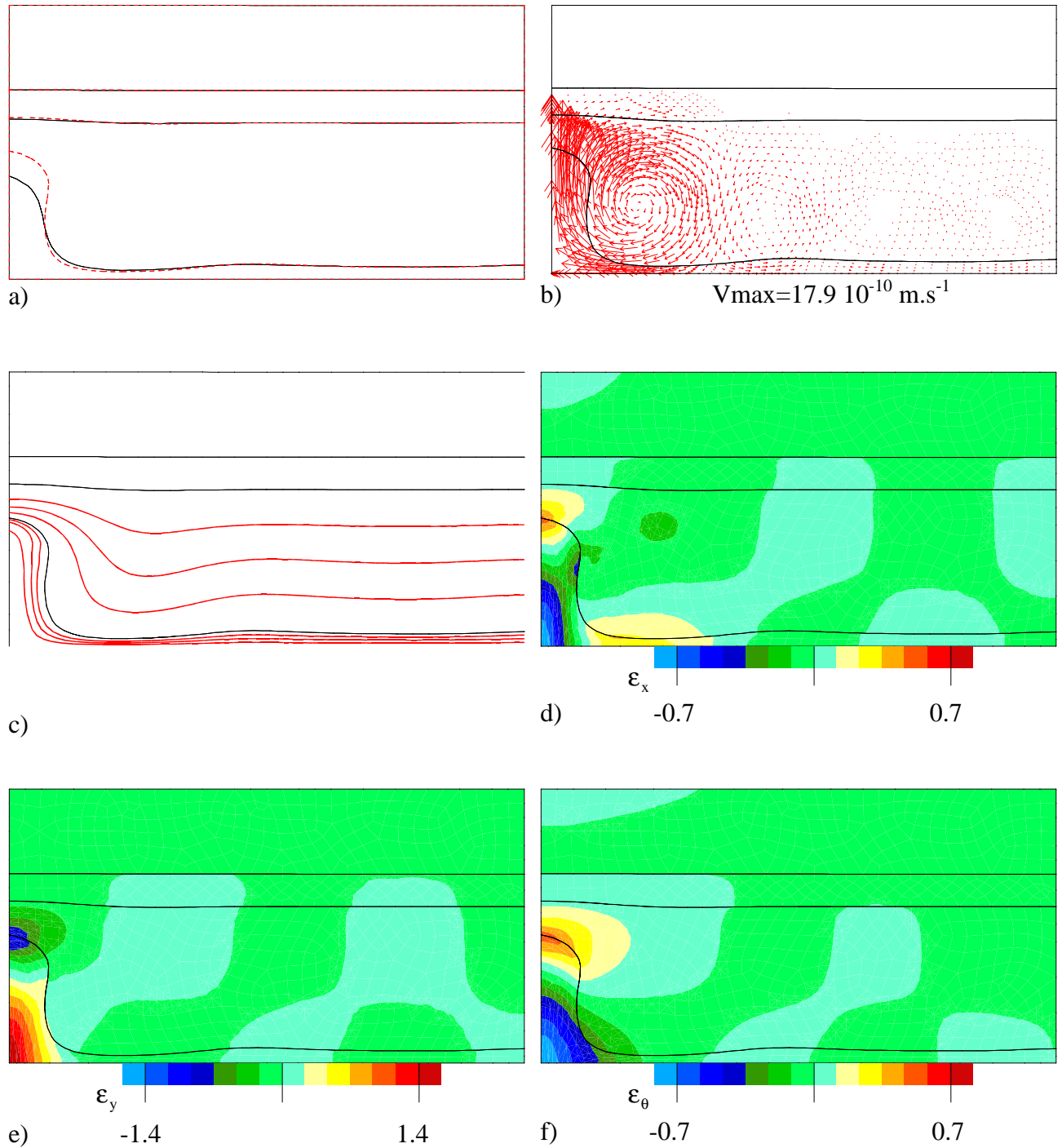


Figure 7.13 Diapir model 1 amplification phase : a) deformed geometry at $t=2.24\text{Ma}$ (full line) and $t=2.39\text{Ma}$ (dashed line), b) velocities at $t=2.39\text{Ma}$, c) passive markers (thick lines) at $t=2.39\text{Ma}$, d, e, f) horizontal, vertical and circumferential components of the strain tensor computed for the time range $2.24\text{Ma} < t < 2.39\text{Ma}$.

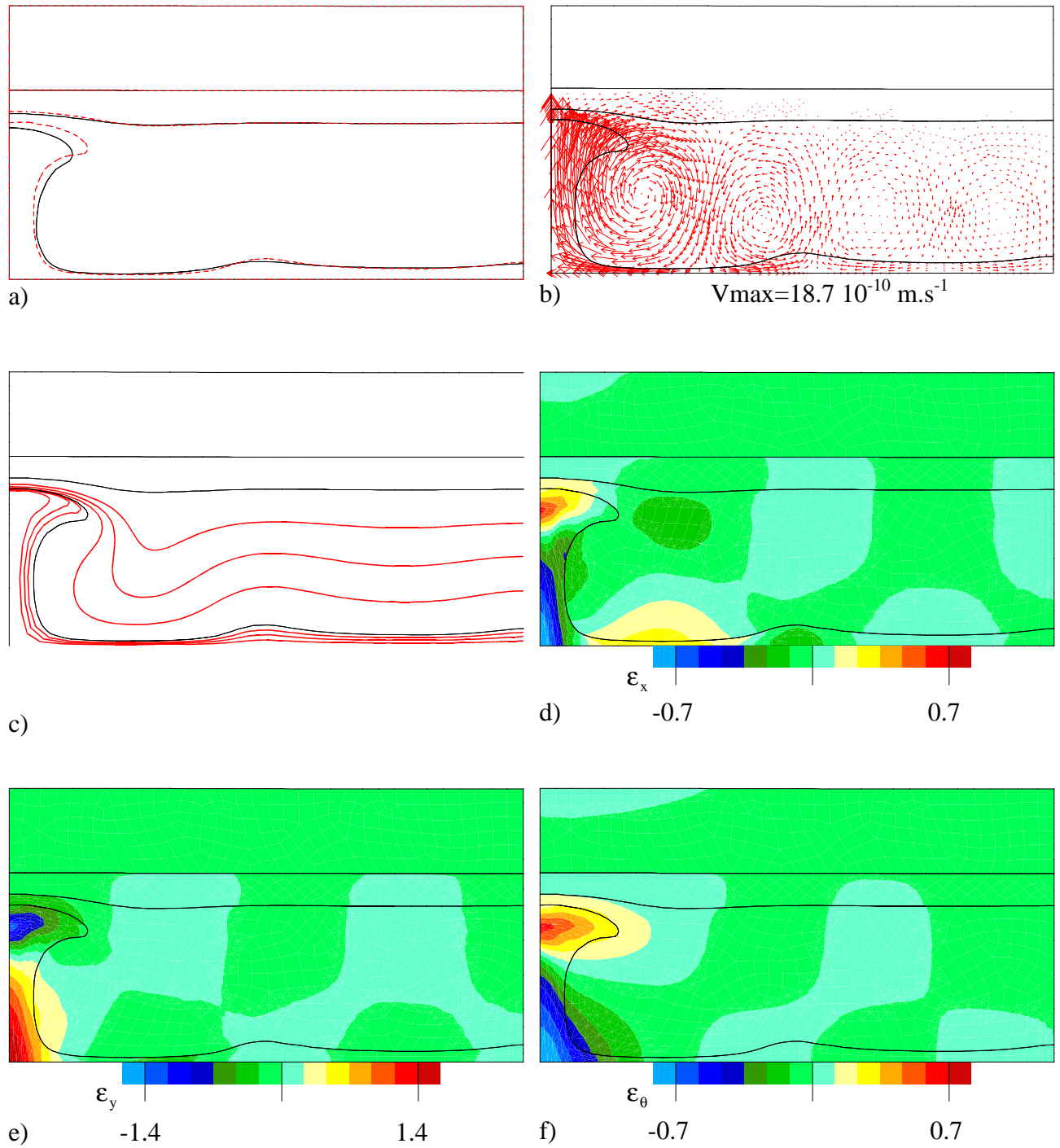


Figure 7.14 Diapir model 1 damping phase : a) deformed geometry at $t=2.65\text{Ma}$ (full line) and $t=2.81\text{Ma}$ (dashed line), b) velocities at $t=2.81\text{Ma}$, c) passive markers (thick lines) at $t=2.81\text{Ma}$, d, e, f) horizontal, vertical and circumferential components of the strain tensor computed for the time range $2.65\text{Ma} < t < 2.81\text{Ma}$.

7.5 Anorthosite thickness and viscosity influence : diapir models 2, 3 and 4

The influence of the anorthosite thickness h_a and viscosity η_a has been investigated in additional simulations. The diapir model 2 is similar to model 1 except that the anorthosite viscosity η_a has been divided by 10, model 3 is similar to model 1 except that the anorthosite thickness h_a has been chosen equal to 5km, and in model 4 both the anorthosite thickness and viscosity have been changed compared to model 1. The modified values are reported in table 7.5.

The geometry evolution is presented on figures 7.15a,c,e, the deformed geometries and deformed markers are presented on figures 7.15b,d,f. When the anorthosite viscosity η_a is close to the norite one η_n (model 1 and 3, $\eta_n/\eta_a=3.8$), the diapir geometry evolves towards a mushroom type geometry. If the anorthosite viscosity is much smaller than the norite one (model 2 and 4, $\eta_n/\eta_a=38$), the diapir geometry evolves towards a bulb geometry. A similar viscosity influence on the diapir shape has been mentioned in previous studies, see for instance [WOIDT, 1978]. As the emplacement duration is shorter when the anorthosite is less viscous (see models 1 and 3), the rim syncline in the lower crust is less developed than in the other cases (see models 2 and 4). Note also that, when the anorthosite layer is thicker (models 3 and 4), the ring-diapirs are well developed and the wavelength increases. However, the axisymmetric assumption is no longer valid, thus their finite geometry is not realistic as they should develop like isolated diapirs. This feature could only be overcome by performing a full three-dimensional analysis. As in model 1, the brittle upper crust is not involved in the diapirism and there is a diffuse zone where the brittle upper crust reaches plasticity above the diapir.

Table 7.5 Varying parameters for diapir models.

<i>Diapir model</i>	h_a (km)	η_a (Pa.s)
1	2	$1.8 \cdot 10^{19}$
2	2	$1.8 \cdot 10^{18}$
3	5	$1.8 \cdot 10^{19}$
4	5	$1.8 \cdot 10^{18}$

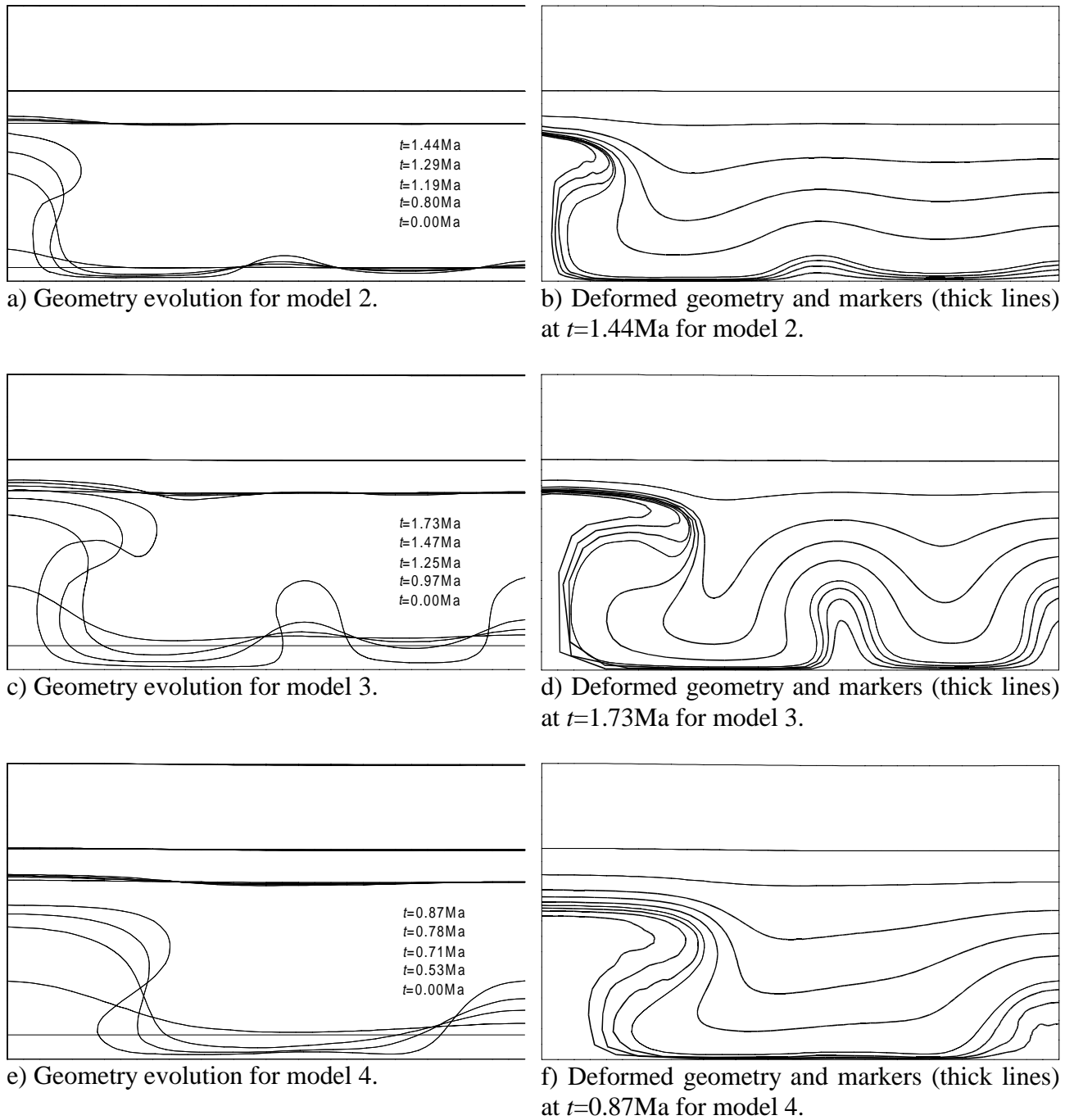


Figure 7.15 Influence of anorthosite viscosity and thickness : a) & b) model 2 ($\eta_a=1.8 \cdot 10^{18}\text{Pa.s}$, $h_a=2\text{km}$), c) & d) model 3 ($\eta_a=1.8 \cdot 10^{19}\text{Pa.s}$, $h_a=5\text{km}$), e) & f) model 4 ($\eta_a=1.8 \cdot 10^{18}\text{Pa.s}$, $h_a=5\text{km}$).

7.6 Comparison with field observations

The stretching directions measured from field observations (structural analysis using HAOM as strain markers) have been reported by [HAVENITH et al., *subm.*]. In this paper, poles of the stretching directions are reported on the general map of the EGOG massif (see figure 7.16). In the north, north-west and south margins of the EGOG massif, most stretching directions lie approximately in an horizontal plane as their poles are roughly on the projection hemisphere border. Moreover, the stretching directions are oriented parallel to the EGOG margins. These two features of the observed strain field are fully consistent with the results obtained from the FE simulations, in which the major extension strain component was the circumferential one.

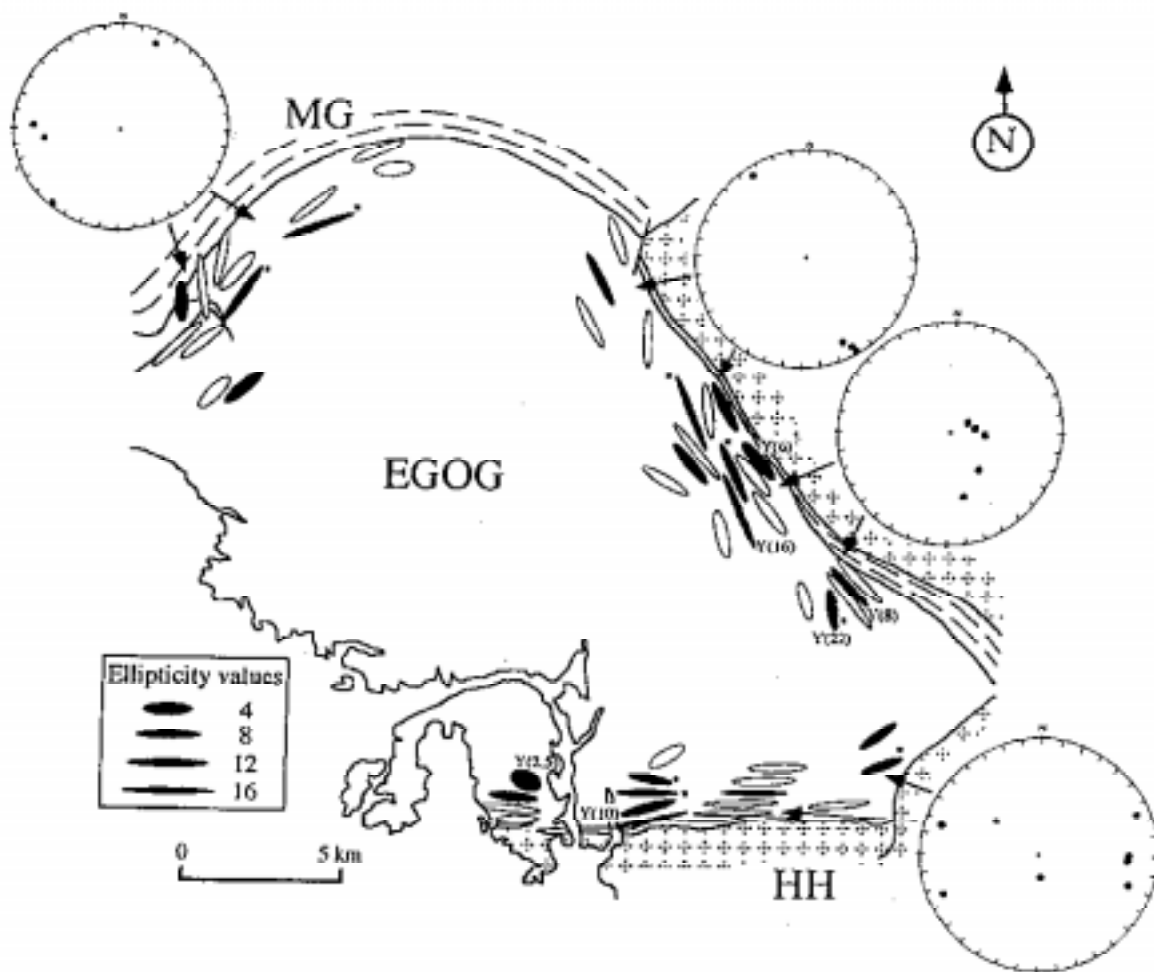


Figure 7.16 Geological map of the Egersund-Ogna anorthosite massif, after [HAVENITH et al., *subm.*].

7.7 Conclusion

The presented modelling of the anorthositic diapirism has been based on published values of rheological parameters for the power law, on the computation of a rheological profile using simplifying assumptions (thermal steady state, constant strain rate), on a geometric model which is coherent with the rheological profile, and on the use of a constitutive model with a simple linear viscosity. Despite its high degree of simplification compared to geological processes and also its uncertainties, the results obtained show that the diapir model for the emplacement of the EGOG anorthosite massif is a mechanically relevant assumption.

A reasonable estimation of the diapir emplacement timing has been found (about 2.5Ma) with the estimated viscosities.

Moreover, the axisymmetric analysis allowed to follow the evolution of the strain tensor, especially the circumferential strain component which becomes the predominant extension component during the flattening phase near the diapir lateral margins. A good comparison with the measured maximum stretching directions is observed, together with the presence of a rim-syncline in the surrounding rocks as attested by passive strain markers.

As possible improvements which could be carried out to such modelling, one can invoke :

- the coupled thermomechanical analysis which would allow to take into account the thermal exchanges between the diapir and surrounding rocks, i.e. the cooling of the diapiric mush and the induced heating of the lower crust. In such analysis, the main effect is likely to be the thermal effect on the mechanical behaviour through the power law equation (7.2). Of course these effects should be non-negligible as they affect the media viscosity. It should lead to an increase of the anorthosite viscosity and to a decrease of the lower crust viscosity.
- From a thermomechanical simulation, a petrological model of phase changes during crystallisation could also be used following a procedure similar than the one presented in [HABRAKEN, 1989].

Non-linear viscosities could also be considered in new models in order to evaluate their influence on the final shape and emplacement timing.

CHAPTER 8

The Garret El Gueffoul anticline structure : faulting and fracturing

8.1 Introduction

In this chapter, a study of faulting and fracturing of the Garret El Gueffoul hydrocarbon trap (Algeria) is presented. The geological interpretation of this field case is mainly based on seismic and borehole data, and on some additional assumptions. These assumptions result from similarity rules often used in geology, based on comparison with well known field cases. The mechanical modelling provides a tool which is able to confirm or infirm the validity of geological assumptions. Thus it can allow to increase the confidence in a particular geological interpretation with respect to potential other ones. It can also be used to study in details the evolution of strain localisation (faulting) and/or fracturing. A previous numerical study performed on this field case showed that the detachment folding hypothesis was relevant [BEEKMAN et al., 1997]. In the present work, such result is confirmed but also new results are obtained.

A brief presentation of the geological context of the Ahnet basin is presented in the first section, based on the presentation of data published in the literature.

In the second section, attention is focused on the Garret El Gueffoul anticline, for which the available data (seismic sections) are concisely presented. The problem of small scale fracturation within the Cambro-Ordovician reservoir unit, which is very important on a production point of view, is discussed. The larger scales structures may control this small scale fracturation : for instance fracturation may be different depending on its structural position with respect to the large scale structure (e.g. limb or hinge of a fold). As a result, the study of the small scale fracturation must be put back into the more general context of the domain structuration.

Consequently, two main families of 2D numerical simulations are carried out, based on radically different initial geometries. They are presented in the next two sections. The first family deals with models which are built from the present day geometry. It aims to study the post-Hercynian faulting and fracturing. The second family of simulations deals with models which are built from a plausible pre-folding phase (Hercynian). For both sets of simulations, several boundary conditions are tested, especially regarding the possible existence of a detachment fault within the basement. The influence of the mechanical heterogeneity of the sedimentary pile, especially the relative weakness of Silurian shales, is studied. The effect of geometrical heterogeneities is also considered.

In the last section, three dimensional effects are investigated in 3D simulations based on the present day geometry.

8.2 Geological settings of the Ahnet basin

8.2.1 Regional geology and stratigraphy

The Ahnet basin (central Algeria) is a large intracratonic sedimentary basin of Palaeozoic age located in the southern Algerian Sahara massif, with an important hydrocarbon potential [KLEMME and ULMISHEK, 1991; MACGREGOR, 1996]. The western border is represented by the Bled-El-Mass on the north and an extension of the Reggane basin on the south (figure 8.1). The Mole d'Arak gives the south-east limit and the Djebel d'Azzaz the north-east one. The detailed stratigraphy [BADSI, 1993] of the Ahnet basin is presented on figure 8.2 and can be divided into six main horizons :

- The basement is represented by thick *Precambrian* rocks (>540Ma) known as "séries pourpres" [BEUF et al., 1971].
- the *Cambro-Ordovician* (540-435Ma) is represented by sandstone series of thickness equal to 560m (units II, III and IV). These sandstones are very important on an economic point of view as they are the usual hydrocarbon reservoirs in south Algerian basins. However, in the Ahnet basin they are usually more compacted and cemented than in other Algerian basins, thus they do not have very high permeabilities and porosities. Consequently, they can be poor reservoirs rocks except if the natural fracturing of these formations improves substantially their petrophysical characteristics [BADSI, 1993].
- The *Silurian* (435-408Ma) is represented by a thick layer (430 to 800m) of marine shales. It represents a source rocks in the Ahnet basin.
- The *Devonian* (408-360Ma) is represented by an alternation of sandstones and shales layers.
- The *Carboniferous* (360-295Ma) is the last Palaeozoic rocks deposited in the Ahnet basin. It is represented again by shales and sandstones. The upper part of the Carboniferous is eroded in most parts of the basin.
- The *Mesozoic* sediments (<245Ma) are represented by shales and coarse sandstones which overly the Hercynian unconformity.

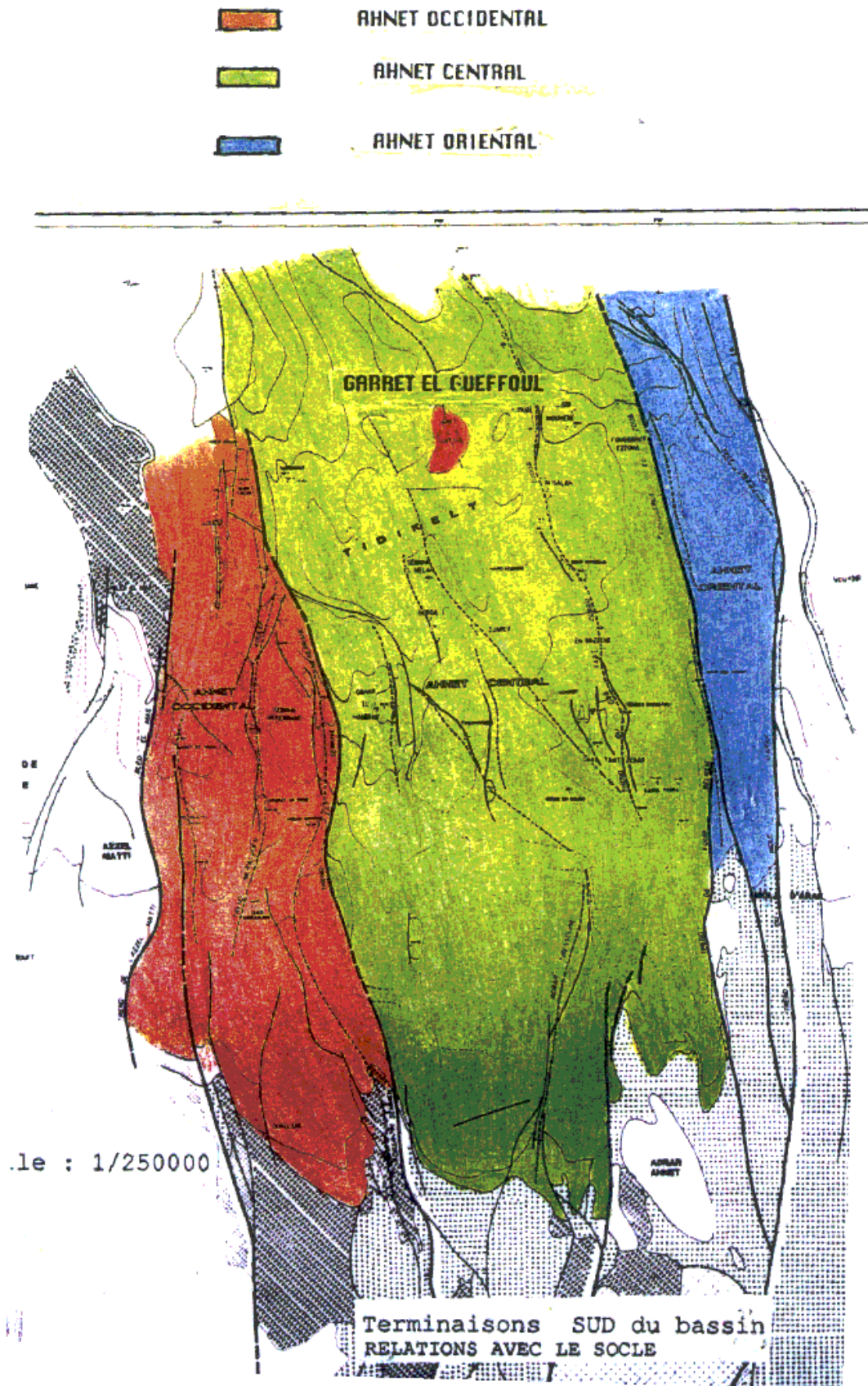


Figure 8.1 Structural interpretation of the Ahnet basin [BADSI, 1993].

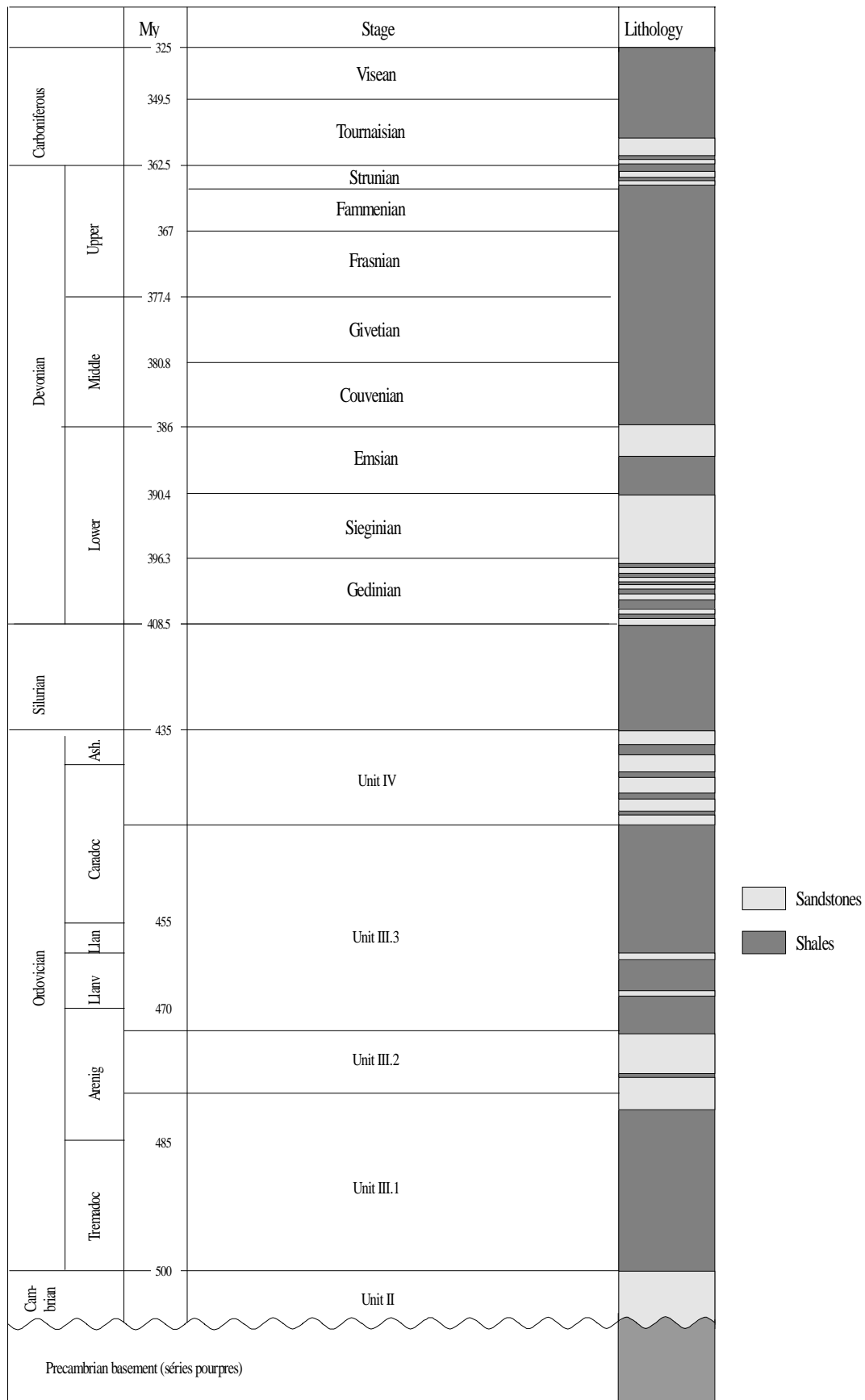
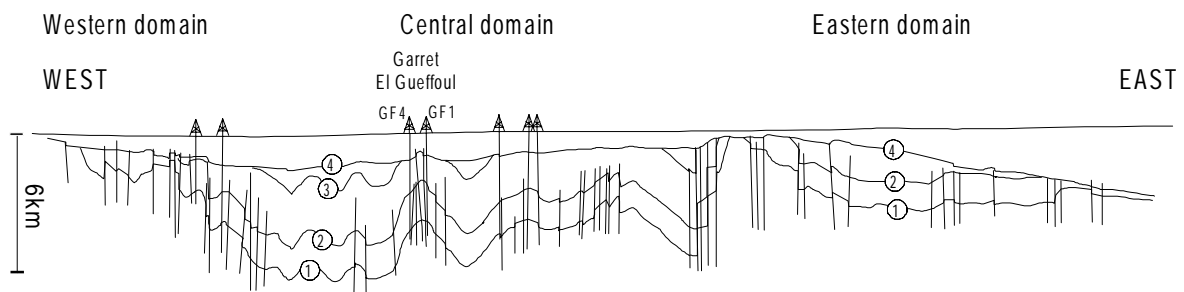


Figure 8.2 Stratigraphic column of the Ahnet basin, modified from [BADSI, 1993].

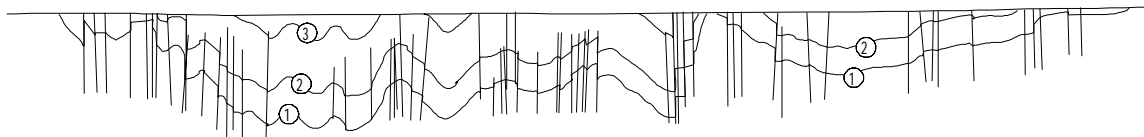
8.2.2 Palaeo-structural evolution of the Ahnet basin

The palaeo-structural evolution of the Ahnet basin is illustrated on figure 8.3 which represents an east-west cross section built from seismic and borehole data [GUIRAUD and MAURIN, 1992]. Folding in the Ahnet basin initiates at the end of the upper Devonian (figure 8.3c). The main folding and faulting phase occurs during the Hercynian phase, and it produces the first order structures of the Ahnet basin (see figure 8.3b). At this stage, the basin is clearly divided in three domains : the central domain is bounded by the uplifted western and the eastern domains. During the Mesozoic and Tertiary, additional deformation occurs in the Ahnet basin, which is evidenced by the displacement of the Hercynian discordance by some reverse faults (see figure 8.3a). An analysis of the orientation of the Hercynian faults located in the anticline limbs [BADSI, 1993] showed that they are predominantly oriented NW-SE or NE-SW, which is coherent with the two principal stress directions (N40 and N120) during the Hercynian phase.

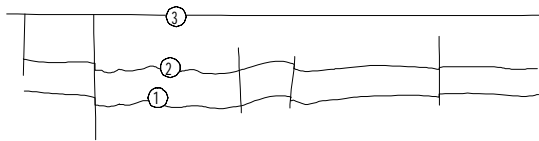
a) Present day structure



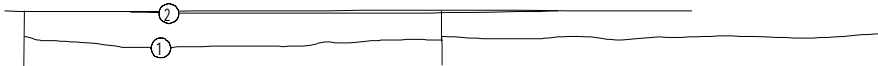
b) End of Hercynian phase



c) End of upper Devonian



d) End of middle Devonian



Scale : 36km

- ④— Hercynian discordance
- ③— Top of Tournaisian
- ②— Top of Givetian
- ①— Top of Ordovician
- ▲ Drill site

Figure 8.3 Paleo-structural evolution of the Ahnet basin, modified from [BADSI, 1993].

8.3 The Garret El Gueffoul anticline structure

8.3.1 Presentation

The Garret El Gueffoul structure is located in the northern part of the central domain of the Ahnet basin (see figure 8.1 and 8.3a). This structure is an anticline with a sub-elliptic shape (dimensions 20×30km) of Hercynian age. Figure 8.4 represents an isochrone contour map of the top Ordovician with faults interpreted from seismic. Clearly, this structure exhibits an asymmetry as the dip of the western flank is higher than elsewhere in this structure.

An east-west reflection seismic section of the Garret El Gueffoul anticline is presented in figure 8.5 (this section is located in figure 8.4). From this section, several observations can be made :

- There is no evidence of any detachment fault in the anticline Precambrian basement; thus the mechanism responsible for the formation of the Garret El Gueffoul anticline is an open question. Two assumptions can be put forward : a detachment fold mechanism and a surface buckling mechanism.
- Several secondary reverse faults have developed locally in the anticline, particularly in the western flank of the anticline. Some of these faults cut the Hercynian discordance, which indicates a post Hercynian activity. Thus, they are either post-Hercynian faults or possibly reactivated Hercynian faults.
- The data do not give any information about the reservoir small scale fracturing as the spatial resolution of the seismic method (>several tens of meters) is much higher than the scale of the reservoir fracturation (mm to cm).

8.3.2 Problems raised and aim of the modelling

Three scales of structures are of interest in the present work.

- The first scale is represented by the small scale fracturation in the Cambro-Ordovician reservoir, as it can play a key role on the production potential of the Garret El Gueffoul trap.
- The second one is the mesoscale reverse faults which seem to affect mostly the western part of the anticline. Their age is at least post Hercynian, however they could have formed at Hercynian and only reactivated latter. They are certainly important to take into account in order to evaluate correctly the small scale fracturation.
- The third one is the large scale structure of the anticline, that is the first order fold as presented on figure 8.4. As already mentioned, this scale of structure is related to the Hercynian phase and may involve a detachment fault within the basement. Again, this spatial scale may have an influence on the present day small scale fracturation which is an important concern of this study.

Although these scales of structures have been separated here, there may exist some coupling between them. For instance, both the large scale controls the lower order ones, and so does the mesoscale.

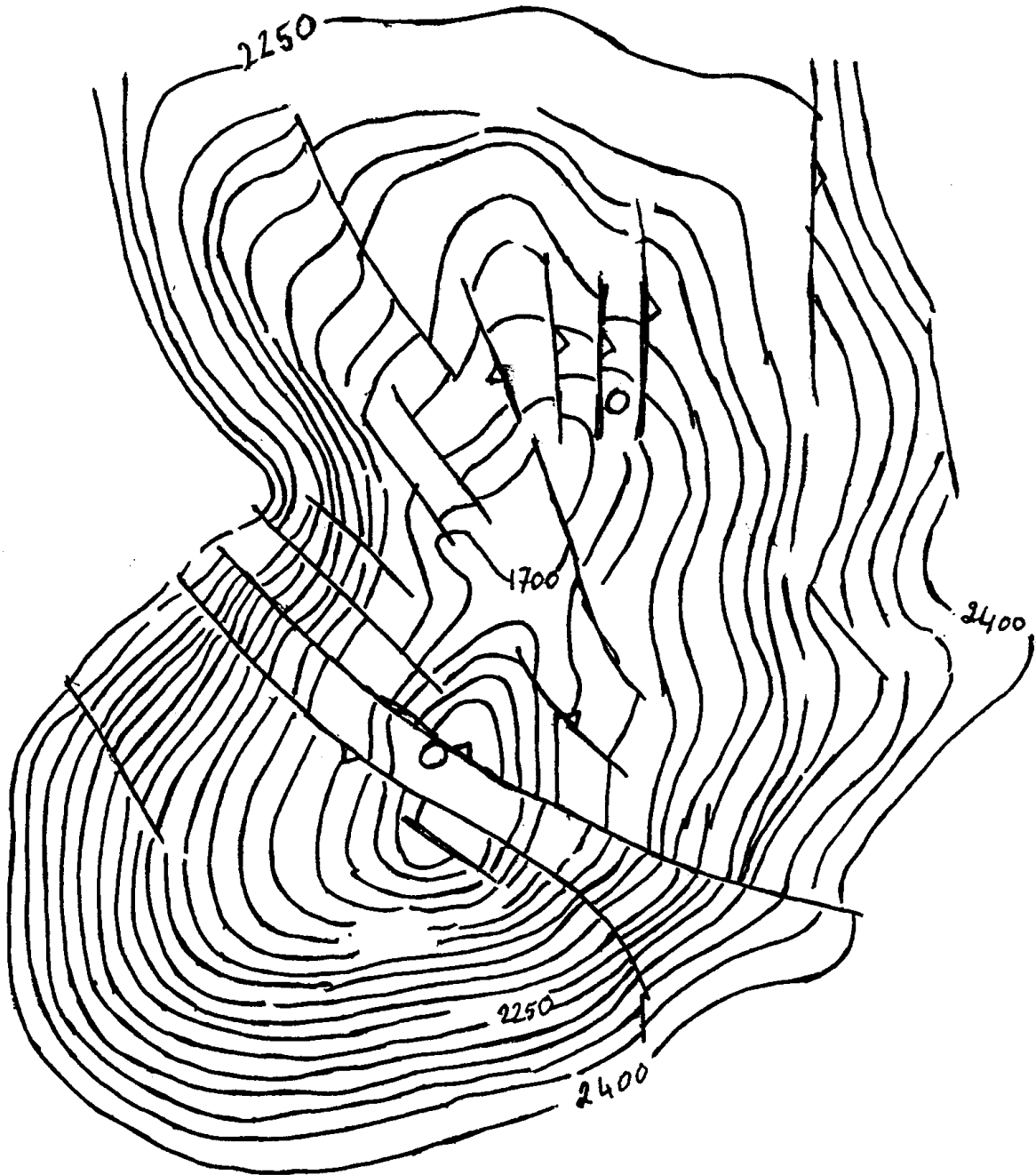


Figure 8.4 Isochrones map of the top Ordovician, from [BADSI, 1993].

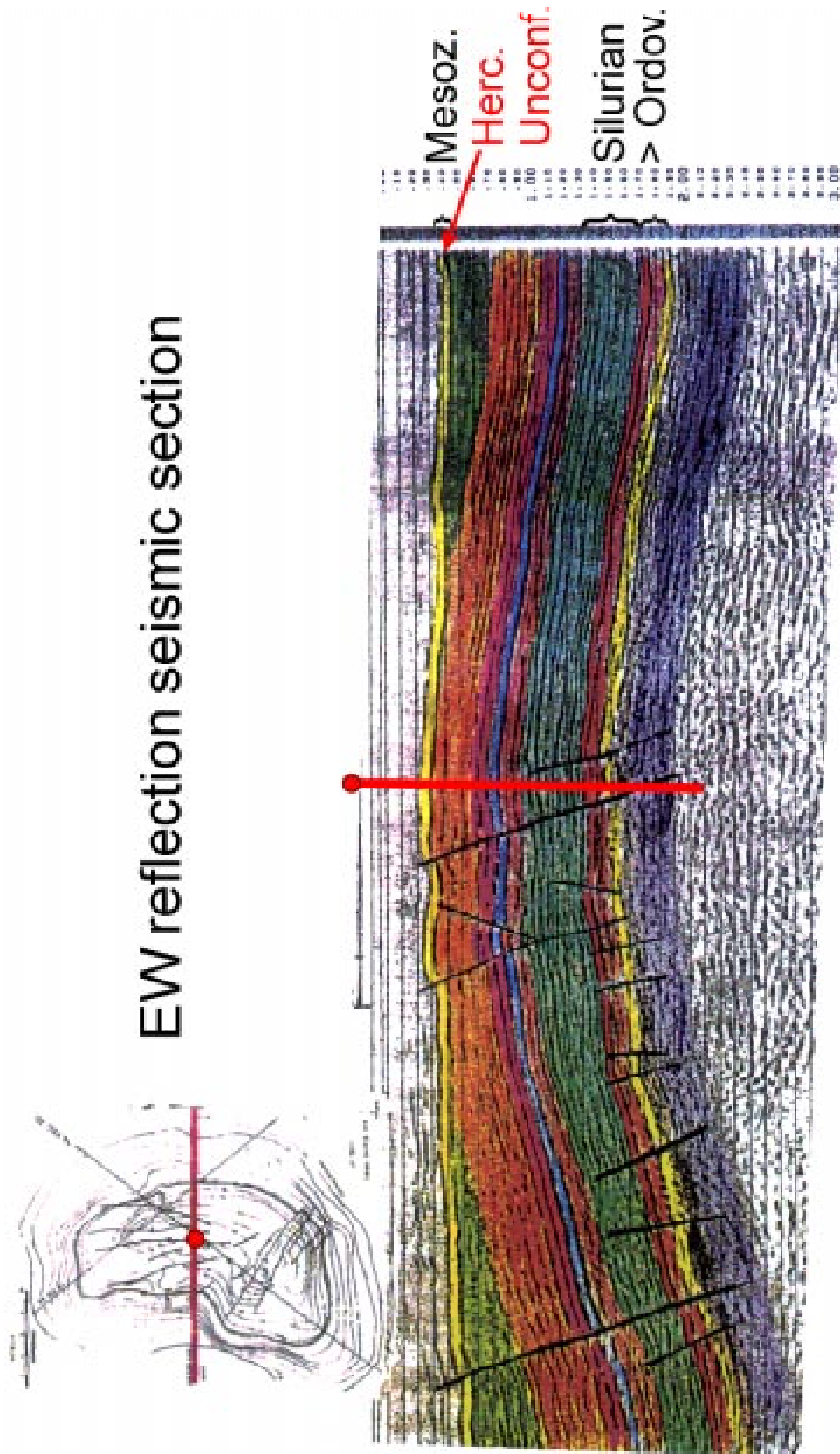


Figure 8.5 Present day east-west reflection seismic section, from [BADSI, 1993], vertical scale in two-way travel time (s).

The main concern of this study is to obtain information about the potential small scale fracturing within the Cambro-Ordovician sandstones. As this fracturing is closely related to the large and mesoscale structure of the Garret El Gueffoul anticline, its study or evaluation cannot be performed without taking into account larger scales. This last point requires to define relevant boundary conditions for the studied problem, i.e. to imagine which boundary conditions may have led to the observed structures, and also to adopt representative mechanical parameters for the rocks. The mechanical modelling allows, from several plausible models, to select the one which gives the results (mainly large and mesoscale structures) which are closest with observations, i.e. to perform a kind of an inverse analysis. If such model is found, the analysis of small scale fracturation can be carried out with a certain degree of confidence as the larger controlling scales are correctly taken into account.

The analysis of the large scale to small scale structures will be based on four criteria (see chapter 2 for a more precise description) :

- the deviatoric part of strains (or equivalent strain), which indicates locations with high values of shear strains,
- an original kinematic criterion based on the increment of deviatoric plastic strain which shows the actual strain localisation in shear bands, taking into account the boundary conditions,
- the bifurcation criterion proposed by RICE [1976] which indicates the possibility of shear band localisation and which gives the directions and mode (I or II) of the band, independently on the boundary conditions,
- the Wallace-Bott stress ratio which gives a geological interpretation of the stress tensor in terms of faulting and fracturing [SASSI and FAURE, 1997] with respect to the tectonic regime, independently on the boundary conditions.

The analysis of the large scale to mesoscale strain localisation will be based on the first three criteria, whereas the analysis of the small scale fracturing will be analysed using the Rice criterion and the Wallace-Bott stress ratio.

8.3.3 Initial geometry, boundary conditions and rheological parameters

The definition of an initial geometry for the study is not straightforward. The term "*initial geometry*" is used here as a synonym for "starting configuration of the modelling".

Present day geometry

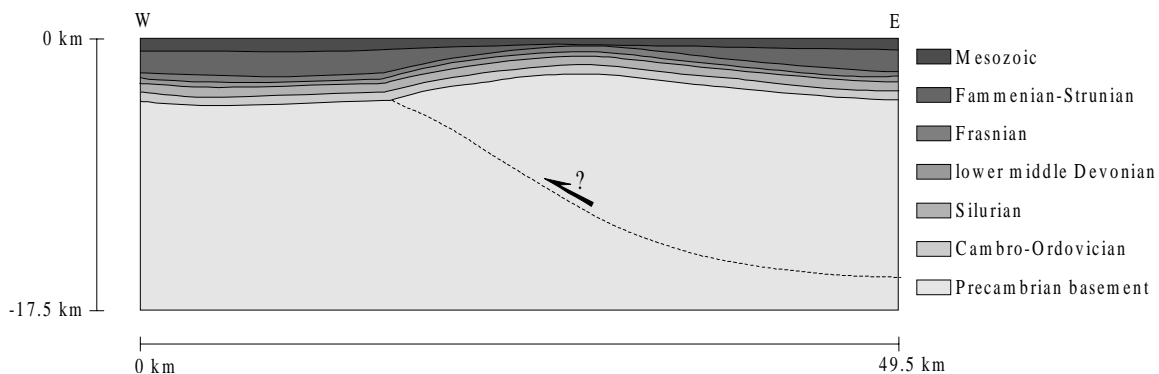


Figure 8.6 Present day east-west simplified section of the Garret El Gueffoul dome.

First of all, the initial two dimensional geometry can be chosen as the present day one, which can be obtained (see figure 8.6) from the seismic (i.e. a time) profile given in figure 8.5, performing a time-depth conversion. Note that the detachment fault is figured with a dashed line as its existence is not evidenced by the available data. In this simplified section, post-Hercynian faults have been deliberately omitted and plane strain conditions are assumed.

The main idea in this case is, from this initial geometry, to apply a loading of the same nature than the last tectonic phase responsible of the structure genesis. Here this loading can be reasonably represented by an additional displacement u along the horizontal direction (represented by the arrows in figure 8.7). It is hoped that : a) the plane strain assumption is quasi valid, b) the stress state obtained will reach a yielding state not too different from the real past stress state (at Alpine), and c) the strain localisation pattern will not be too different to the past one which was produced in the last tectonic phase. Thus, an image of the last strain localisation pattern should be obtained from such analysis. All these assumptions will be discussed latter in light of the results obtained from the simulations.

Obviously, this additional loading must be small enough to avoid a large variation of the initial geometry. As this loading cannot be uniquely defined from the available data, several boundary conditions and loading which can be investigated are presented on figure 8.7. In the first assumption (model 0, figure 8.7a), no detachment fault is assumed but a frictionless basal boundary is chosen. The second hypothesis (model 1, figure 8.7b) adds to the previous one the possibility of a fully developed detachment fault at present day. In the third and fourth hypotheses, a fixed basal boundary is assumed with either a fully developed detachment fault (model 2, figure 8.7c) or a partial detachment fault (model 3, figure 8.7d).

Such present day modelling will not test the global mechanism which produced the first order anticline. Therefore, it may be difficult to determine which boundary conditions and loading assumption are the more representative of the last loading phase and thus the more realistic.

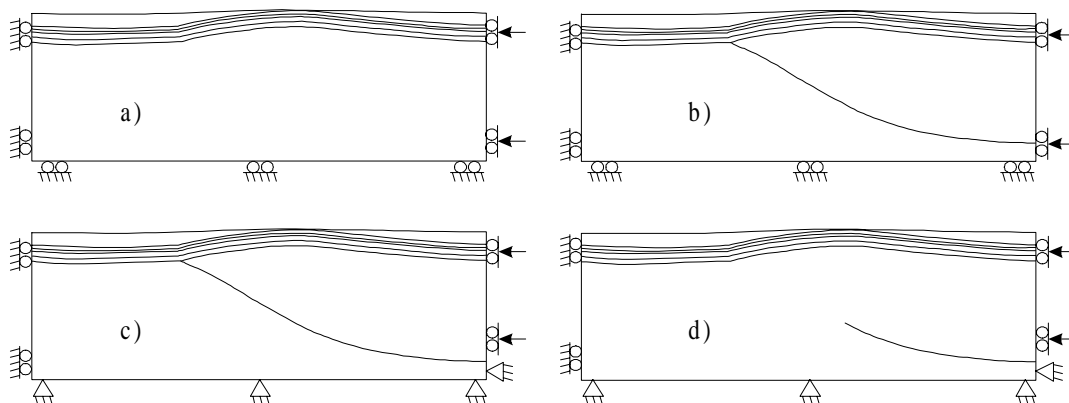


Figure 8.7 Boundary conditions and loading applied for the present day initial geometry models : a) model 0, b) model 1, c) model 2, d) model 3.

Pre-Hercynian geometry

As a first approximation and neglecting the compaction and the out of plane component of strain, it is simple to reconstruct an ideal unfolded geometry of this anticline just at the end of the Frasnian, that is prior to the main Hercynian compression. For this purpose, thickness of

the layers are chosen equal to their actual values, i.e. 550m for the Cambro-Ordovician, 610m for the Silurian, 300m for the lower to middle Devonian and 400m for the Frasnian. The resulting pre-Hercynian geometry section is presented on figure 8.8, again with a possible interpretation for the detachment fault in the Precambrian basement.

Such pre-Hercynian model can be much more helpful to test some boundary condition assumptions as there is one constraint : the geometry obtained from the chosen boundary and loading conditions must be quite close to the present day geometry, including some of its specificity (global asymmetry, possible occurrence of mesoscale faults in the western limb). The considered boundary and loading conditions are represented on figure 8.9. A fixed basal boundary is assumed with either a fully developed detachment fault (model 4, figure 8.9a) or a partial detachment fault (model 5, figure 8.9b). Plane strain condition is assumed.

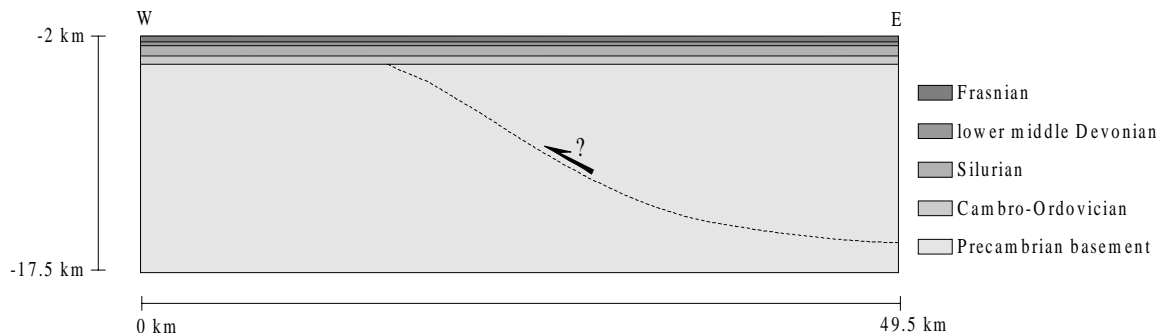


Figure 8.8 Pre-Hercynian (end of Frasnian) possible section of the Garret El Gueffoul dome.

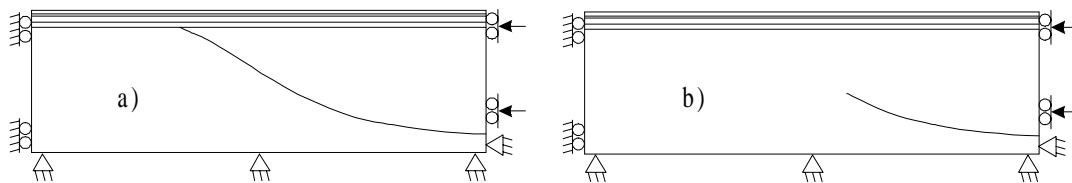


Figure 8.9 Boundary conditions and loading applied for Pre-Hercynian initial geometry models : a) model 4, b) model 5.

This Pre-Hercynian modelling can also be interesting as it will allow to follow a more complete history of the strain localisation and fracturation whereas the present-day models were only expecting to give the very last strain localisation and fracturation events.

Rheological units

Seven main rheological units have been defined, from the bottom to the top : the Precambrian basement (mainly sandstones), the Cambro-Ordovician layer (predominantly sandstones), the Silurian shales layer, the lower-middle Devonian serie of sandstone and shales, the Frasnian sandstone layer, the Famennian-Strunian shales-sandstone and the Mesozoic cover of carbonates. This last carbonate layer has not been taken into account in the simulation as it is posterior to the main Hercynian deformation event.

The mechanical properties of these units (see table 8.1) have been estimated from borehole rock samples except the cohesion c and the dilatancy angle ψ (BEEKMAN et al., 1997).

In the finite element models presented in the next sections, the mechanical behaviour of each layer has been represented using the frictional elastoplastic Van Eekelen surface described in

chapter 2 (see equations (2.96) to (2.101)) and implemented in the law *PLASOL*. When present, the detachment fault is modelled by contact-interface finite elements described in chapter 2. Their behaviour is represented by the Coulomb friction law (*COU2DC* law) described in section 2.4.2.1, with penalty coefficients $K_p=4.10^6\text{Pa}$ and $K_\tau=2.10^6\text{Pa}$ (for significance of these penalty coefficients, see equation (2.147)). Different values of contact friction μ will be used.

Table 8.1 Physical parameters

Stratigraphic unit	Density	E (GPa)	ν	c (MPa)	ϕ ($^\circ$)	ψ ($^\circ$)	Lithology
Famennian-Strunian	2.50	27.5	0.20	20	31	0	shales/sandstone
Frasnian	2.48	27.0	0.25	30	33	0	sandstone
lower-middle Devonian	2.50	27.5	0.20	20	31	0	sandstone/shales
Silurian	2.53	27.0	0.15	10	20	0	shales
Cambro-Ordovician	2.48	28.0	0.25	30	30	0	sandstone
Precambrian basement	2.48	28.0	0.25	50	36	0	sandstone

8.4 Two dimensional models from the present day geometry

The objective of the simulations presented in this section is to estimate the mesoscale faults and the small scale fracturation which occurred in the post-Hercynian times. For this purpose, several hypotheses for the boundary conditions and loading (imposed displacement u) are envisaged, and the amount of applied loading remains small (about 2% of shortening) in order to modify only a little the present day geometry. In all these cases, body forces are taken into account. An initial state of stress is computed in the *LAGAMINE* pre-processor *PREPRO* using the *INSIG* control parameter (see section 2.5 of chapter 2 for details). This stress state is not at equilibrium as the free surface is not horizontal, nor the layers interfaces):

- The lowest altitude of the free surface is $y=-620\text{m}$ and the highest is at $y=-110\text{m}$. The vertical component of stresses is computed from equation (2.155) for all the points with $g=10\text{m}\cdot\text{s}^{-2}$ and using the corresponding values of specific mass reported in table 8.1,
- the horizontal components are obtained from equation (2.156) using $K_0=0.8$.

The model is discretised with refinement within the upper 5 layers whereas in the basement the element size gets coarser (see figure 8.10). There are 2145 nodes, which define 2039 solid elements (4 nodes quadrilateral *PLXLS* with 4 integration points) and up to 16 contact elements *CNTCP*.

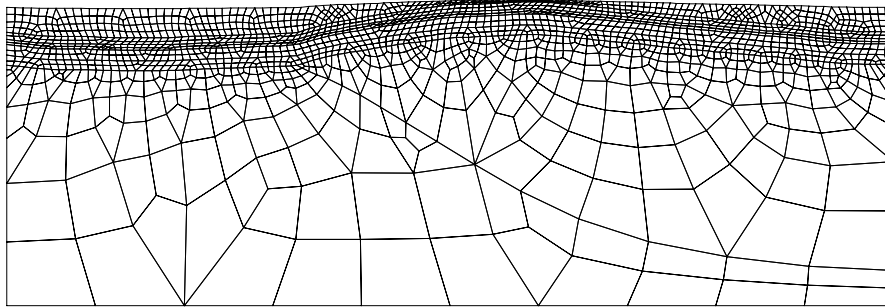
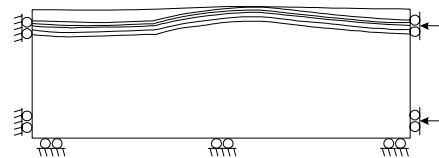


Figure 8.10 Mesh used (2145 nodes, 2039 elements) for the present day model.

The results presented further display only the top central part of the model which is of interest in this study. It corresponds to a window $x\in[8.6\text{km};41\text{km}]$ and $y\in[-9\text{km};0]$. Results are analysed in terms of mobilised friction angle ϕ_m , Wallace-Bott stress ratio R , equivalent strain ϵ_{eq} , kinematic indicator of localisation α and vertical displacements dy .

8.4.1 Model 0 with no detachment fault

In this model, there is no detachment fault. However, the basal boundary condition $dy=0$ and $\tau=0$ plays actually the role of a perfectly sliding interface, which does not have any geological relevance. The modelling requires to define geometric boundaries, and this particular one must really be seen as an arbitrary boundary of the model. It is hoped that this boundary will not perturb significantly the model around the Palaeozoic layers which represent the interesting zone to study. It must be pointed out that this model represents a limit case of the next model (see section 8.4.2) in which the detachment fault has an infinite friction coefficient ($\mu=\infty$).

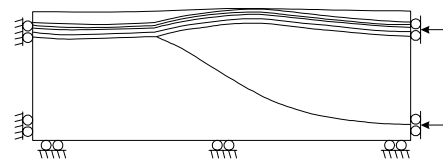


Results displayed on figure 8.11 for a shortening value $u=1000\text{m}$ ($\approx 2\%$) show that :

- The upper 4 km of the model are in plastic state (figure 8.11a) as the obtained ϕ_m values (ϕ_m is computed from equation (5.4), see section 5.3.2.1 for details) are a little larger than the friction angle values of introduced in the plastic model (see table 8.1) : for instance $\phi_m \approx 35^\circ$ in the Cambro-Ordovician sandstones and $\phi_m \approx 22^\circ$ in the Silurian shales. The top of the Precambrian basement is also at yield.
- The R ratio (see chapter 2 for details about computation of this parameter) is rather homogeneous all over the upper part of the structure (figure 8.11b) as the stress regime is mainly compressive ($R \approx 0.5$ in the shales, $R \approx 0.7$ in the sandstones). The difference observed in R between shales and sandstones comes directly from the difference in friction angles between these two rocks. An identical effect has been mentioned in [BARNICHON and CHARLIER, 1996].
- There is localisation of shear strain in the western limb of the anticline as shown by both the ϵ_{eq} and the α maps (figure 8.10c-d). There are two zones of strain concentration : the first one is located at the bottom of the western limb in the Silurian shale layer and it corresponds to the highest dip of the limb, the second one is located in the middle of the western limb and affects all the layers above the Silurian shales. These two shear strain zones correspond to backward reverse faults. It is worth pointing out that almost nothing occurs in the sandstones reservoir. There is also a background switchback pattern of the strain localisation indicator.
- There is a substantial amount of flexural folding amplification as attested by the vertical displacement map (figure 8.11e) : below the shale layer, the iso-contour lines are almost symmetrical with respect to the anticline axis and indicate that the uplift is larger in the hinge of the fold than in its limbs. However, this effect remains small as the uplift difference between hinge and limbs is lower than 10m. The main uplift is actually related to the first zone of strain localisation.

8.4.2 Model 1 with full detachment fault

The only difference between this model with the previous one lies in the presence of a detachment fault which affects the whole Precambrian basement. For this large scale fault, three values for the friction coefficient μ are considered : $\mu=0.57$, $\mu=0.15$ and $\mu=0$ corresponding to friction angle values of 30° , 8.5° and 0° , respectively. Results are presented on figures 8.12 to 8.14 for a shortening value $u=1000\text{m}$:



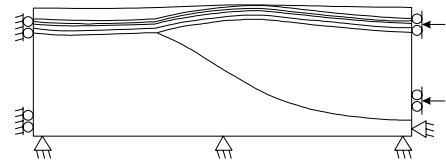
- When the fault friction is high ($\mu=0.57$), the five upper layers of the model are still at yield everywhere (see figure 8.12a), particularly $\phi_m \approx 35^\circ$ in the Cambro-Ordovician sandstones and $\phi_m \approx 22^\circ$ in the Silurian shales. Note the light spots around the detachment fault tip which indicates a local mainly isotropic tensile stress states. However, in the Precambrian basement, yielding is only occurring in the eastern part of the anticline. As the fault friction decreases ($\mu=0.15$), the central part of the sandstones and shales layer is no longer yielding (see figure 8.13a) : $\phi_m \approx 18^\circ$ in the sandstones and $\phi_m \approx 15^\circ$ in the shales. This is even more pronounced when the fault friction becomes nil (see figure 8.14a) : $\phi_m \approx 15^\circ$ in the

sandstones and $\phi_m \approx 15^\circ$ in the shales. Therefore, when the detachment fault friction decreases, the global behaviour of the central part of the anticline remains elastic.

- When the fault friction is high ($\mu=0.57$), the R ratio is again homogeneous in the upper part of the structure (figure 8.12b) and indicates a mainly compressive stress regime ($R \approx 0.5$ in the shales, $R \approx 0.7$ in the sandstones). In the central part of the anticline, as the fault friction decreases, R increases the sandstones and in the shales ($R \approx 0.9$). Thus, as the fault friction decreases, the compression stress state changes from pure compression ($R \approx 0.5$) to uniaxial compression ($R \approx 0.9$).
- In this case, the shear strain is located in two main zones (see the ϵ_{eq} and α maps on figures 8.12c-d to 8.14c-d). The first shear band is actually the extension of the basal detachment fault across the upper layers. This forward reverse fault becomes more and more pronounced as the friction coefficient μ decreases. There is an apparent westward migration of this fault which results from a separation of this main fault in two faults (see figures 8.13d and 8.14d). The second shear band appears in the western limb as a conjugate of the first fault. However, this backward reverse fault does not affect the sandstone reservoir as it initiates from the shale layer and propagates to the top. In the western limb, some other shear bands of the same type are active from time to time, as attested by the kinematic indicator α (figures 8.13d and 8.14d).
- In this case, the vertical displacement maps (figures 8.12e to 8.14e) show clearly that the main mechanism responsible for the vertical uplift is the movement along the detachment fault, as attested by the contour lines which becomes almost vertical. The highest values of uplift are related to the area limited by the two main associated reverse faults.

8.4.3 Model 2 with full detachment fault

In this model, the horizontal basis is assumed to be fixed in the two directions and a full detachment fault is assumed. Horizontal displacement are only applied to the footwall block. Two values for μ are considered : $\mu=0.57$ and $\mu=0.15$, which corresponds to friction angle values of 30° and 8.5° , respectively. Results are presented on figures 8.15 and 8.16 for a shortening value $u=1000m$:

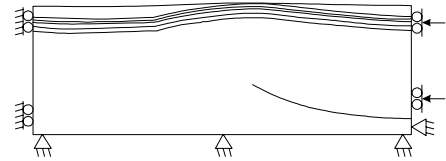


- When the fault friction is high ($\mu=0.57$), the five upper layers of the model are no longer at yield (see figure 8.15a) : $\phi_m \approx 28^\circ$ in the central part of the sandstones layer and $\phi_m \approx 13^\circ$ in shales layer. As the fault friction decreases ($\mu=0.15$), the elastic domain becomes larger in the central part (see figure 8.16a) : $\phi_m \approx 11^\circ$ in the sandstones and $\phi_m \approx 6^\circ$ in the shales. Here again, when the detachment fault friction decreases, the global behaviour of the central part of the anticline remains elastic.
- When the fault friction is high ($\mu=0.57$), the R ratio is again homogeneous in the sandstones layer (figure 8.15b) and indicates a mainly compressive stress regime ($R \approx 0.7$ in the sandstones). In the shales, the stress state indicates an isotropic compression state ($R \approx 0.2$) in the central part. As the fault friction decreases, the stress state evolves toward an uniaxial compression state ($R \approx 0.9$) in the reservoir sandstones (figure 8.16b).

- For this model, the shear strain localisation pattern is very similar to the one obtained in the previous model (fault 1 model), i.e. a conjugate set of reverse faults develops in the cover from the detachment fault tip (see the ϵ_{eq} and α maps on figures 8.15c-d and 8.16c-d). It must be pointed out that, in the western limb, several less developed backward shear bands have developed from the shale layer, as attested by figure 8.15c.
- The vertical displacement maps show that when the friction is high ($\mu=0.57$), the uplift is mainly caused by flexural folding amplification (figure 8.15e). When friction is low ($\mu=0.15$), the uplift is mainly due to the sliding along the detachment fault (figure 8.16e).

8.4.4 Model 3 with partial detachment fault

This model is similar to the fault 2 model except that here the detachment fault is not fully developed in the basement. The values $\mu=0.57$ and $\mu=0.15$ are considered. Results are presented on figures 8.17 and 8.18 for a shortening value $u=1000\text{m}$:



- Regardless of the contact friction, the whole part of the shale layer and reservoir sandstones is at yield (see figures 8.17a and 8.18a).
- For the two considered fault friction, the R ratio is homogeneous in the shales and sandstones layer with $R \approx 0.5$ (figures 8.17b and 8.18b), apart in the central part of the reservoir sandstones where $R \approx 0.7$.
- The shear strain localisation pattern is very similar to the one obtained with the first model in which there is no detachment fault (compare with figure 8.11c-d) : a first backward reverse fault initiates at the bottom of the western limb from the shale layer, a second backward fault also initiates from the shales in the middle of the limb. Note that in the case of a low contact friction ($\mu=0.15$), an additional shear band develops in the extension of the detachment fault (see figures 8.17c-d and 8.18c-d).
- The uplift affects mainly the central part of the anticline when the friction is low (see figure 8.18e) and affects all the whole footwall block when $\mu=0.57$ (see figure 8.17e).

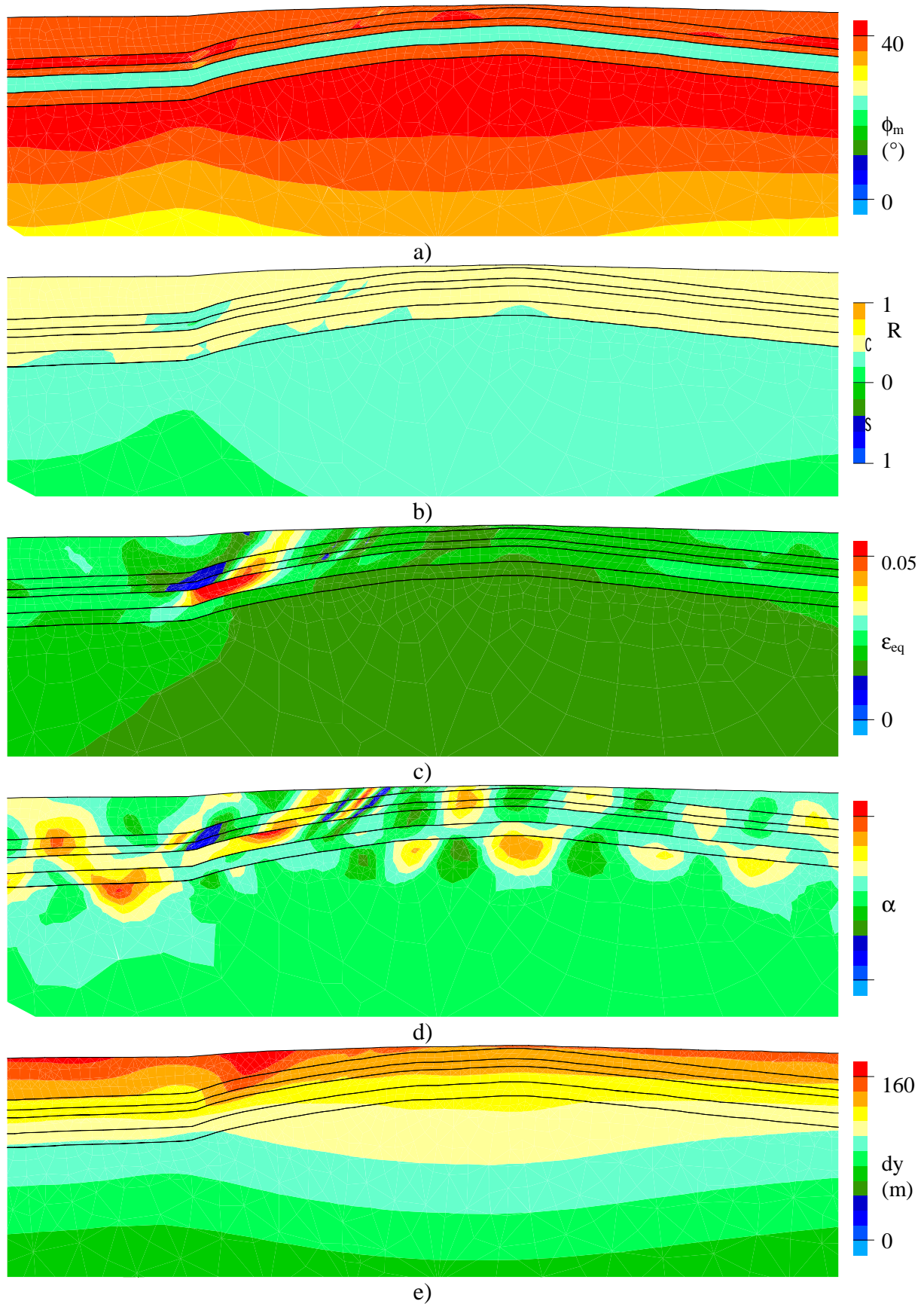


Figure 8.11 Results for model 0 (no fault) at $u=1000m$.

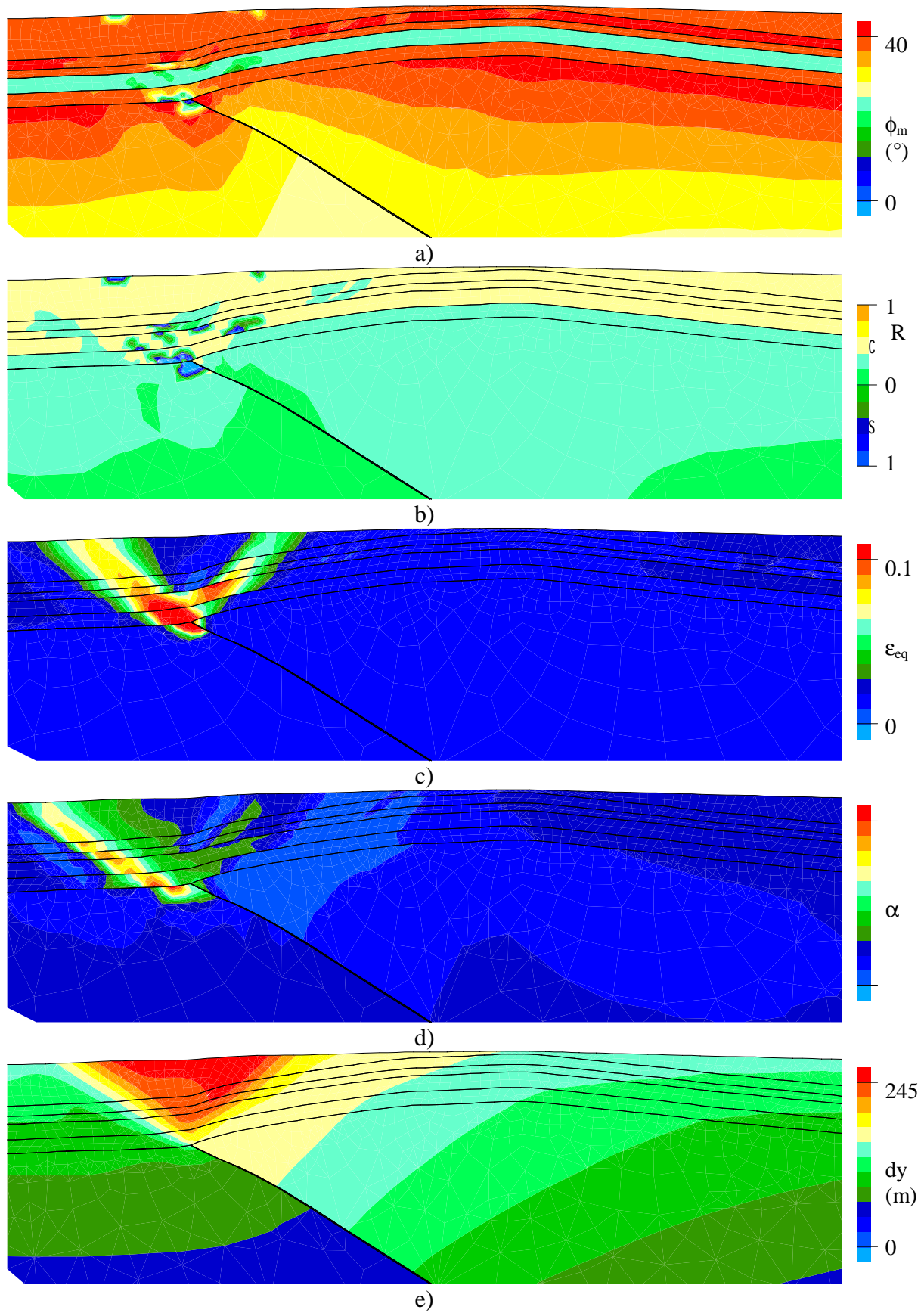


Figure 8.12 Results for model 1 (fault $\mu=0.57$) at $u=1000\text{m}$.

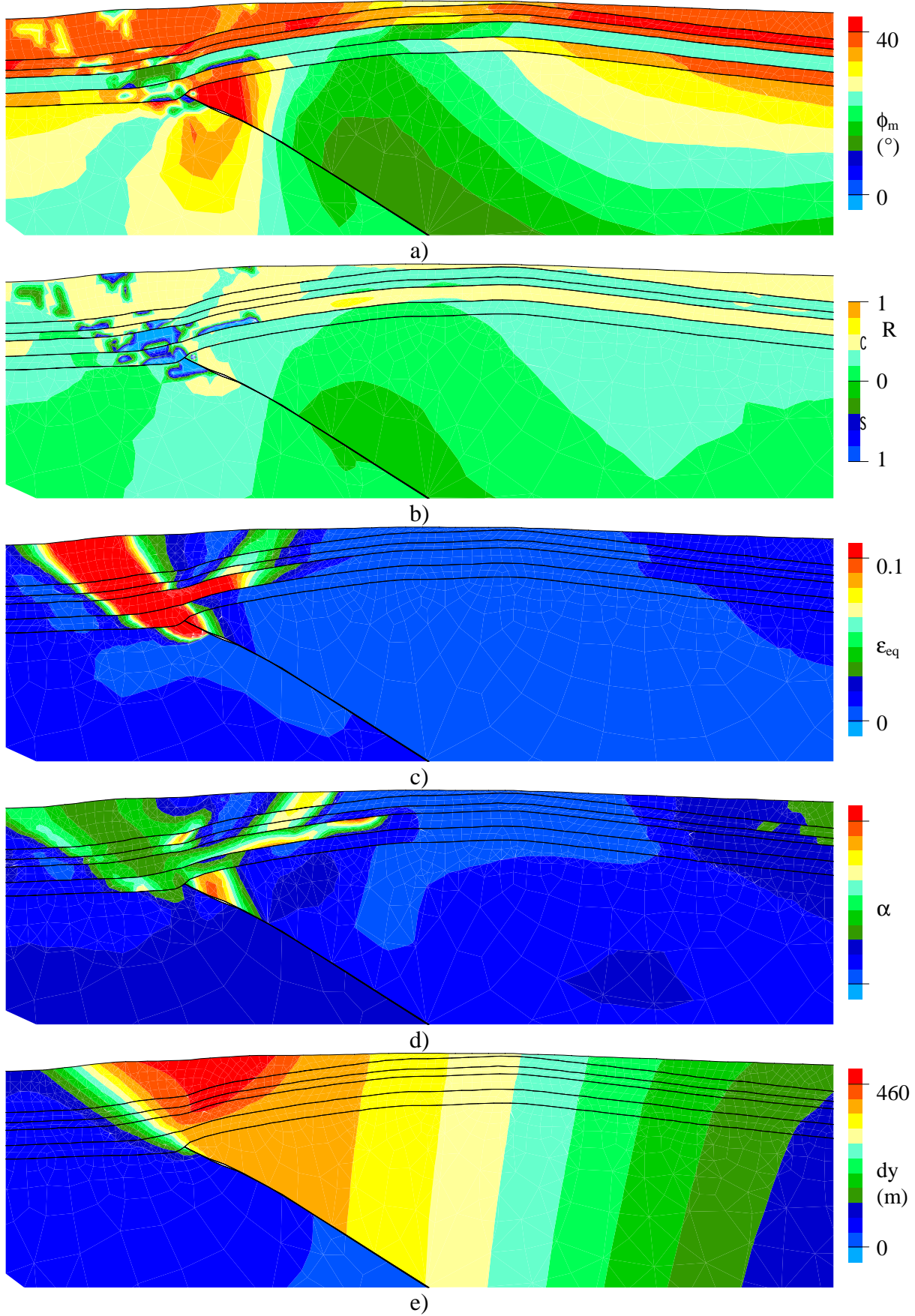


Figure 8.13 Results for model 1 (fault $\mu=0.15$) at $u=1000\text{m}$.

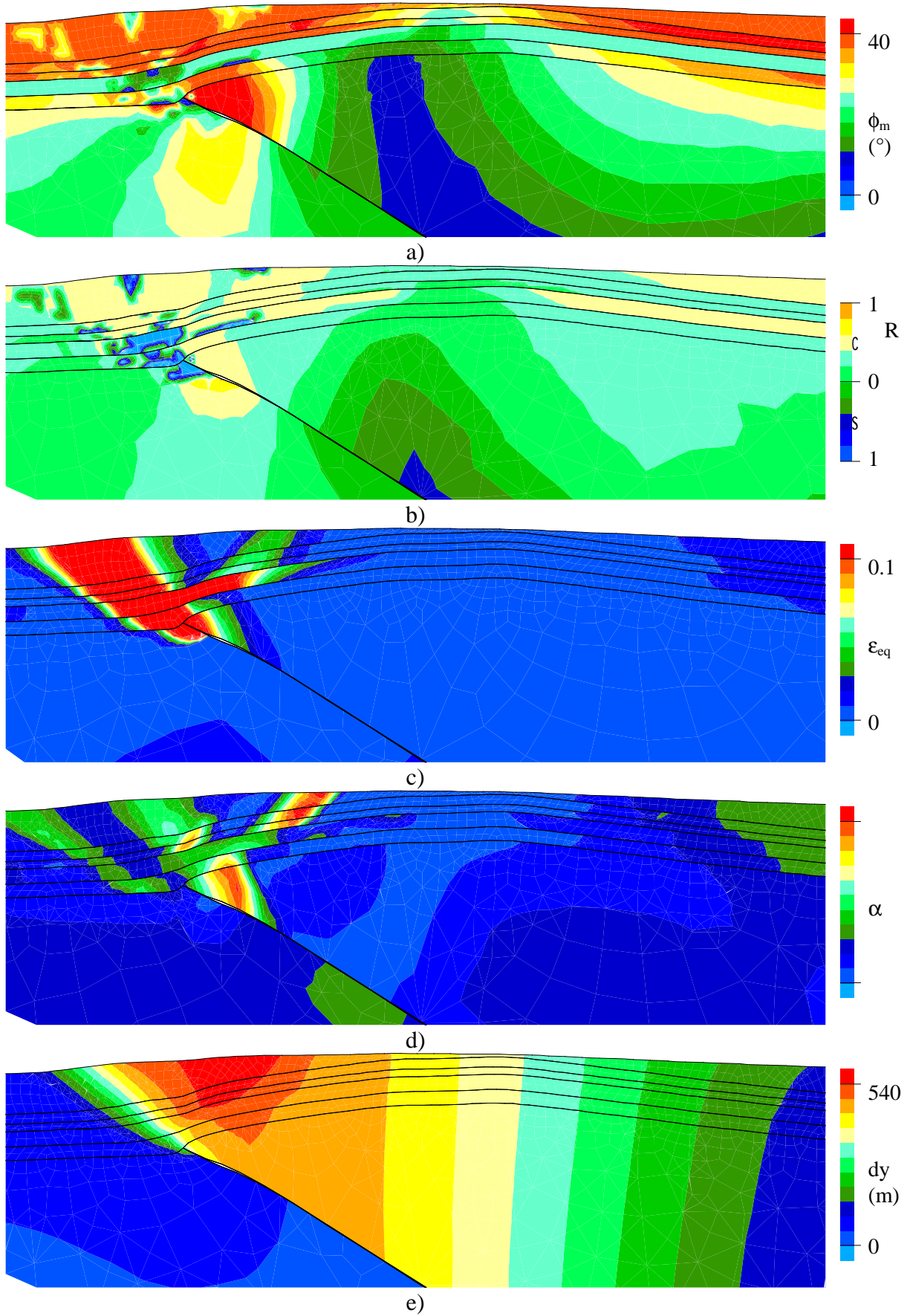


Figure 8.14 Results for model 1 (fault $\mu=0$) at $u=1000\text{m}$.

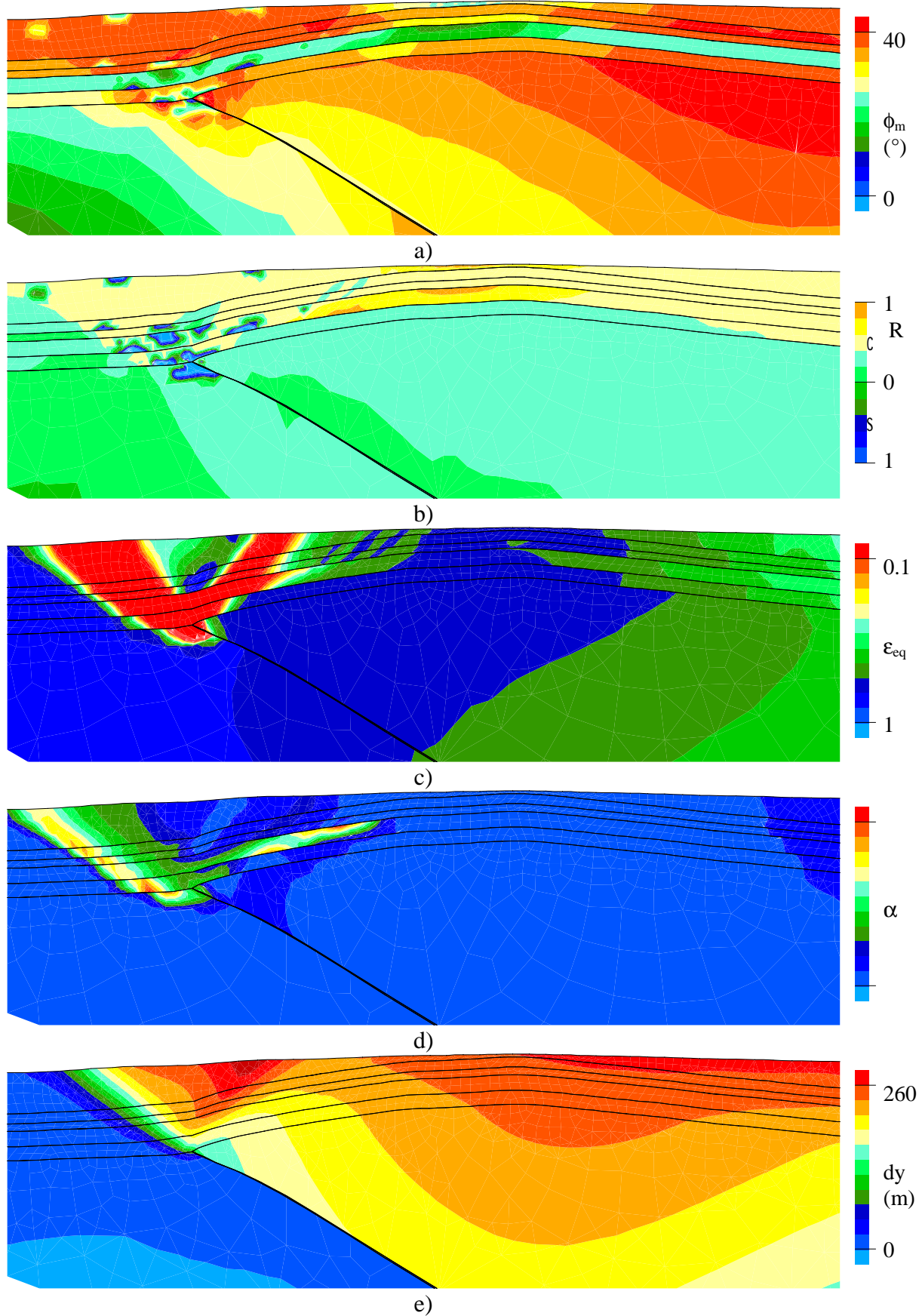


Figure 8.15 Results for model 2 (fault $\mu=0.57$) at $u=1000\text{m}$.

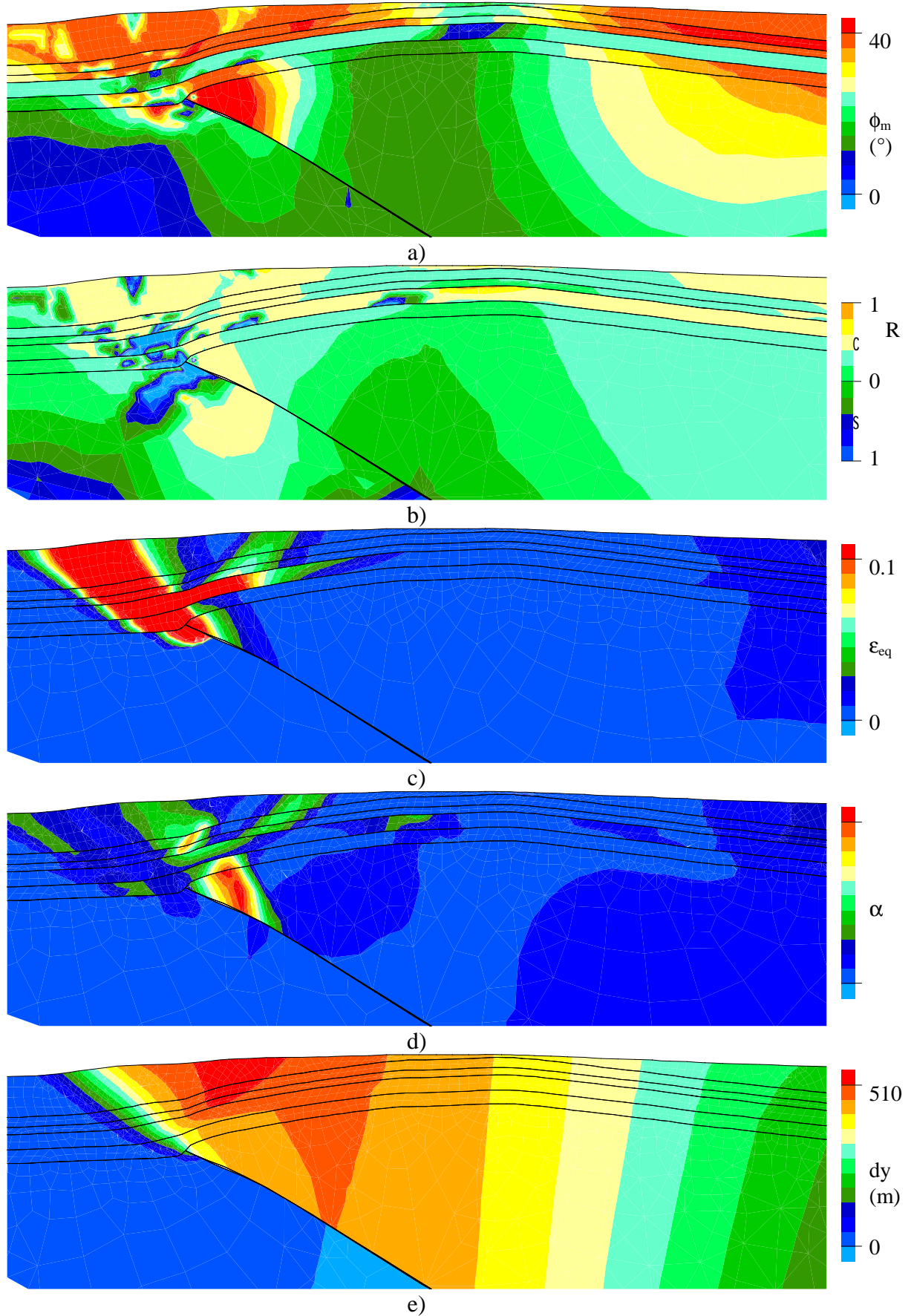


Figure 8.16 Results for model 2 (fault $\mu=0.15$) at $u=1000m$.

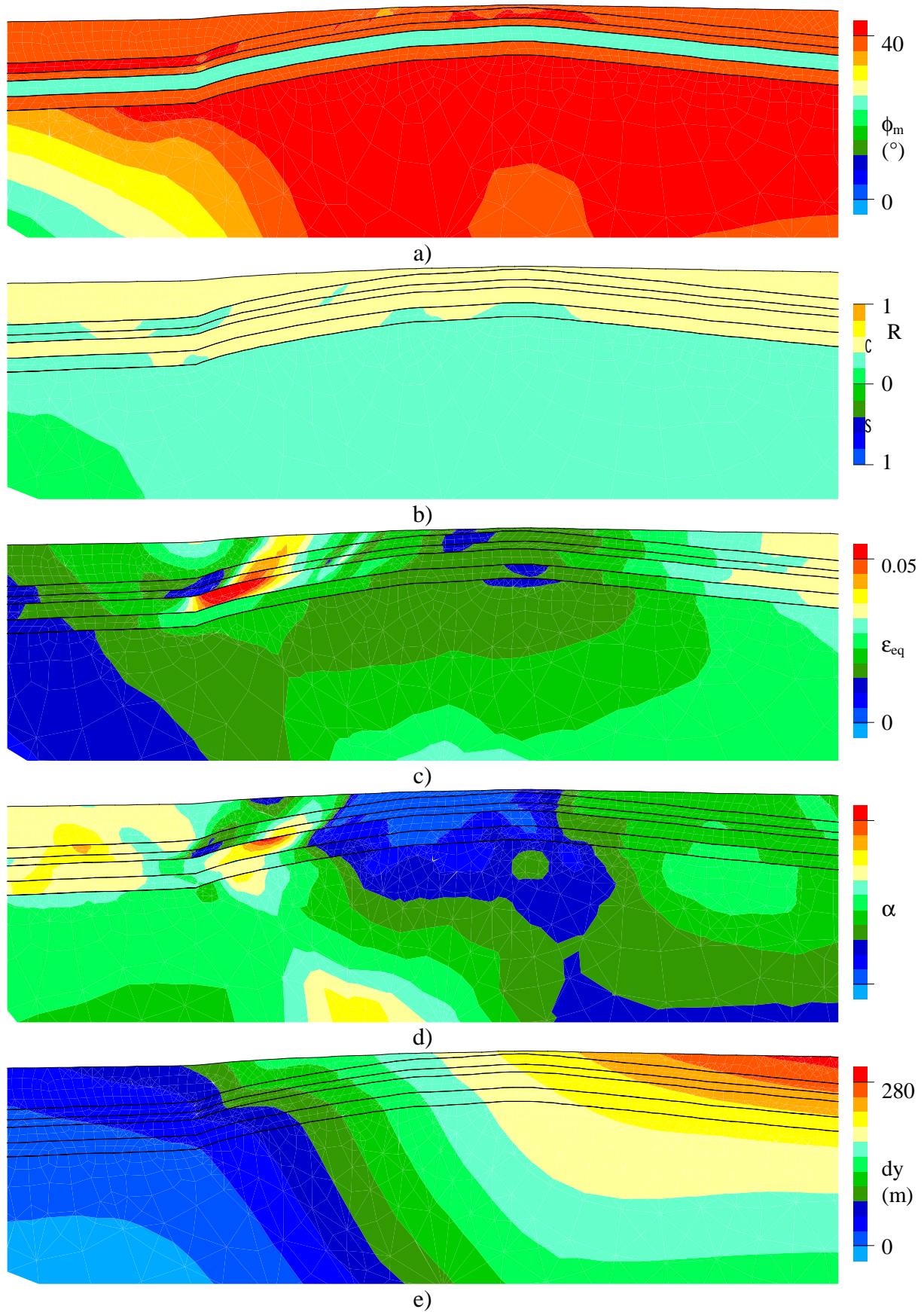


Figure 8.17 Results for model 3 (fault $\mu=0.57$) at $u=1000\text{m}$.

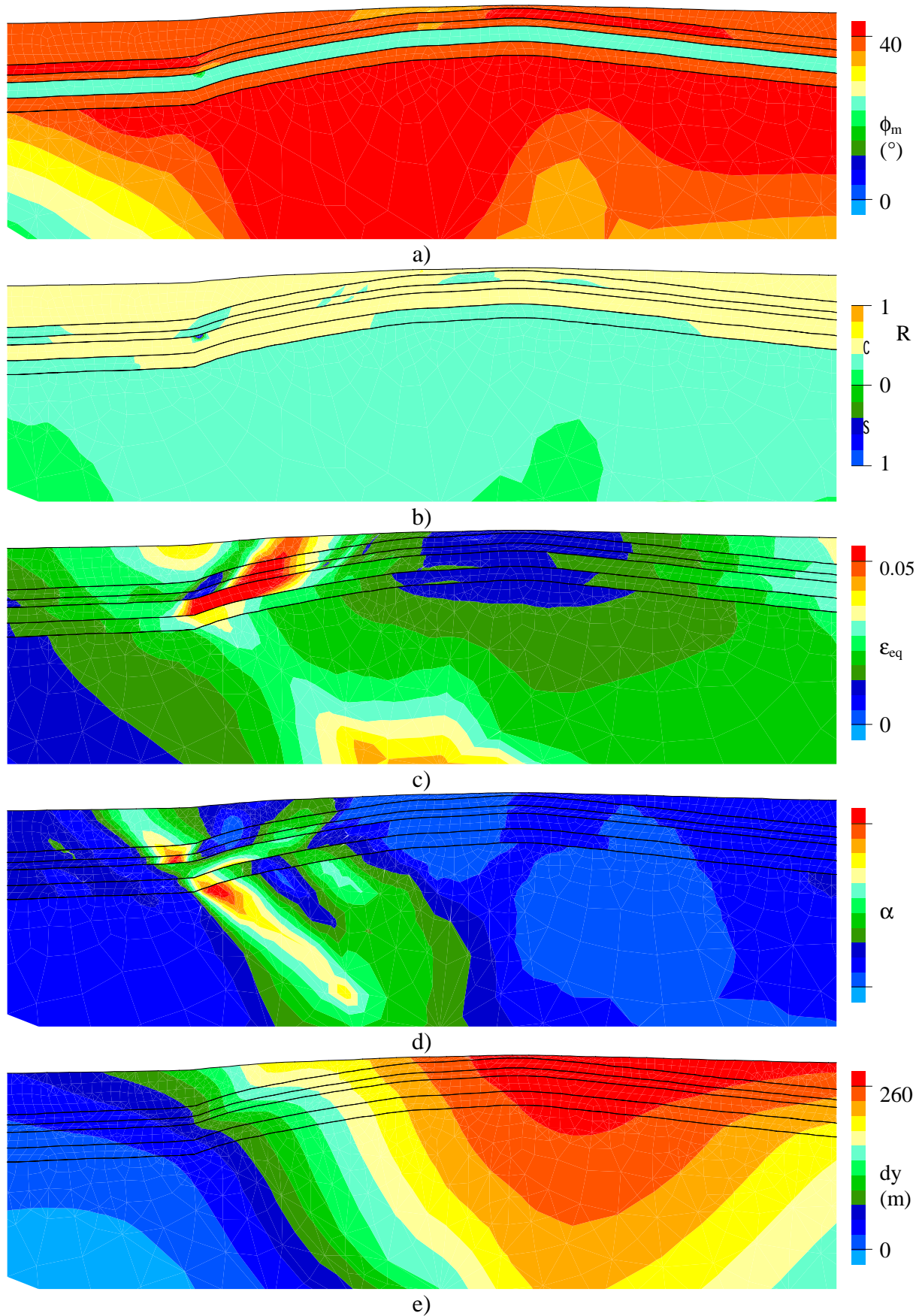


Figure 8.18 Results for model 3 (fault $\mu=0.15$) at $u=1000\text{m}$.

8.4.5 Interpretation

The structural evolution of all the 4 models computed from the present day geometry is summarised on figure 8.19. Two main families of faults can be distinguished.

- A main forward reverse fault (fault 1 on figure 8.19), which appears only in the models assuming a fully developed detachment fault (see model 1 and model 2).
- The backward reverse faults (faults 2 and 2' on figure 8.19), which appear in all the four considered models. In model 1 and 2 where there is a detachment fault, the fault 2 could be interpreted as the conjugate of fault 1. However, it does not explain why this fault does not affect the Cambro-Ordovician sandstones and why it also exists when fault 1 does not develop (model 0 and 3).

8.4.5.1 Origin of the forward reverse fault 1

The development and location of this fault can easily be explained : it represents the extension in the cover of the detachment fault when this latter is fully developed. Due to its intensity (see the map of equivalent plastic strain), this fault is likely to be a second order structure, i.e. of mesoscale importance (with an offset of about 100m). Assuming that the considered boundary conditions are representative of the last tectonic phase, there is no doubt that such structure must have developed.

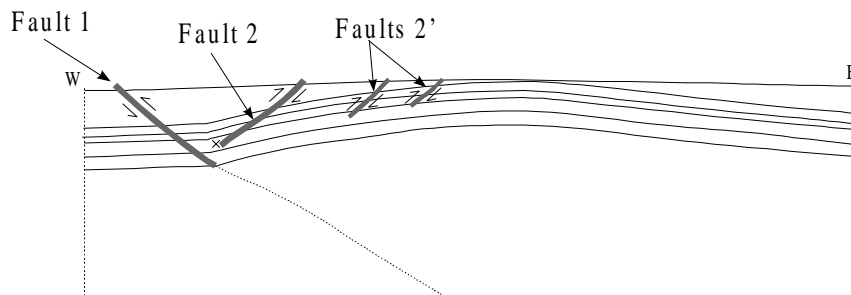


Figure 8.19 Interpretation of the observed structures in the computations from the present day geometry (model 0, 1, 2 and 3).

8.4.5.2 Origin of the backward faults 2 in the western limb

Several arguments can be put forward to explain the development of fault 2.

- First of all, from all the results presented, this fault clearly initiates at the bottom of the western limb. This location corresponds to the place where the limb dip is the largest and also where there is a rapid dip variation. This is a first geometrical heterogeneity.
- Secondly, the fault initiates within the shale which is the weaker material of the model. It represents a rheological heterogeneity.
- And last, the erosion of the upper layer created another geometrical heterogeneity, which may have induced a progressive weakening of the first order anticline.

Let us examine the relative importance of these possible mechanisms.

Effect of erosion

It can be illustrated on a simple example. Let us consider the buckling of an elastic laminated medium with a high slenderness ratio. The lower and upper surfaces are free surfaces and the internal interfaces are perfectly sliding. If body forces are neglected, the orientation of the compressive principal stress follows the boundaries of each layer (figure 8.20a). Let us assume now that the upper part is removed by an external process, leading to the geometry given in figure 8.20b. The principal stress direction will reorient such that it will be parallel to external boundaries near these boundaries. Compared to the first state (figure 8.20a), there will be a stress concentration which will be function of the ratio between the initial and the current section. Obviously, this stress concentration will be the largest in the central part where the eroded part is the largest.

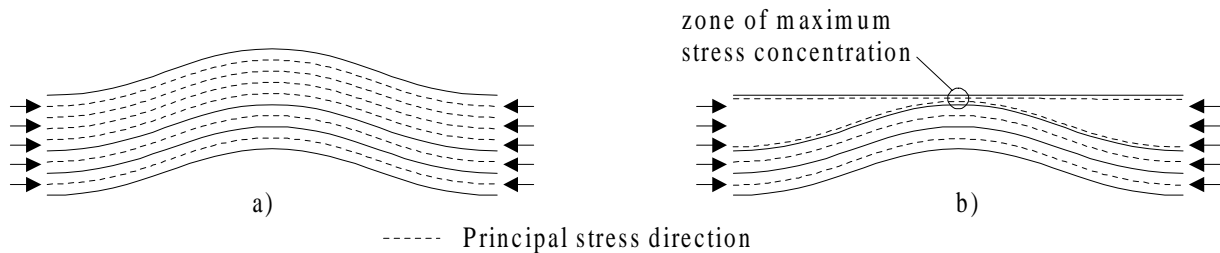


Figure 8.20 Theoretical directions of principal stresses in a buckled elastic laminated medium: a) normal state, b) after partial removing of material.

The transposition of the conclusions made on this simplistic model must be taken carefully. In the real model we are interested in, the bottom surface is not a free surface and body forces are acting. Let us consider a simplified model of the real one : the free surface is flat, density is the same for all the layers which also have the same linear elastic behaviour. In addition only infinitesimal perturbations of the geometry are considered. In this framework, the theorem of superposition is valid and can be applied. It allows to partition the stress field in two parts :

- the stress field resulting from the body forces, which using all the above assumptions is simply a function of the depth following equations (2.155). Assuming a ratio K_0 greater than 1 defines the orientation of the largest compressive stress as being horizontal as represented on figure (8.21a),
- the stress field resulting from the tectonic loading. Considering a perfectly sliding contact between layers, results in a tectonic stress field in which the principal direction are parallel to the layers boundaries (figure 8.21b1). In such an ideal case, the stress concentration would occur in the partially eroded upper layer due to the tectonic stress field, on the anticline axis. The other limit case in which no sliding (i.e. an infinite friction) occurs at the boundary interfaces can be considered. This would results in a tectonic stress field with horizontal principal directions (figure 8.21b2) which would not produce any stress concentration.

The numerical model 0 presented in section 8.4.1 is actually very similar to this last case. Thus no localisation should be observed in this model, which is not the case (see figure 8.11).

Effect of the rheological heterogeneity

It must be recalled that in all the numerical simulations carried out, all the layers have different elastoplastic parameters. Especially, the shale layer is much weaker ($\phi=20^\circ$) than the others ($31<\phi<36^\circ$). This means that during loading, the shale is likely to reach its yield limit before the other layers, although the elastic parameters have also an influence on this phenomenon. The influence of the rheological heterogeneity has been studied in additional computations. The shale layer seems to act here as a mechanical de-coupling layer in the western limb : the mesoscale faults affect only the overlying layers, but not the underlying Ordovician sandstones. Does this de-coupling behaviour mainly related to the shale layer weakness or to the fold asymmetry?

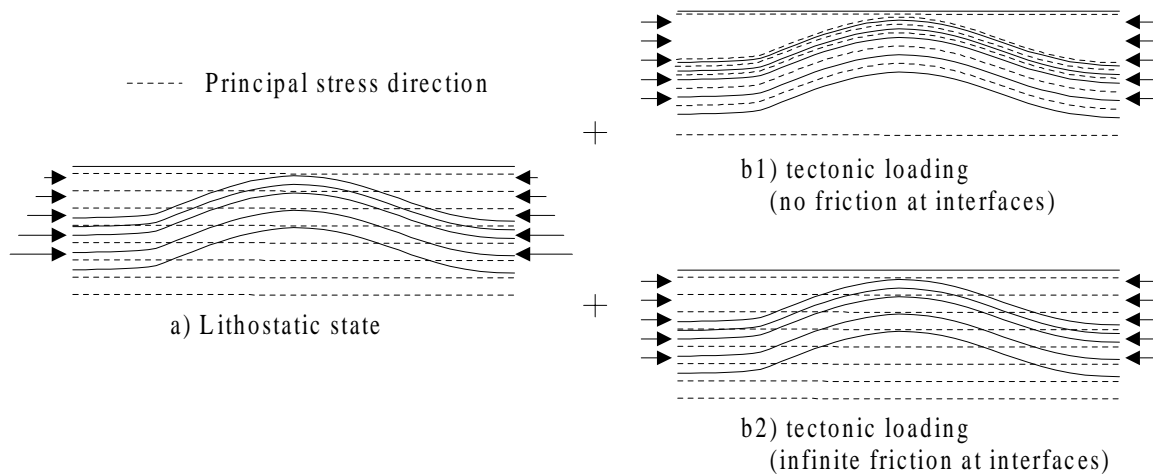


Figure 8.21 Superposition of two state of elastic state of stress for an idealised model of the Garret El Gueffoul : a) lithostatic state, b1) tectonic loading with no friction at interfaces, b2) tectonic loading with infinite friction at interfaces.

In order to answer this question, the significance of the friction for the shale must be discussed. The friction angle values considered in all the models have been measured from borehole rock samples at present time. Considering the behaviour of these rocks some 300Ma ago is a very difficult task which has not been tackled here. However, the rock type which is likely to have its behaviour modified the most significantly are the shales, following the so-called compaction process. Compaction results mainly from the water expulsion from an originally water saturated sample. For instance, the shales porosity can be as high as 0.9 at sedimentation [HEDBERG, 1936] whereas after compaction it can go down to 0.2. It results that a shale is generally "weaker" when it is less compacted. Mechanically, it traduces be a low friction angle for theses rocks. A shales friction angle value of 20° was used in the computations presented so far.

Additional simulations with the four models (models 0 to 3) have been performed with a decreased shale friction angle $\phi=10^\circ$. As it could have been guessed, the same type of backward reverse faults 2 and 2' have been obtained in all the cases.

Other simulations have been carried out from model 0 only. In a first one, the main rheological discontinuity has been removed by choosing a shale friction angle $\phi=30^\circ$. The result shows that strain localisation still occurs in the western limb. Same results have also

been obtained considering a shale behaviour identical to its overlying layer. Thus, the weakness of the shale is not responsible on its own of the strain localisation occurring in the western limb. In a last simulation, the five upper layers have been considered with a unique behaviour, i.e. no rheological discontinuity was present in the cover. Only in this case, there is no longer strain localisation in the western limb.

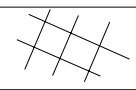

As a conclusion, the origin of the reverse faults located in the western limb is not controlled to the first order by either geometrical (erosion and asymmetry) nor rheological heterogeneities. It is the conjunction of these factors which seems responsible of the location of faults 2 and 2'.

8.4.5.3 Loading direction, plane strain assumption

In all the presented models, the plain strain assumption is made and a shortening along the East-West direction is applied. This loading can represent reasonably a tectonic phase with a N90 orientation. However, it is interesting to investigate the influence of the orientation of the principal direction of the tectonic event on the strain localisation field. The three dimensional analyses presented further in section 8.6 will enable to study this aspect and will also remove the plane strain constraint.

8.4.6 Implication for the reservoir fracturing

For all the models carried out from the presented geometry and presented so far, several indicators (directions and mode computed from Rice criterion, Wallace-Bott stress shape ratio and kinematic indicator of localisation) which characterise the potential fracturing mode within the shales and sandstone layer are summarised on figure 8.22.

East anticline limb				
	n (Rice)	s (Rice)	R	α
Shales		-0.17 (mode II)	0.5	X
Reservoir		-0.44 (mixed mode -I/II)	0.7	X

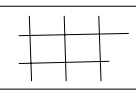

West anticline limb				
	n (Rice)	s (Rice)	R	α
Shales		-0.16 (mode II)	0.5	Localisation
Reservoir		-0.43 (mixed mode -I/II)	0.7	X

Figure 8.22 Summary of several indicators characterising the potential fracturing mode within the Silurian shales and Cambro-Ordovician sandstone layers for the present day models.

In all the models, two domains have been distinguished. The first one, corresponding to the eastern limb of the anticline, shows that a mixed mode (-I/II) of bifurcation is possible (from Rice criterion) within the reservoir sandstone, with 2 conjugate directions oriented at approximately 35° to the bedding plane. In the shales, the angle between the conjugate

directions are at an angle $\approx 90^\circ$, and they are rotated with respect to the bedding plane. The second one, corresponding to the western limb, shows that similar bifurcation mode and orientation than in the eastern limb is predicted within the reservoir sandstone and shale cover, but that direction in shale cover is now parallel and normal to the bedding plane. It traduces the large intensity of deviatoric strain mentioned in the previous sections. In both domains, the Wallace-Bott stress shape ratio R indicates mainly a purely compressive tectonic stress regime ($R \approx 0.5$ with $\sigma_v \approx \sigma_3$).

8.4.7 Conclusion

In all the simulations carried out so far, it is implicitly assumed that initial state is virgin of any plastic strain and does not have pre-existing discontinuities or weakness zones. It implies that, even if Hercynian faults developed during the anticline formation, these early faults were no longer acting as weakness planes during the Alpine phase. For instance, one could invoke a full sealing of these faults between Hercynian and Alpine phases.

Under this assumption of no pre-existing weakness planes, the numerical results show that backward reverse faulting (faults of type 2 on figure 8.19) must have developed in the western limb provided some rheological heterogeneity exists (which they do), and for all the considered boundary conditions. If the shale layer exhibits a low friction angle, it acts as a mechanical de-coupling layer. In the western limb, the mesoscale faults affect mostly the overlying layers, but not the underlying Ordovician sandstones. When assuming that the shales exhibit high friction and that some slight rheological discontinuities exists between the 5 upper layer, the backward reverse faulting is still predicted in the western limb. The only way to avoid such strain localisation is to consider that the five upper layers all have the same mechanical properties, i.e. no rheological heterogeneity exists in the cover (which is a rather unrealistic assumption).

Although the numerical results predict that such type of reverse faulting should have been very active during the Alpine phase, this is not really observed in the seismic section of the Garret El Gueffoul anticline (figure 8.5). The interpreted faults affect the whole part of the western limb, but most of them are forward reverse faults and not backward ones. Also, no faults actually initiate from the Silurian shales. Two arguments can be put forward to explain this discrepancy between the numerical results and the observations :

- The assumed boundary condition and/or loading may be unrealistic compared to the real ones. However, several reasonable types of boundary conditions have been tested together with a potential detachment fault and they all lead to the same results regarding faults 2.
- The assumption of a present day virgin state may be erroneous, i.e. the assumption that the Hercynian faults (if exist) were no longer weakness planes at Alpine may be wrong. In this case, it may be interesting to study the formation of the anticline itself during the Hercynian phase and to check which type of Hercynian faults should have formed at that time. It could help to conclude on the origin of the forward faults observed on seismic, i.e. whether they formed or only reactivate at Alpine. To this aim, simulations of the anticline genesis from the pre-Hercynian geometry are carried out and presented in the next section.

8.5 Two dimensional models from the pre-Hercynian geometry

These simulations aim to study the Hercynian faults which may have developed during the formation of the Garret El Gueffoul anticline. To this purpose, one hypothesis for the boundary condition and loading (imposed displacement u) is made (see figure 8.9). As previously mentioned, the layer which is eroded at present day is not considered. With these assumptions, it is hoped that a geometry quite similar to the present day one will be obtained, both regarding its asymmetry and folding amplitude which is about 1800m at present day.

The model is discretised with refinement within the upper 4 layers whereas in the basement the element size is coarsened (see figure 8.23). There are 2409 nodes defining 2267 solid elements (4 nodes quadrilateral *PLXLS* with 4 integration points) and up to 18 contact elements *CNTCP*.

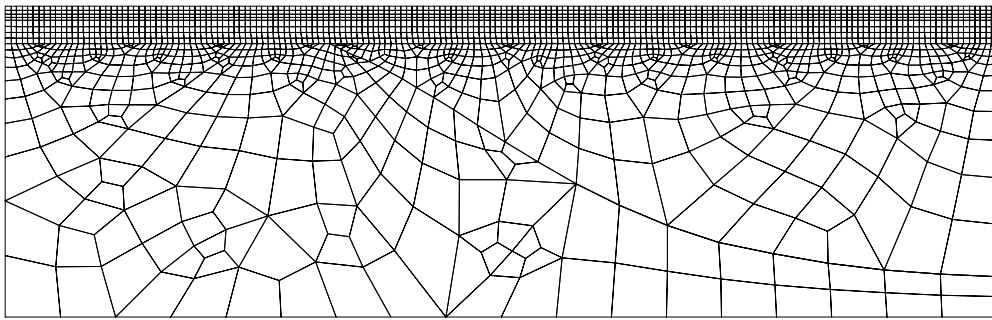


Figure 8.23 Mesh used (2145 nodes, 2039 elements) for the pre-Hercynian model.

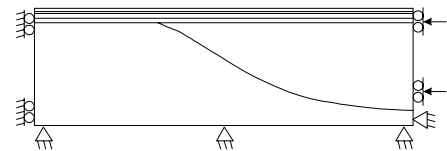
A balanced initial state of stress is computed in the *LAGAMINE* pre-processor from equations (2.155) and (2.156), with $g=10\text{m.s}^{-2}$, $K_0=0.8$ and using the values of specific mass reported in table 8.1. The loading (corresponding to a horizontal displacement u) has been applied until the folding amplitude was about 1800m.

The results presented further display only the top central part of the model which is of interest in this study. It corresponds to the same window as previously ($x \in [8.6\text{km}; 41\text{km}]$ and $y \in [-9\text{km}; 0]$).

Results are analysed in terms of equivalent strain ϵ_{eq} , kinematic indicator of localisation α and Rice bifurcation indicator.

8.5.1 Model 4 with full detachment fault

In this model, the horizontal basis is assumed to be fixed in the two directions and a full detachment fault is assumed. It is equivalent to say that the detachment fault was already present at the beginning of the Hercynian phase. Horizontal displacements are only applied to the footwall block. Two values for μ have been considered : $\mu=0.57$ and $\mu=0.15$, which correspond to friction angle values of 30° and 8.5° , respectively. Results are presented on figure 8.24 for two shortening values, considering the model with high friction coefficient :



- The obtained structure consists in a drape folding of the four layers which overly the fault tip. Such fold results from the bending of the layers induced by the fault sliding. Obviously

its geometry and wavelength is far from the observed present day geometry of the Garret El Gueffoul (see figure 8.6).

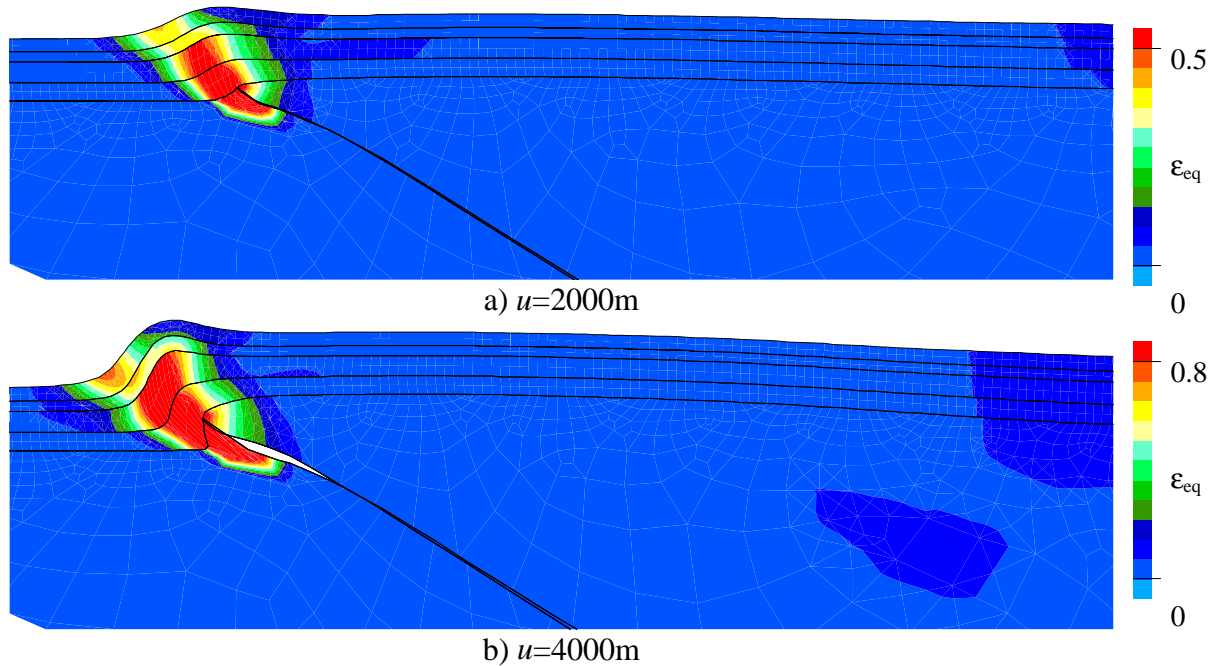


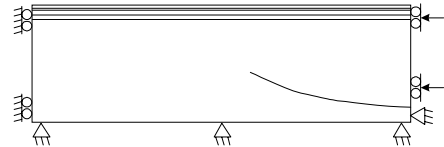
Figure 8.24 ϵ_{eq} for model 4 (fault $\mu=0.57$).

- The corresponding equivalent strain field (see figure 8.24) is too much localised to have any similarity with the present day geometry.

Of course, this drape folding is even more pronounced in the model with a smaller friction.

8.5.2 Model 5 with partial detachment fault

This model is basically similar to model 4 except that the detachment fault is only assumed to be partially developed here. As previously, this fault is supposed to be already present at the beginning of the Hercynian phase. The same μ values have been considered ($\mu=0.57$ and $\mu=0.15$). Results are presented on figures 8.25 to 8.32 for different amount of shortening :



- The evolution of the equivalent plastic strain is shown on figures 8.25 and 8.26 for the high and low friction model, respectively. It is very similar in the two models : a forward shear band appears as an extension of the detachment fault in the basement. As the loading increases, the shear band gets wider. Combined with the formation of a conjugate reverse shear zone in the eastern part, the main zone of strain concentration progressively defines the western limb of an anticline. The structure obtained at $u=4000m$ corresponds to an asymmetrical anticline with approximately 1780m of amplitude. Both the obtained amplitude and geometry are very similar with the present day ones.

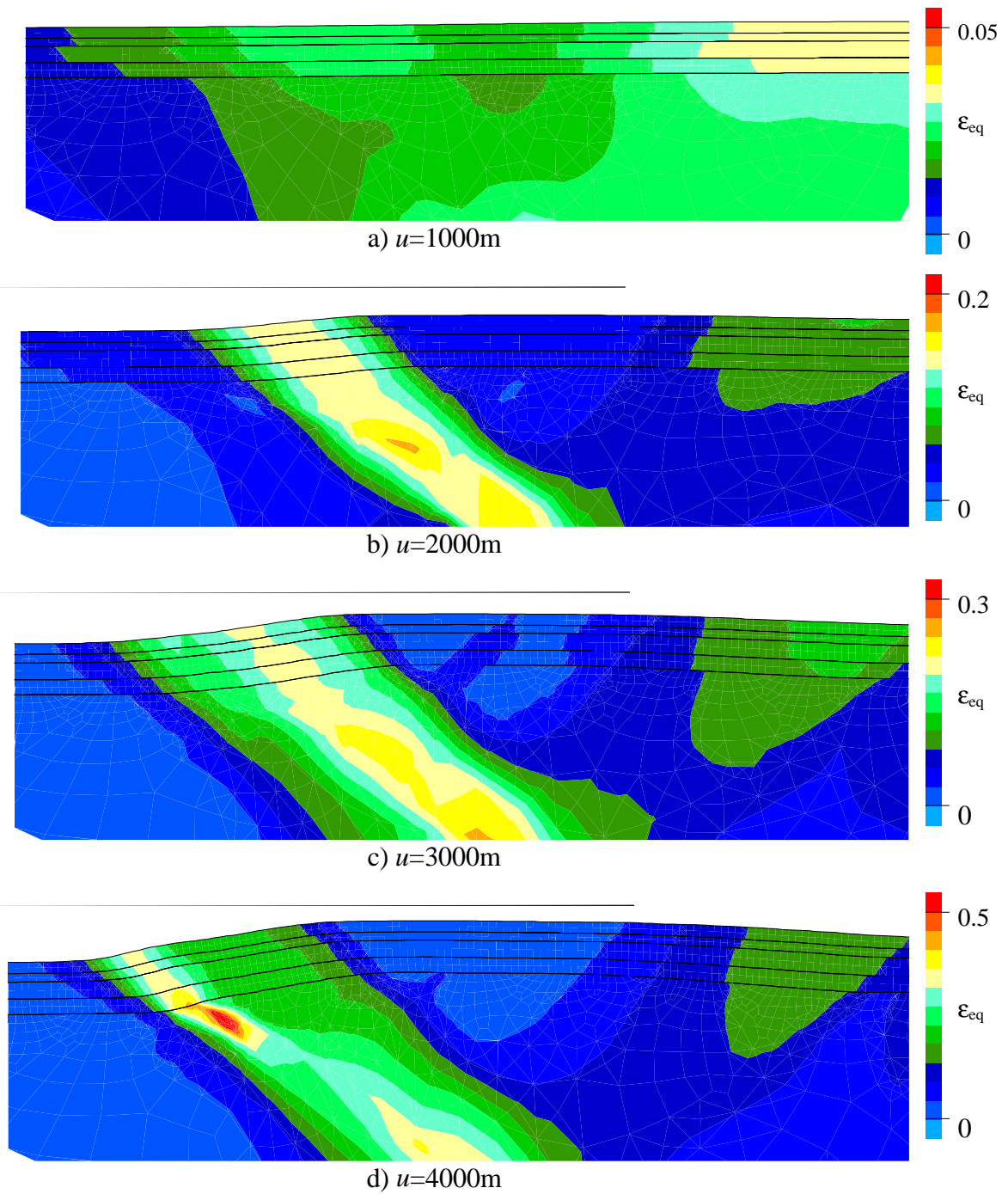


Figure 8.25 ϵ_{eq} for model 5 (fault $\mu=0.57$).

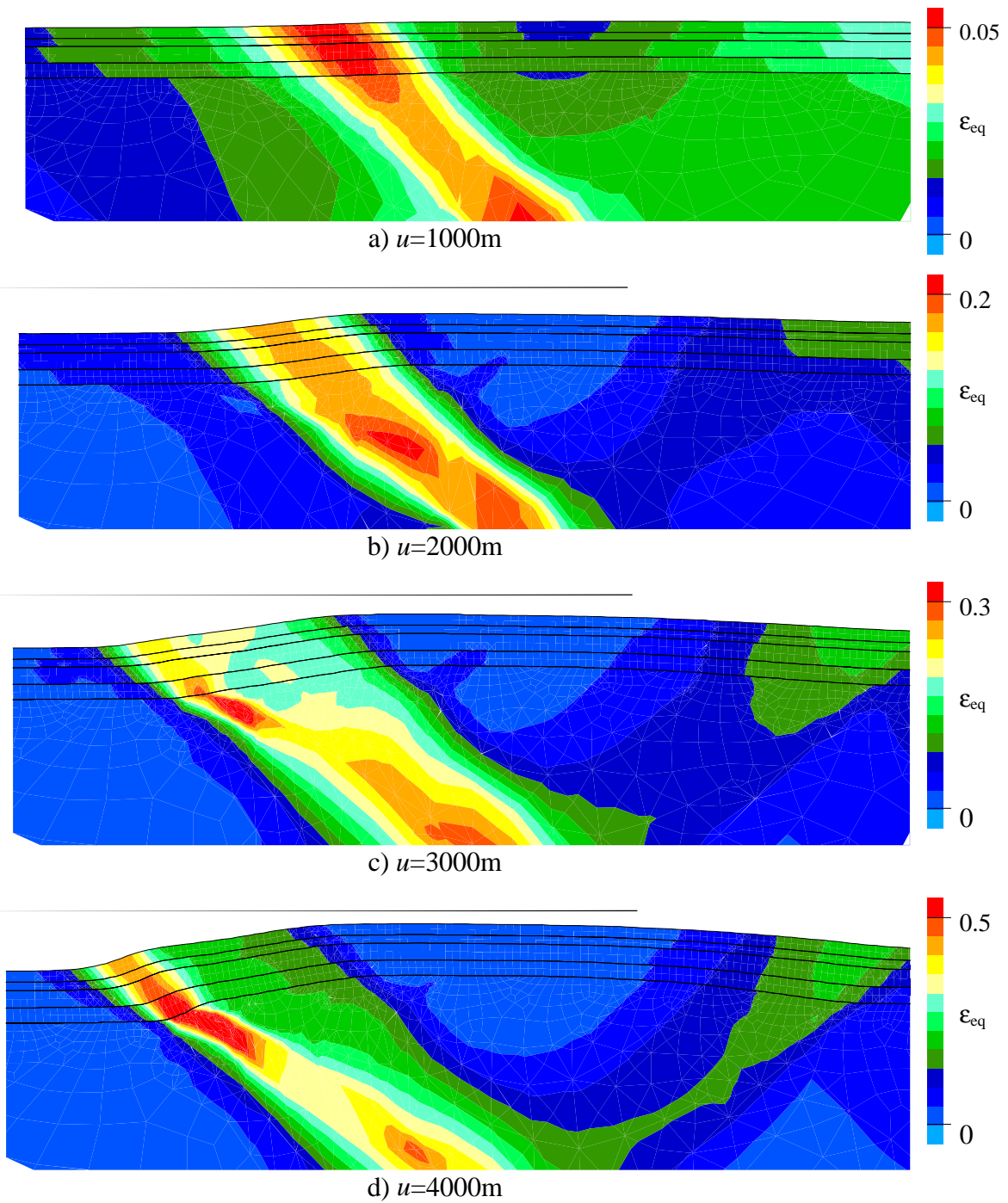


Figure 8.26 ϵ_{eq} for model 5 (fault $\mu=0.15$).

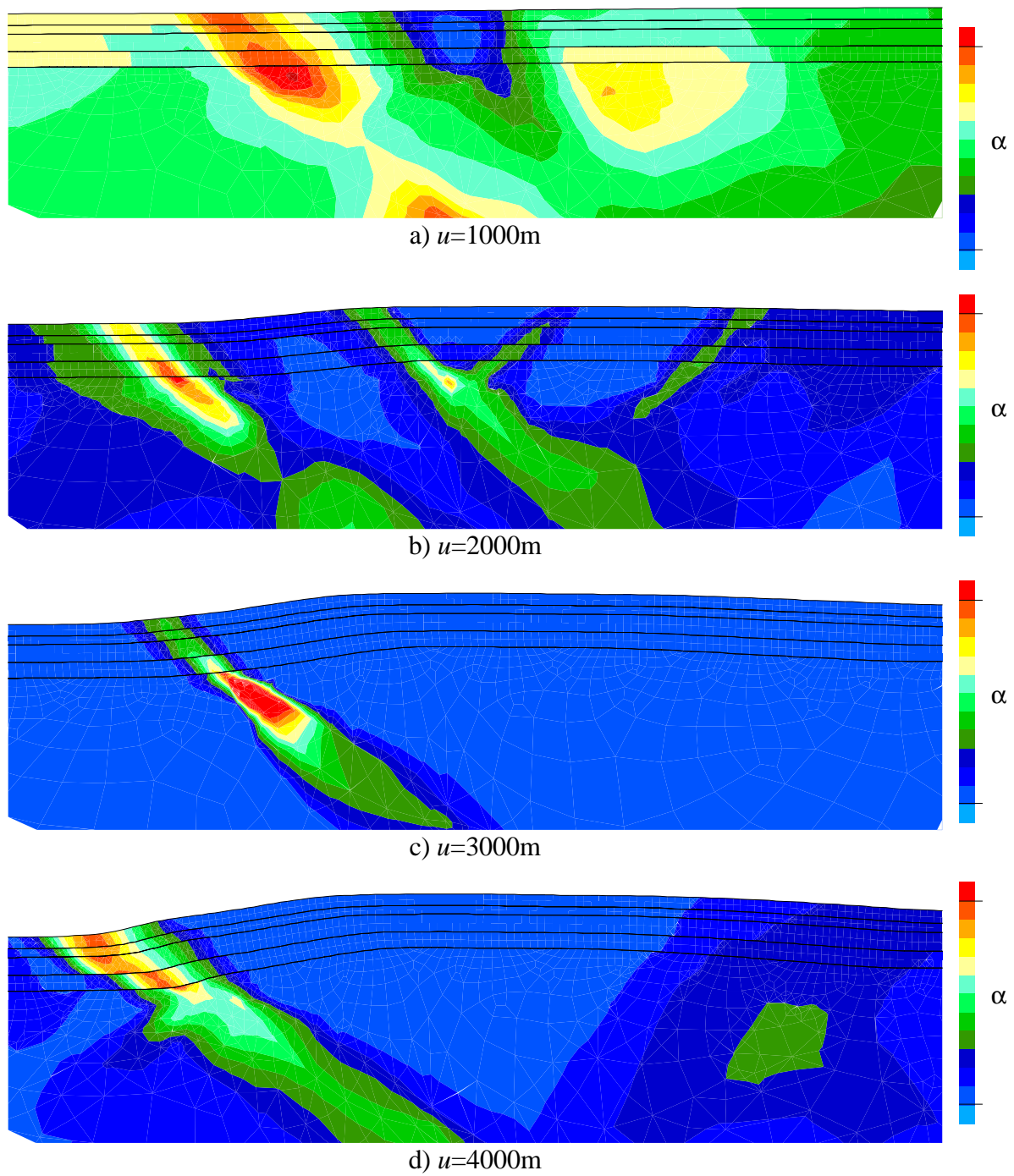


Figure 8.27 Kinematic indicator of localisation (α) for model 5 (fault $\mu=0.57$).

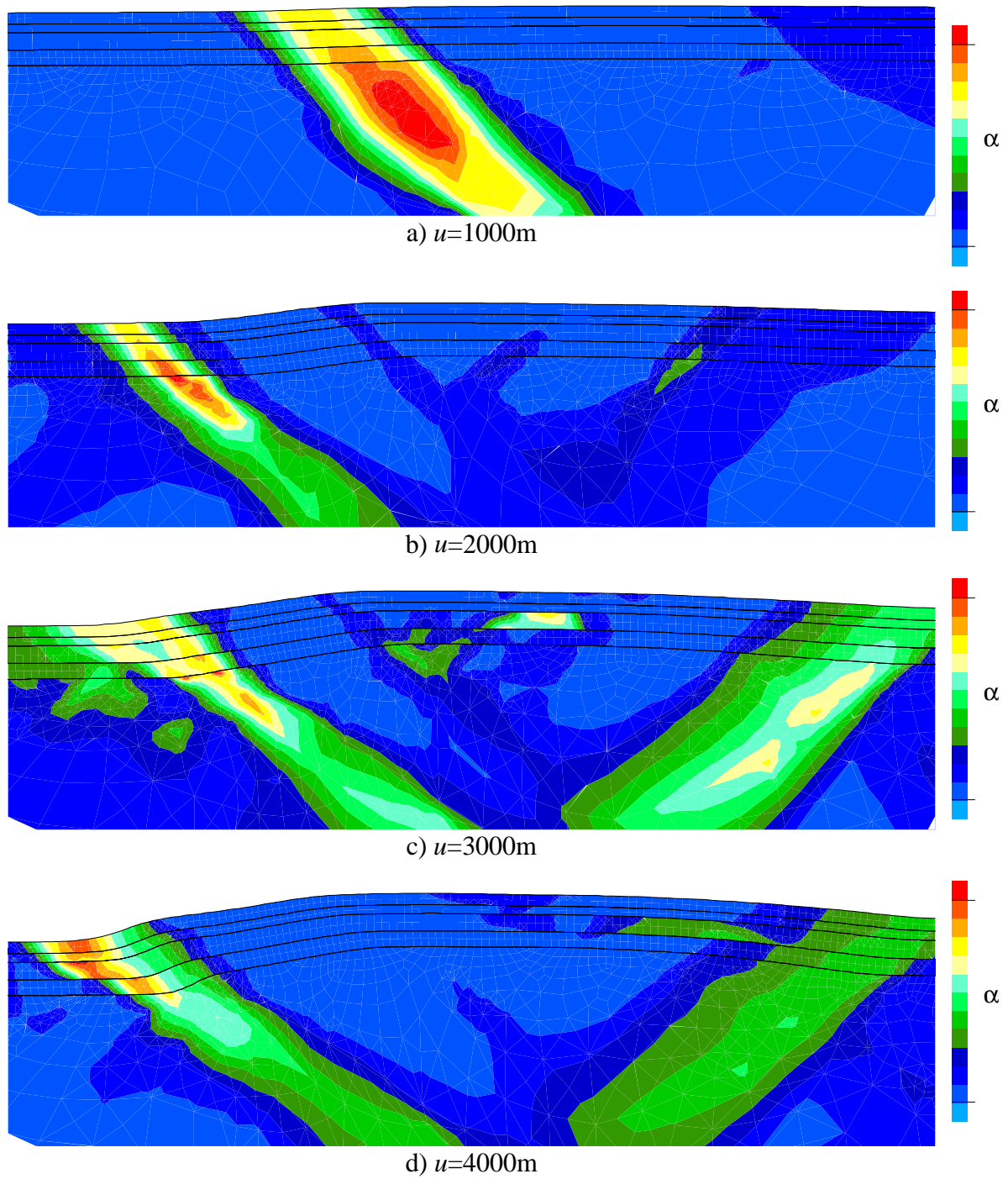


Figure 8.28 Kinematic indicator of localisation (α) for model 5 (fault $\mu=0.15$).

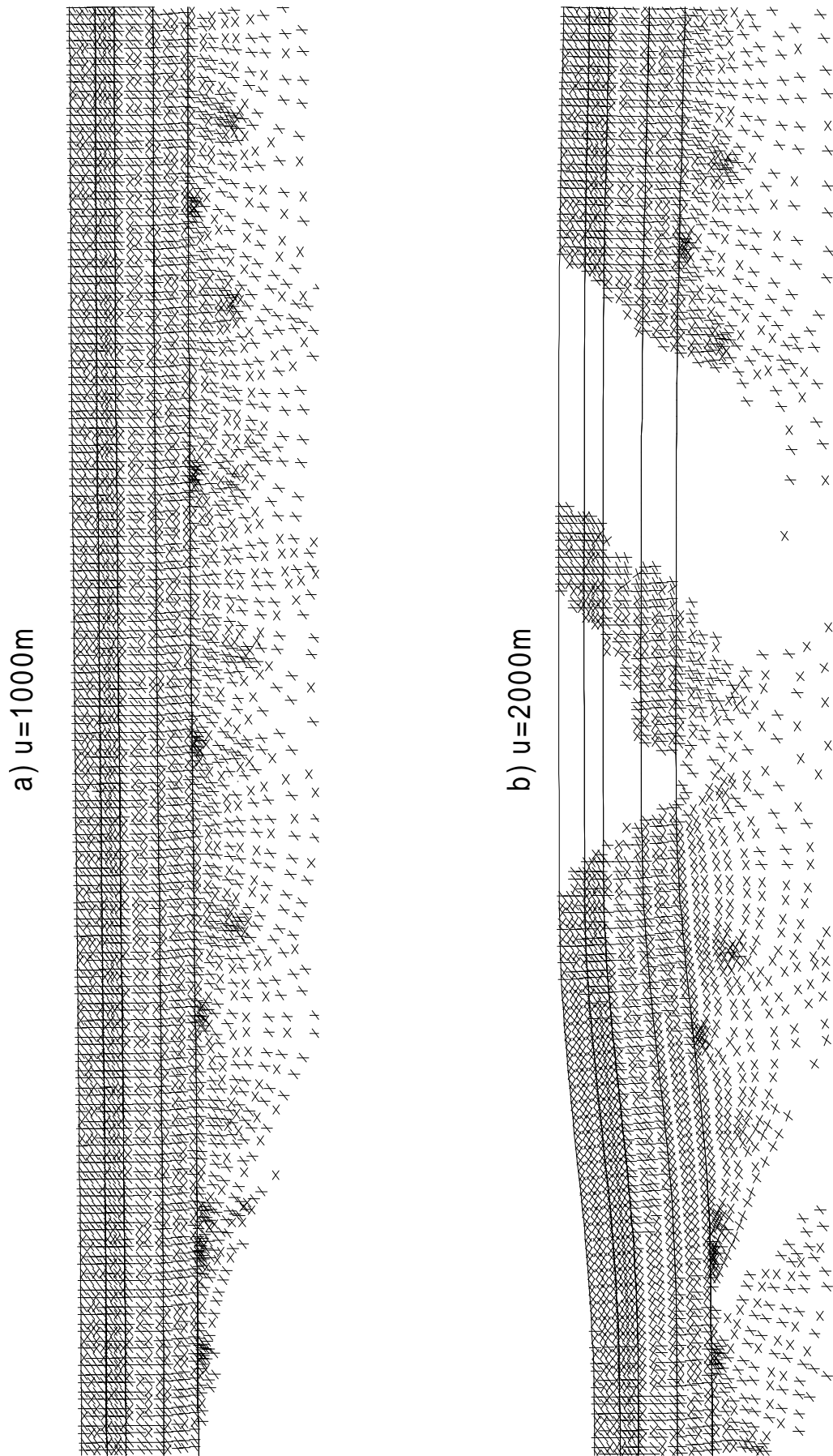


Figure 8.29 Rice bifurcation directions for model 5 (fault $\mu=0.57$) a) $u=1000m$, b) $u=2000m$.



Figure 8.29 Rice bifurcation directions for model 5 (fault $\mu=0.57$) c) $u=3000m$, d) $u=4000m$.

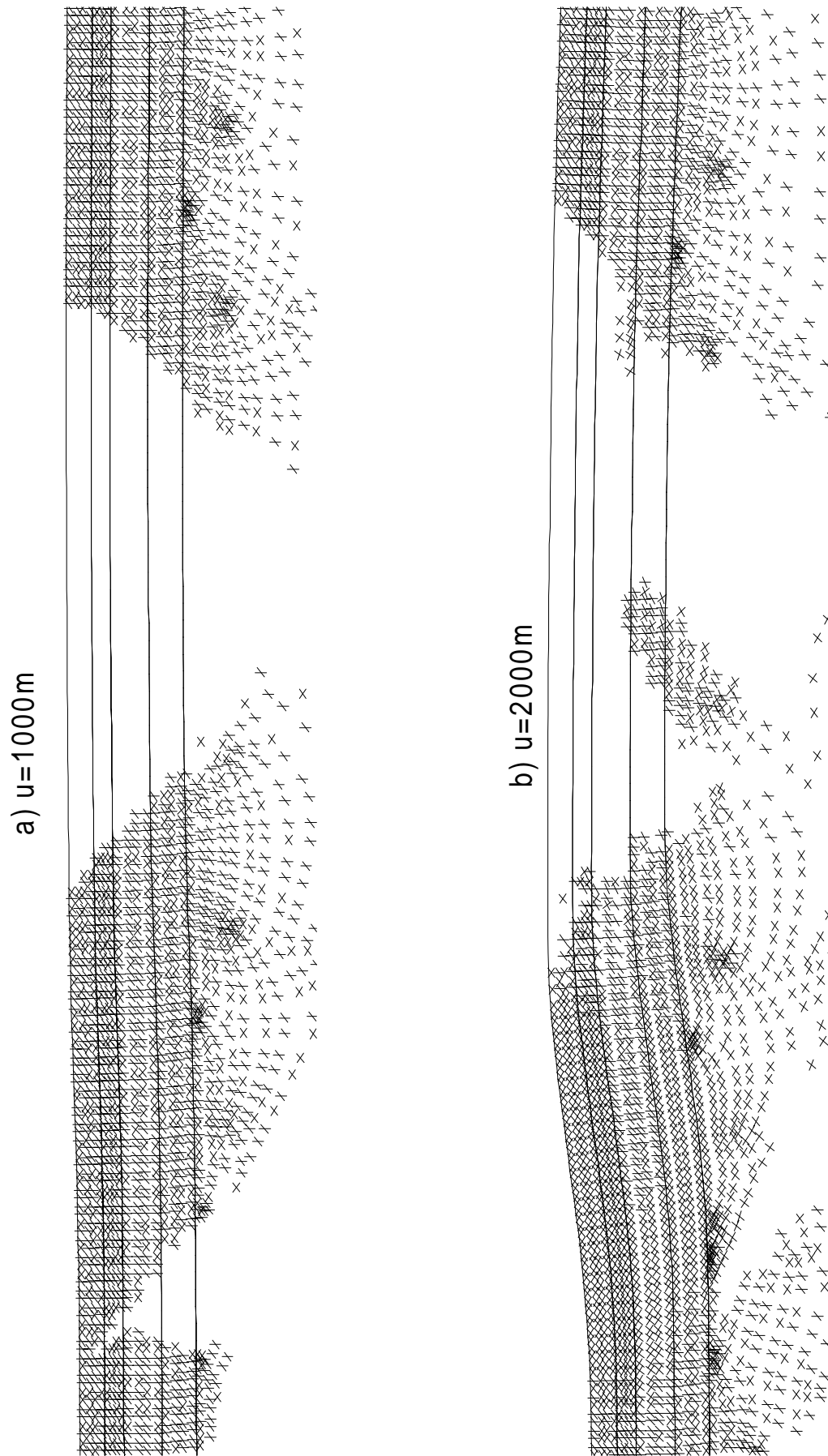


Figure 8.30 Rice bifurcation directions for model 5 (fault $\mu=0.15$) a) $u=1000m$, b) $u=2000m$.

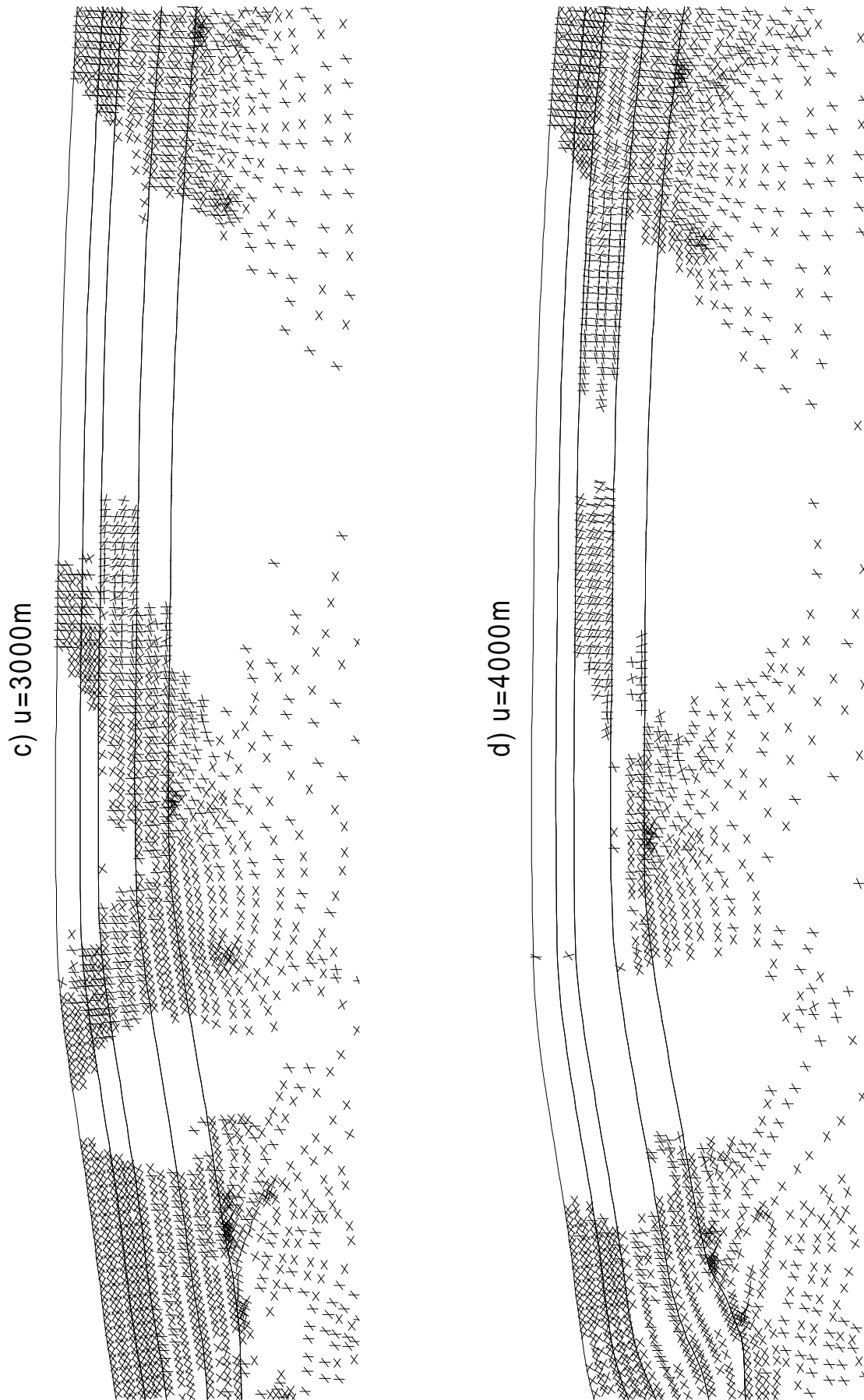


Figure 8.30 Rice bifurcation directions for model 5 (fault $\mu=0.15$) c) $u=3000m$, d) $u=4000m$.

- The evolution of the kinematic indicator shown on figures 8.27 and 8.28 allows to understand the evolution of the deformation mechanism. A first forward reverse fault (fault 1 in figure 8.31) forms in the cover and initiates in the western flank of the anticline. Its associated backward fault (fault 2 in figure 8.31) develops but is less active. Then a second forward reverse fault (fault 3 in figure 8.31) develops from the tip of the detachment fault toward the foreland and progressively accommodates the major part of localisation. Note that the location of fault 3 is kinematically more compatible with the detachment than fault 1. Its backward associated fault 4 will also develop to a lesser extent. Fault 1 and 2 have quite limited offsets compared to their respective evolution (faults 3 and 4). It is worth point out that, between these four main faults or faulted areas, the upper layers are almost unfolded, i.e. they do not accommodate an important amount of deformation.

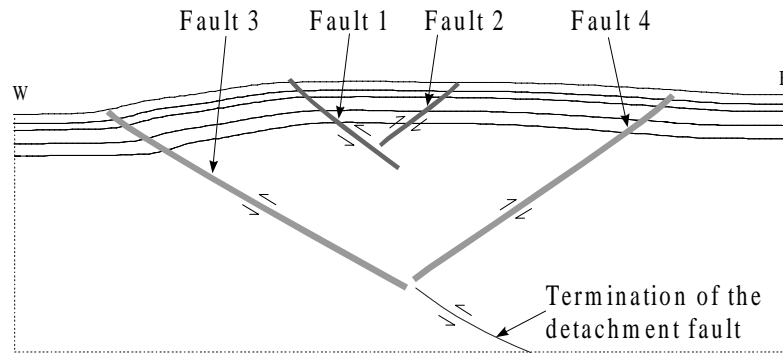


Figure 8.31 Interpretation of the observed structures in the computation from the pre-Hercynian geometry (model 5).

- The evolution of the Rice bifurcation criterion is shown on figures 8.29 for the model with $\mu=0.57$. It gives the locations where the bifurcation is possible and its potential directions. For small values of loading, the bifurcation is possible in the four upper layers (figure 8.29a). This stage corresponds to an almost homogeneous deformation phase, i.e. in which no large scale faulting develops. As loading increases, some strain localisation starts to appear (see for instance the fault 2 on figure 8.29b) which leads to the progressive elastic unloading in the vicinity of the shear bands. At the final stage, which is very similar to the observed present day geometry, most of the central part of the anticline is elastically unloaded, and no strain localisation can be predicted in this area (see figure 8.29d). When looking at the predicted bifurcation mode S in the reservoir sandstone obtained by the Rice criterion (see chapter 2), the value $-0.48 < S < -0.40$ is obtained over the loading process. This corresponds to an intermediate bifurcation mode between a pure closing mode -I and a pure shear mode II (see chapter 2 for more details about parameter S).

For the model with low fault friction ($\mu=0.15$), the evolution is qualitatively similar to the one obtained with high fault friction. However, the first homogeneous phase of deformation is shorter than expected at $u=1000\text{m}$, the large scale faulting is already effective (see figure 8.30a). There is still some localisation activity in the central part of the anticline at $u=4000\text{m}$ (figure 8.30d).

8.5.3 Interpretation

A possible scenario has been verified to explain the formation of the Garret El Gueffoul anticline during the Hercynian orogeny. It is based on a detachment fault or more generally on a weakness zone in the basement, which does not affect the whole thickness of the Precambrian basement (see model 5). Displacement of the footwall block generates an asymmetric anticline structure which is quite similar to the Garret El Gueffoul one. It has been brought to light that a pre-existing fully developed detachment fault is a very unrealistic assumption as the obtained geometry is far from the observed one for both low and high fault friction.

The main goal of the simulations from the pre-Hercynian phase was to investigate the possibility of mesoscale faulting associated with the anticline formation. It is observed that the formation of this fold is closely linked with the development of two main families of reverse shear bands. Each family consists in the association of a forward and a backward fault, the latter one being less pronounced than the other. The first family (faults 1 and 2 in figure 8.31) is located near the anticline top and the second one (faults 3 and 4 in figure 8.31) is located at the anticline bottom. It is worth mentioning that these predicted shear zones seem to correspond with the 2 main reverse faults interpreted from the seismic section presented in figure 8.5. This would indicate that these faults may have formed during the Hercynian phase. Their Alpine offset could therefore be only the reactivation of an older Hercynian structures. It is also worth pointing out that a zone of diffuse shear strain exists in the western limb between the forward faults. In this zone some less important faults are also likely to have developed, which could correlate some secondary faults interpreted on figure 8.5.

8.5.4 Implication for the reservoir fracturing

During the genesis of the first order anticline, the bifurcation potential within the reservoir tends to decrease, which is related to an elastic unloading of the central part of the anticline (see figures 8.29 and 8.30). When potential bifurcation is predicted at some locations (see figures 8.29 and 8.30), the potential fracturing within the shales and reservoir sandstone is schematised on figure 8.32.

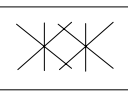
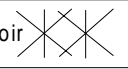
Anticline			
n (Rice)	s (Rice)	R	α
Shales 	-0.16 (mode II)	0.5	Localisation
Reservoir 	-0.43 (mixed mode -I/II)	0.7	Localisation

Figure 8.32 Summary of several indicators characterising the potential fracturing mode within the Silurian shales and Cambro-Ordovician sandstone layers for the present day models.

There is now no important differences between the bifurcation directions within the shales and sandstone layers. Three main directions of bifurcation are predicted (note that these directions are not all predicted at the same point as Rice criterion only gives 2 bifurcation directions). The first two directions are oriented approximately at $\theta = \pm 30^\circ$ with respect to the bedding

plane, which is almost parallel to the maximum compressive principal stress. Therefore, these two bifurcation directions are consistent with the orientation predicted by Coulomb theory

$$\theta = \frac{\pi}{4} - \frac{\phi}{2} \approx 30^\circ \quad (8.1)$$

for the sandstone, although the correspondence is not as good for the shales. The third bifurcation direction is approximately equal to $\theta=90^\circ$. Such orientation could be consistent with an opening (mode I) or a closing mode (mode -I).

Within the sandstone, these three directions of bifurcation have an associated mode of deformation S falling in the range $-0.48 < S < -0.40$ which indicates a mixed mode between mode -I and mode II. Within the shales, the deformation mode is much closer to mode II of bifurcation (pure shear). As in the models from the present day geometry, the Wallace-Bott stress shape ratio indicates a purely compressive tectonic regime within the two considered layers.

These bifurcation characteristics only relate to the Hercynian phase of deformation. The subsequent erosion and sedimentation events and the Alpine phase are not taken into account. However, it has been previously mentioned that the Alpine faults are likely to be re-activated Hercynian faults. If this is the case, the bifurcation associated with Alpine faulting should not be very different from the Hercynian one, both in direction and location.

8.6 Three dimensional models from the present day geometry

The three dimensional modelling presented in this section aims to investigate both the influence of the plane strain assumption made in two dimensional modelling and the influence of the direction of imposed horizontal displacements. As it is much more complicated to obtain the Pre-Hercynian unfolded geometry, only computations from the present day geometry have been carried out.

8.6.1 Initial geometry and boundary conditions

The initial geometry is presented on figure 8.33a in a perspective view, where the East-West section used for the previous 2D models is represented. The rather complex geometry of the hypothetical detachment fault is shown on figure 8.33a and its corresponding isodepth contour lines figure on 8.33b. The isodepth contour lines of the top Ordovician is also given on figure on 8.33c and is similar to figure 8.4.

The upper surface is a free surface and the basal plane is fixed along the vertical direction. In the present case, three directions of shortening are chosen :

- the east-west direction (N90) which was the direction used in the two dimensional models,
- the N120 direction which is one of the Hercynian major direction of deformation in this area,
- and the N40 direction which is the other Hercynian direction.

These 3 shortening directions are equivalent to three uniaxial strain tensors whose principal directions do not coincide with the global axes ($\mathbf{x}, \mathbf{y}, \mathbf{z}$). As a result, the equivalent displacement field \mathbf{u} corresponding the this uniaxial strain tensor reads

$$\mathbf{u} = \begin{bmatrix} Sh(\cos^2 \alpha)x_1 \\ Sh(\sin^2 \alpha)x_2 + Sh(\sin 2\alpha)x_1 \end{bmatrix} \quad (8.2)$$

where Sh is the principal strain component to be applied (for details about the derivation of this relation, see appendix 2). α represents the angle between the principal direction associated with Sh and the \mathbf{x} axis; then the N90, N120 and N40 directions correspond to $\alpha=0^\circ$, $\alpha=-30^\circ$ and $\alpha=50^\circ$, respectively.

The ultimate loading value corresponds to an applied shortening $Sh=0.02$, which is the same than the one applied in the two dimensional models (models 0 to 3). The boundary conditions and imposed displacements are presented for the three studied cases on figure 8.34 : dotted lines represent the initial geometry in the (\mathbf{x}, \mathbf{y}) plane and full lines represent the deformed geometry for the exaggerated loading value $10*Sh$. For the loading N40 and N120, only one point of the boundary has no applied displacement : the one located at the bottom left corner. These boundary conditions correspond exactly to the two-dimensional model 1 presented in section 8.4.2, but here the shortening is not always applied following the N90 direction. Thus the three dimensional model with Sh applied at N90 is the 3-D version of model 1.

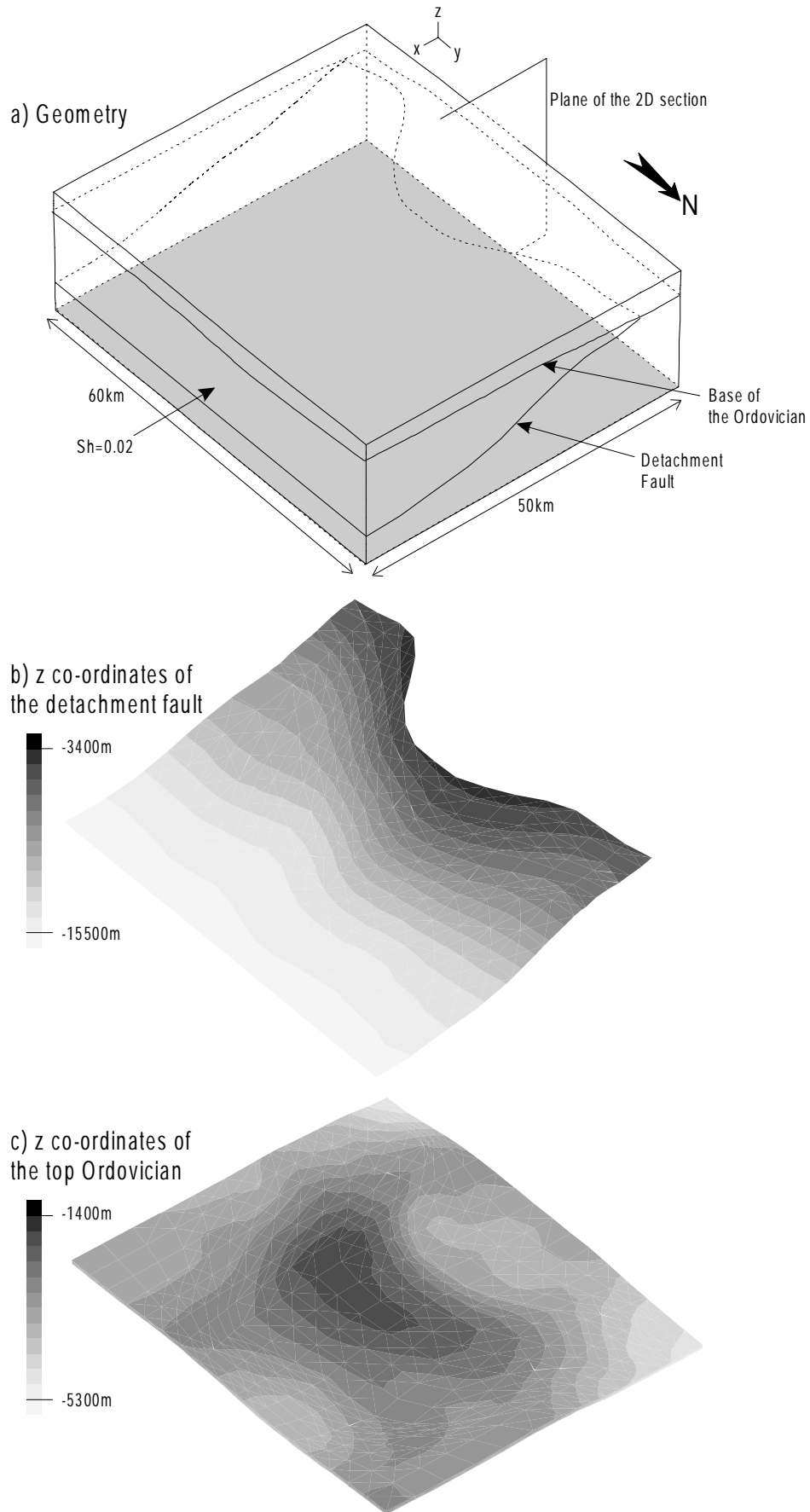


Figure 8.33 Initial geometry for the 3D models.

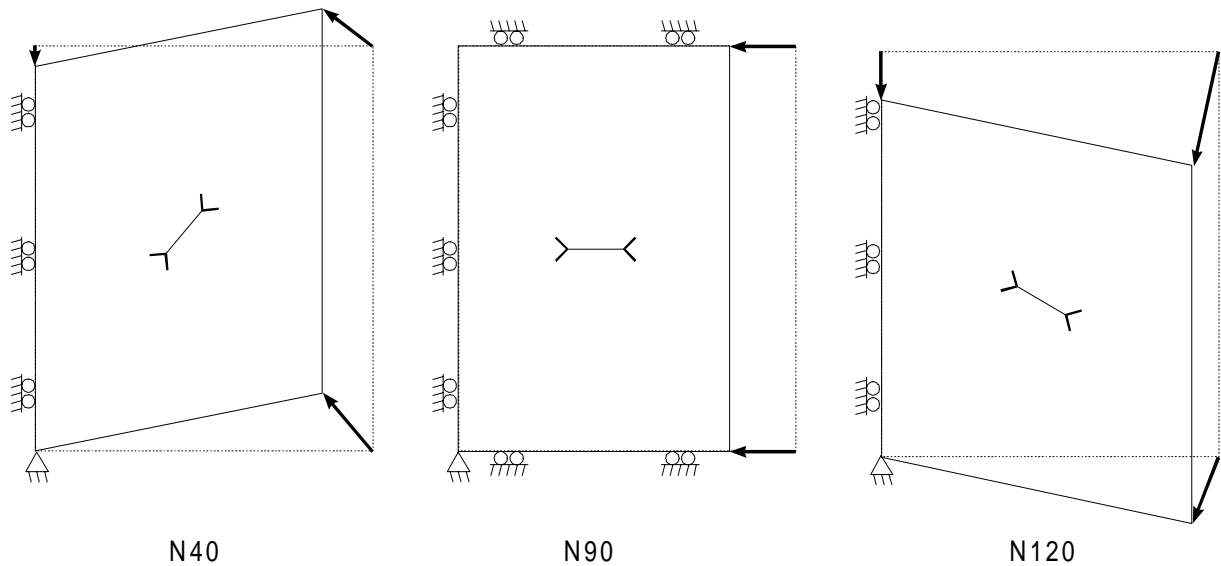


Figure 8.34 Boundary conditions and exaggerated applied displacements for the 3D models for $10 \cdot Sh$.

The discretisation (see figure 8.35) is made up of 4410 nodes which are used to define 3451 solid elements (8 nodes bricks *BRILS* with 4 integration points). The fault is discretised with 221 contact elements *CFI3D*.

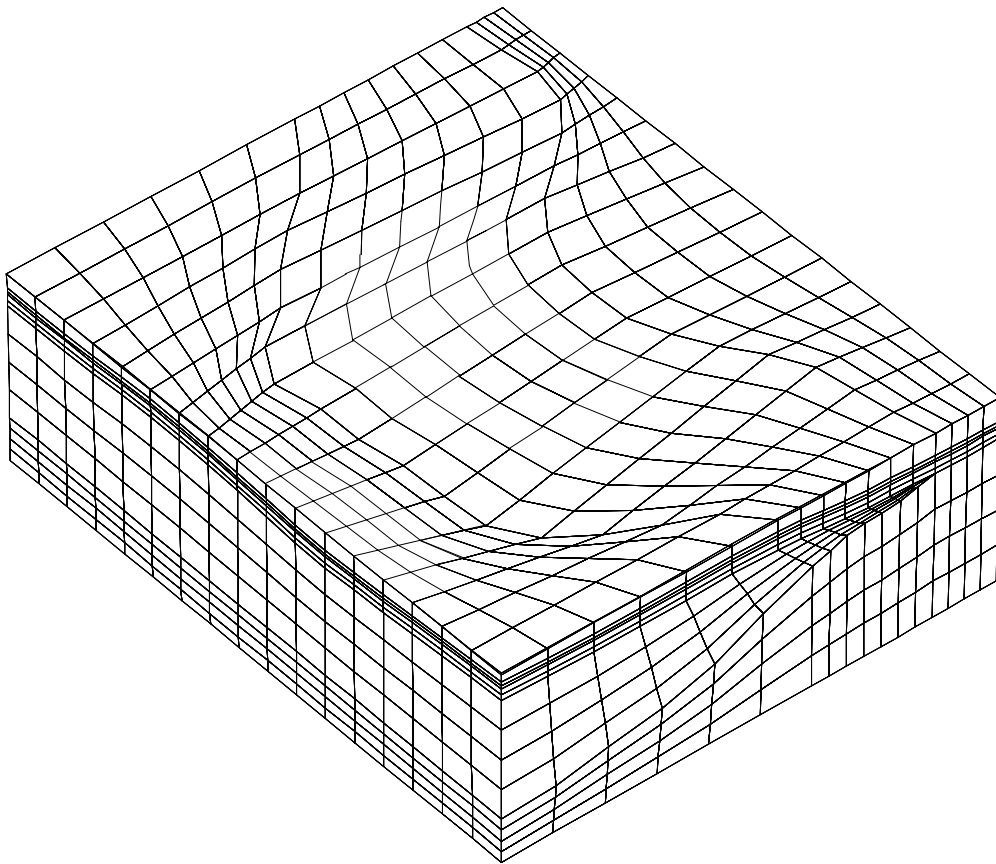


Figure 8.35 Mesh for the 3D models.

8.6.2 Results

As in the two dimensional models, a model with a high friction coefficient ($\mu=0.57$) and a model with a low one ($\mu=0.15$) have been considered. Rheological parameters are similar to the 2D experiments except the shales friction angle which is equal to 10° here (such value has also be tested on models 0 to 3, see section 8.4.5). Map views of the equivalent strain ϵ_{eq} obtained at the loading value $Sh=0.02$ are presented on figure 8.36 and 8.37, in which the figures (a, c, e) refers to the top of the lower-middle Devonian and the figures (b, d, f) refers to the top Ordovician.

In all the ϵ_{eq} maps presented in figures 8.36 and 8.37, zones of strain concentration are located in the western part of the model.

In the case of a N90 applied shortening (see figures 8.36c-d and 8.37c-d), a concave zone follows closely the geometry of the anticline in the central area. To the north and to the south, the high strain zone propagates following a N0 direction. There is a substantial difference in the ϵ_{eq} intensity between the central part of the model on the one hand and the northern and southern parts on the other hand where the ϵ_{eq} values are larger. The shear bands are thinner in the Ordovician sandstones than in the lower-middle Devonian. This can be related to a diffusion of strain within the Silurian shales.

When the applied shortening is either N40 or N120 (see figures 8.36a,b,e,f and 8.37a,b,e,f), the shear bands tend to orient following the direction perpendicular to the shortening direction. Especially for the N40 shortening direction (figures 8.36a-b, 8.37a-b), the orientation of shear bands are in good agreement with the faults observed on figure 8.4. However, certainly due to the coarser discretisation of the 3D model compared to the 2D ones, only one main fault zone appears mostly in the western limb of the anticline, i.e. it is not possible to distinguish between the backward and the forward reverse faults.

A three dimensional representation of the equivalent strain maps is presented on figure 8.38 to 8.40, which allows a better comprehension of the spatial distribution of the strain localisation. The effect of the loading direction is also clearly shown.

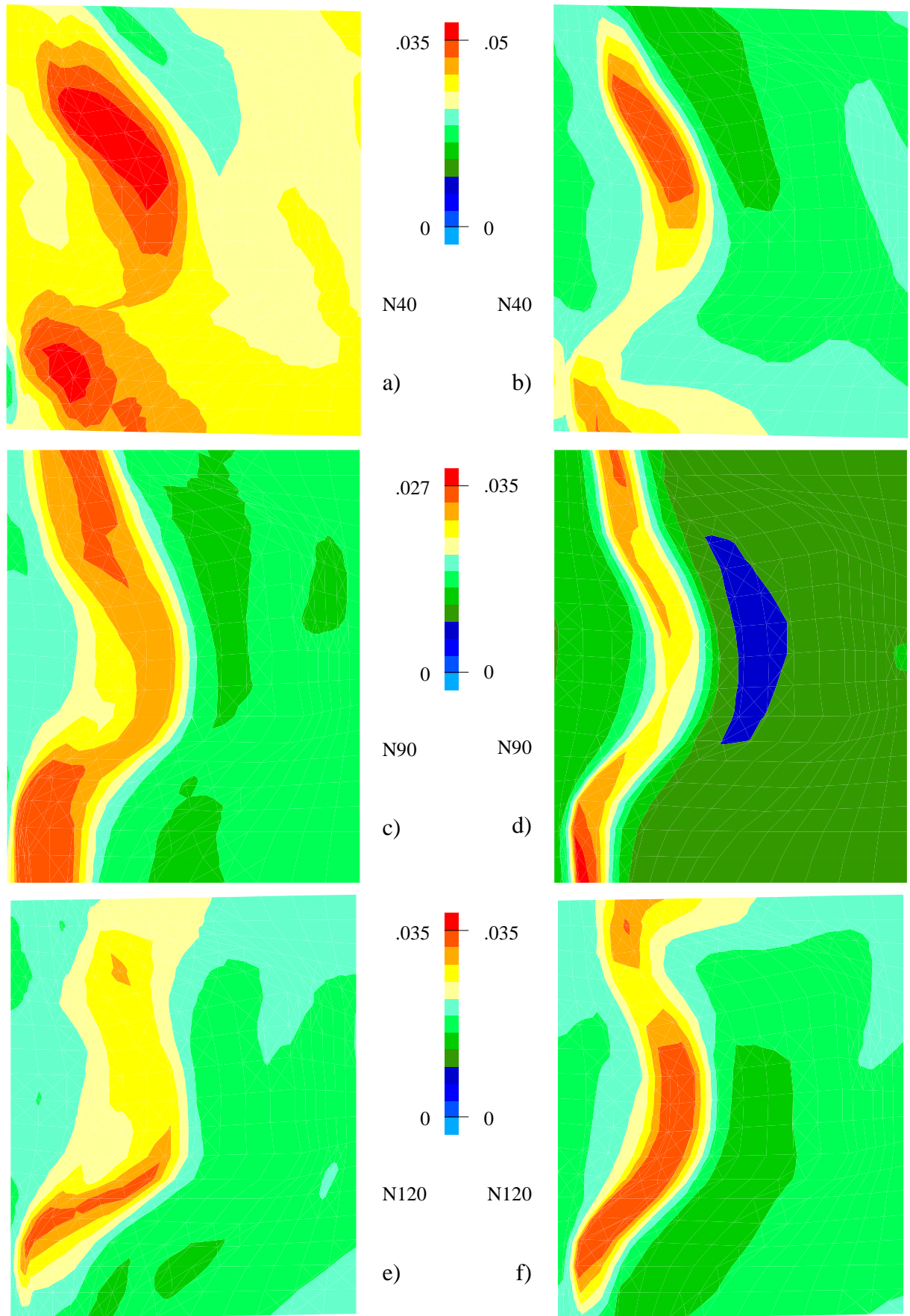


Figure 8.36 ϵ_{eq} for 3D model (fault $\mu=0.57$) at $Sh=0.02$.

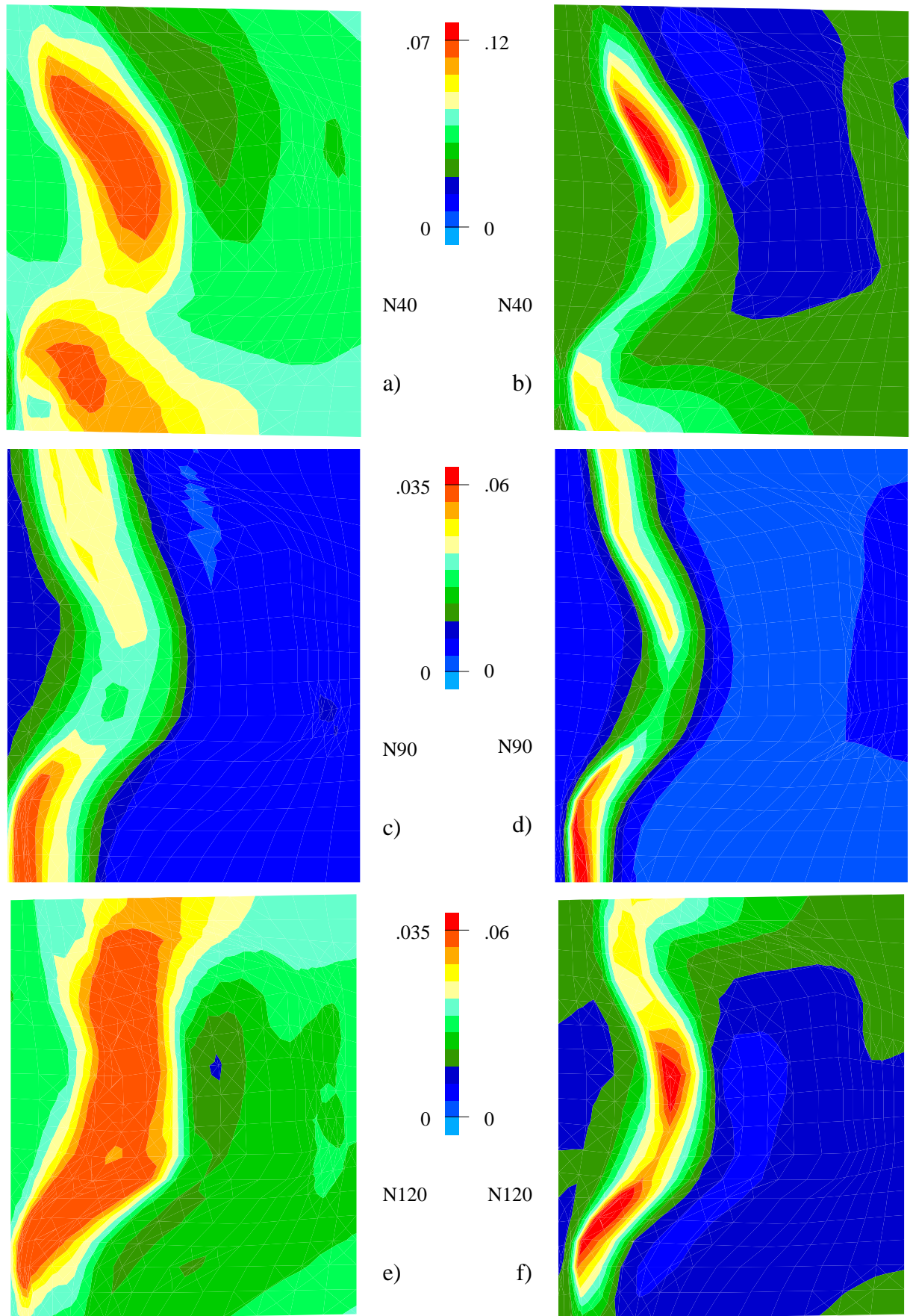


Figure 8.37 ϵ_{eq} for 3D model (fault $\mu=0.15$) at $Sh=0.02$.

N40 compression, $Sh=0.02$

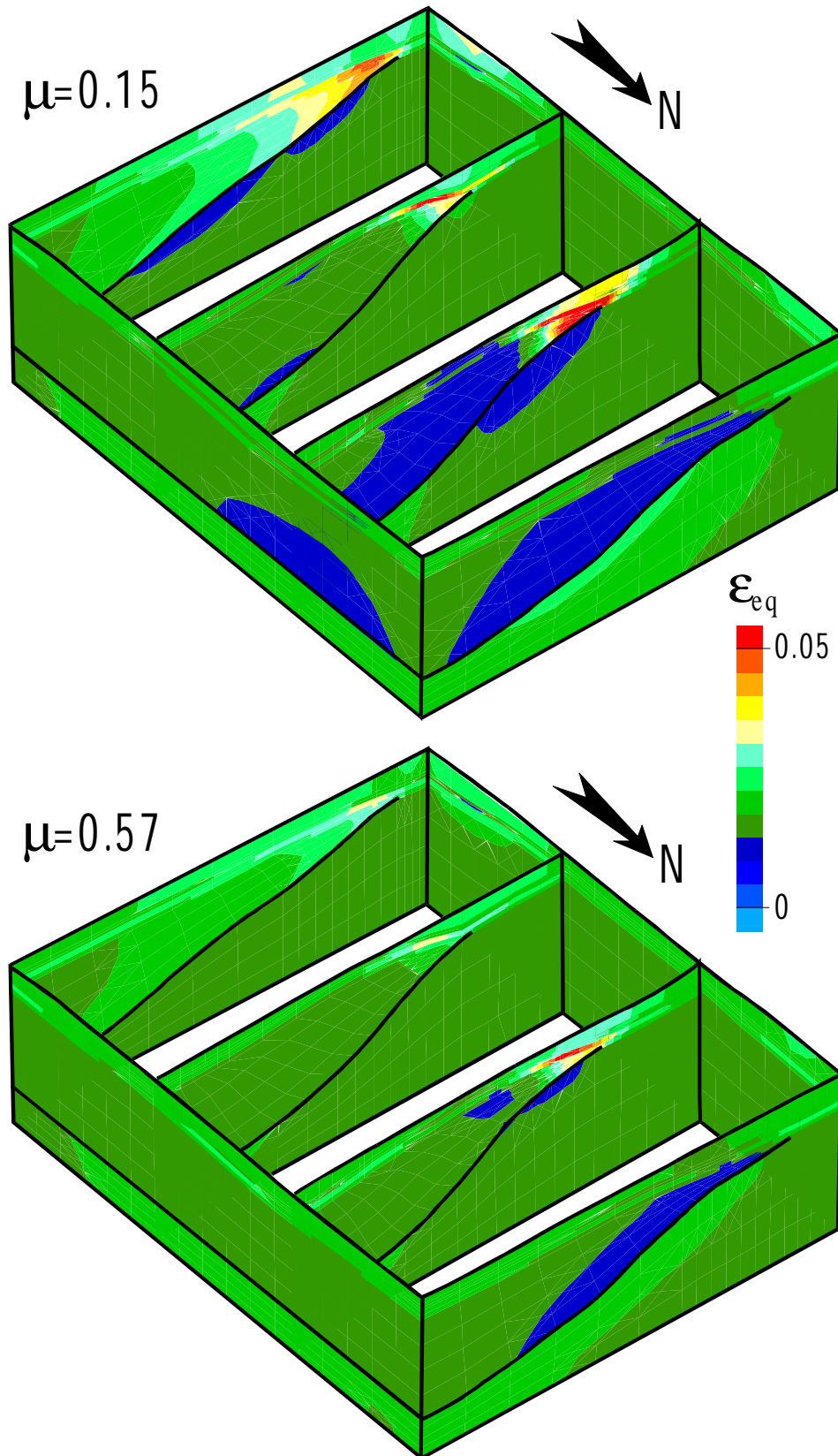


Figure 8.38 ϵ_{eq} for 3D model with N40 compression.

N90 compression, $Sh=0.02$

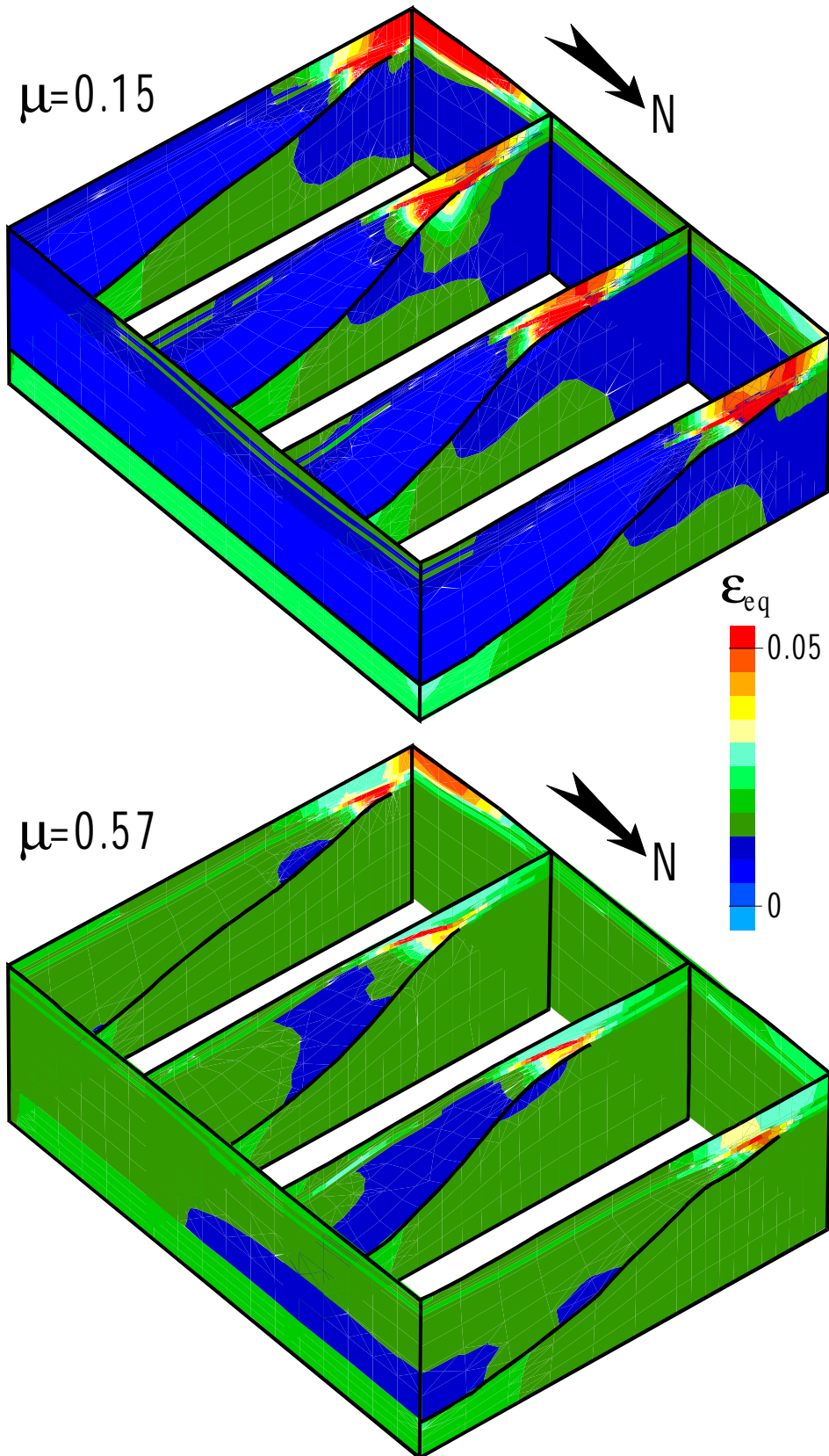


Figure 8.39 ϵ_{eq} for 3D model with N90 compression.

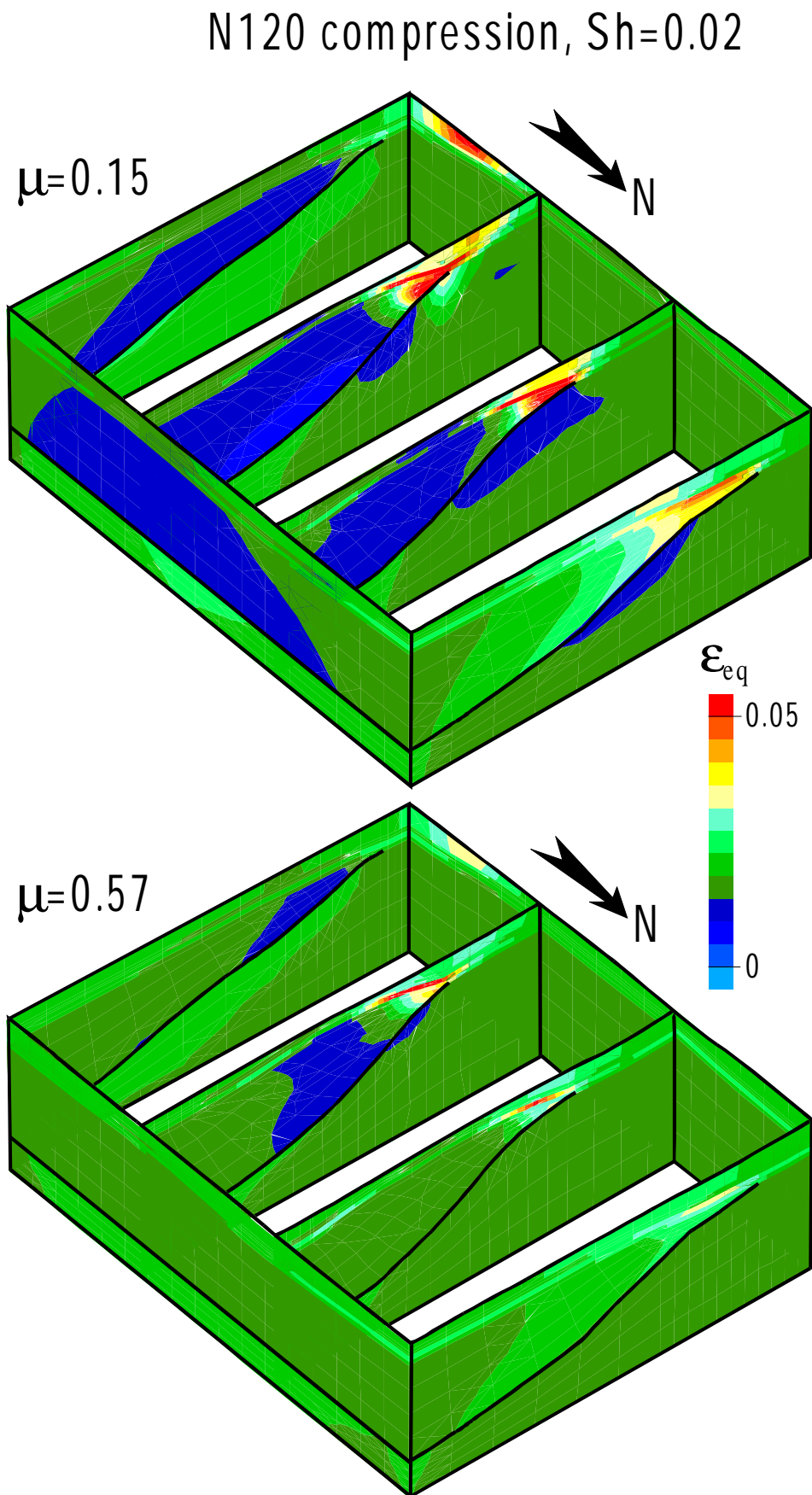


Figure 8.40 ϵ_{eq} for 3D model with N120 compression.

8.7 Conclusion

In the numerical simulations presented in this chapter, quite numerous and different models have been built in order to answer some very important questions on the Garret El Gueffoul field case. The first important one addressed here is the relevance of the geological interpretation of the anticline structure, especially regarding a possible induced basement fault. The second one consists in the evaluation of the potential fracturing within the reservoir sandstone at present day for hydrocarbon potential of this reservoir unit.

As detailed in this chapter, the attempt to model the faulting and fracturing in the Garret El Gueffoul anticline has given some answers but also has brought to light some questions about such modelling.

- A first question comes from the great difficulty to define a realistic initial state. This has been demonstrated particularly by the interpretation of the observed Alpine mesoscale faulting in the western limb. If only the Alpine phase of compression is simulated (provided of course that the boundary conditions are realistic enough) from a present day structure (which is not very different from the pre-Alpine one) in virgin state i.e. removing all its deformation history, the numerical simulations (models 0 to 3) showed that it was not possible to generate to observed forward Alpine faults in the western limb. As similar faults have been predicted in simulations from a pre-Hercynian geometry (model 5), it seems reasonable that the observed Alpine faults are actually Hercynian re-activated ones. The failure of the virgin present day models to predict the forward faults is attributed here to the important geometric changes (due to erosion processes) of the structure in post-Hercynian times.
- A second question lies in the difficulty to define or to imagine realistic boundary conditions for the modelling. However, it can be one aim of the modelling to confirm or infirm a given assumption regarding boundary conditions. For instance, the boundary conditions imagined in model 4 have been discarded because the obtained geometry was too unrealistic compared to the real one. It is sometimes possible to define a family of realistic boundary conditions, but not only one. As an example, the boundary conditions of models 5 (partial detachment fault) gave realistic results, but it could not be argued whether the fault was likely to have a high friction coefficient or a low one.
- A quite important information has also been obtained indirectly from this modelling about the role of the shale layer in the global deformation process. From the presented results, the shale behaviour has a relatively small influence on the deformation of the whole model. This point is quite important as there is a large uncertainty about the shale behaviour some 300Ma ago.

Finally, the main conclusions of this study can be formulated as follow :

- The geological interpretation in which the genesis of the first order anticline (Hercynian) is related to folding and is controlled by basement detachment fault seems realistic. Neither models without detachment nor models with fully developed detachment fault have succeeded to predict a reasonable geometry at the end of Hercynian phase. Only models

with partial detachment fault in the basement have succeeded to reproduce realistic anticline geometries. Note that this conclusion could only be obtained considering pre-Hercynian initial geometries, by neglecting erosion effects.

- The analyses carried out from the present day geometry have led to the observation of an important backward Alpine faulting within the western limb. This result is not supported by seismic data which indicate a main forward thrust faulting which could be attributed to the Alpine phase. Thus it seems that the Alpine faults which are likely to be reactivated Hercynian faults. It has been shown that this major discrepancy between modelling and field data can be attributed to the virgin initial state assumption implicitly made in some models. It tends to show that this assumption is far from being realistic, and consequently that the results obtained with such models may be interpreted with care, especially regarding reservoir fracturing.
- As a consequence, the evaluation of the potential fracturing within the reservoir sandstone at present day for hydrocarbon potential of this reservoir unit could not be performed in an undoubtful way. Estimation could be based either on models computed from the present day geometry and it has been shown that the obtained Alpine faults do not correspond with the observed ones, or either on model from the pre-Hercynian geometry in which the erosion and the Alpine phase were not taken into account. Nevertheless, in all the cases 3 families of bifurcation directions (2 conjugates oriented at $\approx 30^\circ$ to the bedding plane and one oriented perpendicularly to the bedding plane) have been predicted from Rice's criterion, with an associated mixed mode.

Some comments must be formulated on the three-dimensional modelling performed on the Garret El Gueffoul anticline. Simulations only based on the present day geometry have been performed, as it was not possible to build easily a consistent pre-Hercynian geometry as in the two-dimensional cases. It must also be pointed out that the mesh was much coarser than in two-dimensional models in order to limit the CPU time required for the computation. Nevertheless, despite these limitations, the three-dimensional models have shown clearly that the 3D effects could be quite important and also that the effect of the loading direction on the obtained solution could not strictly be neglected. It should be fruitful to carry out more precise (with finer mesh) 3D models, including models from the pre-Hercynian geometry as significant differences can be expected compared with the 2D models.

Eventually, it should be interesting to perform similar simulations considering both the mechanical and the fluid flow problem using a coupled hydromechanical model such as the one presented in chapter 3. Some interesting and certainly more realistic results might be obtained, as in natural situations such coupling exists. However, such study would require additional assumptions regarding the pressure field, which are not available at the present time.

CHAPTER 9

Hydromechanical modelling of compaction

9.1 Introduction

From field observations and measurements, it is known that water (or an other fluid) is present in the porous space (pores and fractures) of geomaterials. In the previously studied cases presented in chapter 6, 7 and 8, the presence of a fluid has been neglected. Experimental and numerical results [CHARLIER et al., 1997] showed that the presence of a fluid in a porous medium can play a role on the strain localisation in biaxial compression experiments. [CHARLIER et al., 1997] and showed that the hydromechanical coupling can inhibit the strain localisation in undrained conditions (low permeability compared to loading velocity).

This chapter aims to illustrate the possible effects of hydromechanical coupling in a very simple case. Particularly, questions arise about the fault genesis in a porous rocks filled by fluids, its propagation when the fault is considered both as a mechanical and hydraulic discontinuity.

The studied case deals with the sedimentary compaction of a multilayered model made up of two materials, the whole model being crossed by a fault. It is based on very simplifying assumptions regarding both the loading and the mechanical constitutive relation for the sand and shales. Only the transverse transmissivity of the fault is considered here.

9.2 A simple compaction model with fault

A simple compaction model is considered to illustrate the coupling effects between the mechanics and the fluid flow. Particularly, the effect of fault permeability in the transversal direction is investigated.

In the initial state, a model made up of two materials and crossed by a fault is considered (see figure 9.1a, sand in white, shales in grey). In the left block there are two shales layers of 25m thick each, and in the right block only one shale layer of 100m. The total height of the model is equal to 250m. The fault which separates the two blocks has a dip of 60° . The model lies on a rigid impermeable substratum.

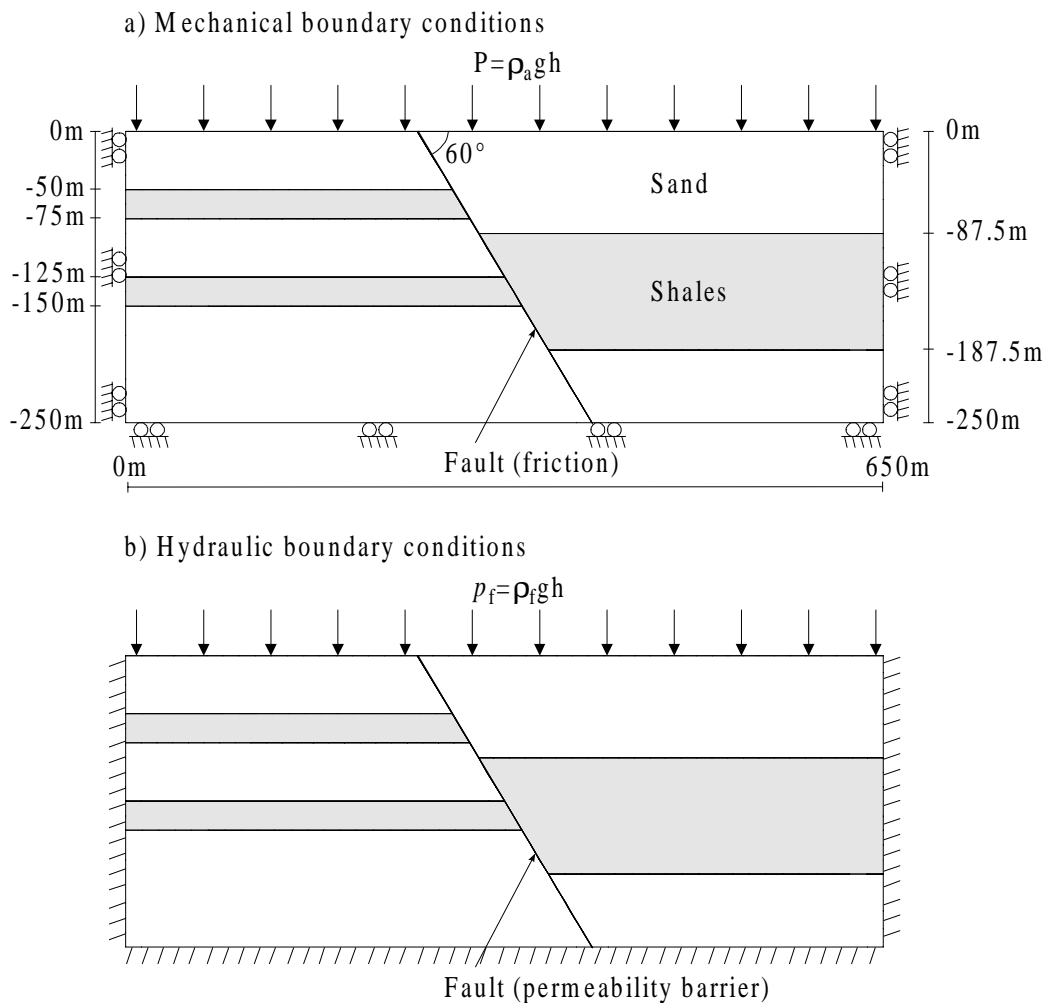


Figure 9.1 Simple compaction model a) geometry and mechanical boundary conditions, b) hydraulic boundary conditions.

In the initial configuration, the model upper surface is considered to be a free surface, i.e. the mechanical pressure $P=0$ and the fluid pressure $p_f=0$ at $y=0$.

Due to sedimentation, which is considered to occur at a constant rate, the studied model is brought to depth by applying on the upper surface a loading which corresponds to :

- the weight of the sediment column saturated by water (applied using *LICHA* pressure elements, see *LAGAMINE* reference manual for details) considering an apparent specific mass ρ_a which is constant,
- the fluid pressure corresponding to the weight of the water column (applied using *DISPL* function, see *LAGAMINE* reference manual for details).

Of course, this is a simplification of real phenomena as in reality, the apparent specific mass of the sediment is function of the depth of burial and the correct modelling of the compaction process is much more complex [LAMOUREUX-VAR, 1997].

Nevertheless, the main goal of the present simulation is to evaluate first order effects of compaction processes with the interactions between a fault and the surrounding porous domain.

To this purpose, the boundary conditions presented on figure 9.1a and 9.1b are considered. It is important to point out that in this model, the fault acts both as a mechanical (displacement) discontinuity and a hydraulic discontinuity (pressure) through the Coulomb law and the Darcy flow law within the interface.

The mechanical behaviour is considered to be frictional elastoplastic (*PLASOL* law presented in chapter 2) with a Van Eekelen yield surface. Mechanical parameters are reported in table 9.1. Again, such behaviour is not very realistic for underconsolidated materials, it would be more realistic to chose a Cam Clay type of model as such model is able to :

- represent plastic collapse under isotropic loading, which is not the case for the Van Eekelen (nor for Drucker-Prager) model,
- account for the non linear relation between the volumetric strain and the pressure which is commonly experimentally observed on clays materials.

Coulomb contact law is considered for the fault. It is recalled that calculations are carried out on the effective stress tensor for the porous media, and in effective pressure/total shear stress for the frictional contact (see chapter 3 for details). The discretisation (see figure 9.2) is made up of 1064 nodes and 958 *CSOL2* coupled elements (4 integration points) described in chapter 3.

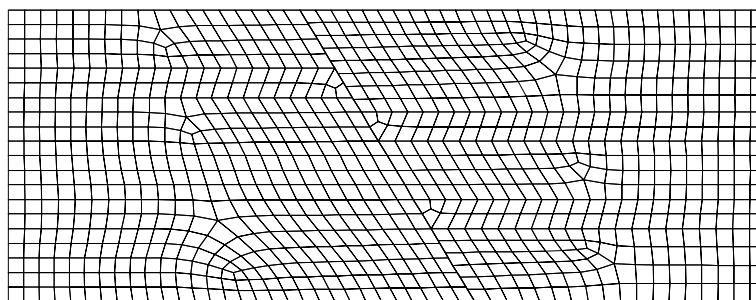


Figure 9.2 Mesh of the simple compaction model (1064 nodes, 958 *CSOL2* elements with 4 nodes and 4 integration points).

Table 9.1 Mechanical parameters of the compaction model

	ρ_s	E' (MPa)	ν'	c' (MPa)	ϕ' (°)	ψ' (°)	K_P (MPa)	K_τ (MPa)	μ'
Sand	2650	200	0.25	10	35	10			
Shales	2700	100	0.20	1	25	10			
Fault				0	30	0	10	10	0.57

Table 9.2 Hydraulic parameters of the compaction model

	ρ_f	K_f (GPa)	n	K (m.s ⁻¹)	T_t (m.s ⁻¹ .Pa ⁻¹)
Sand	1000	3	0.5	10 ⁻⁶	
Shales	1000	3	0.5	10 ⁻¹¹	
Fault					Variable

The hydraulic behaviour of the porous media is considered to follow Darcy flow law given in equation (3.60). Water compressibility is taken into account. The initial porosity is chosen equal to 0.5 in both the sand and shales. Flow parameters are reported in table 9.2. The shales permeability is chosen 10⁵ times smaller than the sand permeability, which is a realistic value for shales.

The fault is supposed to be impermeable in the longitudinal direction, but with a transverse hydraulic transmissivity T_t , which gives a transverse fluid velocity v_t following

$$v_t = T_t(p_f^F - p_f^S) \quad (9.1)$$

where p_f^F and p_f^S represent the fluid pressure on each side of the contact (the superscript ^S refers to the solid side and the superscript ^F refers to the foundation side). Two models have been studied : in the first one the fault is transversally impermeable (i.e. is very small) and in the second model the fault is very permeable ($T_t=10^{-7}$ m.s⁻¹.Pa⁻¹).

Two sedimentation rates have been considered in the simulation : the first one corresponds to a geologically realistic (though high) value of 0.5mm/year and the second one is a very exaggerated (and not geologically realistic) value of 5m/year.

Computations were performed using an initial pressure increment of 5Pa and increasing the step according to the convergence quality.

9.2.1 Models with low sedimentation rate

The models are studied here considering a sedimentation of 0.5mm/year for both the permeable and impermeable fault model.

As in the consolidation problem presented in section 3.4, it is expected here that the sediment which accumulate on top of the model induces a progressive loading of the model which will result both in a fluid overpressure (short term solution) and a compaction (vertical displacement) of the model according to the water compressibility and water expulsion (short and long term).

Due to the very low sedimentation rate, no fluid overpressure is generated for both models (or more precisely all the fluid overpressure has dissipated), whatever the reached total loading value. Thus, it is pointless to present graphical results of these modelling.

As the chosen permeability seems reasonable for both sand and shales, such result is questioning. It would tend to show that it is not possible to generate fluid overpressure in shales materials at reasonable sedimentation rates and considering a tectonically stable domain (tectonic compression has not been considered). However, this results must be interpreted with care remembering that the frictional behaviour considered is not very realistic for such materials. A Cam Clay type or Cap model would certainly give more volumetric strain (and consequently more fluid overpressure) than the present one.

9.2.2 Models with very high sedimentation rate

In order to generate some fluid overpressure, the sedimentation rate has been increased to the unrealistic value of 5m/year. Results are presented for the impermeable and permeable fault model.

In the permeable fault model (figure 9.3 and 9.4), there is no fluid overpressure compared to the imposed fluid pressure at top boundary in the upper layers of sand (including the intermediate layer of the left block). It is due to its high relative permeability compared to the shales, both for 500m of sedimentation ($t=100$ years, figure 9.3b) and for 1600m of sedimentation ($t=320$ years, figure 9.4b). Dissipation of fluid pressure was possible in the intermediate sand layer (left block) due to the relatively high fault transmissivity compared to the shales barrier. This is particularly visible on the representation of Darcy fluid velocity vectors (see figures 9.3a and 9.4a). Note that the layers in which the intensity of Darcy velocity is comparable are plotted together. It explains why the three upper sand layers are plotted separately from the other layers as the fluid velocity is much lower in the later. In the bottom layer of sand, there is a substantial fluid overpressure (almost twice the normal fluid pressure) as the pressure dissipation is inhibited by the relatively impermeable shales barriers. The volumetric strain (figure 9.3c and 9.4c) is consistent with the fluid pressure distribution. Note that plasticity is reached in the shales at 1600m of sedimentation (see figure 9.4c), and that there is almost no sliding along the fault.

In the impermeable fault model (figure 9.5 and 9.6), there is no fluid overpressure compared to imposed fluid pressure at top sand layers, as in the permeable fault model (see figure 9.5b). One difference comes from the extent of the overpressured zone which now affects all the

other sand and shales layers. This comes directly from the impermeability fault condition which now inhibits the pressure dissipation in the intermediate sand layer of the left block. (see plots of Darcy velocity vectors on figure 9.5a and 9.6a which are parallel to the contact). The most important effect of the impermeability condition of the fault comes from the coupling of fluid flow onto the frictional contact on the fault : the fluid overpressure has induced the sliding of the upper portion of the fault (figure 9.6) due to the reduction of the effective contact pressure. The faulting has then been induced by the build-up of fluid overpressure. This is the most interesting aspect of this simulation.

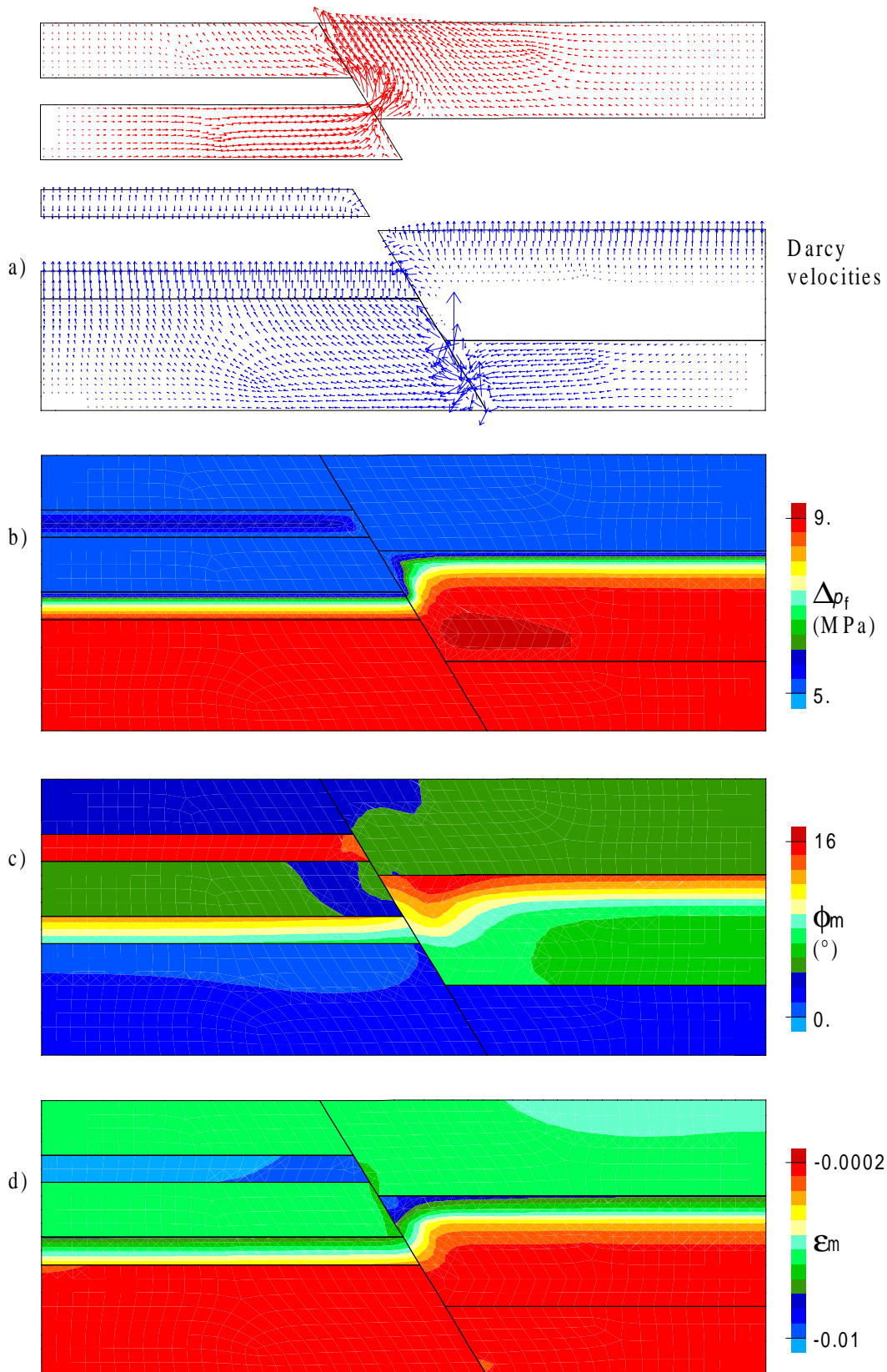


Figure 9.3 Results for the compaction model 1 (permeable fault) at $t=100$ years and for 500m of sedimentation : a) Darcy velocity vectors, b) fluid pressure variation, c) Coulomb's mobilised friction angle, d) volumetric strain.

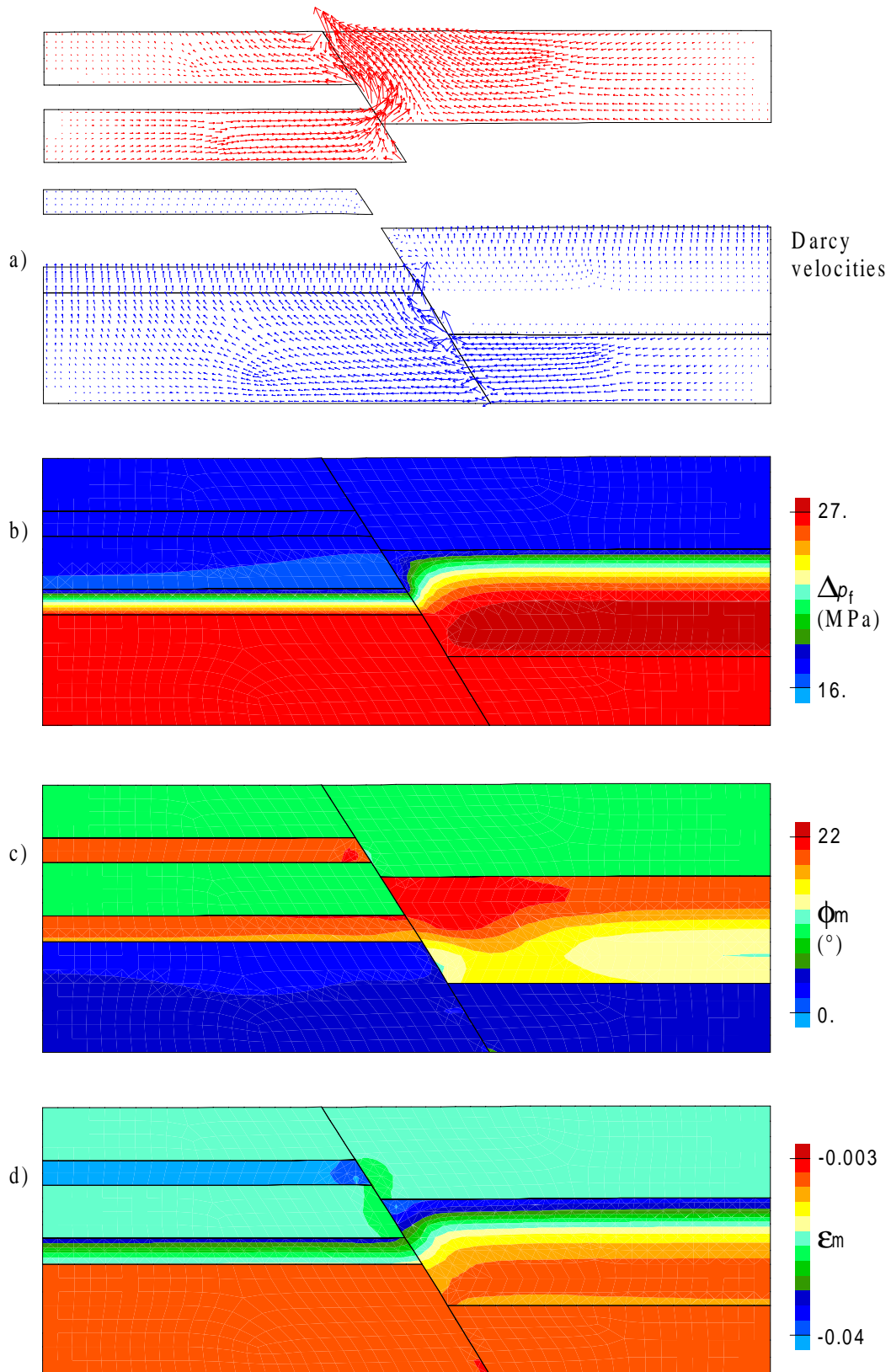


Figure 9.4 Results for the compaction model 1 (permeable fault) at $t=320$ years and for 1600m of sedimentation : a) Darcy velocity vectors, b) fluid pressure variation, c) Coulomb's mobilised friction angle, d) volumetric strain.

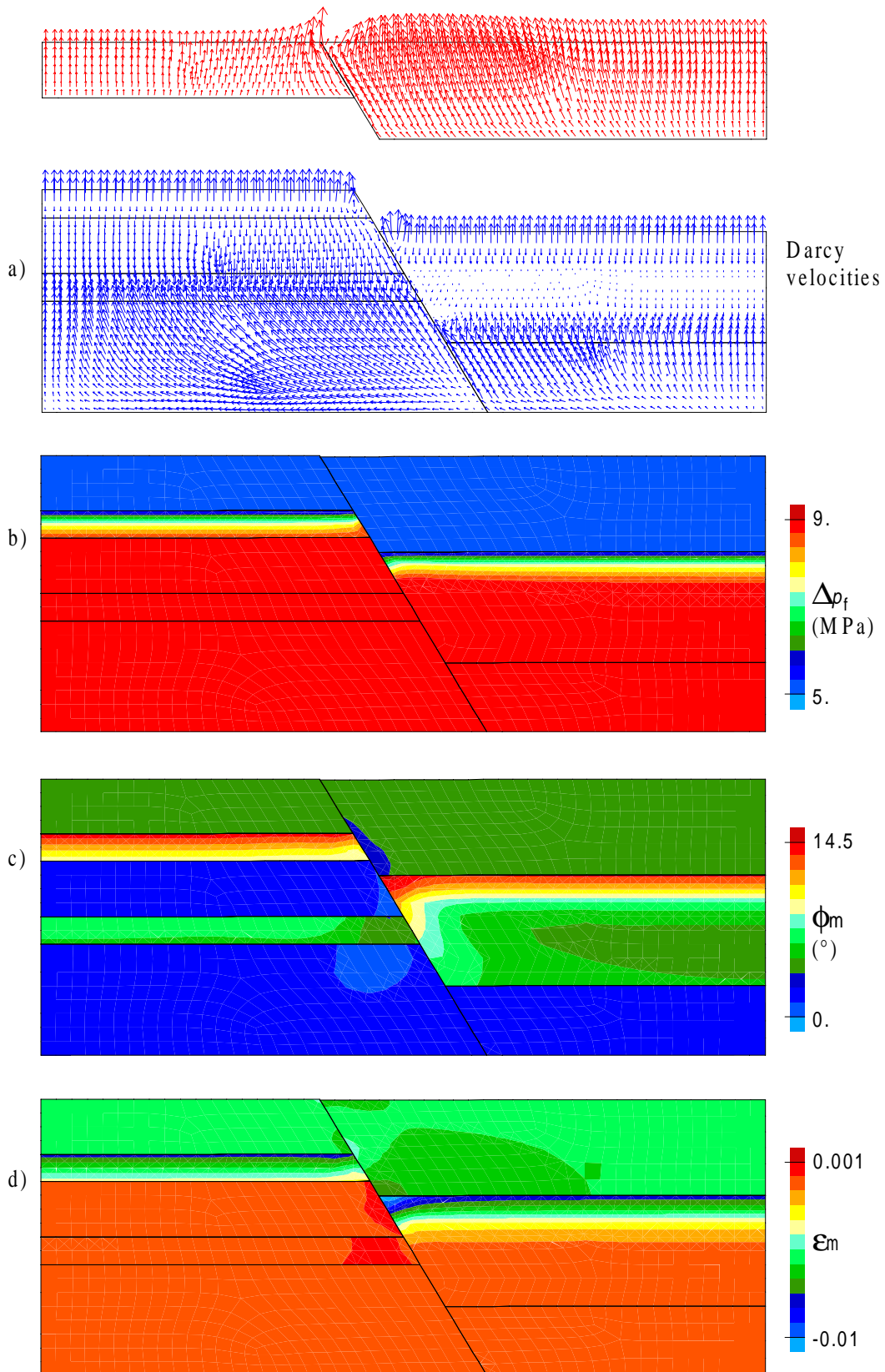


Figure 9.5 Results for the compaction model 1 (impermeable fault) at $t=100$ years and for 500m of sedimentation : a) Darcy velocity vectors, b) fluid pressure variation, c) Coulomb's mobilised friction angle, d) volumetric strain.

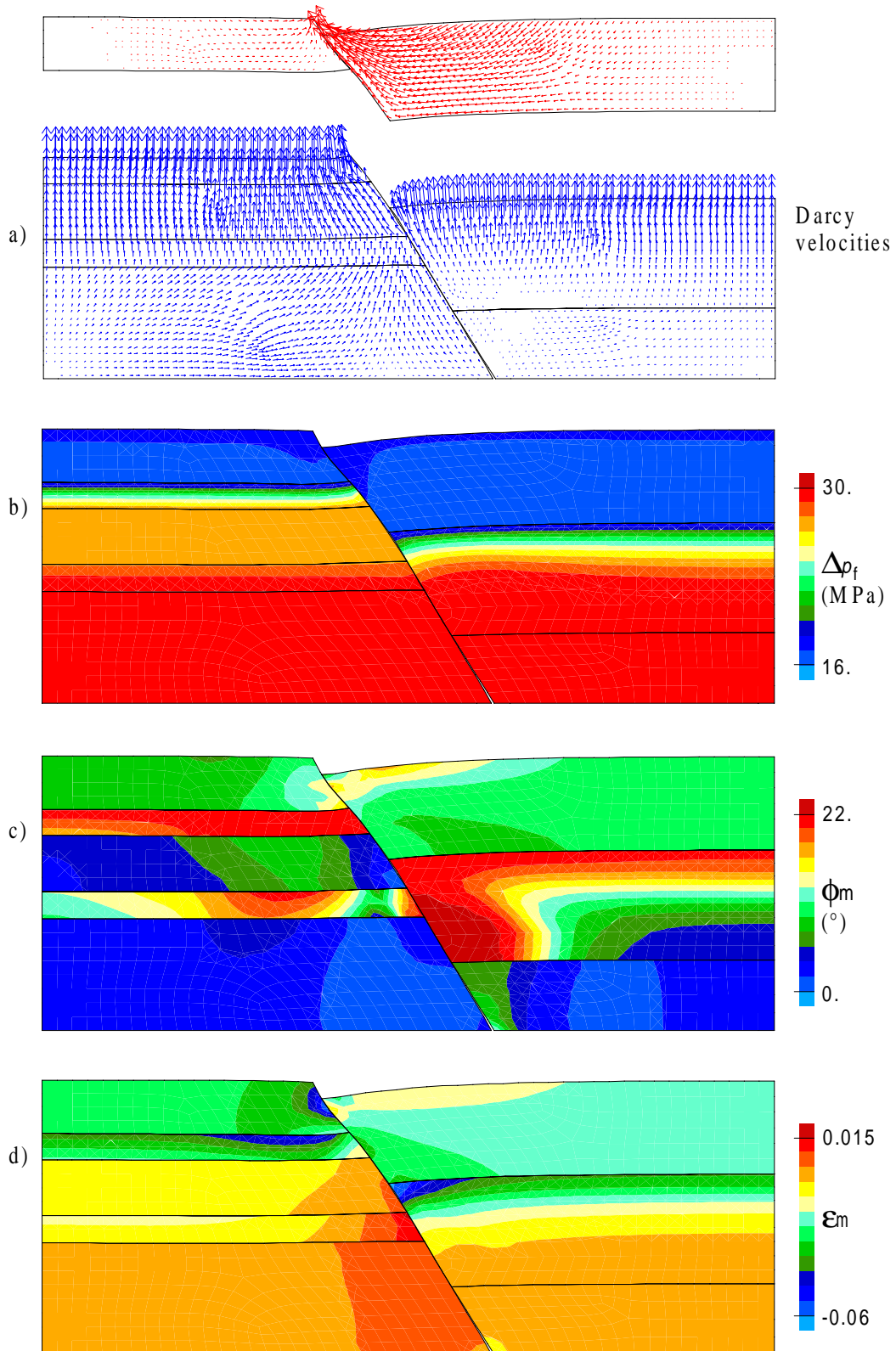


Figure 9.6 Results for the compaction model 1 (impermeable fault) at $t=320$ years and for 1600m of sedimentation : a) Darcy velocity vectors, b) fluid pressure variation, c) Coulomb's mobilised friction angle, d) volumetric strain.

9.3 Conclusion

The simple and simplistic simulations performed in this chapter aimed to show the interest and potentiality of taking into account the coupling between mechanics and fluid flow for geological problems such as compaction.

As mentioned throughout the chapter, the presented simulation did not aim to present a refined study on such interactions as the mechanical behaviour considered was not very suitable for the represented rock materials. A Cam Clay or Cap model should give more reliable and realistic results than the purely frictional model used. Although, approximations were made to represent the overlying sediments which were considered to have a constant specific mass. Thus, the hydraulic and mechanical boundary condition chosen at the upper surface can be easily criticised.

Nevertheless, two interesting comments can be formulated from the presented models :

- It seems impossible, considering simple compaction, to generate fluid overpressure even in quite impermeable geological formation such as shales if reasonable geological sedimentation rates and simple frictional models are considered. The problem is that it is well known from field evidences (well bores) that such fluid overpressure must exist in such materials. This apparent discrepancy may come from the irrelevance of classical permeability measurements when considering very large time scales and from the inability of simple frictional laws to represent volumetric behaviour of shales. The influence of tectonic loading can also be invoked to explain partially such result.
- In the case where fluid pressure are generated, the flow behaviour of faults has a very important influence on the mechanical behaviour of this fault. Such effect could be modelled successfully in the presented simple model.

As a conclusion, the interaction between coupled behaviour of porous media and fault systems seems very promising for future applications. Particularly, a longitudinal permeability for the faults could also be considered, which could then give a better representation of the dual behaviour of fault in geological system which may either act as barriers or drains.

CHAPTER 10

General conclusions and perspectives

10.1 General conclusion

The first part of this work consisted in the development related to the finite element method in the particular context of structural and petroleum geology applications. The second part consisted in studying real application cases, using numerical algorithms developed in a theoretical framework. It summarises the multi-disciplinary aspect of this thesis.

The developed constitutive law (Van Eekelen criterion) has shown to be very efficient for the treated applications. Particularly, its superiority over the Drücker Prager model to predict more realistic stress states has been widely detailed, both on a theoretical point of view and through different application cases. It has also been shown that the choice of the yield criterion has a strong influence in problems with frictional contact. Although such type of model is not new, it is surprisingly not so used in geological applications. It is worth pointing out that the required additional programming effort and CPU cost are reasonable compared to more simple models, therefore such type of constitutive model is highly recommended for practical applications. Note also that this concept can be (and has been) extended to other yield criteria types such the modified Cam-Clay model for which similar advantages hold.

The quite simple elastoviscoplastic law used to simulate deep rocks (lower crust) has shown to reproduce quite accurately the time dependent natural phenomenon of diapirism. Following, the validity of the diapir model for the anorthosite emplacement is confirmed. Such simulation with very large strains has only been possible in the Lagrangian *LAGAMINE* finite element thanks to the quite efficient re-meshing algorithm developed. The re-meshing has also allowed a very good reproduction of some sandbox experiments in which strong strain localisation occurred. It can easily be imagined that this method could be used to study other geological problems involving large strains.

In the presented applications cases, the analysis of strain localisation and potential fracturing has been based on the study of several criteria (equivalent strain, kinematic indicator of localisation, Rice criterion, Wallace Bott stress shape ratio, principal stress direction). It has been shown that these criteria are complementary, each of them adding its own contribution to the global interpretation of the phenomena. Although it is more tedious to analyse the results as they are more numerous, such richer information allows to better follow and interpret the physical processes which occur. A very interesting aspect of these simulations lies in the requirement of an inverse type of analysis : in both the sandbox and the Garret El Gueffoul models, a physically correct result (though not proved it is the unique one) has been obtained by a succession of try-errors, until the results matched the available control data; it led to an inverse estimation of the experimental basal friction angle for the sandbox model and to the highly probable reactivated origin for the western limb faults of the Garret El Gueffoul anticline.

Attention has also been paid to the coupling phenomena occurring between porous media and saturating fluids. Some extensions to finite strains formulation have been clarified, e.g. the definition of the storage law in finite strain context. The treated application has only shown potentiality and interest of such method in a simplistic imaginary case. In the same time it has also shown that, given the very long time scales considered in geological problems, the

classical definition or parameter meaning of the Darcy permeability law fails to explain observed overpressures. This simple example also highlighted the need to use more realistic model for describing the behaviour of shales such as Cam Clay family ones. However, the problem of shear band localisation in underconsolidated shales with such constitutive models is matter to controversy.

10.2 Perspectives

To open perspectives for future work, I would like to mention some of the aspects which I have not considered in this work, and which are certainly some of the key problems to be tackled or to be continued in future research.

As already mentioned, the problem of strain localisation which leads to an undefined shear band thickness is not yet fully solved, although some very important progress has been made recently. Particularly, the regularisation method based on gradient plasticity seems a promising track, although not yet mature for industrial applications. The interposition of interface elements is potentially another way of treating the post localisation behaviour, which could quite easily be integrated in a particular re-meshing procedure.

Some work needs also to be done for pursuing the development of new constitutive relations such as the incrementally non-linear laws, and the gap must be filled between their theoretical developments already advanced and their potential industrial applications.

Considering the modelling of diapirism or similar problems, some benefit should be gained considering more complex models including thermomechanical coupling (with a mechanical law explicitly dependent on temperature), non-linear viscosity and phases changes resulting from crystallisation process.

The development of multi-coupled models (thermohydromechanical, multiphase fluids) should give new fields of application and insights to new geological and petroleum geology problems (faulting, fluid migration, hydrocarbon generation) as it is already the case in the field of geomechanics (e.g. nuclear waste disposals).

Simulation of the geological compaction processes in which strain are quite large will certainly require to refine the large strain formulation given in this work, particularly the existing links between porosity, permeability, and Biot's coefficient. Such work would also require to develop more realistic methods of sedimentation than the one presented in chapter 9, e.g. by an algorithm which would generate material at the model top. This can be viewed again as a particular case of re-meshing method for which most of the concepts developed in this work still hold.

Following the same idea, the modelling of the hydrocarbon structure presented in chapter 8 was limited to fixed geometries, i.e. they neglected the erosion and sedimentation processes. This limitation could also be overcome by geometric modifications which could again be managed in the frame of re-meshing procedures.

APPENDIX

APPENDIX 1 - Storage law in finite transformation

Let us start from the definition of the increase in fluid mass content given in equation (3.6)

$$m = J \rho_f^B n^B - \rho_f^A n^A \quad (A1.1)$$

with the definition (3.7) of J

$$J = \frac{d\Omega^B}{d\Omega^A} \quad (A1.2)$$

Introducing the fluid state equation (3.14)

$$\rho_f^B = \rho_f^A \left(1 + \frac{p_f^B - p_f^A}{K_f} \right) \quad (A1.3)$$

into equation (A1.1) yields

$$m = J \left(\rho_f^A + \rho_f^A \frac{p_f^B - p_f^A}{K_f} \right) n^B - \rho_f^A \frac{d\Omega_v^A}{d\Omega^A} \frac{d\Omega^B}{d\Omega^B} \quad (A1.4)$$

which can be re-written

$$m = J \rho_f^A n^B + J \rho_f^A \frac{p_f^B - p_f^A}{K_f} n^B - J \rho_f^A \frac{d\Omega_v^A}{d\Omega^B} \quad (A1.5)$$

$$m = J \rho_f^A \left(n^B - \frac{d\Omega_v^A}{d\Omega^B} \right) + J \rho_f^A \frac{p_f^B - p_f^A}{K_f} n^B \quad (A1.6)$$

$$m = J \rho_f^A \left(\frac{d\Omega^B - d\Omega_s - d\Omega^A + d\Omega_s}{d\Omega^B} \right) + J \rho_f^A \frac{p_f^B - p_f^A}{K_f} \frac{d\Omega_v^B}{d\Omega^B} \frac{d\Omega^A}{d\Omega^A} \quad (A1.7)$$

$$m = J \rho_f^A \left(1 - \frac{1}{J} \right) + \rho_f^A \frac{p_f^B - p_f^A}{K_f} \frac{d\Omega_v^B}{d\Omega^A} \quad (A1.8)$$

$$m = \rho_f^A (J - 1) + \rho_f^A \frac{p_f^B - p_f^A}{K_f} \frac{d\Omega_v^B}{d\Omega^A} \frac{d\Omega^B}{d\Omega^B} \quad (A1.9)$$

$$m = \rho_f^A (J - 1) + \rho_f^A \frac{p_f^B - p_f^A}{K_f} J n^B \quad (A1.10)$$

Using the definition (3.58) of n^B , the later equation writes after simplification

$$m = \rho_f^A (J - 1) + \rho_f^A \frac{p_f^B - p_f^A}{K_f} ((J - 1) + n^A) \quad (A1.11)$$

This relation gives the variation of fluid mass content considering finite transformation. If infinitesimal transformation is considered, then $J \approx 1$ which implies that

$$(J - 1) + n^A \approx n^A \quad (A1.12)$$

In this case, equation (A1.11) becomes identical to equation (3.38).

APPENDIX 2 - Imposed displacement field on the lateral boundaries

It is often required to impose a displacement field \mathbf{u} at the lateral vertical boundaries which would induce a homogeneous and uniaxial strain field $\boldsymbol{\varepsilon}$ in the horizontal direction. There is no imposed strain in the vertical direction, then the problem can be studied in two dimensions under the plane strain assumption.

In the most simple case where the imposed displacement vector \mathbf{u} is either colinear or normal to the lateral boundaries of the model, the principal strain axes and the global axes coincide. For instance, the displacement vector \mathbf{u} which is colinear to the x_1 -axis writes

$$\mathbf{u} = \begin{bmatrix} u_1 \\ 0 \end{bmatrix} \quad (\text{A2.1})$$

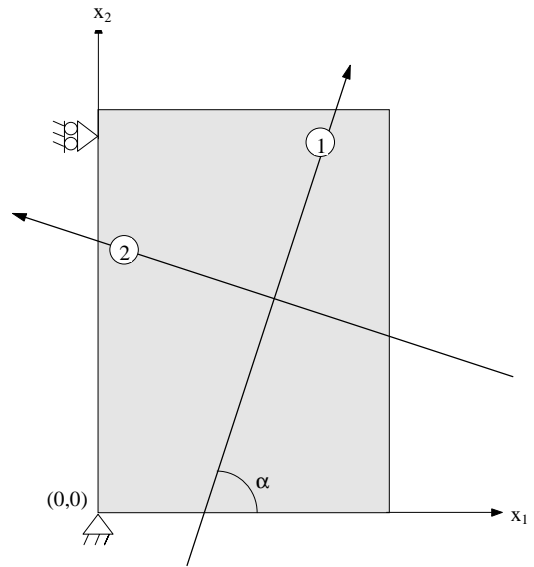


Figure A2.1 Interpretation.

The general definition of the infinitesimal strain tensor

$$\boldsymbol{\varepsilon} = \frac{1}{2} \left[\left(\frac{\partial \mathbf{u}}{\partial \mathbf{X}} \right) + \left(\frac{\partial \mathbf{u}}{\partial \mathbf{X}} \right)^T \right] \quad (\text{A2.2})$$

where \mathbf{X} is the co-ordinates vector in the reference configuration gives, for plane strain conditions

$$\boldsymbol{\varepsilon} = \begin{bmatrix} \frac{\partial u_1}{\partial X_1} & \frac{1}{2} \left(\frac{\partial u_1}{\partial X_2} + \frac{\partial u_2}{\partial X_1} \right) \\ \frac{1}{2} \left(\frac{\partial u_1}{\partial X_2} + \frac{\partial u_2}{\partial X_1} \right) & \frac{\partial u_2}{\partial X_2} \end{bmatrix} \quad (\text{A2.3})$$

Incorporating equation (A2.1) into (A2.3) yields after simplification

$$\boldsymbol{\varepsilon} = \begin{bmatrix} du_1 / dX_1 & 0 \\ 0 & 0 \end{bmatrix} = \begin{bmatrix} Sh & 0 \\ 0 & 0 \end{bmatrix} \quad (\text{A2.4})$$

where Sh is the principal strain component.

However, if the imposed displacement vector \mathbf{u} is not colinear nor normal to the lateral boundaries of the model, the principal strain axes and the global strain axes (\mathbf{x}, \mathbf{y}) do not coincide. As a result, the strain tensor $\boldsymbol{\varepsilon}$ expressed in global axes (\mathbf{x}, \mathbf{y}) is no longer diagonal

$$\boldsymbol{\varepsilon} = \begin{bmatrix} \varepsilon_{11} & \varepsilon_{12} \\ \varepsilon_{21} & \varepsilon_{22} \end{bmatrix} \quad (\text{A2.5})$$

In this case, the corresponding imposed displacement field u must be defined. Let us consider the uniaxial principal stress tensor $\boldsymbol{\varepsilon}^\alpha$ which is oriented at an angle α with respect to the \mathbf{x} axis

$$\boldsymbol{\varepsilon}^\alpha = \begin{bmatrix} Sh & 0 \\ 0 & 0 \end{bmatrix} \quad (\text{A2.6})$$

Such strain field is represented on figure A2.1, where the direction 1 corresponds to the eigen vector associated with the principal value Sh , and direction 2 corresponds to a nil strain direction. The relation between $\boldsymbol{\varepsilon}$ and $\boldsymbol{\varepsilon}^\alpha$ is given by

$$\boldsymbol{\varepsilon} = \mathbf{c}\boldsymbol{\varepsilon}^\alpha\mathbf{c}^T \quad (\text{A2.7})$$

where \mathbf{c} is the rotation matrix defined by

$$\mathbf{c} = \begin{bmatrix} \cos\alpha & \sin\alpha \\ -\sin\alpha & \cos\alpha \end{bmatrix} \quad (\text{A2.8})$$

which gives

$$\boldsymbol{\varepsilon} = Sh \begin{bmatrix} \cos^2\alpha & \sin 2\alpha / 2 \\ \sin 2\alpha / 2 & \sin^2\alpha \end{bmatrix} \quad (\text{A2.9})$$

Combining equation (10.3) with the latter one gives the components of the global strain tensor

$$\begin{aligned} \varepsilon_{11} &= \frac{\partial u_1}{\partial X_1} = Sh \cos^2 \alpha \\ \varepsilon_{22} &= \frac{\partial u_2}{\partial X_2} = Sh \sin^2 \alpha \\ \varepsilon_{12} &= \frac{1}{2} \left(\frac{\partial u_1}{\partial X_2} + \frac{\partial u_2}{\partial X_1} \right) = Sh \sin 2\alpha / 2 \end{aligned} \quad (\text{A2.10})$$

Using the condition that the strain tensor is constant over the considered domain,

$$\varepsilon_{11} = cste, \quad \varepsilon_{22} = cste, \quad \varepsilon_{12} = cste \quad (\text{A2.11})$$

Integration with boundary conditions as given in figure A2.1 gives eventually

$$\mathbf{u} = \begin{bmatrix} Sh(\cos^2 \alpha)X_1 \\ Sh(\sin^2 \alpha)X_2 + Sh(\sin 2\alpha)X_1 \end{bmatrix} \quad (\text{A2.12})$$

This is the displacement field to be applied to the model boundaries, which corresponds to the uniaxial strain tensor $\boldsymbol{\varepsilon}^\alpha$.

REFERENCES

- AELAAI M. R. - Contribution à l'étude de la modélisation des grandes déformations élasto-plastiques - *Thèse* de l'Université de Technologie de Compiègne, 1986.
- ANDERSON E. M. - The dynamics of faulting - 2nd edn Edinburgh: Oliver & Boyd, 1951.
- ARTHUR J.R.F, DUNSTAN T., AL-ANI Q.A.J.L. and ASSADI A. - Plastic deformation and failure in granular media - *Géotechnique*, 27, 53-74, 1977.
- ASHWAL L. - Anorthosites - Springer, Berlin, Heidelberg, 422p, 1993.
- BADSI M. - Failles et fractures dans le bassin de l'Ahnet. Apport du retraitement sismique - *Mémoire de DEA Géosciences*, ENSPM, Paris, 1993.
- BARNICHON J.D. - Finite element simulation of folded structures : theoretical models and application to lithospheric buckling - *Unpublished report*, Elf Aquitaine 64018 Pau (ref 317/93), 1994.
- BARNICHON J.D. and CHARLIER R. - Finite element modelling of the competition between shear bands in the early stages of thrusting - Strain localisation analysis and constitutive law influence - *Modern developments in structural interpretation, validation and modelling*, Geological Society Special Publication n°99, 235-250, 1996.
- BARNICHON J.D., HOFFER B., CHARLIER R., JONGMANS D. and DUCHESNE J.C. - The deformation of the Egersund-Ogna anorthosite massif, Southern Norway. Part B: Finite Element modelling of diapirism - submitted to *Tectonophysics*.
- BEEKMAN F., BADSI M. and SASSI W. - Faulting, reservoir fracturing and in situ stress in the Ahnet basin, Algeria : a finite element study of the Garret El Geffoul field - *Institut Français du Pétrole, report n°43447*, Division Géologie et Géochimie, 1997.
- BEUF S., BIJU DUVAL B., DE CHARPAL D., ROGNON R. and BENNACEF A. - Les grès du paléozoïque inférieur au Sahara. Sedimentation et discontinuités : évolution structurale d'un craton - *Publications Institut Français du Pétrole, College Sciences et Technologie du Pétrole* 18, Technip ed. Paris, 1971.
- BIOT M.A. - Theory of folding of stratified visco-elastic media and its implications in tectonics and orogenesis - *Geological Society of America Bulletin*, 72, 1595-1620, 1961.
- BIOT M.A. - Variational Lagrangean-thermodynamics of nonisothermal finite strain mechanics of porous solids and thermomolecular diffusion - *Int. J. Solids Structures*, 13, 579-597, 1977.
- BOTT M.H.P - The mechanisms of oblique slip faulting - *Geol. Mag.*, 96, 109-177, 1959.
- BOURGEOIS E. and DORMIEUX L. - Consolidation of a nonlinear poroelastic layer in finite deformations - *European Journal of Mechanics, A/Solids*, 15, 4, 575-598, 1996.
- BOUTECA M., SARDA J.P. and LAURENT J. - Rock mechanics contribution to the determination of fluid flow properties - *Second European Core Analysis Symposium (Eurocas II)*, London, 20-22May 1991.

- BOUTECA M. and SARDA J.P. - Mesure expérimentale des coefficients thermoporoélastiques - *Ecole de Mécanique des Milieux Poreux*, Aussois, organised by le Comité Français de Mécanique des Roches, 33-42, 1994.
- BURGER A., RECORDON E., BOVET D., COTTON L. and SAUGY B. - Thermique des nappes souterraines - Presses Polytechniques Romandes, 1985.
- BYERLEE J.D. - Friction of rocks - *Pure and Applied Geophysics*, 116, 615-626, 1978.
- CAMPBELL I.H., ROEDER P.L. and DIXON J.M. - Plagioclase buoyancy in basaltic liquids as determined with a centrifuge furnace - *Contrib. Mineral. Petrol.*, 67, 369-377, 1978.
- CARTER N.L. and TSENN M.C. - Flow properties of continental lithosphere - *Tectonophysics*, 136, 27-63, 1987.
- CESSOTTO S. and CHARLIER R. - Frictional contact finite elements based on mixed variational principles - *International Journal for Numerical methods in Engineering*, 36, 1681-1701, 1993.
- CHAMBON R. and CROCHEPEYRE S. - Daphnis : a model, consistent with CloE, for the description of post-localization behaviour - *Numerical Models in Geomechanics, Pietruszczak & Pande (eds)*, Balkema, Rotterdam, 187-192, 1997.
- CHAPMAN D.S. - Thermal gradient in the continental crust - *The nature of the lower continental crust, Geological Society Special Publication n°24*, 63-70, 1986.
- CHARLIER R. - Approche unifiée de quelques problèmes non linéaires de mécanique des milieux continus par la méthode des éléments finis - *Thèse de Doctorat, Université de Liège*, 1987.
- CHARLIER R. and CESCOTTO S. - Modélisation du phénomène de contact unilatéral avec frottement dans un contexte de grandes déformations - *Journal of Theoretical and Applied Mechanics (special issue, supplement)*, 7(1), 1988.
- CHARLIER R. and PIERRY J. - Finite element modelling of rock drilling - *Assessment and Prevention of Failure Phenomena in Rock Engineering* - Balkema Rotterdam, 921-926, 1993.
- CHARLIER R., RADU J.P. and BARNICHON J.D. - Water movement effect on the strain localisation during a biaxial compression - *Numerical Models in Geomechanics, Pietruszczak & Pande (eds)*, Balkema, Rotterdam, 219-224, 1997.
- COLLETTA B., LETOUZEY J., PINEDO R., BALLARD J.F. and BALE P. - Computerized X-ray tomography analysis of sandbox models: examples of thin-skinned thrust systems - *Geology*, 19, 1063-1067, 1991.
- COSSERAT E. and COSSERAT F. - Théorie des Corps Déformables - Herman, Paris, 1909.
- COUSSY O. - Mechanics of Porous Continua - Wiley, London, 1995.
- CRISFIELD M. A. - Plasticity computations using the Mohr-Coulomb yield criterion - *Eng. Comput.*, 4, 300-308, 1987.

-
- DAVY P. and COBBOLD P.R. - Experiments on shortening of a 4-layer model of the continental lithosphere - *Tectonophysics*, 188, 1-25, 1991.
- DE BORST R. and SLUYS L.J. - Localisation in a Cosserat continuum under static and dynamic loading conditions - *Computer Methods in Applied Mechanics and Engineering*, 90, 805-827, 1991.
- DE BORST R. - Gradient-dependent plasticity : formulation and algorithmic aspects - *International Journal for Numerical and Analytical Methods in Geomechanics*, 35, 521-539, 1992.
- DE BORST R. - A generalisation of J_2 -flow theory for polar continua - *Computer Methods in Applied Mechanics and Engineering*, 103, 347-362, 1993.
- DE BREMAECKER J.C. and BECKER E.B. - Finite element models of folding - *Tectonophysics*, 50, 349-367, 1978.
- DESAI C.S. and SIRIWARADANE H.J. - Constitutive laws for engineering materials with emphasis on geologic materials - Prentice-Hall, 1984.
- DESEGAULX P., BOBINEAU J.P., ZALESKI S. and CHEDMAIL J.F. - Numerical modelling of tectonical deformations - *Expanded abstract*, Society of Exploration Geologists annual meeting, 1991.
- DETOURNAY and CHENG - Fundamentals of poroelasticity - *Comprehensive Rock Engineering: Principles, Practice and Projects*, vol. 2, Pergamon Press, 1991.
- DRÜCKER D.C. and PRAGER W. - Soil mechanics and plasticity analysis or limit design - *Quarterly Applied Mathematics*, 10 (2), 157-165, 1952.
- DUCHESNE J.C. and MAQUIL R. - The Egersund-Ogna massif - *The Geology of Southernmost Norway: an excursion guide. Norges Geol. Unders. Special publication*, 1, 50-56, 1987.
- DUCHESNE J.C. and SCHÄRER U. - The anorogenic Rogaland anorthosites and their possible relation to granite petrogenesis in S-Norway - Submitted to *Terra Nova*.
- DYDUCH M. - Adaptive methods in finite element simulation of metal forming processes - *Thèse de Doctorat*, Université de Liège, 1996.
- ENDIGNOUX L. and WOLF S. - Thermal and kinematic evolution of thrust basins : a 2D numerical model - *Petroleum and Tectonics in Mobile Belts*, J. Letoueuzy (Ed.) and Editions Technip, Paris, 181-192, 1990.
- ENGLAND R.W. - The identification of granitic diapirs - *Journal of the Geological Society*, London, 147, 931-933, 1990.
- FJAER E., HOLT R.M., HORSRUD P., RAAEN A.M. and RISNES R. - Petroleum related Rock mechanics - *Developments in Petroleum Sciences* 33, Elsevier, 1992.
- GALLIMARD L., LADEVEZE P. and PELLE J.P. - Error estimation and adaptivity in elastoplasticity - *International Journal for Numerical and Analytical Methods in Geomechanics*, 39, 189-217, 1996.
-

- GENS A. and POTTS D.M. - Critical state models in computational geomechanics - *Eng. Comput.*, 5, 178-197, 1988.
- GIBBS A.D. - Balanced cross-section construction from seismic sections in areas of extensional tectonics - *Journal of Structural Geology*, 5, 2, 153-160, 1983.
- GODINAS A. - Personal communication, 1995.
- GUIRAUD M., LABORDE O. and PHILIP H. - Characterization of various types of deformation and their corresponding deviatoric stress tensors using microfault analysis - *Tectonophysics*, 170, 289-316, 1989.
- GUIRAUD R. and MAURIN J.C. - Early cretaceous rifts of western and central Africa, an overview - *Tectonophysics*, 266, 101-119, 1992.
- HABRAKEN A.M.H. - Contribution à la modélisation du formage des métaux par la méthode des éléments finis - *Thèse de Doctorat, Université de Liège*, 1989.
- HABRAKEN A.M.H. and CESCOTTO S. - An automatic remeshing technique for finite element simulation of forming processes - *International Journal for Numerical and Analytical Methods in Engineering*, 30, 1503-1525, 1990.
- HABRAKEN A.M.H. and CESCOTTO S. - Contact between deformable solids. The fully coupled approach - *Journal of Mathematical and Computer Modelling (Special issue : Recent advances in contact and impact mechanics)*, 1996.
- HALL J. - The physical properties of layered rocks in deep continental crust - In : *The nature of the lower continental crust, Geological Society Special Publication n°24*, 51-62, 1986.
- HAMMAD W.I. - Modélisation non linéaire et étude expérimentale des bandes de cisaillement dans les sables - *Thèse de Doctorat, Université Joseph Fourier, Grenoble I (Mécanique)*, 1991.
- HAVENITH H.B., JONGMANS D. and DUCHESNE J.C. - The deformation of the Egersund-Ogna anorthosite massif, Southern Norway. Part A: a structural analysis - submitted to *Tectonophysics*.
- HEDBERG H. - Gravitational compaction of clays and shales - *American Journal of Sciences*, 31, 241-287, 1936.
- HOFFER B. - Modélisation numérique de la mise en place d'un pluton anorthositique par diapirisme - *Unpublished Geology Civil Engineer thesis, Liège University*, 1996.
- HUBBERT M.K. - Theory of scale models as applied to the study of geologic structures - *Bulletin of the Geological Society of America*, 48, 1459-1520, 1937.
- HUSTON R.L. and PASSERELLO C.E. - Finite element methods - *Mechanical engineering*, 25, Faulkner and Menkes Ed., 1984.
- JACKSON M.P.A. and SENI S.J. - Evolution of salt structures, East Texas Diapir Province, 2. Patterns and rates of halokinesis - *American Association of Petroleum Geologists Bulletin*, 67, 8, 1245-1274, 1983.

- KLEMME H.D. and ULMISHEK G.F. - Effective petroleum source rocks of the world : stratigraphic distribution and controlling depositional factors - *American Association of Petroleum Geologists Bulletin*, 75, 1809-1851, 1991.
- KOYI H. - Mushroom diapirs penetrating overburdens with high effective viscosities - *Geology*, 19, 1229-1232, 1991.
- LAMOUREUX-VAR V. - Modélisation de la compaction dans les bassins sédimentaires. Approche mécanique - *Thèse de Doctorat*, Ecole Polytechnique, 1997.
- LANIER J. - Special stress paths along the limit surface of a sand specimen with the use of a true triaxial apparatus - *Advanced triaxial testing of soil and rocks*, ASTM STP 977, Donaghe, Chaney, Silver Ed., ASTM, 859-869, 1988.
- LI X. and CESCOTTO S. - Finite element method for gradient plasticity at large strains - *International Journal for Numerical Methods in Engineering*, 39, 619-633, 1996.
- LONGHI J., FRAM M.S., VANDER AUWERA J. and MONTIETH J.N. - Pressure effects, kinetics, and rheology of anorthositic and related magmas - *Amer. Mineral.*, 78, 1016-1030, 1993.
- MACGREGOR D.S. - The hydrocarbon systems of North Africa - *Marine and Petroleum Geology*, 13, 3, 329-340, 1996.
- MALAVIEILLE J. - Modélisation expérimentale des chevauchements imbriqués : application aux chaînes de montagnes - *Bulletin de la Société Géologique de France*, XXVI, 1, 129-138, 1984.
- MARTIGNOLE J. - Tectonic setting of anorthositic complexes of the Grenville Province, Canada - *Petrology and geochemistry of magmatic suites of rocks in the continental and oceanic crusts. A volume dedicated to Jean Michot*. ULB-MRAC, Brussels, 3-18, 1996.
- MARTINOD J. - Instabilités périodiques de la lithosphère (flambage, boudinage en compression et en extension) - *Mémoires et Documents du Centre Armoricaïn d'Etude Structurale des Socles n°44*, 1991.
- MATSUOKA H. and NAKAI T. - A new failure condition for soils in three-dimensional stresses - *Proceedings IUTAM conference Deformation and Failure of Granular Materials*, Delft, 253-263, 1982.
- NETTLETON L.L. - Fluids mechanics of salt domes - *American Association of Petroleum Geologists Bulletin*, 18, 9, 1175-1204, 1934.
- NETTLETON L.L. - Recent experimental and geophysical evidence of mechanics of salt-dome formation - *American Association of Petroleum Geologists Bulletin*, 27, 1, 51-63, 1943.
- NIEUWLAND D.A. and WALTERS J.V. - Geomechanics of the South Furious field. An integrated approach towards solving complex structural geological problems, including analogue and finite-element modelling - *Tectonophysics*, 226, 143-166, 1993.

- ORD A. and HOBBS B.E. - The strength of the continental crust, detachment zones and the development of plastic instabilities - *Tectonophysics*, 158, 269-289, 1989.
- PALUDAN J., HANSEN U.B. and OLESEN, N.Ø. - Structural evolution of the Precambrian Bjerkreim-Sokndal intrusion, South Norway - *Norsk Geolog. Tidsskr.*, 74, 185-198, 1994.
- PAMIN J. - Gradient-dependent plasticity in numerical simulation of localization phenomena - *PhD Delft University Press, the Netherlands*, 1994.
- PARRISH D.K. - A non-linear finite element fold model - *American Journal of Science*, 273, 318-334, 1973.
- PEERLINGS R.H.J., DE BORST R., BREKELMANS W.A.M., DE VREE J.H.P and SPEE I. - Some observations on localisation in non-local and gradient damage models - *European Journal of Mechanics*, 3, 1996.
- PELTZER G., TAPPONIER P. and COBBOLD P. - Les grands décrochements de l'Est Asiatique, évolution dans le temps et comparaison avec un modèle expérimental - *Comptes Rendus de l'Académie des Sciences, Paris*, 294, 1341-1348, 1982.
- PIERRY J. - Modélisation des bandes de cisaillement et adaptation de maillages. Application à la coupe des roches - *Thèse de Doctorat, Université de Liège*, 1997.
- POLIAKOV A.N.B., CUNDALL P.A., PODLADCHIKOV Y.Y. and LYAKHOVSKY V.A. - An explicit inertial method for the simulation of viscoelastic flow : an evaluation of elastic effects on diapiric flow in two and three-layers models - *Flow and creep in the solar system: Observations, Modelling and Theory*, D.B. Stone and S.K. Runcorn (eds.), Kluwer Academic Publishers, 1993.
- POLIAKOV A.N.B., PODLADCHIKOV Y.Y., DAWSON E.CH. and TALBOT C.J. - Salt diapirism with simultaneous brittle faulting and viscous - *Salt tectonics, Geological Society Special Publication n°100*, 291-302, 1996.
- RADU J.P. and CHARLIER R. - Modelling of the hydromechanical coupling for non-linear problems: fully coupled and staggered approaches - *8th International Conference of the International Association for Computer Methods and Advances in Geomechanics*, West Virginia, USA, May 1994.
- RAMBERG H. - Gravity, Deformation and the Earth's Crust - Academic Press, London, 1981.
- RAYNAUD S. - Les premiers stades de la déformation dans une zone de relais entre décrochements : exemples naturels et expérimentaux - *Bulletin de la Société Géologique de France*, III 3, 583-590, 1987.
- RICE J.R. - The localization of plastic deformation - *Theoretical and applied mechanics, Proceedings of the 14th IUTAM congress*, Delft, The Netherlands, 207-220, 1976.
- RICHARD P., MOCQUET B. and COBBOLD P.R. - Experiments on simultaneous faulting and folding above o basement wrench fault - *Tectonophysics*, 188, 133-141, 1991.

- RITZ J.F. and TABOADA A. - Revolution stress ellipsoids in brittle tectonics resulting from an uncritical use of inverse methods - *Bulletin de la Société Géologique de France*, 164, 4, 519-531, 1993.
- RIVES T., RAWNSLEY K.D. and PETIT J.P. - Analogue simulation of natural orthogonal joint set formation in brittle varnish - *Journal of Structural Geology*, 16, 3, 419-429, 1994.
- RÖNNLUND P. - Viscosity estimates from natural Rayleigh-Taylor instabilities - *Terra Nova*, 1, 344-348, 1989.
- SASSI W., COLLETTA B., BALE P. and PAQUEREAU T. - Modelling of structural complexity in sedimentary basins: the role of pre-existing faults in thrust tectonics - *Tectonophysics*, 226, 97-112, 1993.
- SASSI W. and FAURE J.L. - Role of faults and layer interfaces on the spatial variation of stress regimes in basins - *Tectonophysics*, 266, 101-119, 1997.
- SCHÄRER U., WILMART E. and DUCHESNE J.C. - The short duration and anorogenic character of anorthosite magmatism : U-Pb dating of the Rogaland complex, Norway - *Earth Planetary Science Letters*, 139, 335-350, 1996.
- SCHMELING H. - On the relation between initials conditions and late stages of Rayleigh-Taylor instabilities - *Tectonophysics*, 133, 65-80, 1987.
- SCHWEIGER H.F. - On the use of Drücker-Prager failure criteria for earth pressure problems - *Computers and Geotechnics*, 16, 223-246, 1994.
- SIBSON R.H. - Frictional constraint on thrust, wrench and normal faults - *Nature*, 249, 542-544, 1974.
- SIMO J.C., TAYLOR R.L. - Consistent tangent operators for rate-independent elastoplasticity - *Computer Methods in Applied Mechanics and Engineering*, 48, 101-118, 1985.
- TALBOT C.J., RÖNNLUND P., SCHMELING H., JACKSON M.P.A. and KOYI H. - Diapiric spoke patterns - *Tectonophysics*, 188, 187-201, 1991.
- TAYLOR D. - *Fundamentals of Soil Mechanics* - London Wiley, 1948.
- TRUSHEIM F. - Mechanisms of salt migration in North Germany - *American Association of Petroleum Geologists Bulletin*, 44, 9, 1519-40, 1960.
- TURCOTTE D.L. and SCHUBERT G. - *Geodynamics Applications of Continuum Physics to Geological Problems* - John Wiley & Sons, New-York, 1982.
- VANDER AUWERA J. and LONGHI J. - Experimental study of a jotunite (hypersthene monzodiorite): constraints on the parent magma composition and crystallization conditions (P, T, fO₂) of the Bjerkreim-Sokndal layered intrusion - *Contrib. Miner. Petrol.*, 118, 60-78, 1994.

- VAN EEKELEN H.A.M. - Isotropic yield surfaces in three dimensions for use in soil mechanics - *International Journal for Numerical and Analytical Methods in Geomechanics*, 4, 98-101, 1980.
- VILOTTE J.P., POZZI J.P., PHILIPPE C., PASTOR M., ZIENKIEWICZ O.C., DAUDRE B. and BARDES P. - Modes localisés de la déformation dans les matériaux crustaux - Rapport scientifique, GRECO Géomatériaux, 1990.
- VIGNERESSE J.L. - Crustal regime of deformation and ascent of granitic magma - *Tectonophysics*, 249, 187-202, 1995.
- WALLACE R.E. - Geometry of shearing stress and relation to faulting - *J. Geol.*, 59, 118-130, 1951.
- WANG X.C. - Modélisation numérique des problèmes avec localisation en bandes de cisaillement - *Thèse de Doctorat*, Université de Liège, 1993.
- WOIDT W.D. - Finite element calculations applied to salt-dome analysis - *Tectonophysics*, 50, 369-386, 1978.
- ZALESKI S. and JULIEN P. - Numerical simulation of Rayleigh-Taylor instability for single and multiple salt diapirs - *Tectonophysics*, 206, 55-69, 1992.
- ZHU Y. - Contribution to the local approach of fracture in solid dynamics - *Thèse de Doctorat*, Université de Liège, 1992.
- ZIENKIEWICZ O.C. and TAYLOR R.L. - *The Finite Element Method* - fourth edition, 1987.
- ZIENKIEWICZ O.C. and HUANG M. - Localization problems in plasticity using finite elements with adaptive remeshing - *International Journal for Numerical and Analytical Methods in Geomechanics*, 19, 127-148, 1995.